Single-cell studies of *Mycobacterium smegmatis* cell cycle using time-lapse fluorescence microscopy

Thèse N° 9756

Joëlle Xiao Yuan VEN

2019

ÉCOLE POLYTECHNIQUE
FÉDÉRALE DE LAUSANNE

Acknowledgements

I would also like to thank my students. Camille Perret and Shinji Kondo for being my first team with whom the first mission was to put a condom on the AFM. Ian Andrews for beating me and letting me win at badminton! Marie Malier for the being part of the cloning team and for the amazing chocolate cakes!

I would also like to thank my friends (particulièrement Marine, Virginie, Léa, Laureline, Julie, Livia et Alice et les +1 bien sûr! Evelyne and Adri) for the amazing time we have together, making my life great even after a rough week. I would especially want to thank Damien Jacot for his talk about Gibson assembly, which revolutionized my way of cloning as well as Simon Blanchoud for his help.

J'aimerais aussi remercier Marie-José (ou Mimi!) pour tous les messages de soutien et le temps passé ensemble à cueillir des herbes ou partager de délicieux repas!

Nothing would have been possible without the support of my family who I love so much. Even when we are spread from Sydney, Hong Kong and Zurich I can rely on you and you will always be close in my heart.

And last but not least, my rock(star), Jonathan who I deeply thank for his patience and the joy he brings me in life with or without chocolates!

Lausanne, October 21th 2019

Abstract

Cell division is one of the most primordial cellular processes and is essential for life propagation. It is composed of crucial events, namely genome duplication, chromosomes segregation and membrane separation. Failure of these processes will have dramatic impacts on the development of any organisms, including cell death, polyploidy, or cell cycle arrest. In the case of bacterial pathogens, blocking cell division efficiently using targeted drugs is of interest to cure bacterial infections. However, despite its ancestral origin, the mechanisms of cell division have diverged amongst organisms. Given its crucial role, as well as the potential therapeutic applications, cell division is an intensive field of research and many aspects are yet to be fully understood.

Amongst bacteria, the phyla Proteobacteria and Firmicutes have been intensively studied using their respective model organisms *Escherichia coli* and *Bacillus subtilis*. However, there is a paucity of research on cell division in Actinobacteria, the phylum that contains the world's leading pathogen, *Mycobacterium tuberculosis*. In particular, the molecular players involved in the process of chromosome segregation and the timing of cell division have not been fully investigated. In the well-studied bacteria *E. coli* and *B. subtilis* the Min system determines the division site localization, while the nucleoid occlusion system (Noc or SlmA, respectively) determines the timing of division. In mycobacteria, however, no homologs for the Min or Noc systems have been identified thus far. However, the partitioning (*par*) genes are currently thought to be responsible for symmetric chromosome segregation. In addition, FtsK has been identified as a homolog of the *B. subtilis* protein SpoIIIE, which is responsible for rescuing DNA in the forming septum and pulling it in the forespore during starvation-induced sporulation. Overall, the role and dynamics of DNA, where FtsK might play a role, during mycobacterial cell division, still remain to be uncovered.

Current methods to study DNA localization using snapshot microscopy typically utilise DNA dyes, such as DAPI, Hoechst, or SYTO. However, these compounds impair cell growth, preventing the dynamic study of mycobacterial division. To circumvent this shortcoming, I constructed a *Mycobacterium smegmatis* reporter strain expressing a Dendra2 fusion protein in-frame to the histone-like protein Hlp, and compared it to conventional DNA dyes. Additionally, I characterized FtsK and, for the first time, demonstrated its essentiality in *M. smegmatis*. As FtsK is essential I adapted a dual repression system to knock down FtsK, which proved to be a synthetic rescue with the *par* genes deletion. Using a custom-made microfluidic device and long-term time-lapse microscopy, the distribution and dynamics of both Hlp and FtsK fluorescent reporter proteins were followed at the single-cell level. This approach allowed the spatial and temporal characterization of these proteins with respect to other septal genes in wild-type cells as well as in Δ*par* mutants. Finally, I propose a new model where the *par* genes are important for chromosome orientation and FtsK is important for chromosome segregation.

Altogether, this thesis represents a step forward towards a better understanding of the mechanisms underlying cell division in mycobacteria and in the long-term, a potential source of novel treatments to control the division of *M. tuberculosis*, for instance by targeting FtsK.

Keywords: Bacterial cell division, cell cycle, chromosome segregation, NAPs, Hlp, FtsK, ParA, ParB, time-lapse microscopy.

Résumé

La division cellulaire est un des procédés cellulaires le plus primordial et essentiel pour la propagation de la vie. Elle est composée d'étapes cruciales: la duplication du génome, la ségrégation des chromosomes ainsi que la separation de la membrane. L'échec de n'importe lequel de ces processus auront un impact drastique sur le dévelopement de n'importe quel organisme, allant de la mort cellulaire à la polyploïdie ou encore l'arrêt du cycle cellulaire. Dans le cas des bactéries pathogènes, bloquer la division cellulaire efficacement en utilisant des drogues ciblées est intéressant pour guérir des infections bactériennes. Cependant malgré son origine ancestrale, les mécanismes de la division cellulaire ont divergé selon les organismes. Etant donné son rôle crucial ainsi que les applications thérapeutiques potentielles, la division cellulaire est un champ de recherche intensif et nombreux de ses aspects restent à être complétement compris.

Parmi les bactéries, les phyla Protéobactéries et Firmicutes ont été intensivement étudiées en utilisant leurs organismes modèles respectifs *Escherichia coli* et *Bacillus subtilis*. Cependant un manque de recherche existe sur la division cellulaire des Actinobactéries, le phylum qui contient le principal pathogène terrestre, *Mycobacterium tuberculosis*. En particulier, les acteurs moléculaires impliqués dans le processus de la segregation des chromosomes et de la dynamique de la division cellulaire n'ont pas encore été totalement investigués. Dans les bactéries très étudiées telles que *E. coli* et *B. subtilis* le système Min détermine la localisation du site de division alors que le système d'occlusion du nucléoide (respectivement Noc et SlmA) déterminent le moment de la division. Cependant, dans les mycobactéries aucun homologue pour les systèmes Min ou Noc n'ont été identifiés jusqu'à present. Cependant, les genes de partition (*par*) sont actuellement considérés comme responsables de la ségrégation symétrique des chromosomes. De plus, FtsK a été identifié comme un homologue de la protein appartenant à *Bacillus subtilis*, SpoIIIE, responsable de sauver l'ADN piégé dans le septum en formation et de le tirer dans le pré-spore pendant la sporulation suite à un manque de ressources. Globallement, le rôle et la dynamique de l'ADN, où la protéine

FtsK pourrait jouer un role, durant la division cellulaire des mycobactéries est encore à découvrir.

Les méthodes actuelles pour étudier la localisation de l'ADN en utilisant la microscopie par snapshot utilisent typiquement des colorants d'ADN tels que DAPI, Hoechst ou SYTO. Cependant, ces composés inhibent la croissance cellulaire par conséquent empêchant l'étude dynamique de la division des mycobactéries. Pour éluder ce problème, j'ai construit un reporter exprimant la protein fluorescente Dendra2 fusionnée dans le cadre à la protéine "histone-like" (Hlp) de *Mycobacterium smegmatis* et je l'ai comparée aux colorants de l'ADN conventionnels.

De plus, j'ai characterisé FtsK et démontré pour la première fois son essentialité dans *M. smegmatis*. Comme FtsK est essentiel, j'ai adapté un système de répression double pour réprimer l'expression de FtsK qui a prouvé être un sauvetage synthétique avec la délétion des gènes *par*. En utilisant un device microfluidique fait sur mesure et la microscopie par time-lapse sur une période de temps étendue, la distribution et dynamique des reporters fluorescents à la fois de Hlp et FtsK ont été suivies au niveau de la cellule. Cette approche a permis la characterization spatiale et temporelle de ces protéines par rapport à d'autres genes du septum, dans des cellules de type sauvage ainsi que dans les mutants Δ*par*. Finallement je propose un nouveau modèle où les gènes *par* sont importants pour l'orientation des chromosomes et FtsK est important pour la ségrégation des chromosomes.

Cette thèse représente un pas en avant vers une meilleure compréhension des méchanismes sous-jacents de la division cellulaire des mycobactéries et ainsi dans le long terme une source potentielle de nouveaux traitements pour contôler la division de *M. tuberculosis*, par exemple en ciblant FtsK.

Mots clés: Division bactérienne, NAPs, Hlp, FtsK, ParA, ParB, microscopie time-lapse.

Contents

1.1 List of Figures

1.2   List of Tables & Equations

1.3 List of abbreviations

ATC: anhydrotetracycline

bp: base pairs

B. subtilis: *Bacillus subtilis*

C. crescentus: *Caulobacter crescentus*

KOPS: FtsK orienting polar sequences

HA: hemagglutinin

INH: isoniazid

IP: immunoprecipition

ori: origin of replication

L. lactis: *Lactococcus lactis*

M. smegmatis: *Mycobacterium smegmatis*

M. tuberculosis: *Mycobacterium tuberculosis*

MDR: multi-drug resistant

PDMS: polydimethylsiloxane

S. coelicolor: *Streptomyces coelicolor*

SIM: Structured illumination microscopy

SMC: structural maintenance of chromosome

SOFI: Super-resolution optical fluctuation imaging

S. *pneumoniae*: *Streptococcus pneumoniae*

SRRF: Super-Resolution Radial Fluctuations

ter: terminus of replication

WHO: World Health Organisation

wt: wild-type

XDR: extensively-drug resistant

Chapter 2 Introduction

2.1 Scope of the thesis

Although my thesis is focused on the model organism *Mycobacterium smegmatis*, in this introductory chapter I will start by introducing the human disease tuberculosis, which is caused by the closely related organism *Mycobacterium tuberculosis*. *M. smegmatis* is a fast-growing non-pathogenic organism, whereas *M. tuberculosis* is a slow-growing human pathogen that requires biosafety level 3 containment. Consequently, *M. smegmatis* is often used as a more tractable model organism to study fundamental processes in mycobacteria, such as the mycobacterial cell cycle, which is the biological focus of this thesis. After briefly introducing tuberculosis, the introductory chapter will focus on what is currently known about the mycobacterial cell cycle, with a special emphasis on the molecular players involved. I will review what is known about the biological roles of these molecular players in mycobacteria and other bacteria, with a special emphasis on the genes that I have studied myself using targeted mutations and genetically-encoded fluorescent reporters. Finally, I will briefly present the main tools that I used to study these mutants and reporters at the single-cell level, such as microfluidics and time-lapse microscopy.

2.2 Tuberculosis

Tuberculosis (TB) is an ancient infectious disease (Gutierrez et al. 2005) caused by the microorganism *Mycobacterium tuberculosis.* Every fourth person in the global population is estimated to be latently infected with TB and at risk of reactivation (WHO 2018). In 80 % of cases TB affects the lungs and to a lesser extent the pleura, lymph nodes, abdomen, genitourinary tract, skin, joints and bones, or meninges (Lee 2015). It spreads through the air when infected individuals sneeze, cough, or expectorate (Figure 1). The bacterium then invades and replicates in pulmonary alveolar macrophages, which leads to

an active disease in about 10% of individuals. In the other cases, the immune response contains the bacterial growth, and in about 10% of cases may even completely eradicate the disease. If not eradicated, TB enters a latent phase but can be re-activated if the immune system is compromised, a main cause of reactivation being HIV infections.
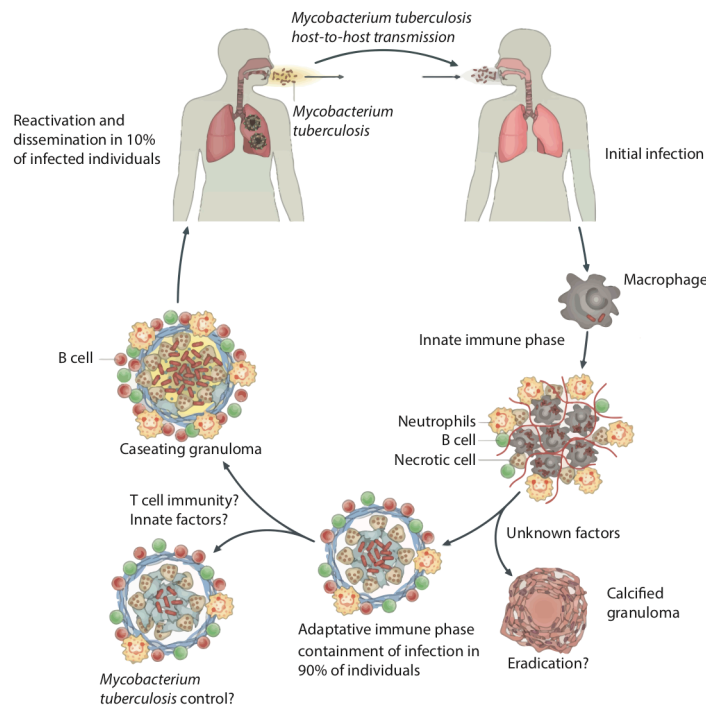
Figure 1. TB pathogenesis and cycle of infection

TB is transmitted through the inhalation of mycobacteria in aerosols. In most cases the innate immune system contains the infection and forms a granuloma. However, in some cases reactivation occurs, which drastically increases in immunocompromised individuals. This leads to active TB and *M. tuberculosis* can then be transmitted further. (adapted from Nunes-Alves et al. 2014)

Although TB is a very ancient disease, it was only in 1882 when Dr. Robert Koch identified the "tubercle bacillus" that progress in preventing and treating the disease could be made (Gradmann 2001). In 1908, Calmette and Guérin passaged the closely related organism *Mycobacterium bovis* more than 200 times, until its virulence disappeared (Schrager et al. 2019). The resulting vaccine was first administered in 1921 and is still used today,

although its efficacy, especially against pulmonary TB among adults, is controversial (Lawn & Zumla 2011). TB is a treatable and curable disease using antibiotics. The current treatment regimen recommended by the WHO for treating active and drug-sensitive TB requires taking multiple drugs over a period of 6 months. In the first phase, a combination of frontline drugs (isoniazid, rifampicin, pyrazinamide, and ethambutol) are taken for two months, followed by a second phase during which isoniazid and rifampicin are taken for four months (WHO 2018). The last first-line antibiotic used to cure TB was discovered in 1965 (Figure 2).

BCG vaccine   Isonazid
                     Pyrazinamide   Rifampicin

1921   1952   1965   2019

                           1962
                      Ethambutol
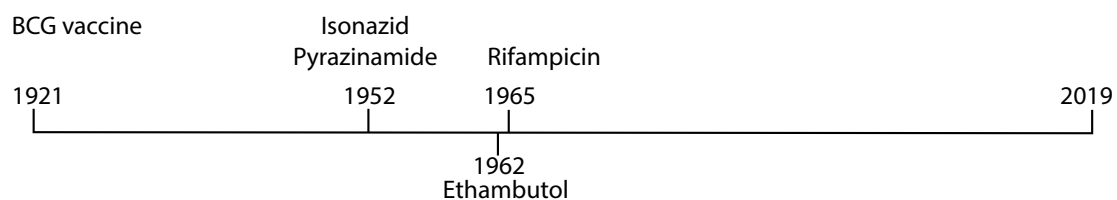
Figure 2. Time-line in scale of first-line antibiotics discoveries from BCG vaccine discovery to 2019

(Adapted from Swindells 2012 and Al-Humadi et al. 2017)

Standard therapy requires daily administration of a combination of multiple drugs for at least 6 months, which is difficult to comply with, especially in the resource-limited countries where TB is most prevalent (WHO 2018). The complexity of the disease, duration of the treatment, and difficulty in accessing the drugs, has led to the emergence of drug resistant, multi-drug resistant (MDR), and extensively drug resistant (XDR) forms of TB. MDR is defined as resistance to isoniazid (INH) and rifampicin, the two most efficacious first-line anti-TB drugs. XDR is defined as resistance to first-line as well as second-line anti-TB drugs, often leaving patients without any further treatment options. In 2017 alone, 160 684 cases of MDR-TB were reported throughout the world. A combination of second- or third-line TB drugs is used to treat MDR-TB and the treatment is extended to 18 - 24 months (Gandhi et al. 2010). In 2016, the treatment success rates for MDR-TB and XDR-TB were low, with estimates at 54% and 30%, respectively (WHO 2018).

Despite being a treatable disease, TB is still among the world's top 10 causes of death and the deadliest among infectious diseases, above even HIV/AIDS. In 2017, 6.4 million people fell ill with TB and 1.3 million HIV-negative people died from the disease (WHO 2018). As TB is still a major disease worldwide and with the development of resistance to antibiotics, a better understanding of the organism's infection process, metabolism, and mechanisms of division is therefore required to discover new compounds with high enough specificity to reach the WHO's goals: ending the global TB epidemic, reducing TB deaths by 95%, and reducing new cases by 90% between 2015 and 2035.

2.3   *Mycobacterium smegmatis* – A model organism for tuberculosis

M. tuberculosis is a pathogenic, slow-growing bacterium with a doubling time of approximately 24 hours *in vitro* and during the acute phase of infection in mice (Muñoz-Elías et al. 2005). Experiments using *M. tuberculosis* are very time consuming due to its slow growth and must be performed in Biosafety Level 3 facilities, which requires special safety procedures and expensive equipment. These challenges can be by-passed by using related model organisms, such as the soil-inhabiting *Mycobacterium smegmatis*, which is non-pathogenic (Biosafety Level 1) and relatively fast growing, with a doubling time of 3-4 hours (Santi et al. 2013, Sao Emani et al. 2018). Although encoding homologs for many of the genes implicated in *M. tuberculosis* virulence (Reyrat & Kahn, 2001), *M. smegmatis* is not suitable for studies of pathogenesis *per se*, as it is not a pathogen. *M. tuberculosis* and *M. smegmatis* have 4173 and 6938 identified genes (Kapopoulou et al. 2011), respectively, with a GC-rich genome of 4,411,529 (Cole et al. 1998) and 6,988,269 (Mohan et al. 2015) base pairs. *M. smegmatis* therefore has about a 40% larger genome and more genes. However, much of the molecular machinery involved in the fundamental processes of cell growth, chromosome replication and segregation, and cell division is highly conserved between the two species. Therefore, *M. smegmatis* has proven to be a widely used model

organism for analysis of basic cellular processes, including cell cycle processes, of *M. tuberculosis* (Hett & Rubin 2008). Because these processes are essential for life, understanding the roles of specific genes in these processes could lead to the identification of new targets for development of drugs or other intervention strategies.

2.4 Division in Mycobacteria

Mycobacteria belong to the phylum Actinobacteria (Fu & Fu-Liu 2002). They are very different from the well-studied bacterial model organisms such as *Escherichia coli* and *Bacillus subtilis* although being rod-shaped (Figure 3). They possess an unusually thick cell wall composed of peptidoglycan, arabinogalactan, and mycolic acids, which in *M. tuberculosis* is surrounded by a protein and polysaccharide capsule (Hett & Rubin 2008; Sani et al. 2010; Kieser & Rubin 2014). One of the particularities of *M. tuberculosis* is its ability to persist in a dormant state for decades before resuming its growth (Hett & Rubin 2008).
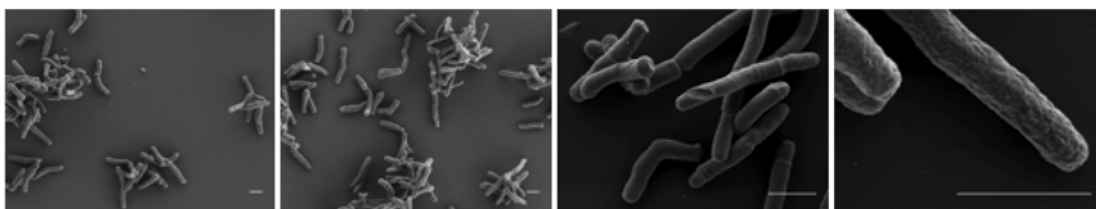
Figure 3. Scanning electron microscopy images of *M. tuberculosis* H37Rv

Images of *M. tuberculosis*. Scale bars: 1 µm. (Adapted from Kolly et al. 2014)

Furthermore, mycobacteria grow exclusively by polar elongation whereas most rod-shaped bacteria grow by sidewall extension (Cameron et al. 2015; Botella et al. 2017, Figure 4A). Another particularity is that mycobacteria divide slightly asymmetrically (at 55 ± 4% of cell length when measured using a fluorescently tagged DiviVA homolog, Wag31-

GFP, as a cytokinesis marker), with a skew towards the new cell pole (Aldridge et al. 2012, Santi et al. 2013, Figure 4B).
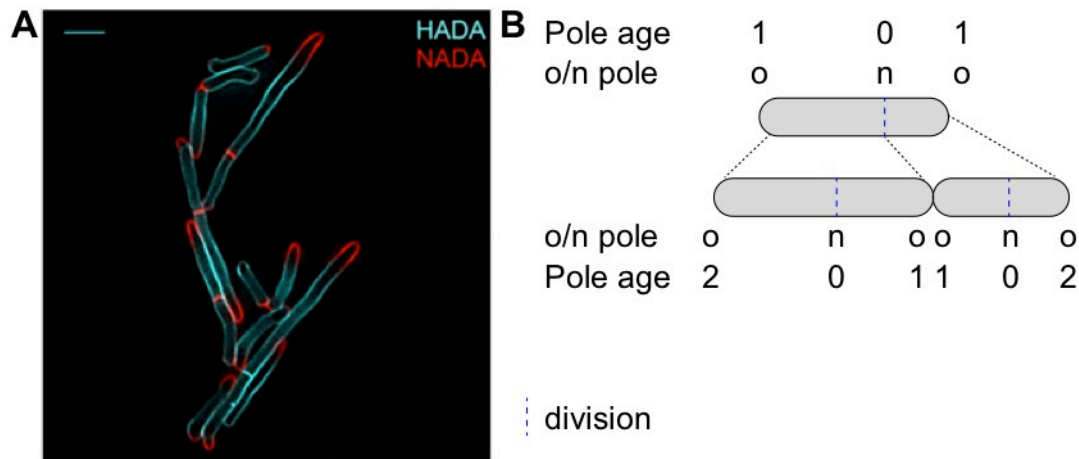
Figure 4. Polar elongation and schematic pole representation of *M. smegmatis* cells

(A) Super-resolution snapshot microscopy of the cell membrane labeled sequentially using two different colors of fluorescent D-amino acids, which are incorporated into synthetized peptidoglycans. HADA (HCC-amino-D-alanine in cyan) was added for 4 h, then NADA (NBD-amino-D-alanine in red) for 30 min to highlight the most recent peptidoglycan synthesis. Scale bar, 2 μm. Short-pulsed D-alanine analogs incorporated asymmetrically at the two poles. Adapted from Botella et al. 2017. **(B)** Schematic representation of the pole age as well as the old (o) or new (n) poles locations

2.4.1 Chromosome segregation and the ParABS system

To survive, bacteria need to coordinate cell growth and division with replication and transmission of their genetic material to their daughter cells. Indeed, once chromosomes are duplicated, it is essential that they are segregated correctly to the daughter cells in a tightly organized manner. For example, failure to segregate chromosomes prior to cell division could result in a fatal guillotining of a chromosome by the ingrowing division septum. But how are chromosomes segregated, and how is chromosome segregation coordi-

nated with cell division? In eukaryotes, a microtubule-based spindle drives chromosome segregation, which is very conserved between species (Oliferenko 2018). However, in bacteria, chromosome segregation is still not well understood, despite its importance for successful cell division (Lim et al. 2014). In well-characterized organisms like *E. coli*, the minicell (Min) and nucleoid occlusion (Noc) systems are responsible for controlling cell division in space and time, ensuring that cells divide symmetrically after completion of chromosome replication and segregation. Homologs of the Min and Noc systems are absent in mycobacteria (Singh et al. 2013) and it is not understood how these organisms maintain the observed high fidelity of cell division, chromosome replication, and partitioning. The driver for chromosome segregation in mycobacteria is currently thought to be the ParABS chromosome partitioning system. This system is present in most bacteria except the gamma-proteobacteria, which includes *E. coli* (Mierzejewska & Jagura-Burdzy 2012). An interesting fact is that even though *E. coli* lacks the ParABS system for segregating its chromosomes, it still uses the plasmid-encoded Par system for segregation of its plasmids (Bouet & Funnell 1999).

The parABS system is made of three components. ParB is a DNA-binding protein that interacts with specific *parS* sequences adjacent to the chromosomal origin of replication (*oriC*). ParB also interacts with ParA (an ATPase motor protein) and forms large multimeric nucleoprotein complexes that somehow mediate the high fidelity of chromosome segregation (Jakimowicz et al. 2007; Santi & McKinney 2015). There are two *parS* sites in *M. smegmatis* with the exact same nucleotide sequence located near *oriC* and separated by 78 base pairs. A third *parS* site with one nucleotide substitution that binds ParB more weakly is also present on the other side of *oriC* (Jakimowicz et al. 2007).

In the current scientific literature, there are two competing models for Par organization and function, derived mainly from studies in the model organism *Caulobacter crescentus*. However, the interaction between ParA and ParB is conserved in the two models, where ATP bound to ParA promotes the dimerization of ParA. ParA dimers bind to DNA.

The dissociation from DNA and of the dimers requires a high ParB concentration (Lim et al. 2014, Ptacin et al. 2010, Figure 5A). The first model ("spindle model") proposes that dynamic filaments of ParA may form a chromosome-segregating contractile apparatus similar to the eukaryotic mitotic spindle, in which contraction of the spindle is driven by a "burnt bridge" ratchet mechanism (Ptacin et al. 2010, Wang et al. 2013, Figure 5B). In this model ParA is organized as a spindle and its depolymerization is promoted by ParB. This reaction results in a directed movement of the ParB-*parS* complex along the retracting ParA filament towards the opposite cell pole. The second model ("DNA-relay model") proposes a DNA relay mechanism, where the elasticity of the chromosomes enables a directed movement of the ParB-*parS* complex through a ParA gradient. The ParB-*parS* complex binds to a cytoplasmic ParA-ATP dimer and promotes the hydrolysis and dissociation of ParA-ATP to ADP; conversion of ParA-ATP to ParA-ADP causes the release of the ParB-*parS* complex; the released ParB-*parS* complex moves up the ParA-ATP dimer gradient (towards the cell pole) via the elastic movement of the chromosome and binds to the next ParA-ATP dimer to restart the cycle (Lim et al. 2014, Figure 5C).

Less is known about the role of the Par system in mycobacteria. In *M. smegmatis*, recent studies showed that ParA is organized as a gradient (Ginda et al. 2017, Uhía et al. 2018), which directs the diffusion-based movement of the ParB/ParS complex. ParA has also been shown to interact with the cytokinesis marker Wag31 (Pióro et al. 2019) and forms a gradient such that the highest concentration of ParA is located at the new pole (Ginda et al. 2017, Uhía et al. 2018). In my opinion, however, these observations do not clarify which of the two models (if either) is valid in *M. smegmatis*.
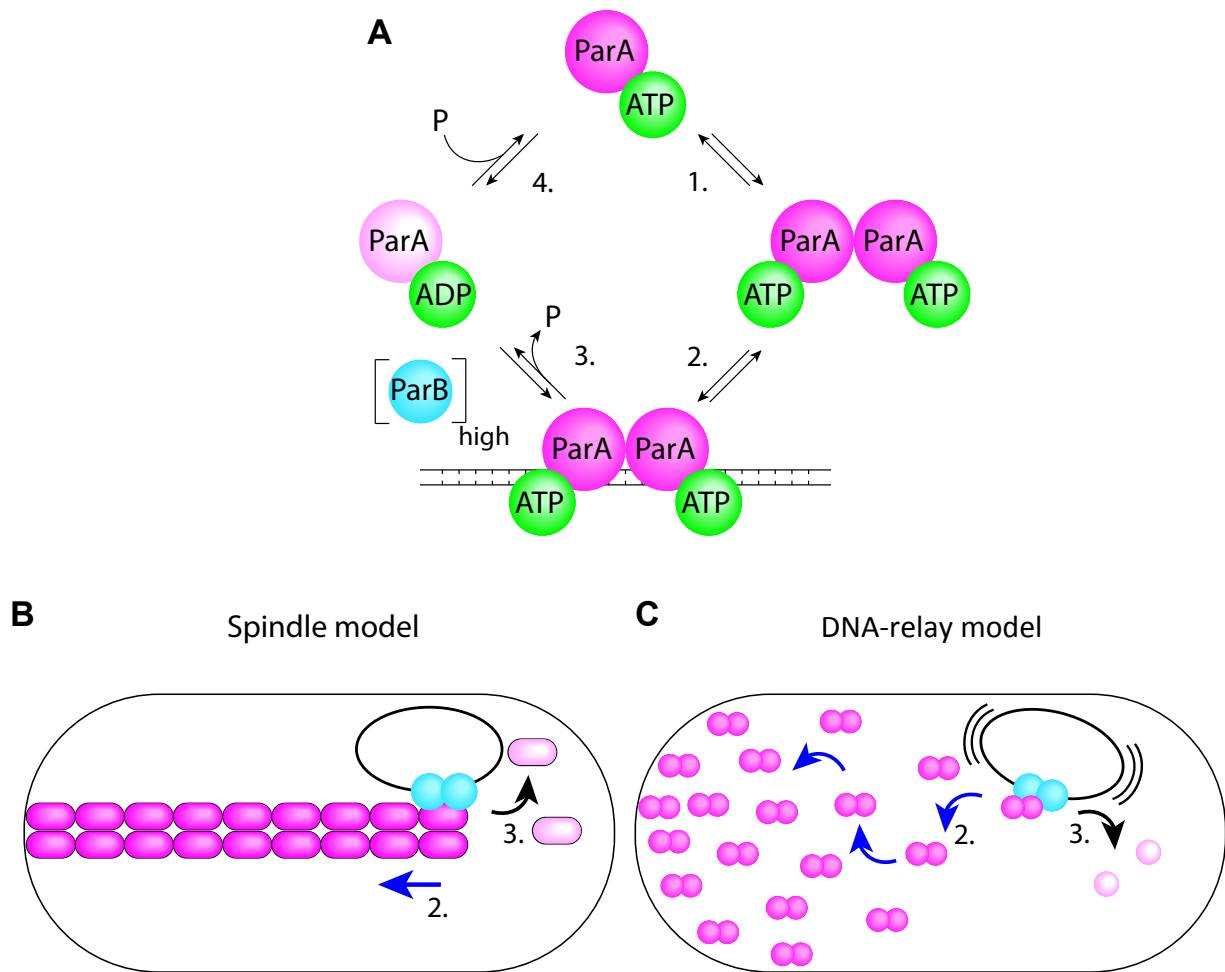
Figure 5 ParA dynamics and models of bacterial chromosome segregation

ParA dynamics explained in **(A)** are valid in the two models described in **(B)** and **(C)** where the same numbering is used. **(A)** ParA dynamic cycle. 1) ATP binding promotes ParA dimerization. 2) ParA-ATP dimers can bind DNA. 3) A high concentration of ParB enables ATP hydrolysis and dissociation of the ParA dimers. 4) Reinitiation of the cycle by conversion of ParA-ADP to ParA-ATP. **(B)** "Spindle model" adapted from Ptacin et al. 2010. The ParB-*parS* complex interacts with ParA-ATP filament and promotes its hydrolysis to ParA-ADP and depolymerization (black arrow). The binding to the next ParA dimer on the filament results in a movement towards the opposite pole (blue arrow). **(C)** "DNA-relay model" adapted from Lim et al. 2014. DNA-bound ParA-ATP dimers fluctuate randomly according to the elastic movement of the associated DNA. When the ParB-DNA complex interacts with ParA-ATP dimers it stimulates ATPase activity, resulting in the dissociation of ParA from the DNA (black arrow). The DNA elastic movement enables the complex to reach the next ParA dimer (blue arrow).

In some species, such as *C. crescentus* and *Myxococcus xanthus,* the *parAB* genes are essential (Mohl et al. 2008; Harms et al. 2013; Iniesta 2014). In *C. crescentus*, *parA* or *parB* could only be deleted at the *par* genomic locus if an extra copy was inserted at an ectopic locus (Mohl & Gober 1997). Depletion of ParB or overexpression of ParA in *C. crescentus* resulted first in formation of anucleate cells, then in smooth filamented cells, lack of FtsZ ring formation, and stalled cell cycle (Mohl et al. 2008). However, in other bacteria such as *B. subtilis,* deletion of the *par* genes results in a mild phenotype, as only a small percentage of cells show an anucleate cell phenotype when both the *soj* (*parA* homolog) and *spo0J* (*parB* homolog) genes are deleted. Interestingly, if the ratio of Soj to Spo0J increases, the proportion of anucleate cells also increases (Ogura et al. 2003; Becker & Pogliano 2007). Unlike in other bacteria, Spo0J is required both during vegetative division and sporulation (Ireton et al. 1994). Spo0J is indeed required to initiate sporulation. Soj antagonizes Spo0J's effect, inhibiting the phosphorylation of Spo0A, which is required for the initiation of sporulation (Ireton et al. 1994).

In *Streptomyces* spp., ParAB is required only during sporulation and deletion of *parA* or *parB* in *S. coelicolor* results in the formation of about 25% or 20% of anucleate spores, respectively (Donczew et al. 2016, Kois et al. 2009). Other organisms, such as *Streptococcus pneumoniae,* lack the Min and Noc system and possess only a partial ParABS system, as a ParA homolog is missing (Minnen et al. 2011). ParB is not essential in *S. pneumoniae* and knocking out *parB* results in a mild phenotype with only 3.5% anucleate cells.

In mycobacteria the phenotype of *parA* and *parB* mutants is diverse and depends on the strain studied and on the levels of the proteins (Table 1). For example, *parA* and *parB* are essential in *M. tuberculosis* (De Jesus et al. 2017) but not in *M. smegmatis*. However, in *M. smegmatis, parA* gene deletion or (more modestly) *parB* gene deletion leads to a high frequency of asymmetric cell division, resulting in the formation of anucleate and polyploid cells (Jakimowicz et al. 2007; Ginda et al. 2013). If one of the proposed models

for ParA and ParB interactions is correct (the DNA-relay model or ratchet model), deleting *parA* or *parB* should lead to the same phenotype. Unexpectedly, deletion of both *parA* and *parB* genes results in a less severe phenotype than deletion of either gene singly (Jakimowicz et al. 2007). But if the Par system is responsible for chromosome segregation (according to the current thinking in the field), then what is responsible for chromosome segregation in Δ*parAB* cells? This could mean that, similar to the case in *B. subtilis*, maintaining the correct ratio of these proteins is essential for maintaining a normal cell ploidy (Ogura et al. 2003). Overproducing ParB increases the percentage of anucleate cells in *M. tuberculosis* but not in *M. smegmatis* (Maloney et al. 2009). Overexpressing *M. tuberculosis* ParA in *M. smegmatis* results in only a slight increase of the percentage of anucleate cells (Maloney et al. 2009). This only slight increase could be due to the fact that *M. tuberculosis* ParA is not a functional homolog compared to the *M. smegmatis* ParA. However overexpressing *M. smegmatis* ParA in *M. smegmatis* results in 9% anucleate cells (Ginda et al. 2013).

	% anucleate cells in		Source
strain	*M. tuberculosis*	*M. smegmatis*	
Δ*parA*	essential[5.]	30[3.]	1. Jakimowicz 2007
Δ*parB*	essential[5.]	10-11[1.][3.]	2. Maloney 2009 (*TB* protein in *M.smegmatis*)
parA↗	1-3[2.]	9[3.]	3. Ginda 2013
parB↗	26[2.]	no phenotype[1.]	4. Ginda 2017
Δ*parAB*	essential[5.]	1-10[3.][1.]	5. DeJesus 2017
WT	?	0.2-0.8[3.][1.]	

Table 1. Percentage of anucleate cells in *M. smegmatis* and *M. tuberculosis*

The *parA* and *parB* genes are essential in *M. tuberculosis* but not in *M. smegmatis*. Maintaining the correct ratio of ParA to ParB seems critical for preventing the formation of anucleate cells.

2.5   DNA compaction and organization

2.5.1   Nucleoid associated proteins (NAPs) and structural maintenance of chromosome (SMC)

The chromosomes need to be segregated once replicated but how are the chromosomes organized and compacted in a cell? Most bacteria contain one chromosome of 2-8 Mbp which needs to be compacted more than 1000 times to fit in the cells (Wang et al. 2013). In bacteria, DNA is organized by nucleoid-associated proteins (NAPs), also called "histone-like proteins", such as HU, IHF, H-NS, and FIS (Anuchin et al. 2011) as well as structural maintenance of chromosome (SMC) condensin complexes (Wang et al. 2013). The precise function of SMC is still to be discovered but it is involved in the organization and condensation of the chromosomes (Minnen et al. 2011).

The nucleoid associated proteins are chromosome-associated proteins serve biological roles in bacteria similar to histones in eukaryotic cells. NAPs are often positively charged, low molecular weight dimeric proteins, which modulate DNA by bending, wrapping, and bridging DNA (Kriel et al. 2018). Mycobacterial NAPs are less abundant and structurally different compared to other species. Hlp and Lsr2 are two principal NAPs in *Mycobacterium tuberculosis*. Hlp is one of the most abundant (Datta et al. 2019).

The highly conserved SMC complex is composed of the SMC proteins, ScpA and ScpB. The *E. coli* structural and functional analogs of SMC are MukB, MukF, and MukE (Wang et al. 2013). The SMC proteins of *B. subtilis* and *C. crescentus* are essential above 23 °C (Mascarenhas et al. 2002). Deletion of SMC/MukBEF leads to a slight increase (0.1%) in anucleate cells formation in *C. crescentus* at 20°C (Jensen & Shapiro 2009, Table 2) and a higher increase in other bacteria like *E. coli* and *B. subtilis* (Nolivos & Sheratt 2014). In *M. smegmatis*, deletion of SMC results in a modest (0.3%) increase of anucleate cells (Santi & McKinney 2015). In *B. subtilis*, SpoOJ recuits the SMC complex to the *parS* site and deletion of either *spoOJ* or the *parS* sites disrupts the localization of the SMC complex (Sullivan et

al. 2009). In *B. subtilis*, during vegetative growth, when *spoOJ* is deleted 0.3% of the cells show an anucleate phenotype but when *soj* is deleted a smaller proportion than 0.04% of the cells show an anucleate phenotype. However, the combination of both *soj* and *smc* or *spoOJ* and *smc* is synthetic defective, with nearly 20% of anucleate cells, whereas deletion of *smc* alone only gives 2% of anucleate cells (Lee & Grossman 2006). In *B. subtilis* deleting *parB* inhibits sporulation (Ireton et al. 1994) but the double deletion Δ*parA* Δ*parB* resumes sporulation but with 20% of anucleate spores (Becker & Pogliano 2007). In *S. coelicolor*, deletion of *parA*, *parB*, or *smc* results in about 25%, 20% and 8% of anucleate cells respectively. However, the double mutants Δ*parA* Δ*smc* or Δ*parB* Δ*smc* both, unlike in *B. subtilis* where the effect is greater with the double mutants, only results in 25 % of anucleate cells (Kois et al. 2009). Likewise, in *S. pneumoniae* the double mutant Δ*smc* Δ*parB* only results in 2.8% of anucleate cells, which is not a cumulative defect of Δ*smc* or Δ*parB* alone, which results in 1.8 % and 3.5 % anucleate cells, respectively (Minnen et al. 2011). As *S. pneumoniae* lacks a *parA* homolog (Minnen et al. 2011), if *par* and *smc* are responsible for chromosome segregation, it is surprising that most cells have a normal phenotype. Similarly, if the Par system is absolutely required for chromosome segregation then it is unclear why knockout of the Par or Smc system results in only a partial (and, in some cases, very mild) phenotype (formation of anucleate cells). It is also unclear why deletion of the *parA*, *parB*, and *smc* genes, either alone or in combinations, should have different (and, in some cases, *opposite*) effects in different organisms (Table 2).

	Δsmc	ΔparA (soj)	ΔparB (spo0J)	ΔparAB	ΔparAΔsmc	ΔparBΔsmc
M. smegmatis	0.3%[1]	30%[2]	20%[2]	1[3]-10%[4]	?	?
B. subtilis (*sporulation*)	?	?	no sporulation[5]	20%[6]	?	?
B. subtilis (*vegetative*)	2[7]-10%[8]	<0.1%[5,7]	0.3[7]-1.4%[5]	1.4%[5]	18%[7]	19[7]-26%[8]
S. coelicolor	8%[9]	25%[9]	13-20%[9,10]	13%[10]	25%[9]	25%[9]
S. pneumoniae	1.8%[11]	no *parA*[11]	3.5%[11]	no *parA*[11]	no *parA*[11]	2.8%[11]
C. crescentus	0.1%[12]	essential[12]	essential[12]	essential[12]	essential[12]	essential[12]

1. Santi et al. 2015
2. My thesis
3. Ginda et al. 2013
4. Jakimowicz et al. 2007
5. Ireton et al. 1994
6. Becker & Pogliano 2007
7. Lee & Grossman 2006
8. Britton et al. 1998
9. Kois et al. 2009
10. Kim et al. 2000
11. Minnen et al. 2011
12. Jensen & Shapiro 1999

combined effect:

— lower   — similar   — higher

Table 2 Summary anucleate phenotype in different organisms

The percentage of anucleate cells is represented in single or multiple gene knock out strains. The combined effect of two gene deletions could have a lower (blue), similar (green) or higher (red) phenotype compare to a single gene deletion.

2.5.1.1 Hlp structure and role

One of the most abundant NAPs in *M. smegmatis* is the histone-like protein (*hlp*) (Datta et al. 2019). We are particularly interested about NAPs as we want to follow the DNA dynamics in *M. smegmatis* and one approach would be to construct a fluorescent reporter using an abundant NAP. The *M. smegmatis* histone-like protein, encoded by the *hlp* (MSMEG_2389) gene, and its *M. tuberculosis* homolog *hupB* (Rv2986c), are conserved among mycobacteria (Pandey et al. 2014). The C-terminal domain, rich in lysine (K) and arginine (R), is structurally similar to the eukaryotic histone H1, with PAKK and PAAK repeats (composed of proline (P), Alanine (A) and Lysine (K)), specific to mycobacteria, while

the N-terminal domain is similar to the *E. coli* homolog HU (Kriel et al. 2018; Pandey et al. 2014). Hlp is conserved in all known genome sequences of eubacteria as homodimers or heterodimers (Dame 2005; Grove 2011; Figure 6).

Figure 6. Secondary structure of *M. tuberculosis* HupB (Hlp homologue)

M. tuberculosis HupB (residues 1–99 on the N-terminal side) dimer (protomer A coloured red; protomer B coloured teal). In the dimer, alpha-helices α1 and α2 assemble to form a four-helix bundle, while β2, β3, β4, and β5 define a DNA-binding β cleft (Bhowmick et al. 2014).

Hlp has a regulatory role as well as a structural role. It is involved in the regulation of many genes, including some implicated in virulence and stress responses. Hlp expression has, for instance, been correlated with increased bacterial survival after UV light exposure (Li & Waters 1998; Miyabe et al. 2000), cold shock, heat shock, and nutrient starvation (Wada et al. 1988). When the *hlp* gene was deleted in *M. smegmatis*, the bacteria were unable to regrow following a cold-shock and were more susceptible to UV irradiation and isoniazid (INH) exposure (Shires & Steyn 2001; Whiteford et al. 2011). Hlp is also an inhibitor of the *katG* gene encoding catalase. INH is a prodrug that requires conversion by the KatG catalase peroxidase to its active form (Wakamoto et al. 2013). It was also shown that in cold-shocked *M. smegmatis,* Hlp is highly upregulated and accounts for 20-25% of the total produced proteins, compared to 1-2% at 37°C (Shires & Steyn 2001). Another important role has been shown for Hlp linked to the level of intracellular iron. Under iron-

sufficient conditions, *hupB* and genes encoding siderophores are repressed; conversely, when iron is low, expression of these genes is enhanced (Kriel et al. 2018). Conditions of iron or nutrient deprivation are particularly interesting to study in *M. tuberculosis*, as they correspond to the conditions inside an infected macrophage. Indeed, deletion of *hupB* is predicted to lead to growth defects in *M. tuberculosis* (DeJesus & al. 2017) and the *hupB* mutant has been shown to be unable to survive in macrophages (Pandey & al. 2014). HupB was also shown to be required for the formation of isoniazid-resistant mutants and the Δ*hupB* strain was more susceptible to INH compared to WT cells (Sakatos et al. 2018).

Acetylation of Hlp's lysine residues by the N-acetyltransferase Eis protein leads to a decreased affinity of acetylated Hlp for DNA as well as its decompaction (Ghosh et al. 2016). The de-acetylation of Hlp's lysine residues is a reversible process, which can be performed by Sir2 proteins and results in a recompacted nucleoid (Kriel et al. 2018). Hlp is also a target for the serine/threonine protein kinases PknB, PknE, and PknF, which are more abundant during the exponential phase of growth, in contrast to Hlp, which is more abundant during the stationary phase. Phosphorylation by these kinases regulates the DNA-Hlp interaction.

Hlp has been shown to introduce turns in the DNA structure (Dame 2005). It binds to DNA non-specifically but seem to favor distorted DNA structures such as bends, gaps, and cruciforms.

2.5.1.2   Lsr2

Lsr2 is another abundant NAP (Datta et al. 2019) which could be a potential fluorescent reporter to follow DNA dynamics during the cell cycle. Lsr2 (MSMEG_6092) is a small nucleoid-associated protein (NAP) present in Actinobacteria, including the mycobacteria. It is a functional analog to the *E. coli* histone-like nucleoid structuring protein (H-NS),

and mycobacterial Lsr2 protein can complement the phenotype of an H-NS mutant in *E. coli*. Lsr2 is the first nucleotide-associated protein identified in Gram-positive bacteria and the most abundant NAP in *E. coli* (Gordon et al. 2008). Unlike Hlp, it binds preferentially to AT-rich regions forming large complexes. It has a structural role, as it generates supercoiling and bends in the chromosomal DNA. It binds in the minor groove of the DNA helix and bridges distant DNA fragments into loops and hairpins. Lsr2 also has a regulatory role, as it inhibits transcription and topoisomerase I activity *in vitro* (Kriel et al. 2018). The C-terminal domain of Lsr2 (residues 51-112) binds to DNA while the N-terminus is a dimerization domain (residues 1-65). The *lsr2* deletion mutant of *M. smegmatis* is more susceptible to oxidative stress, and Lsr2 in *M. tuberculosis* mediates tolerance to the antituberculosis drugs ethambutol and isoniazid (Kriel et al. 2018).

2.6 Filamenting temperature sensitive genes

For successful division events to happen many proteins, including the Fts proteins, localize at the septum. The *fts* genes take their name from the "filamenting temperature-sensitive" phenotypes generated when they are inactivated. Indeed, when *fts* gene expression is knocked down using conditional gene-repression mutants, the strains filament (Ricard & Hirota 1973; Wang & Lutkenhaus 1998; Wu et al. 2018). Several *fts* genes have been identified in *E. coli*, including *ftsA* to *ftsG* (Ricard & Hirota 1973)*, ftsK, ftsI, ftsQ, and ftsZ* (Addinall et al. 1996)*. The well-studied model organisms *E. coli* and *B. subtilis* share some *fts* gene homologs with mycobacteria (*ftsI, ftsK*, and *ftsQ*) or some conserved domains or secondary structure (*ftsB* and *ftsL*) (Wu et al. 2018)

2.6.1 FtsZ controlled by the Min and Noc system determines the localization and timing of division

One crucial step in the cell cycle is division. But how is the localization and timing of division controlled? FtsZ is thought to be the earliest-appearing marker of the future cell division site and is present in most bacterial species. It is the most well-known *fts* gene and encodes the bacterial tubulin homolog which is a GTP-binding protein. (Rowlett & Margolin 2013). FtsZ assembles as a ring that constricts and recruits cell division machinery components for the synthesis of new cytoplasmic membrane and cell wall material.

In *E. coli* and *B. subtilis,* the Min system determines where the FtsZ ring will assemble and the Noc system determines when it can assemble.

In *E. coli* the Min system is composed of MinC, MinD, and MinE. MinD, an ATPase, assembles at the cell poles and tethers MinC to the membrane when bound to ATP. MinE forms an oscillating ring, which travels from one pole to the other and disassembles the MinCD complex by hydrolyzing ATP bound to MinD. *B. subtilis* does not have a MinE protein but uses a different protein, DivIVA (homolog of the mycobacterial Wag31 protein), to localize the MinCD complex to the poles (Edwards & Errington 1997). MinC depolymerizes FtsZ by stimulating the hydrolysis of FtsZ-bound GTP. Pole-to-pole oscillation of the MinCD complex creates a spatiotemporal gradient that is more concentrated at the cell poles and less concentrated at the middle of the cell, resulting in the polymerization of FtsZ exclusively at midcell (Wu & Errington 2011, Figure 7). *M. tuberculosis* encodes two MinD-like proteins, Rv1708 and Rv3660c, which are annotated as a putative initiation inhibition protein and a putative septum-site-determining protein, respectively (Slayden et al. 2006). However, no other Min proteins have been identified in mycobacteria.
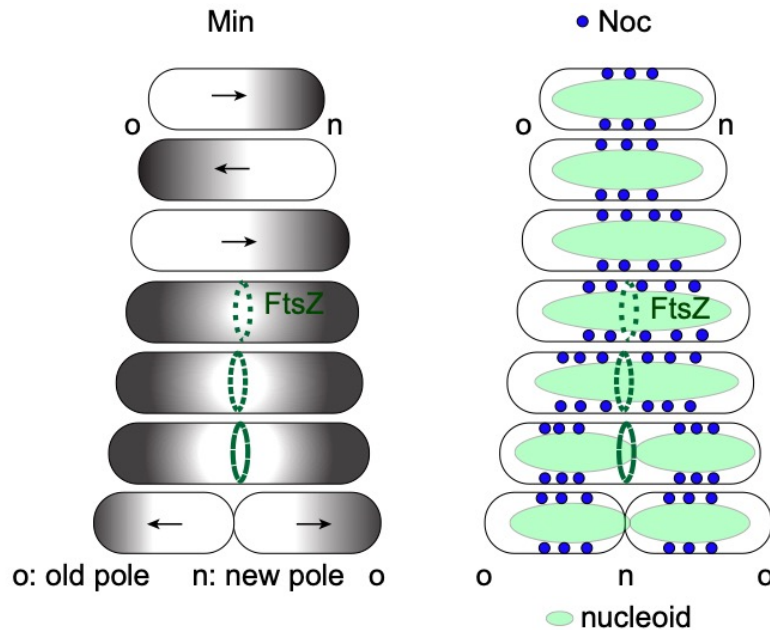
Figure 7 Min and Noc system determine where and when division occur

On the other hand, the timing of FtsZ ring assembly is determined by the SlmA protein in *E. coli* and the unrelated Noc protein in *B. subtilis*. Specific SlmA-binding sequences are distributed on the nucleoid and sparse or absent near the replication terminus (Pazos et al. 2014). The SlmA and Noc proteins inhibit FtsZ polymerization. Therefore, until chromosome segregation is completed, FtsZ cannot assemble.

The actin-like protein FtsA stabilizes FtsZ assembly in many organisms including *E. coli*, *B. subtilis*, and *Streptococcus pneumoniae*, but an FtsA homolog is not present in mycobacteria (Donovan & Bramkamp 2014; Mura et al. 2017). FtsZ requires either FtsA or ZipA for membrane attachment (Ramirez-Diaz et al. 2018). Two ZipA-like proteins, Rv2345 and Rv3835, exist in *M. tuberculosis* and have *M. smegmatis* homologs (Slayden et al. 2006; mycobrowser). In organisms like *C. crescentus*, FtsZ is sometimes present at the cell poles, and then assembles as a discontinuous rotating ring (Holden et al. 2014; Figure 8A). In *B. subtilis*, FtsZ treadmilling movement is required for peptidoglycan synthesis by the Pbp2b penicillin-binding protein, which has the same constriction shape as the FtsZ ring (Bisson Filho et al. 2017; Figure 8B).
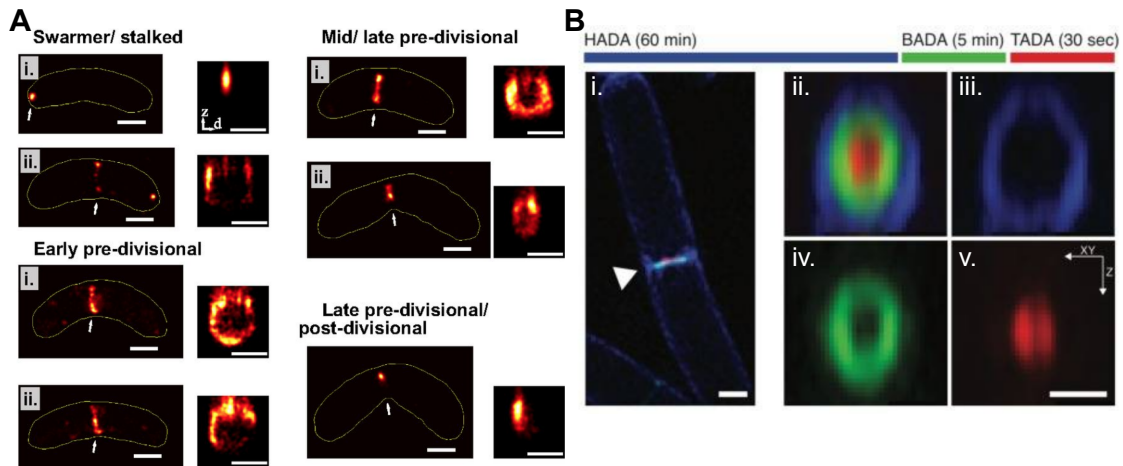
Figure 8. FtsZ assembles as a constricting discontinuous ring that drives peptidoglycan assembly

(A) Representative PALM images of FtsZ localization throughout the *C. crescentus* cell cycle, in *xy* (*Left*) and in *zd* cross-section (*Right*), where *d* is lateral distance from the cell midplane in transformed *xy* coordinates, which removes the effect of cell curvature. Arrow indicates region shown in *z* cross-section. Yellow line indicates automatically determined cell outline. Scale bars, 500 nm. Adapted from Holden et al. 2014. **(B)** 3-D SIM (structured illumination microscopy) images of sequential fluorescent D-amino acids labeling of *B. subtilis* division septa shows outside-in synthesis. (Right) 90° rotations of septa. Adapted from Bisson Filho et al. 2017.

Although mycobacteria have a FtsZ protein, there are no known homologs for the Min and Noc systems. So how is division controlled? The Par system is currently thought to be responsible for chromosome segregation (explained earlier in **Chapter 2.4.1**). However, I will propose a model where the Par genes are responsible for chromosome organization and FtsK is responsible for chromosome segregation. But what is known about FtsK?

2.6.2 FtsK

FtsK is another Fts protein which is a DNA translocase. Its *B. subtilis* homolog, SpoIIIE, has an important role especially in forespore formation during starvation-induced sporulation. In *E. coli*, FtsK is a fast motor protein, which translocates DNA in the *ori* to *ter*

direction and recruits recombinases for decatenation of chromosomes. FtsK forms a ring-like shape at the nascent division septum after FtsZ, which is required for its assembly.
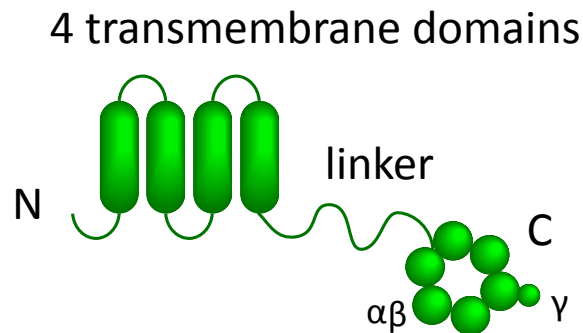
Figure 9 FtsK structure

FtsK has three distinct domains. 1) The N-terminal transmembrane domain. 2) The linker domain. 3) The motor domain composed of alpha and beta subunits organized in hexamers as well as the gamma subunit.

In *E. coli* FtsK has three distinct domains (Figure 9) (Sivanathan et al. 2009), con-served in other bacteria such as *B. subtilis* (Shin et al. 2015) and *Pseudomonas aeruginosa* (Bigot et al. 2007). These three domains seem conserved in *M. smegmatis* according to the Uniprot protein structure predictions. The C-terminal domain is a fast ATPase motor. It translocates DNA at a speed of 5 kbp per second (Pease et al. 2005). The motor can be subdivided into three components: α, β, and γ. The α and β domains form a hexamer with a central pore for DNA passage. The γ domain determines the directionality of DNA move-ment by binding to the FtsK orienting polar sequences (KOPS: 5'-GGGNAGGG-3'). It trans-locates DNA in the *ori* to *ter* direction until in *E. coli* it reaches the *dif* site at the terminus (Figure 10). In bacteria with circular chromosomes, including *E. coli*, *C. crescentus*, or *M. smegmatis*, replication starts bidirectionally at the unique *ori* site, which is then actively segregated towards the cell poles followed by the rest of the chromosomes, each loci hav-ing a precise conserved location (Stouf et al. 2013; Viollier et al. 2004). Replication of the

terminus near the division plane coincides with the recruitment of the early divisome components. Each *dif* site carries a binding site for XerC or XerD recombinase, which after the assembly of a recombination complex leads to a two-step recombination event. First, a strand is exchanged by XerD, leading to a Holliday junction intermediate, which is then resolved by XerC (Fournes et al. 2016). Deletion of the *xerC* gene resulted in a high frequency (10-15%) of cell death, which is reduced in the double mutant Δ*xerC* Δ*recA*. However, in both cases *dif* is properly segregated in both daughter cells, which is not the case in *ftsk* mutants (Stouf et al. 2013).
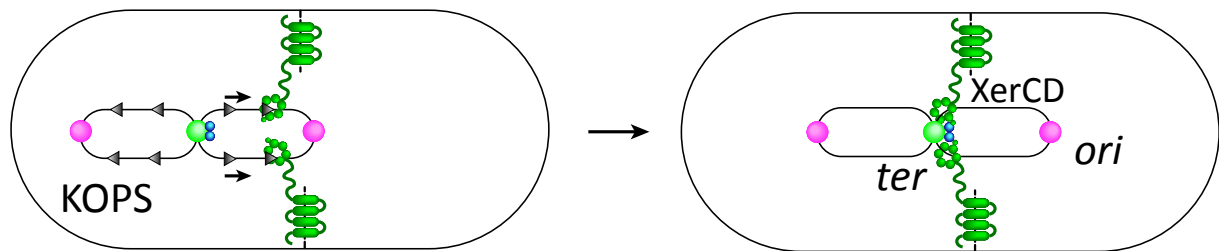
Figure 10 Schematic chromosome displacement by FtsK

Figure FtsK pulls the chromosomes by binding the KOPS sequences from *ori* to *ter*

The N-terminal domain of FtsK has four transmembrane-spanning domains (Wang and Lutkenhaus 1998), which localize the protein at the septum by interacting with FtsZ, where it participates in the assembly of the cell-division machinery.

The third domain of FtsK is a linker domain that is less conserved between species (Crozat & Grainge 2010). It is particularly long in *E coli*, having an extra hydrophobic segment near the N-terminal side, rich in proline and glutamine (Wang & Lutkenhaus 1998). FtsK is a powerful motor, as it has been shown that the *B. subtilis* homolog SpoIIIE completely removes proteins bound to DNA during forespore formation (Marquis et al. 2008),

when membrane fusion has already occurred and creates a pore in the forespore membrane (Burton et al. 2007).

In *E. coli*, the first 202 codons of the FtsK N-terminal domain are necessary and sufficient for correct FtsK localization, whereas the C-terminal domain is not essential. FtsK localization at the septum is dependent on FtsZ or FtsA. FtsZ is able to localize at the division site in FtsK-depleted cells, indicating the dispensability of FtsK for FtsZ localization, however FtsK may have a stabilizing role for FtsZ ring formation (Wang & Lutkenhaus 1998). FtsK has numerous functions, as it is also upregulated after DNA damage but requires RecA and LexA to be induced as part of the SOS response (Wang & Lutkenhaus 1998).

During *B. subtilis* sporulation, the forespore membrane closes around the forespore chromosome (Figure 11). The SpoIIIE (FtsK homolog) pore then translocates two-thirds of the trapped chromosome from the mother cell compartment into the nascent forespore compartment. As shown using 3D structured illumination microscopy (SIM), as well as PALM microscopy, both during symmetric division (vegetative growth) and asymmetric division (leading to spore formation), SpoIIIE is dynamically driven by the constricting septa, localizing at the FtsZ ring (Fiche et al. 2013). During sporulation, the forespore chromosome has a defined orientation at septation, with *ori* located in the forespore compartment (Wu & Errington 2002, Becker & Pogliano 2007). In *B. Subtilis* the Soj-Spo0J (ParA-ParB homologs) proteins are thought to be important for chromosome partitioning, and 20% of forespores in a *Δsoj Δspo0J* mutant are anucleate. Interestingly, expression of a *spoIIIE73-11* allele in *Δsoj Δspo0J* mutant mitigates the phenotype, whereby the proportion of anucleate forespores is reduced to 2.6%. SpoIIIE73-11 differs from wildtype SpoIIIE, by possessing intact DNA binding but defective ATP hydrolysis (Becker & Pogliano 2007). Another link between the *fts* and *par* genes has been seen in the sporulation efficiencies of combinatorial mutants, as the temperature-sensitive *ftsA* mutant has a sporulation rate of 0.17%, compared to 100% in WT, *Δsoj*, and *Δsoj Δspo0J* strains. However, sporulation effi-

ciency is reduced to 0.7% in the Δ*spo0J* strain and, more surprisingly, the double mutant Δ*soj* Δ*spo0J* as well as the temperature-sensitive mutant *ftsA* have a partially rescued phenotype with 16 % sporulation (Ireton et al. 1994).
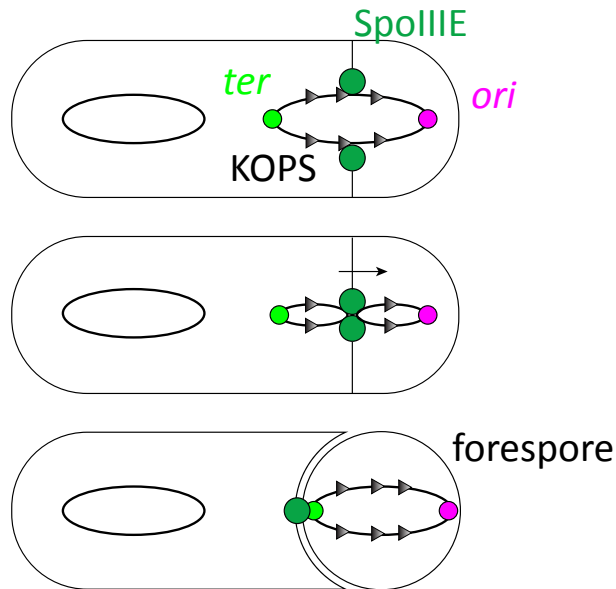
Figure 11 SpoIIIE during *B. subtilis* sporulation

SpoIIIE pulls the chromosome from the mother cell to the forming forespore. It binds the SRS (SpoIIIE recognition sequences) equivalent to the KOPS sequences (FtsK orienting polar sequences). *ori*: origin of replication. *ter*: terminus of replication.

In mycobacteria, so far none of the results related to FtsK described in other organisms have been reported. However, it has been reported that *M. smegmatis* FtsK localizes at the septum or as foci at the poles in a strain expressing an FtsK-GFP fusion protein (Singh et al. 2013). Depletion of *ftsZ, ftsI, ftsQ, ftsL,* and *ftsB* all result in a filamented phenotype. FtsQ, FtsL, FtsB, and FtsK all colocalize with FtsZ, which is the first *fts* gene product to arrive at the nascent division septum at the beginning of cell division. FtsK ring formation at the septum is dependent on FtsZ localization but not on FtsQ, FtsL, or FtsB (Wu et al. 2018).

2.7 Current knowledge of mycobacterial cell cycle

Bacterial multiplication involves many of the most fundamental biological processes, including cell growth, chromosome replication, chromosome segregation, and cell division. The mechanisms that coordinate these processes are only partly understood in well-studied model organisms (such as *E. coli*, *B. subtilis*, and *C. crescentus*), and are largely unknown in mycobacteria. My thesis is focused on the coordination of chromosome segregation and cell division. If bacteria divide when the chromosomes are not yet segregated this can lead to multiple defects. For example, if the septum closes before chromosome segregation is completed, this could result in guillotining of the chromosome, double-stranded DNA breaks, cell cycle arrest, and, ultimately, cell death. The cell cycle has been extensively studied in model organisms; however, some fundamental cellular processes appear to be quite different in mycobacteria. For example, most rod-shaped bacteria grow by insertion of new material into the sidewalls, whereas mycobacteria display the opposite pattern of growth: insertion of new material exclusively at the cell poles. Thus, we cannot assume that the knowledge obtained by the study of model organisms will necessarily apply to mycobacteria as well, and it is therefore important to study these processes directly in mycobacteria, which is the aim of this thesis.

Other cell cycle processes such as multifork replication occur in *E. coli* (Nielsen et al. 2007) and *B. subtilis* (Wang et al. 2014), but not in *C. crescentus* (Collier 2012) but are debatable in *M. smegmatis*. Multifork replication happens in *E. coli* under optimal growth conditions, when the time required to replicate the chromosome is longer than the inter-division time. Under these conditions, cells initiate a new round(s) of DNA replication before completion of the previously initiated round, resulting in cells with multiple replication forks and multiple origins of replication but only a single terminus of replication. Although multifork replication has been reported in a minority of cells (11%) in *M. smegmatis* (Trojanowski et al. 2017), in the majority of cells multifork replication is not observed. However, after completion of the first round of chromosome replication and segregation,

reinitation often happens before the division of the mother cell and the daughter cells are each born with a chromosome that has already been partially replicated (Santi et al. 2013, Logdson et al. 2017). These two biological processes (multifork replication versus reinitiation before division) could easily be mistaken for each other, and it is notable that these apparently conflicting observations have been obtained by different groups using different reporters (Logsdon & Aldridge 2018). According to my observations, looking at either time-lapse experiments with fluorescently tagged DnaN and ParB or DnaN and *attB*-GFP (as a proxy for the terminus of replication), I am not convinced that multifork replication occurs in *M. smegmatis*. However, at this point, there is still no consensus in the field whether multifork replication does or does not occur in mycobacteria.

What, then, do we know about chromosome dynamics in mycobacteria? First, it has been shown that the origin of replication is replicated bidirectionally by the replisome and the newly replicated origins are segregated towards opposite cell poles while replication of the chromosome continues (Figure 12). As chromosome replication proceeds, the terminus relocalizes from the new cell pole to midcell and is replicated last. Appearance of a ring-like structure of Wag31 at the nascent division septum coincides with cytokinesis, defined as the time when compartmentalization of the mother cell into two daughter cells with non-mixing cytoplasms is completed. When a cell divides, the newly formed poles are called the "new poles" and the two outer poles, inherited from the mother cell, are called the "old poles". An unusual feature of mycobacteria, as discussed above, is that a new round of DNA replication can start after chromosome replication and segregation are completed but before the division of the mother cell (Santi et al. 2013, Richardson et al. 2016).
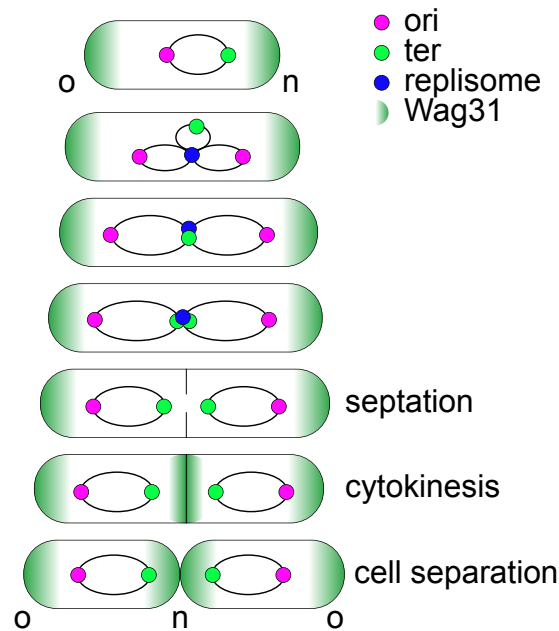
Figure 12 Mycobacterial cell cycle

2.8 Tools for single-cell microscopy

2.8.1 Fluorescent reporters constructed and used

In light of what is currently known about the *M. smegmatis* cell cycle, I constructed several combinations of fluorescent reporters to investigate their localization and dynamics in wild-type and different knockout (Δ*parA* or Δ*parB*) or knockdown (repressed FtsK) strains, which I will explain in further details in the related chapters of my thesis (Figure 13). Reporter strains expressing an in-frame fusion of the chromosome-binding Hlp protein (described above) to the Dendra2 fluorescent protein (**Hlp-Dendra2 reporter**) was constructed in order to follow chromosomal DNA dynamics in live cells. Reporter strains expressing an in-frame fusion of the ParB protein (described above) to the mCherry fluorescent protein (**ParB-mCherry reporter**) was used to follow the movement of the chromosomal origin in live cells, as described previously (Santi et al. 2013). Reporter strains expressing an in-frame fusion of the TetR protein to GFP and containing an array of TetR-binding sites (*tetO* sequences) inserted at the unique terminus-proximal *attB* site in the

chromosome (***attB*::GFP reporter**) was used to follow the movement of the chromosomal terminus in live cells, as described previously (Santi & McKinney 2015). Reporter strains expressing the FtsK protein (described above) fused in-frame to the GFP fluorescent protein (**FtsK-GFP reporter**) were constructed in order to follow the dynamics of FtsK localization in live cells. Reporter strains expressing an in-frame fusion of the Wag31 protein to either GFP or mCherry fluorescent proteins (**Wag31-GFP** and **Wag31-mCherry reporters**) were used to identify the time and place of cytokinesis in live cells, as described previously (Santi et al. 2013).
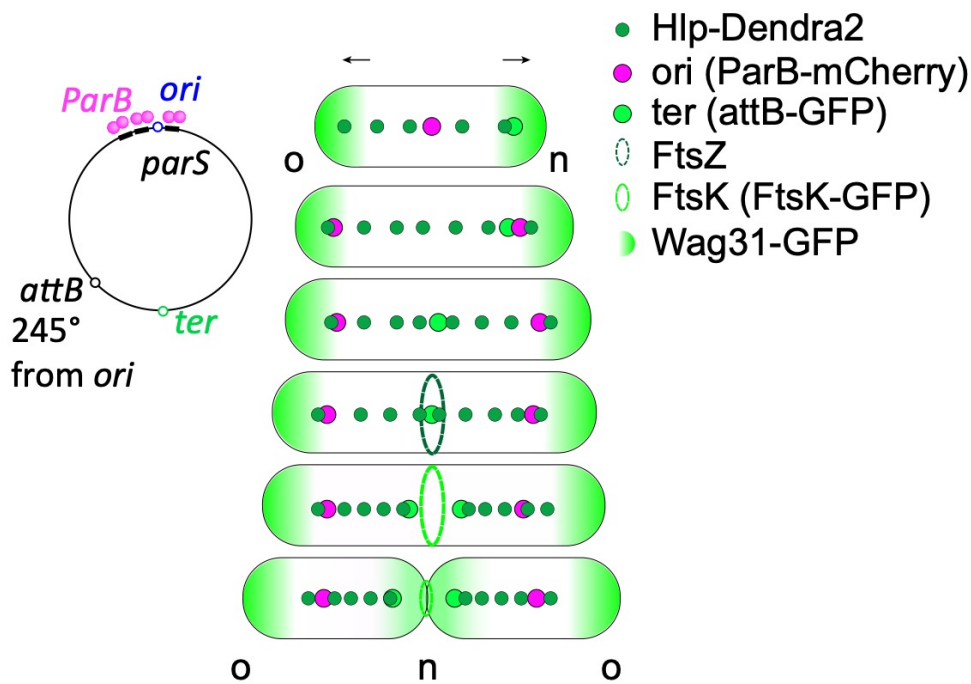
Figure 13 Fluorescent reporters constructed and used

2.8.2   Time-lapse fluorescence microscopy

In the late 17th century, Antoine van Leeuwenhoek was the first scientist to build and use a microscope with about 270 times magnification. The first time-lapse microscopy image series were made in the early 1900s, when Jean Comandon realized a time-lapse in 1909 by mounting a camera on an ultra-microscope (Bayly 1910). More recently, modern

molecular cloning techniques and discovery of the *Aequorea victoria* jellyfish's green fluorescent protein (GFP) (Shimomura et al. 1962) have enabled the construction of fluorescent reporter strains, by fusing gene sequences with GFP, starting in the 1990s (Chalfie et al. 1994). Following the discovery of GFP, other fluorescent proteins have been discovered or engineered, enabling multi-color live-cell imaging (Jakobs et al. 2000; Shaner et al. 2004).

A major advantage of time-lapse microscopy is that it allows the observation of dynamic processes such as the *M. smegmatis* v-snapping at division (Zhou et al. 2019) or the pulsatile expression of proteins such as KatG (Wakamoto et al. 2013), which would be missed by taking microscopy snapshot images only.

Nowadays, continuous time-lapse imaging can be performed over weeks or even months. However, it can be challenging to maintain the stability of an automated microscopy system as well as optimal culture conditions for extended periods of time. There is also a tradeoff between imaging of organisms at a frequency high enough to follow a particular dynamic process without inducing phototoxicity or photobleaching. Also, high-frequency time-lapse imaging over extended periods of time generates large amounts of data that must be stored, analyzed, and intepreted. For mycobacteria this is particularly challenging due to their growth behavior, as they tend to stick together and form clumps, to undergo abrupt v-snapping with large positional changes, or to divide along the same axis, and stay aligned. Efforts have been made to develop algorithms for automated image segmentation and analysis. These tend to work well for other organisms such as *E. coli* (Garner 2011, Paintdakhi et al. 2015, Ducret et al. 2016), or to detect mycobacterial microcolonies (den Hertog et al. 2010; Alva et al. 2013), but they have proven to be problematic for segmentation and analysis of single cells in mycobacteria, as the cell segmentation is more difficult to achieve compared to organisms like *E. coli* and *B. subtilis*.

2.8.3 Microfluidic devices

To observe the *M. smegmatis* reporters through several rounds of growth and division, a time-lapse experiment typically needs to last for at least 24 hours. For this purpose, we devised a homemade microfluidic device comprising a serpentine micropatterned polydimethylsiloxane (PDMS) chip, a homemade semipermeable membrane (in nitrocellulose or agarose), and a glass coverslip sandwiched between two metal holders (Figure 14) (Wakamoto et al. 2013). A syringe pump is used to deliver a constant flow of heated medium through microchannels in the PDMS chip. The bacteria are inoculated so that they are immobilized between the glass coverslip and the semipermeable membrane. The bacteria are nourished by diffusion of nutrients across the membrane; their metabolic waste products are removed by diffusion in the opposite direction. The microfluidic device assembly (which is clamped to the microscope stage) and the syringe pump containing the flow medium are set up within an environmental chamber where the temperature is maintained at 37°C.
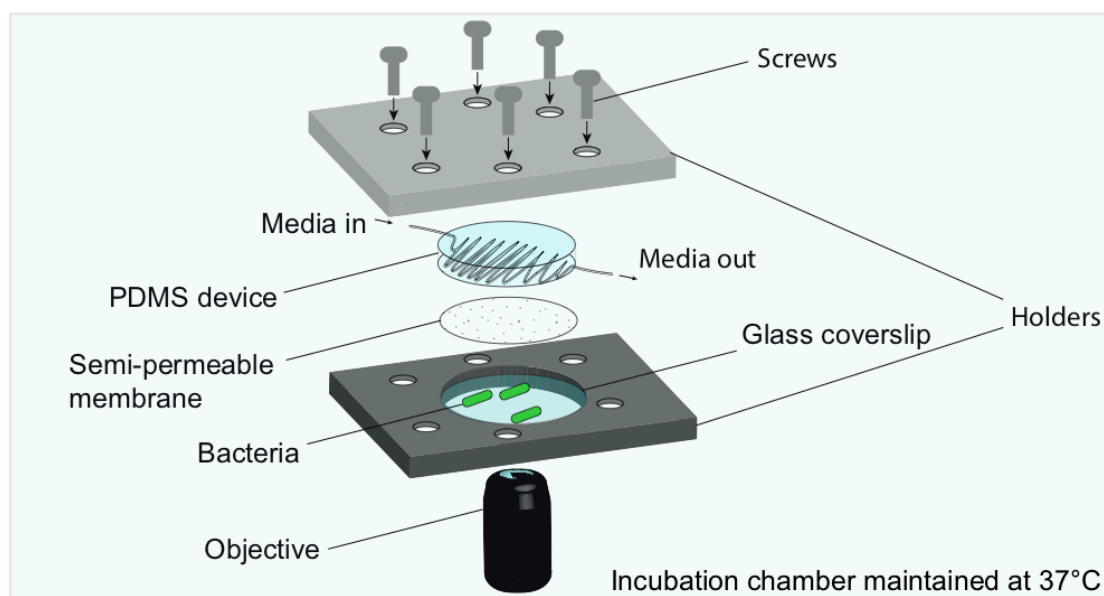
Figure 14. Schematic of a simple microfluidic device for time-lapse optical microscopy

The device is composed of a glass coverslip, a semipermeable membrane, and a PDMS chip that conducts nutrient medium through micropatterned flow channels.

2.8.4 Atomic Force Microscopy and fluidic system

An atomic force microscope (AFM) was used briefly in **Chapter 4.16** and for one part of my thesis presented in the appendix in **Chapter 9** which was a collaborative project. This project was linked to the subject of my thesis but with a different approach and addressing the question: what determines the site of division in *M. smegmatis*?

The atomic force microscope was invented in 1986 by Binnig, Quate and Gerber; it is based on the earlier scanning tunneling microscope (STM), which is used for atomic-scale characterization of metals and semiconductors. Compared to STM, the main technical advance of AFM is that it allows imaging of non-conducting samples, including biological materials.

In brief, the AFM scans a sample, in a raster-scanning mode, using a nanometer-scale tip attached to a silicon or silicon nitride cantilever. As the cantilever moves across the sample, a feedback loop adapts the vertical position of the cantilever to maintain a constant force between the cantilever and the sample (Figure 15).
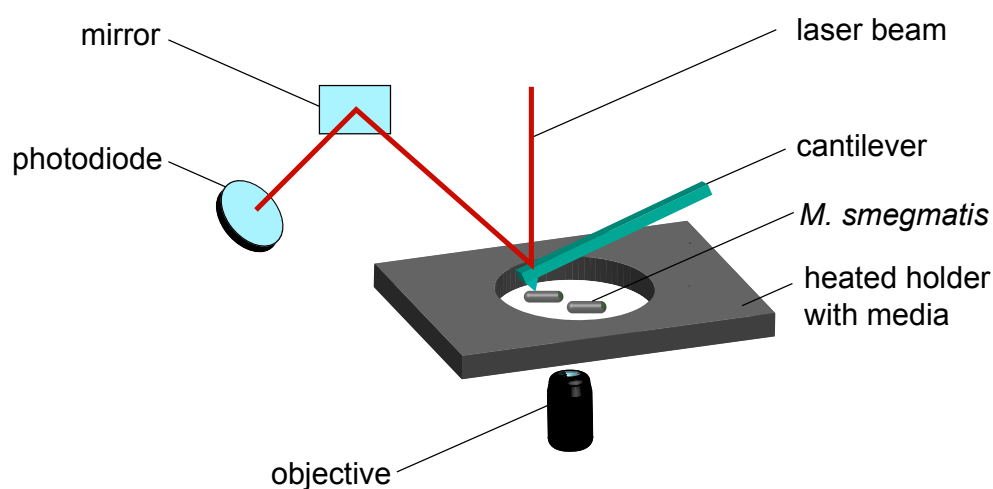
Figure 15. Schematic of dual AFM and fluorescence microscope system

The AFM provides a powerful new tool to study the growth of living bacteria, especially the 3D topology of the bacterial surface. Optical microscopy resolution is limited by the wavelength of light and the numerical aperture of the objective and reaches 250 nm and 400 nm lateral and vertical resolutions respectively. The AFM has a much greater spatial resolution, especially in the z direction, with a vertical resolution of ≥0.1 nm. The resolution is sufficiently powerful to allow real-time imaging of biomolecular process, such as myosin moving along an actin filament (Ando 2014), fine-resolution scanning of bacterial membranes (Dufrêne 2014), or real-time tracking of bacterial death after exposure to antimicrobial peptides (Fantner et al. 2010). AFM can also be used for fine-resolution nano-

mechanical mapping (stiffness, adhesion, etc.) of cell surfaces (Aguayo et al. 2015). In the Fantner lab, we have constructed a dual instrument that combines fluorescence microscopy and atomic force microscopy for long-term time-lapse imaging of live cells (Odermatt et al. 2015; Eskandarian et al. 2017).

2.9 Concluding remarks

In this thesis, I investigated the mechanisms that coordinate chromosome segregation and cell division in *M. smegmatis*. The ParABS system is currently thought to be responsible for chromosome segregation in bacteria. However, deletion of either *parA* or *parB* results in only a partial anucleate phenotype, which suggests that the Par system may not play an absolutely essential role in chromosome segregation. Furthermore, although ParA and ParB are supposed to work together in the same pathway to effect chromosome segregation (ParA binds to ParB, which binds to *parS* sequences in the chromosome), deletion of either *parA* or *parB* (or both genes together) does not lead to the same phenotype. In light of these questions, the goal of my thesis was to clarify the role of the Par system in chromosome segregation in mycobacteria; in the course of these studies, I also uncovered an unexpected role for the FtsK protein. Using fluorescent reporter strains, gene knockout strains, and time-lapse optical microscopy as the main experimental tools, I obtained results that challenge the current paradigm and suggest a new model in which the Par system is responsible for correct orientation of the chromosomes while the FtsK protein is actually responsible for the orientation-dependent segregation of the chromosomes.

Project description and overall goals

One of the major unanswered questions in bacterial cell cycle research is, "What is the role of DNA in the division process?" Indeed, mycobacteria are thought to lack nucleoid occlusions proteins, which link chromosome segregation and cell division in other bacteria. Using a custom-made microfluidic device as well as a controlled environment for stable growth, I used long-term time-lapse microscopy to study cell cycle and division in the model organism *Mycobacterium smegmatis*. One of my first goals was to determine if division could occur on top of unsegregated DNA, i.e., prior to the completion of chromosome duplication and segregation. To study the localization of DNA during the division process, I optimized the use of the DNA stain SYTO 17 and characterized the Δ*parA* and Δ*parB* chromosome partitioning mutants (**Chapter 3**).

To study the dynamics of chromosomal DNA in living cells without the toxic side effects of DNA stains, I constructed a fluorescent reporter strain of *M. smegmatis* expressing a nucleoid-associated protein (NAP) fused with the Dendra2 fluorescent protein. Hlp, the most abundant NAP, was selected. I then compared the Hlp-Dendra2 reporter strain to cells stained with conventionally used DNA stains such as DAPI, Hoechst 33342, and SYTO 17. In particular, the fidelity of the staining, its stability, toxicity, and suitability for long-term time-lapse microscopy experiments were evaluated (**Chapter 4**). I also showed the suitability of the Hlp-Dendra2 marker to discriminated anucleate cells from nucleated cells in a Δ*parA* mutant strain. As I observed that Δ*parB* cells (and likely Δ*parA* cells) sometimes divide with a small proportion of DNA still in the future anucleate cell at division, I investigated if DNA guillotining was occurring by examining whether the RecA-mediated SOS DNA damage response was occurring in Δ*parB* sibling cell pairs in which one of the siblings was anucleate.

SpoIIIE (FtsK homolog) is a known DNA translocase in *B. subtilis*. I hypothesized that FtsK, its mycobacterial homolog, might be responsible for preventing chromosome

guillotining by translocating DNA across the septum in the direction of the nucleated daughter in Δ*par* mutants. I therefore used a FtsK-GFP reporter strain and characterized its expression during the cell cycle in relation to other known division markers, such as the cytokinesis marker Wag31-GFP (**Chapter 5**). I determined FtsK's essentiality and also investigated the movement of DNA in relation with FtsK's localization. Unexpectedly, I found that, in a Δ*parB* mutant background, FtsK-GFP showed a marked localization defect. I tested if altered FtsK protein levels might be responsible for this defect, which proved not to be the case. Time-lapse microscopy observations suggested that FtsK and ParB might colocalize, but I was not able to confirm their physical interaction in co-immunoprecipitation experiments. As I showed the essentiality of FtsK, I constructed a dual repression system to down-regulate FtsK expression in WT and Δ*par* strains of *M. smegmatis.* Unexpectedly the repression of FtsK in a Δ*par* background rescues its anucleate phenotype. The localization of ori and ter suggests misoriented chromosomes in the Δ*par* background.

Finally, I propose a model where the *par* genes are responsible for the correct chromosome orientation whereas FtsK is responsible for chromosome segregation.

Chapter 3 Cell division in mycobacteria

3.1 Contribution

In the following chapter I have realized all the work presented here. I have used the strains Δ*parA* Wag31-GFP*,* Δ*parB* Wag31-GFP and WT Wag31-GFP, which were made by Isabella Santi, a former postdoc in the McKinney lab.

3.2 Introduction

Homologs of the Min and Noc proteins are absent in mycobacteria (Singh et al. 2013), but the ParABS partitioning system is thought to be responsible for the correct and symmetric segregation of chromosomes. This system is composed of three units: the ParB protein, the ParA protein, and the *parS* sequences. ParB proteins bind to the parS sequences and is thought to be moved by the motor ATP-ase ParA proteins. It has previously been reported that Δ*parA* (Ginda et al. 2013) and Δ*parB* (Santi & McKinney 2015; Eskandarian et al. 2017) mutants of *M. smegmatis* sometimes divide asymmetrically and thereby produce anucleate cells that are smaller, on average, than wild-type cells. DNA localization in Δ*parB* mutant cells has been examined using SYTO staining and snapshot microscopy (Santi & McKinney 2015); however, no long-term time-lapse microscopy experiments have been done so far to assess the dynamics of chromosomes in Δ*par* cells.

In this chapter the aim is to characterize and compare chromosome dynamics in WT, Δ*parB*, and Δ*parA* strains of *M. smegmatis*. Especially the DNA dynamics and the process of anucleate cells formation in Δ*par* cells have not been reported so far. Using time-lapse fluorescence microscopy and DNA staining by the cell-permeant nucleic-acid staining dye SYTO 17 at optimized working concentrations, the DNA dynamics will be followed and compared among the WT, Δ*parB*, and Δ*parA* strains.

3.3 Characterization of chromosome dynamics in wild-type, ΔparA, and ΔparB strains of *M. smegmatis*

Cell division in *M. smegmatis* is slightly off-centered and skewed towards the new cell pole (Aldridge et al. 2012; Santi et al. 2013). To characterize and compared the division symmetry of *M. smegmatis* Δpar mutants, I performed time-lapse optical microscopy experiments using a custom-made microfluidic device and WT, ΔparA, and ΔparB strains expressing a Wag31-GFP fusion protein (Figure 16A). Characterization of both ΔparA (Ginda et al. 2013, Ginda et al. 2017) and ΔparB (Santi et al. 2013, Santi & McKinney 2015) mutants has already been reported, but the aim of my experiments was to confirm these published results and to characterize DNA dynamics in the Δpar mutants.

The strains ΔparA Wag31-GFP and ΔparB Wag31-GFP were constructed by Isabella Santi, a former postdoc in the McKinney lab. The Wag31-GFP cytokinesis marker enables the precise measurement of the timing and localization of division (Santi et al. 2013). I then analyzed the image series from the time-lapse microscopy experiments. Consistent with previous observations (Aldridge et al. 2012; Santi et al. 2013), I found that the WT Wag31-GFP strain divides at an average position of 56 % relative to the old cell pole and a standard deviation of 4.8% (Figure 16A). In accordance with division skewed towards the new pole, on average the birth size of the old pole daughter cell is larger (3.7 ± 0.6 µm) compared to the new pole daughter cell (2.9 ± 0.6 µm) (Figure 16B). Wild-type cells divide on average at a cell length of 6.7 ± 1.1 µm (Figure 16C). In contrast, I found that ΔparB Wag31-GFP cells divide with a similar average symmetry for septum placement (56 %), but their standard deviation is larger (11.6 %) compared to WT cells (4.8%) (Figure 16A). Both the ΔparB Wag31-GFP old-pole daughter cell and new-pole daughter cell are larger more variable in size compared to WT cells, with an average birth length of 5.1 ± 1.9 µm and 4.1 ± 1.5 µm, respectively (Figure 16B). ΔparB Wag31-GFP cells divide on average at 9.2 ± 2.4 µm, which represents a 27% increase compared to WT Wag31-GFP cells (Figure 16C). Δpa-

rA Wag31-GFP cells divide even more asymmetrically and have a larger variability, with their septum placement on average at 62 ± 19 % relative to the old cell pole (Figure 16A). The old-pole daughter cells in Δ*parA* Wag31-GFP and Δ*parB* Wag31-GFP are very similar, with an average of 5.0 ± 2.0 μm and 5.1 ± 1.9 μm, respectively (Figure 16B). However, Δ*parA* Wag31-GFP new-pole daughter cells are smaller on average at birth (3.2 ± 2.0 μm). This shift compared to Δ*parB* Wag31-GFP new-pole daughter cells is due to the generation of very small anucleate daughter cells. The length at division in Δ*parA* Wag31-GFP cells is on average smaller (8.2 ± 2.3) compared to Δ*parB* Wag31-GFP cells (9.2 ± 2.4 μm), but in both cases the distribution is broader compared to WT cells (Figure 16C).

The Δ*parA* mutant and, to a lesser extent, the Δ*parB* mutant have a broader range of division size compared to WT cells. The Δ*par* cells also give birth to 22% anucleate cells in Δ*parB* and 30% in Δ*parA*, which can be as small as 0.5 μm in Δ*parA* cells, in a manner that resembles the successive budding of a small portion of the cell.
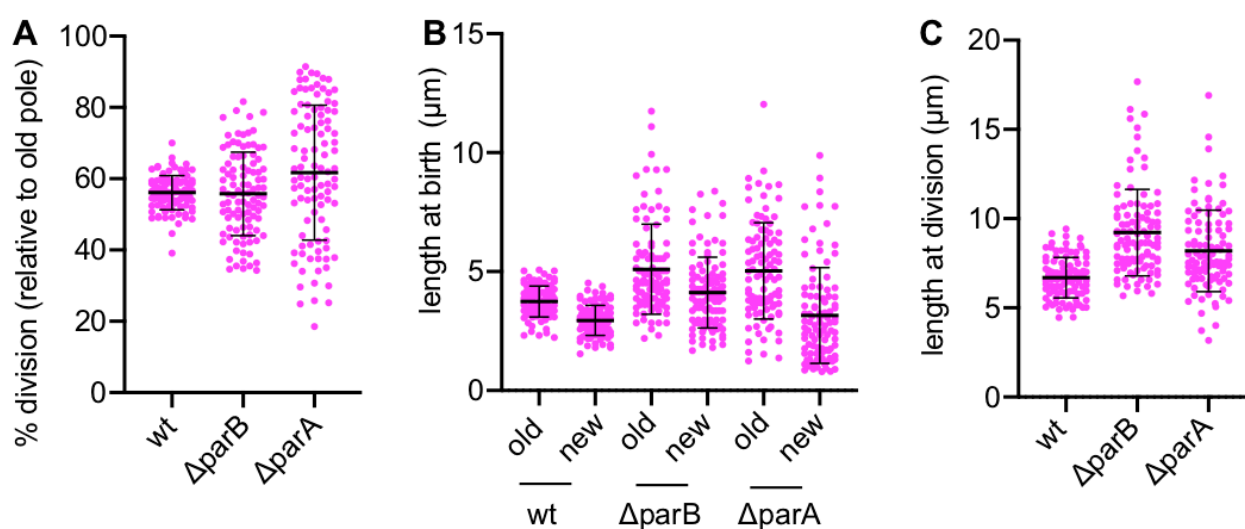
Figure 16. Δ*par mutants* divide at a broader range of cell sizes compared to WT cells

WT, Δ*parB*, and Δ*parA* strains were imaged by time-lapse microscopy and measured for **(A)** the localization of division site placement relative to the old cell pole (in %), **(B)** the length at birth for the old-pole cell and the new-pole cell, and **(C)** the length at division.

3.4 Characterizing the anucleate cells fraction in the *M. smegmatis* Δ*parB* mutant strain using the SYTO17 DNA staining dye

As mentioned earlier, one of the striking phenotypes observed in *M. smegmatis* Δ*parB* mutant cells was that the bacteria sometimes divided with gross asymmetry, generating one normal-sized to abnormally large-sized cell (usually the old-pole daughter cell) and one very small cell (usually the new-pole daughter cell). Since the small cell failed to continue growing and dividing, I hypothesized that it might be anucleate. I addressed this issue by attempting to follow the dynamics of chromosome segregation and translocation in the Δ*parB* mutant strain. To define more precisely the cell division event, I used a Δ*parB* strain that expressed the Wag31-GFP fusion protein as a marker of cytokinesis (Santi et al. 2013). The formation of anucleate cells by a Δ*parB* mutant has already been reported (Santi & McKinney 2015); however, in this published study, only single-timepoint microscopy "snapshots" were shown, whereas one of my goals in this thesis was to characterize the movement of chromosomal DNA during formation of anucleate cells using time-lapse microscopy.

Time-lapse microscopy experiments were carried out on the *M. smegmatis* Δ*parB* Wag31-GFP strain with SYTO17 dye included in the microfluidic flow medium. SYTO17 is a cell-permeant nucleic-acid staining dye commercially available from Molecular Probes that exhibits fluorescence enhancement upon binding nucleic acids. This dye reportedly stains both live and permeabilized (membrane-compromised) bacteria and, in combination with SYTOX dyes, which stain only permeabilized cells, is often used for differentiating live and dead bacteria. However, most of the reported studies use high concentrations of the dye for capturing single-time-point snapshots of stained bacterial populations. When I used SYTO17 in our continuous flow microfluidic devices, I observed that the dye was quite toxic and very soon prevented growth of the bacteria. I was unable to prevent the toxicity of the dye even upon titrating down the dosage over several orders of magnitude, as the dye

continued to accumulate in the continuous flow setup. After several trials, the only conditions under which I could use the dye to stain the DNA was to allow the bacteria to grow on the microfluidic chip over a few generations and then pulse-label the cells with the dye for a brief amount of time (Figure 17). This allowed visualizing the chromosomes for a few hours after addition of the dye. However, this staining fades over time, as the cells continue to grow and dilute the dye, which may also fade due to photobleaching. Also, I noticed that the staining and fading is quite heterogeneous, with some cells staining rapidly whereas neighboring cells are stained very weakly. This heterogeneity in SYTO17 staining does not seem to be dependent on time or cell length (Figure 17, example of cells with faint staining indicated by the green arrows at 6 hours). The very small and putatively anucleate cells were indeed observed to remain unstained and therefore probably lacked DNA (Figure 17, white arrows at 4h30). However, the marked heterogeneity and transience of staining with SYTO17 was not optimal for tracking the localization and movement of chromosomes over time.

In summary, while one could use SYTO17 staining to capture the instantaneous distribution of chromosomes in a population of bacteria, its toxicity and transient staining precludes its use in long-term time-lapse microscopy experiments. Indeed, if low (non-toxic) concentrations of SYTO17 are used, the nucleoid is not visible, and if the concentration is too high then the cells fail to grow and divide. This suggests that we need a better reporter of the nucleoid content in mycobacteria – a reporter that is non-toxic, exhibits uniform staining in all of the cells, and allows us to follow over time the dynamics of nucleoid distribution and segregation.
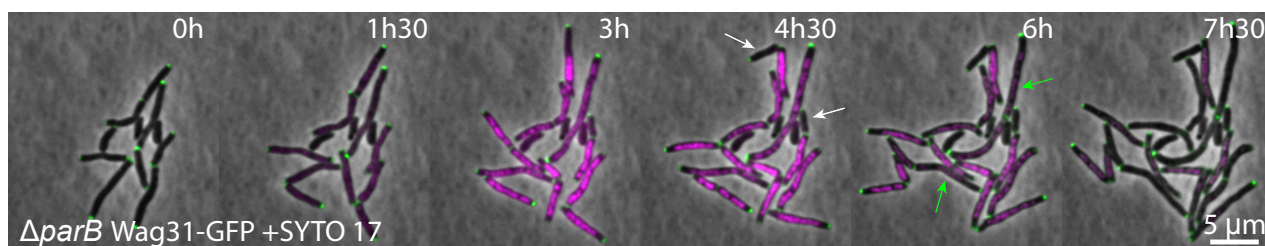
Figure 17. Time-lapse microscopy of Δ*parB* Wag31-GFP cells stained with SYTO17

A Δ*parB* Wag31-GFP strain of *M. smegmatis* was cultured in a microfluidic device and imaged by time-lapse microscopy at 15-minute intervals until small colonies were obtained. At t = 0 hours, SYTO17 was added to the microfluidic flow medium. At time 4h30, anucleate cells are highlighted by white arrows. At time 6h, cells with faded SYTO17 staining are highlighted by the green arrows.

3.5 Blocking efflux pumps using Verapamil provides prolonged SYTO17 fluorescence in Δ*parB* mutants but is cytotoxic

It has been reported previously that fluorescent dyes such as Hoechst 33342, ethidium bromide (Blair and Piddock 2016), or acridine orange (Martins & Amaral 2012) can be used to measure the activity of efflux pumps. Verapamil is a phenylalkylamine derivative, which antagonises calcium influx through the slow channels of vascular smooth muscle and cardiac cell membranes (McTavish & Sorkin 1989) and has been identified as a mycobacterial efflux pump inhibitor (Li et al. 2015). Since SYTO17 is a nucleic acid dye similary to Hoechst 33342 and ethidium bromide, I investigated whether the addition of Verapamil to the SYTO17-stained cells would inhibit the fading of stained cells. Therefore, I set up two different liquid cultures stained with SYTO17, in parallel, with and without Verapamil (170 µM final concentration). I then took microscopy snapshots after 24 hours (Figure 18). With the addition of Verapamil, the cells indeed maintained their fluorescence. However, the culture of cells exposed to both Verapamil and SYTO17 had a lower optical density com-

pared to the culture of cells with SYTO17 alone. As these cells had a marked growth defect, I concluded that Verapamil or the combination of Verapamil and SYTO17 seems to have a toxic effect. As my aim was to study chromosome dynamics by performing live-cell time-lapse microscopy on growing and dividing cells, this approach was therefore abandoned.

In summary, we conclude that Verapamil blocks the fading of SYTO17 staining but Verapamil or the combination of Verapamil and SYTO17 is too cytotoxic for use in live-cell time-lapse microscopy.
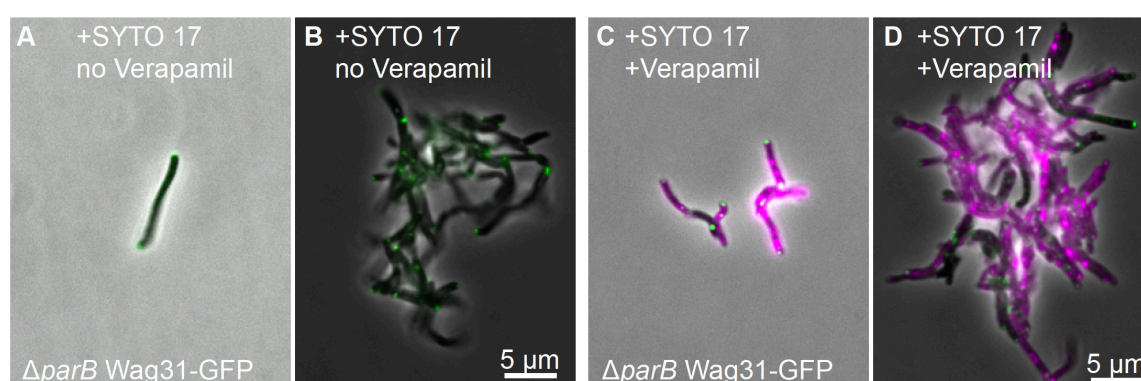
Figure 18. Verapamil maintains SYTO17 staining over time but is cytotoxic

Snapshot fluorescence images were taken of Δ*parB* Wag31-GFP cells grown in liquid culture with SYTO17 after 24 hours without Verapamil **(A, B)** or with Verapamil at 170 μM **(C, D)** added to the culture. Two snapshots are shown for each condition after 24 hours to show that the loss or retention of SYTO17 was relatively homogeneous not depending wether the cells were organized as a clump or as single cells.

3.6   The majority of anucleate Δ*par* cells are produced by divisions skewed towards the new cell pole

It has previously been reported that mycobacterial Δ*parA* (Ginda et al. 2013) and Δ*parB* (Santi et al. 2013) mutants divide asymmetrically (**Chapter 3.3**) and some cells are

born without a chromosome (anucleate daughter cells). However, it is still not understood why some divisions give rise to one anucleate daughter cell and one nucleated daughter cell, whereas other divisions give rise to two apparently normal nucleated daughters. One of my aims in this thesis was to test the idea that (mis)orientation of a chromosome in Δ*parA* or Δ*parB* cells could be responsible for subsequent formation of an anucleate daughter cell due to mis-segregation of the mis-oriented chromosome into the "wrong" daughter cell, resulting in formation of one daughter with no chromosome and one daughter with two chromosomes.

Time-lapse microscopy experiments were carried out on *M. smegmatis* wild-type*,* Δ*parA*, or Δ*parB* cells expressing Wag31-GFP in the presence of SYTO17 dye to stain the chromosomal DNA using the optimized conditions described in **Chapter 3.4**. By analyzing the division of cells stained with SYTO17, I determined that all wild-type cells divide to give birth to two nucleated daughter cells. In Δ*parA* cells, although the majority of the cells (64%) divide to give two nucleated daughter cells, a fraction of cells (23%) give birth to an anucleate new-pole daughter cell and a smaller fraction (13%) give birth to an anucleate old-pole daughter cell. The distinction between anucleate old-pole or new-pole daughter cells was so far unreported, to the best of my knowledge. In Δ*parB* cells, the same trend can be observed: a majority of cells (78%) give birth to two nucleated daughter cells, a fraction of cells (20%) give birth to an anucleate new-pole daughter cell, and a smaller fraction of cells (2%) give birth to an anucleate old-pole daughter cell (Figure 19).

	wt	ΔparA	ΔparB
1.	100	64	78
2.	0	23	20
3.	0	13	2
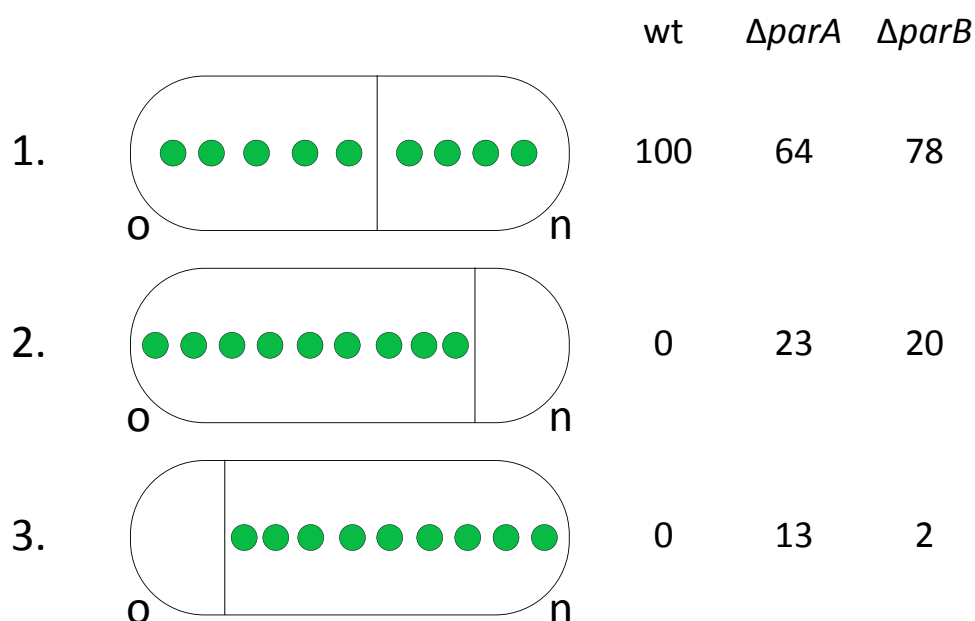
Figure 19 Distribution of nucleated versus anucleate old or new poles daughter cells in wt Δ*parA* and Δ*parB* cells

1. Cells which result in two nucleated daughter cells. **2.** Cells which result in an anucleate new pole daughter cell. **3.** Cells which result in an anucleate old pole daughter cell. Corresponding calculated percentage in wt, Δ*parA* or Δ*parB* strains. (o) old pole. (n) new pole. The green dots represent the DNA.

Analyzing Δ*parB* divisions in greater details (Figure 20), the cells are comparable to wild-type cells, as they divide on average at 53% of the cell length (WT: 55%) when measured from the old cell pole. The remaining 22% of dividing cells give birth to one nucleated daughter cell and one anucleate daughter cell. The majority (91%) of anucleate cells are new-pole daughters, while the minority (9%) of anucleate cells are old-pole daughters. Anucleate new-pole daughters divide on average at 65% relative to the old cell pole and their division position ranges from about 40% to 85% of the cell length relative to the old pole.
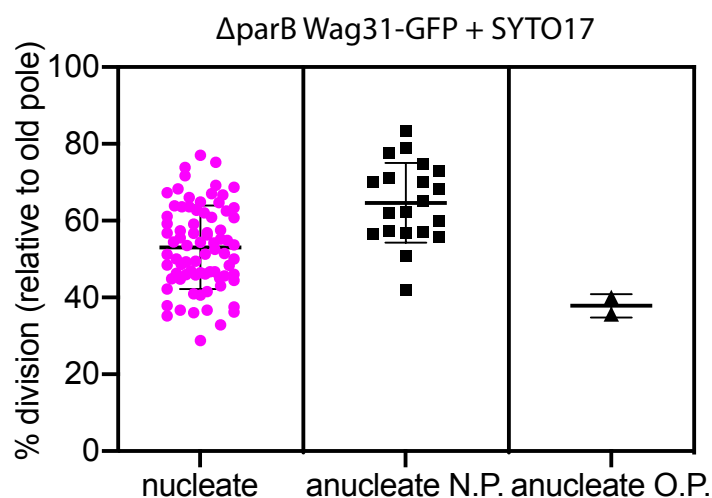
Figure 20. Δ*parB* anucleate cells are on average skewed towards the new cell pole

Δ*parB* Wag31-GFP cells stained with SYTO17 divide on average at 53% for nucleated cells, 65% for divisions that generate anucleate new pole daughters, and 38% for divisions that generate anucleate old-pole daughters, relative to the old cell pole (n = 100).

We conclude that the nucleated Δ*parB* cells ressembles the distribution of wt cells (Figure 20) and that the anucleate new pole or old pole daughter cells extend the range where Δ*parB* cells can divide. Therefore, it suggests that even if ParB is deleted in every cell, most Δ*parB* cells divide like wt cells, proving that the phenotype is not 100% pene-trant. Only a minority of cells (22%) behave in a different way and either divide giving an anucleate new pole in 20% of the cases or an anucleate old pole in 2% of the cases. It then brings the question what determines if a cell will have an anucleate old pole or new pole? To try to answer to this latter question, understanding the dynamics of DNA during division is crucial.

3.7 Δ*parB* cells stained with SYTO17 reveal the transient presence of DNA in anucleate cells

To understand the formation of anucleate cells, the anucleate cell formation during time-lapse microscopy experiment were analysed in further detail. As no homolog for nucleoid occlusion (Noc) proteins exist in *M. smegmatis*, I asked whether division can occur where chromosomal DNA is present. In Δ*parB* cell divisions giving birth to nucleated cells, the completion of cytokinesis, indicated by appearance of the Wag31-GFP marker at the division septum (Santi et al. 2013), appears at a local DNA minimum (Figure 21A). In some divisions giving birth to anucleate cells, Wag31-GFP also appears at a DNA minimum (Figure 21B). However, in some cases DNA can be detected in the future anucleate cell and seems to disappear after cytokinesis (between the frames at 15 minutes and 45 minutes) (Figure 21B).

We conclude that some Δ*parB* cells complete cytokinesis with DNA still detectable on both side of the septum. However, the small amount of DNA that is originally localized in the smaller daughter cell seems to disappear over time, resulting in an anucleate daughter cell.
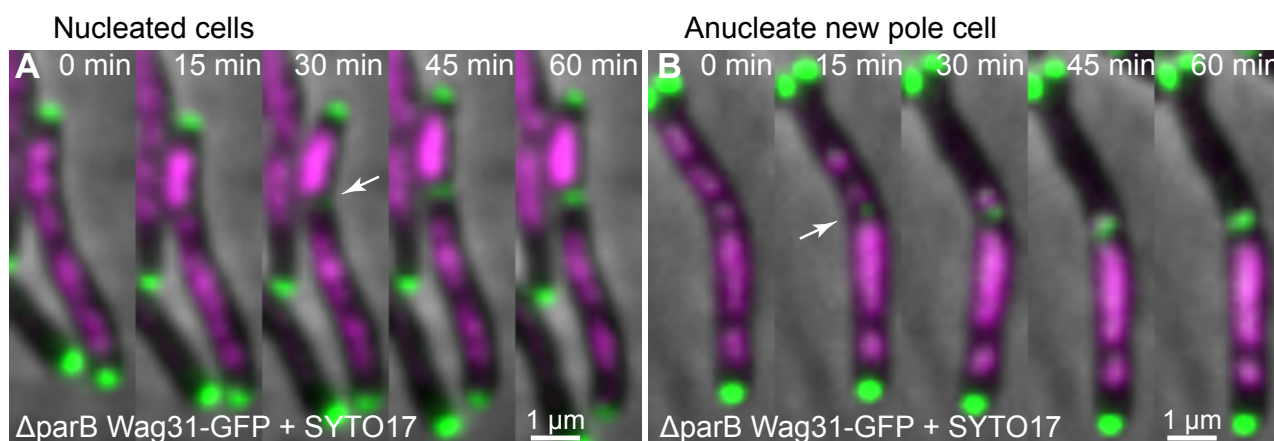
Figure 21. Persistence and gradual disappearance of DNA in anucleate daughter cells after cytokinesis

Δ*parB* Wag31-GFP cells were imaged by time-lapse microscopy at 15-minute intervals and stained with SYTO17. **(A)** Formation of two nucleated daughter cells. **(B)** Formation of an anucleate new-pole daughter. The first appearance of Wag31-GFP, signaling the completion of cytokinesis, is indicated by the white arrows.

As DNA seems to disappear from the anucleate daughter cell over time, I asked whether this DNA might be transferred from the anucleate daughter cell into the nucleated daughter cell post-cytokinesis. To try to answer to this question, I plotted the amount of SYTO17 fluorescence in an anucleate cell and its sister cell before and and after cytokinesis. I observed some cells where no DNA is visible in the anucleate cell at the time of cytokinesis (Figure 22A) and some cells where DNA is still present in the anucleate cell at cytokinesis (Figure 22B). In the first case, the fluorescence is quite stable (at background levels) in the anucleate cell over time. In the second case, there is a progressive decrease of SYTO17 fluorescence between -15 minutes and cytokinesis. In both cases, fluorescence of the nucleated daughter cell increases between -15 minutes and cytokinesis. However, this pattern is less visible for cells where division occurs at the end of the time-lapse (Figure 22C). Indeed, as will be decribed in more detail in **Chapter 4.5**, the SYTO17 fluorescence takes a few hours to be visible after addition to the microfluidic flow medium and then diminishes over time. In the third profile (Figure 22C), the nucleated cell fluorescence does

not increase. This could be explained by the fading SYTO17 fluorescence at the end of the time-lapse experiment. As the SYTO17 fluorescence is not stable over time, these results must be interpreted with caution, as a decrease or increase of fluorescence might not reflect directly the amount of DNA present in the cell depending on when the cells are observed during the time-lapse experiment.

We conclude that SYTO 17 fluorescence in the nucleated sister cell increases after cytokinesis, while SYTO 17 fluorescence in the corresponding anucleate sister cell seems to decrease over time. This increase could be due to a directed chromosome movement from the future anucleate daughter cell to the nucleated daughter cell, or DNA could be guillotined by the closing septum and then degraded. This degradation would presumably lead to an SOS response, which will be investigated later (in **Chapter 4.12**). However, these results must be interpreted with caution, as the SYTO17 staining is heterogeneous and transient during time-lapse experiments.
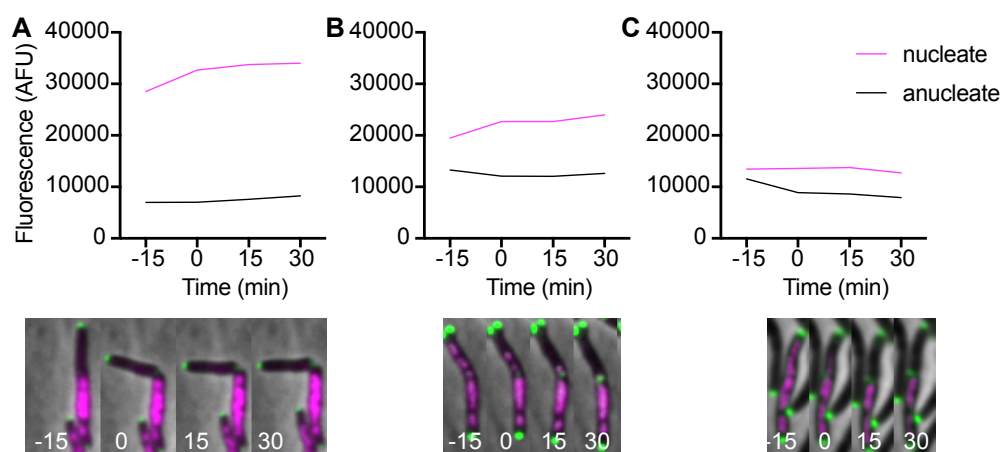
Figure 22. DNA staining diminishes in Δ*parB* anucleate daughters while increasing in nucleated daughters

SYTO17 fluorescence in nucleated and anucleate sister cells is represented for 3 different cells at 15-minute intervals, with 0 minutes corresponding to the time of cytokinesis. An example of each situation is shown under each graph for **(A)** a division event where DNA is not detectable in the anucleate daughter before cytokinesis, **(B)** a cell where some DNA is present in the future anucleate daughter at the time of cytokinesis, and **(C)** a cell that divides late in the time-lapse experiment.

3.8   Conclusion

Compared to WT cells, Δ*parA* and Δ*parB* cells divide over a broader range of division symmetry. The average length at division is larger in Δ*par* cells compared to WT cells, suggesting that cell division may be delayed in Δ*par* cells. The birth size distribution of Δ*par* cells is also broader, especially for Δ*parA* cell divisions that give rise to anucleate new-pole daughter cells and very long old-pole daughter cells. Using the dye SYTO17 at an optimized concentration (the dye being toxic for the cells at high concentrations), we could identify anucleate cells arising from divisions of Δ*parB* cells. Interestingly, the average localization of the septum is comparable in both Δ*parB* nucleated cells and WT cells. In Δ*par* cells, similar to WT divisions, the majority of the cells divide more around the center of the cell length and gives birth to two nucleated daughter cells. A minority of Δ*par* cells divide giving birth to an anucleate new pole cell and an even smaller minority give birth to unreported anucleate old pole daughter cells. As reported previously, the Δ*par* phenotype is not a replication defect as the nucleated cell has two or more chromosomes (Ginda et al. 2017) but a segregation defect. As the phenotype is not 100 % penetrant, it argues in favor of an alternative mechanism working with the *par* genes for a correct chromosome segregation.

In some Δ*parB* cells divisions that result in formation of an anucleate daughter cell, the cytokinesis marker Wag31-GFP appears with SYTO17-stained DNA still detectable on both sides of the septum. In these cases, the amount of SYTO17 fluorescence progressively decreases in the anucleate cell with a corresponding increase in the nucleated sister cell. This increase must, however, be interpreted with caution, as SYTO17 staining is not constant over time. Therefore, a better reporter of the nucleoid content in mycobacteria is needed, one that is non-toxic, exhibits uniform staining in all of the cells, and allows us to follow the dynamics of nucleoid distribution and segregation over time. But what could then happen to DNA if this observation is still seen using a better marker? The DNA could

either be degraded or pulled towards the nucleated daughter cell. I will later on investigate about the DNA fate in these anucleate cell formation divisions.

Chapter 4 Live-cell imaging of mycobacterial chromosomes with fluorescently tagged histone-like protein (Hlp)

4.1 Contribution

In the following chapter I have constructed all the reporters and realized all the work presented here. The exceptions being the following. The structured illumination microscopy (SIM) images were done at the EPFL Bioimaging and Optical Platform (BIOP) with the help of Thierry Laroche. I re-analyzed the archived movies from a *M. smegmatis* reporter strain Wag31-GFP and DnaN-mCherry time-lapse experiment performed by Isabella Santi, a former postdoc in the McKinney lab. Mélanie Hannebelle, a PhD student in the Fantner and McKinney labs helped me for the atomic force microscopy imaging.

4.2 Introduction

As observed in the previous chapter, conventionally used DNA dyes are not stable over time. These dyes also seem to have a toxic effect, as stained cells grow more slowly, especially after prolonged exposure to SYTO17. Therefore, as these dyes do not seem to be compatible with long-term time-lapse microscopy experiments, my goal was to construct and use a nucleoid-associated protein (NAP) fused to a fluorescent protein as an alternative marker for chromosomal DNA. Ideally, this reporter could be used to follow DNA over an extended time period by selecting a NAP that is constitutively expressed at a high level. The fluorescent NAP reporter strain would then be evaluated in comparison to conventionally used DNA dyes. Two nucleoid-associated proteins, Lsr2 and Hlp, were selected to

construct fluorescent reporter strains, as they are two of the principal and highly abundant NAPs in *M. tuberculosis* (Datta et al. 2019). Hlp-Dendra2 was superior to Lsr2-Dendra2 as a reporter for intracellular DNA localization as demonstrated by the comparisons of their intracellular fluorescence profiles with those observed using conventional DNA staining. Images of single cells expressing Hlp-Dendra2 showed fluorescence localization profiles that were similar to images of single cells that were stained using conventional DNA dyes, therefore validating the use of Hlp-Dendra2 as a reporter for intracellular DNA localization. In contrast, images of Lsr2-Dendra2 cells did not display intracellular fluorescence profiles that were comparable to those observed using DNA staining. Consequently, Hlp-Dendra2, and not Lsr-Dendra2, was selected for further characterization. In particular, the fidelity of the staining, its stability, toxicity, and suitability for long-term time-lapse microscopy experiments were investigated. The ability to distinguish anucleate Δ*par* cells was also evaluated. The compatibility of Hlp-Dendra2 with super-resolution microscopy was also tested. The movement of Hlp-Dendra2 stained chromosomes was tracked throughout the cell cycle in WT and Δ*par* mutant cells, both alone and relative to well-characterized chromosomal loci such as the origin of replication, which has a defined location during the cell cycle (Santi et al. 2015; Ginda et al. 2017). The localization of newly produced Hlp-Dendra2 was quantified using light-induced photoswitching of the Dendra2 fluorophore. Finally, super-resolution microscopy techniques such as super-resolution radial fluctuations (SRRF) (Gustafsson et al. 2016) and structured illumination microscopy (SIM) (Rego & Shao 2015) were used to characterize the subcellular organization of Hlp-Dendra2 stained chromosomes.

4.3 Characterization of Lsr2-Dendra2 pattern in *M. smegmatis* mutant

Due to SYTO17's observed cytotoxicity, as an alternative method to visualize chromosomes in living cells I constructed a reporter strain of *M. smegmatis* expressing a

fusion of a nucleoid-associated protein (NAP) with a fluorescent protein. As Lsr2 is one of the most abundant NAPs in mycobacteria, I used the Gibson assembly method to construct a reporter plasmid containing the constitutive *hsp*60 promoter driving the expression of a PCR-amplified Lsr2 sequence fused at its C-terminus with the PCR-amplified sequence encoding the Dendra2 fluorescent protein. This plasmid expresses a phage integrase that mediates the integration of the plasmid into the *M. smegmatis* genome by a site-specific recombination event between the phage attachment sequence *attP* and the corresponding bacterial attachment sequence *attB* (Peña & al. 1997). The *M. smegmatis* Lsr2-Dendra2 strain was cultured in a custom-made microfluidic device and imaged by time-lapse microscopy (Figure 23A). I then analysed the Lsr2-Dendra2 fluorescence and plotted its intensity and subcellular distribution over time from birth to division (Figure 23B). At birth there is a maximum intensity of Lsr2-Dendra2 near the old cell pole, presumably corresponding to the newly inherited chromosome, which is gradually displaced to mid-cell, where this maximum is gradually split in two. These Lsr2-Dendra2 maxima then separate and move from midcell to the cell poles.

Unfortunately, the Lsr2-Dendra2 marker did not show a homogeneous distribution along the cell length at any time during the cell cycle. Furthermore, it did not resemble the profiles of DNA stained with conventional DNA dyes. My motivation to construct this strain was to follow the dynamics of DNA and, in particular, the formation of anucleate cells during division of Δ*par* mutant cells. As nucleated cells showed a non-uniform Lsr2-Dendra2 fluorescence, this reporter is not a reliable tool to distinguish between nucleate or anucleate cells. Therefore, the use of the Lsr2-Dendra2 reporter strain to study DNA localization and dynamics during the mycobacterial cell cycle was abandoned.
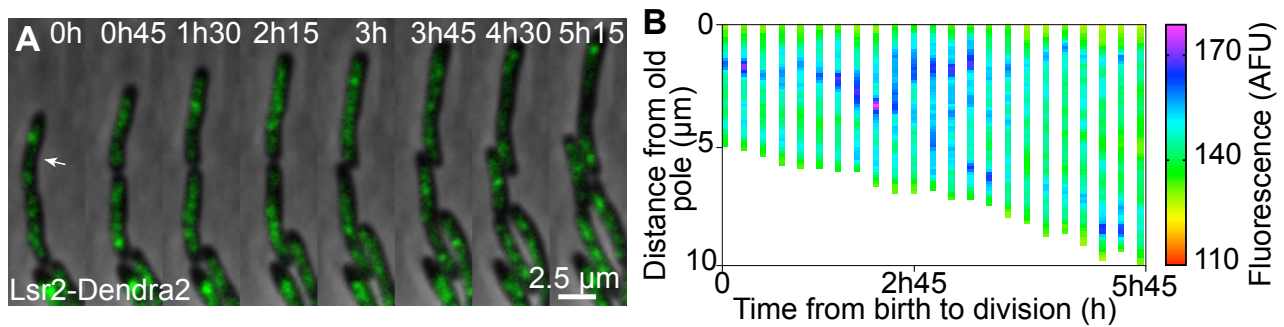
Figure 23. Time-lapse microscopy and analysis of a Lsr2-Dendra2 reporter strain

(A) *M. smegmatis* Lsr2-Dendra2 cells were cultured in a microfluidic device and imaged by time-lapse microscopy at 15-minute intervals. **(B)** Fluorescence profile along the long axis of the cell indicated by the white arrow in (A) is plotted from birth to division, magenta being the maximum intensity of Lsr2-Dendra2 fluorescence.

4.4   The genetically encoded marker Hlp-Dendra2 is superior to conventional DNA stains for imaging chromosomes in mycobacteria

DNA dyes such as DAPI, Hoechst 33342, or SYTO are commonly used to stain DNA. However, the application of DNA stains can be problematic due to high background fluorescence, broad emission peaks that overlap with other fluorescent markers, inconsistent staining over time, and cytotoxicity. In order to follow DNA in a dynamic fashion using time-lapse microscopy I constructed a *M. smegmatis* Hlp-Dendra2 strain. I first constructed a plasmid using the Gibson assembly method containing the constitutive *hsp*60 promoter driving the expression of the PCR-amplified *hlp* gene fused at its C-terminus with the PCR-amplified sequence encoding the Dendra2 fluorescent protein. This plasmid expresses a phage integrase that mediates the integration of the plasmid into the *M. smegmatis* genome by a site-specific recombination event between the phage attachment sequence *attP* and the corresponding bacterial attachment sequence *attB* (Peña & al. 1997). The Hlp-

Dendra2 strain was grown to exponential phase, stained with SYTO17, DAPI, or Hoechst 33342, and imaged by phase and fluorescence microscopy (Figure 24 A-C). I first compared the fluorescence profiles of Hlp-Dendra2 to the DNA dyes along the long axis of the stained cells (Figure 24 D). The DNA stains as well as the Hlp-Dendra2 marker revealed a beads-on-a-string structure. The fluorescence profile of SYTO17-stained cells was quite similar to the fluorescence profile of the Hlp-Dendra2 marker but with a high background fluorescence level and more cell-to-cell variation. We avoided permeabilizing the cells, as our goal was to have a suitable tool for live-cell time-lapse imaging, which could explain the poor staining that was obtained with DAPI. The Hoechst 33342 dye revealed a very well-resolved staining. Unfortunately, however, *M. smegmatis* is auto-fluorescent when imaged on the blue fluorescence channel (Patiño et al. 2008).
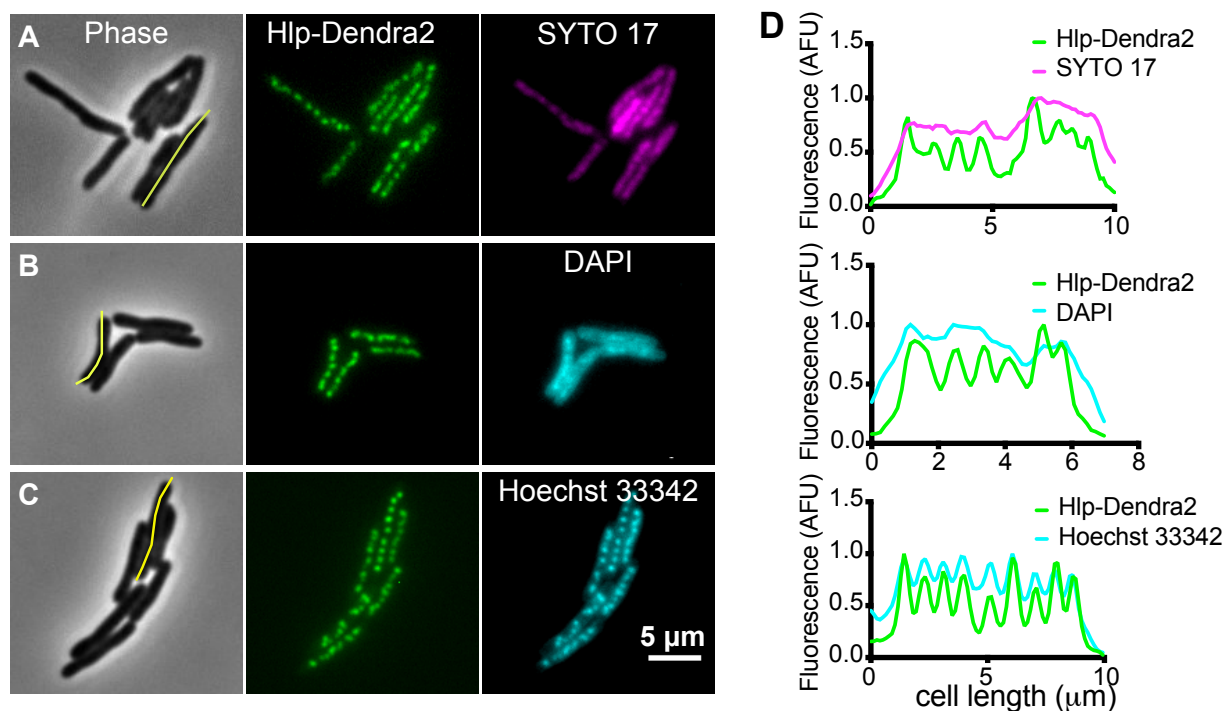
Figure 24. The genetically encoded marker Hlp-Dendra2 is superior to conventional DNA stains for imaging bacterial chromosomes

(A-C) A strain of *Mycobacterium smegmatis* expressing the histone-like protein Hlp fused to Dendra2 was grown to exponential phase in batch culture and cells were stained with the DNA stains SYTO17 **(A)**, DAPI

(B), or Hoechst **(C)**. Images were taken by phase-contrast and fluorescence microscopy. **(D)** Fluorescence intensity along the longitudinal axis of representative cells, as indicated by yellow lines in the phase images in panels A-C.

4.5 Hlp-Dendra2 fluorescence is more stable and homogeneous than SYTO17 or Hoechst 33342 staining

Microscopic snapshots of stained cells revealed that Hlp-Dendra2 provides superior resolution and lower background fluorescence compared to SYTO17, DAPI, or Hoechst 33342 staining (Figure 25). However, time-lapse microscopy also requires that the fluorescence signal be stable over time, with minimal photobleaching, and evenly distributed among the imaged cells. Therefore, we grew bacteria expressing Hlp-Dendra2 in a microfluidic device under a constant flow of 7H9 medium and imaged them at 15-minute intervals as microcolonies formed (Figure 25A). We found that the area occupied by a microcolony expanded exponentially (Figure 25C, green symbols), as expected for cells growing normally. In parallel, total fluorescence of the microcolony also increased exponentially (Figure 25E, green symbols), as expected if Hlp-Dendra2 production continues without extensive photobleaching. Indeed, Hlp-Dendra2 fluorescence per unit area of the microcolony remained stable over time, increasing slightly at later time points, perhaps due to crowding and overlapping of cells in large microcolonies (Figure 25F, green symbols).

In separate experiments, Hlp-Dendra2 cells were grown in a similar way to obtain small microcolonies, except that SYTO17 (Figure 25B) or Hoechst 33342 (Figure 25C) was added to the flow medium at time 0 and imaging was continued as before at 15-minute intervals. After addition of SYTO 17, microcolonies continued to expand for a few hours before growth slowed sharply (Figure 25D, magenta symbols). Total SYTO17 fluorescence began to increase only after a lag of several hours, reached a peak at about 6 hours, and then declined progressively over time despite the continued presence of SYTO17 in the flow medium (Figure 25E, magenta symbols). In parallel, SYTO17 fluorescence per unit area

of the microcolony followed a similar pattern over time (Figure 25F). At the single-cell level, staining with SYTO17 was very uneven, increasing and decreasing at different rates in different cells (Figure 25B). Cells stained with Hoechst 33342 rapidly arrested growth (Figure 25D, cyan symbols). Total fluorescence increased rapidly and reached a plateau at about 6 hours, then stabilized for the duration of the experiment (Figure 25E, cyan symbols). In parallel, Hoechst 33342 fluorescence per unit area of the microcolony followed a similar pattern over time, rising after a lag, plateauing at about 6 hours, and remaining constant thereafter (Figure 25F, cyan symbols). We did not perform time-lapse imaging of cells stained with DAPI, which requires permeabilization of the cells prior to staining and is therefore incompatible with live-cell time-lapse imaging.

We conclude that Hlp-Dendra2 fluorescence provides superior stability for time-lapse imaging compared to either SYTO17 or Hoechst 33342 staining.
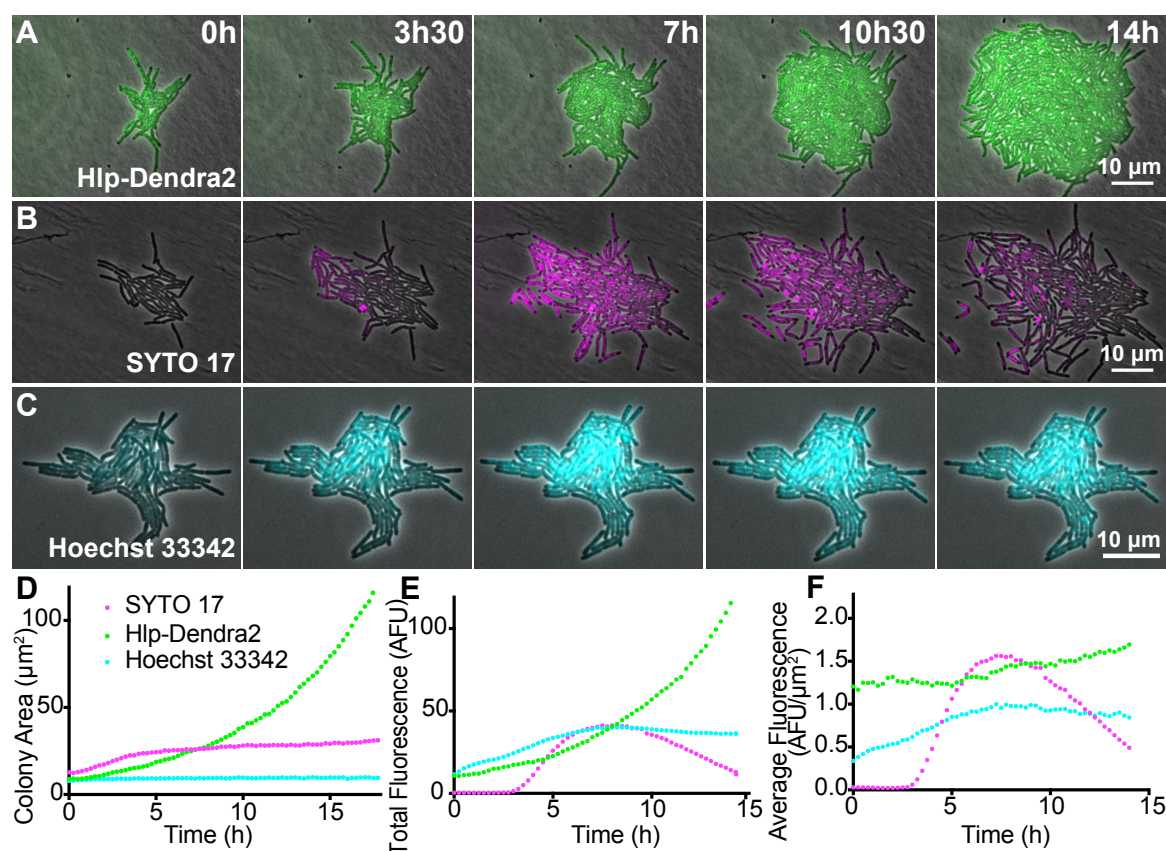
Figure 25. Hlp-Dendra2 fluorescence is more stable and homogeneous than SYTO17 or Hoechst 33342 staining

(A-C) *M. smegmatis* expressing Hlp-Dendra2 was cultured in a microfluidic device and imaged by time-lapse microscopy at 15-minute intervals until small colonies were obtained. At t = 0 hours, SYTO17 **(B)** or Hoechst 33342 **(C)** was added to the flow medium and imaging was continued. **(D-F)** Microscopic analysis of representative microcolonies of Hlp-Dendra2 cells (green) stained with SYTO17 (magenta) or Hoechst (cyan) starting at t = 0 hours. **(D)** Microcolony area (μm^2) over time. **(E)** Total fluorescence over time. **(F)** Average fluorescence per unit area (μm^2) over time.

4.6 Fluorescence imaging with Hlp-Dendra2 does not impede cell growth whereas SYTO 17 or Hoechst 33342 staining is growth inhibitory

We asked whether the conditions used for fluorescence imaging of DNA using the Hlp-Dendra2 reporter or staining with SYTO17 or Hoechst 33342 might be detrimental for bacterial growth (Figure 26). Under each growth condition, we calculated the colony doubling time (CDT) according to the following equation:

$$(1)\ CDT = \frac{\ln(2)\,t}{\ln\left(\frac{N}{N_0}\right)}$$

Equation 1. Colony doubling time

where t is the time elapsed between the beginning and end of the experiment, N_0 is the number of cells at the beginning of the experiment, and N is the number of cells at the end of the experiment.

We found that the doubling times of the wild-type and Hlp-Dendra2 strains were not significantly different under all of the conditions that we tested (Figure 26A, B). Similarly, fluorescence excitation at 475/28 nm (to visualize Hlp-Dendra2) or 632/22 nm (to visualize SYTO17) had no significant effect on bacterial growth (Figure 26A). However, addition of SYTO17 to the growth medium strongly inhibited growth (Figure 26A). We also found that fluorescence excitation at 390/18 nm (to visualize Hoechst) was strongly growth inhibitory, with or without addition of Hoechst to the flow medium (Figure 26B).

We conclude that fluorescence imaging of Hlp-Dendra2 cells does not significantly affect cell growth, whereas fluorescence imaging of cells stained with SYTO17 or Hoechst 33342 is strongly growth inhibitory.
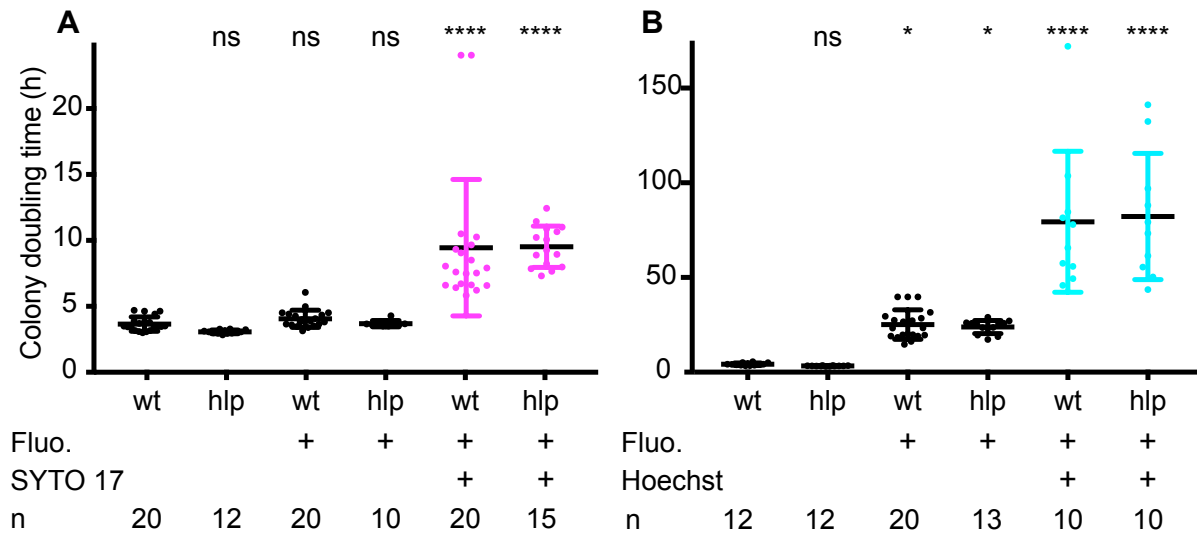
Figure 26. SYTO 17 and Hoechst staining are cytotoxic

Wild-type *M.* smegmatis (wt) and *M. smegmatis* expressing Hlp-Dendra2 (hlp) were cultured in a microfluidic device and imaged by time-lapse microscopy at 15-minute intervals. Colony doubling times were calculated as described in the text. Colonies contained 75 cells on average at the end of the experiment. Each symbol represents one colony (n = number of colonies measured). One-way ANOVA was used to compare wild-type bacteria imaged without staining or fluorescence excitation vs. all other conditions tested: ns, not significant; * P = 0.03; **** P < 0.001. **(A)** Cells were imaged +/- fluorescence (Fluo.) excitation at 632/22 nm (far-red) and 475/28 nm (green), and +/- addition of SYTO17 to the flow medium, as indicated. **(B)** Cells were imaged +/- fluorescence (Fluo.) excitation at 390/18 nm (UV), and +/- addition of Hoechst 33342 to the flow medium, as indicated.

4.7 Hlp-Dendra2 is a more reliable marker than SYTO17 to distinguish between nucleated and anucleate cells

The highly conserved ParA and ParB proteins are involved in chromosome partitioning during the bacterial cell cycle, although their mechanism of action is not completely understood (Surovtsev & Jacobs-Wagner 2018). In *M. smegmatis*, deletion of the *parA* or *parB* gene results in chromosome partitioning defects and formation of anucleate cells that fail to grow (Jakimowicz et al. 2007; Santi & McKinney 2015; Eskandarian et al. 2017).

Therefore, I constructed Δ*parA* Hlp-Dendra2 strains using the Hlp-Dendra2 plasmid described earlier. I then performed time-lapse microscopy experiments with the *M. smegmatis* Δ*parA* Hlp-Dendra2 strain with a SYTO17 endpoint staining. In time-lapse microscopy experiments, all wild-type cells expressing Hlp-Dendra2 were scored as Hlp-Dendra2-positive and all cells grew and divided normally without generating Hlp-Dendra2-negative cells at detectable frequencies (Figure 27A). In contrast, Δ*parA* cells expressing Hlp-Dendra2 generated Hlp-Dendra2-negative cells at a frequency of about 20% (Figure 27B, arrows). Without exception, cells scored as Hlp-Dendra2-negative failed to grow after birth, confirming that they were anucleate.

We compared the accuracy of Hlp-Dendra2 and SYTO17 staining for detection of anucleate cells. As mentioned, SYTO17 staining is heterogeneous and transient (Figure 25). At the peak of SYTO17 staining, all Hlp-Dendra2 cells were scored as SYTO17-positive (Figure 27C,D), although SYTO17 uniformly stained all cells only during a limited window of time (about 5 hours). Before and after the peak of SYTO17 staining, many growing cells were scored as SYTO17-negative, which, together with its toxicity (Figure 26), further limits the usefulness of this marker for time-lapse studies. In Δ*parA* cells, SYTO17 staining was less reliable. All Δ*parA* cells that were scored as Hlp-Dendra2-negative were also scored as SYTO17-negative; without exception, these cells failed to grow after birth, confirming their identification as anucleate cells (Figure 27E; Figure 27F, black symbols). However, in some cases, Δ*parA* cells were scored as Hlp-Dendra2-positive but SYTO 17-negative; without exception, these cells grew and divided, confirming their identification as nucleated cells (Figure 27E, arrows; Figure 27F, colored symbols).

We conclude that Hlp-Dendra2 is a more reliable marker than SYTO17 staining to distinguish between nucleated and anucleate cells, as we did not identify false negatives (growing cells that were scored as Hlp-Dendra2-negative) or false positives (non-growing anucleate cells that were scored as Hlp-Dendra2-positive) at detectable frequencies.
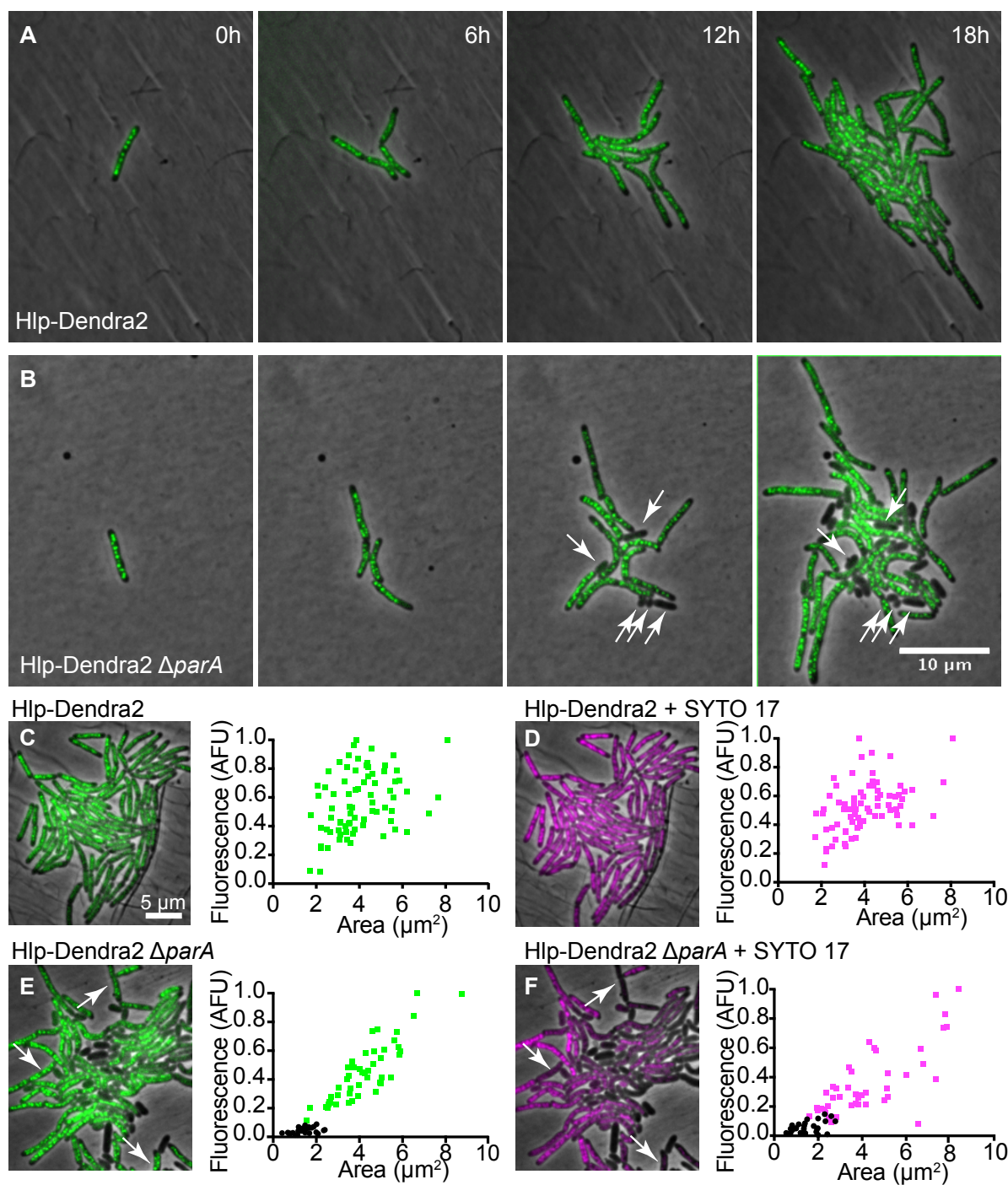
Figure 27. Hlp-Dendra2 is more reliable than SYTO 17 for distinguishing between nucleated and anucleate cells

M. smegmatis Hlp-Dendra2 and Δ*parA* Hlp-Dendra2 cells were cultured in a microfluidic device and imaged by time-lapse microscopy at 15-minute intervals. Anucleate cells were scored as non-fluorescent cells that

failed to grow. **(A)** Hlp-Dendra2 cells grew and divided normally without generating anucleate cells. **(B)** *ΔparA* Hlp-dendra2 cells generated anucleate cells (arrows) in about 20% of all division events. **(C-F)** Hlp-Dendra2 cells and *ΔparA* Hlp-dendra2 cells were stained with SYTO17. **(C)** All Hlp-Dendra2 cells were scored as Hlp-Dendra2-positive and grew. **(D)** All Hlp-Dendra2 cells were scored as SYTO17-positive and grew. **(E)** All *ΔparA* Hlp-dendra2 cells that were scored as Hlp-Dendra2-positive grew (green symbols), whereas all cells that were scored as Hlp-Dendra2-negative failed to grow (black symbols). **(F)** All *ΔparA* Hlp-Dendra2 cells that were scored as SYTO17-positive grew (magenta symbols). The majority of cells that were scored as SYTO17-negative failed to grow (black symbols). Some *ΔparA* Hlp-dendra2 cells were scored as Hlp-Dendra2-positive but SYTO17-negative (arrows in panels E and F); all of these cells grew and divided, indicating that Hlp-Dendra2 was a more reliable marker of their nucleated status. **(C,D)** All Hlp-Dendra2 cells were scored as Hlp-Dendra2-positive and grew. **(E,F)** All *ΔparA* Hlp-dendra2 cells that were scored as Hlp-Dendra2-positive grew (green symbols in panel F), whereas all cells that were scored as Hlp-Dendra2-negative failed to grow (black symbols in panel F). In a few cases, cells were scored as Hlp-Dendra2-positive but SYTO17-negative (arrows in panel E); all of these cells grew and divided, indicating that Hlp-Dendra2 was a more reliable marker of their nucleated status.

4.8 Subcellular organization of Hlp-Dendra2 can be imaged using super-resolution radial fluctuations (SRRF) microscopy

Super-resolution microscopy techniques such as super-resolution radial fluctuations (SRRF) microscopy (Gustafsson et al. 2016) involve high-frequency fluorescence imaging (Figure 28), which requires fluorescent markers that are relatively resistant to photobleaching. We stained exponentially growing Hlp-Dendra2 and *ΔparA* Hlp-Dendra2 cells with FM4-64, a membrane stain, and imaged them by SRRF (Figure 28A,B). The Hlp-Dendra2 marker proved to be compatible with this imaging technique, which revealed a beads-on-a-string organization of Hlp-Dendra2 foci similar to the organization revealed by conventional widefield microscopy but at higher spatial resolution. The SRRF reconstruction technique clearly identified unusually small cells lacking Hlp-Dendra2 foci (anucleate cells) in the *ΔparA* Hlp-Dendra2 strain (Figure 28B). The "beads-on-a-string" organization

of Hlp-Dendra2 foci appeared somewhat disordered in a subset of Δ*parA* cells, consistent with the postulated role of ParA in chromosome organization and segregation (Surovtsev & Jacobs-Wagner 2018). Furthermore, no Hlp-Dendra2 was detected in anucleate Δ*parA* Hlp-Dendra2 cells (Figure 28B, white arrow).

We conclude that fluorescence of the Hlp-Dendra2 marker provides sufficiently high stability (low photobleaching) to be used with super-resolution microscopy techniques that require high-frequency fluorescence imaging, such as SRRF. SRRF enables the differentiation between WT Hlp-Dendra2 and Δ*parA* Hlp-Dendra2 cells, in which Hlp-Dendra2 organization is destructured.
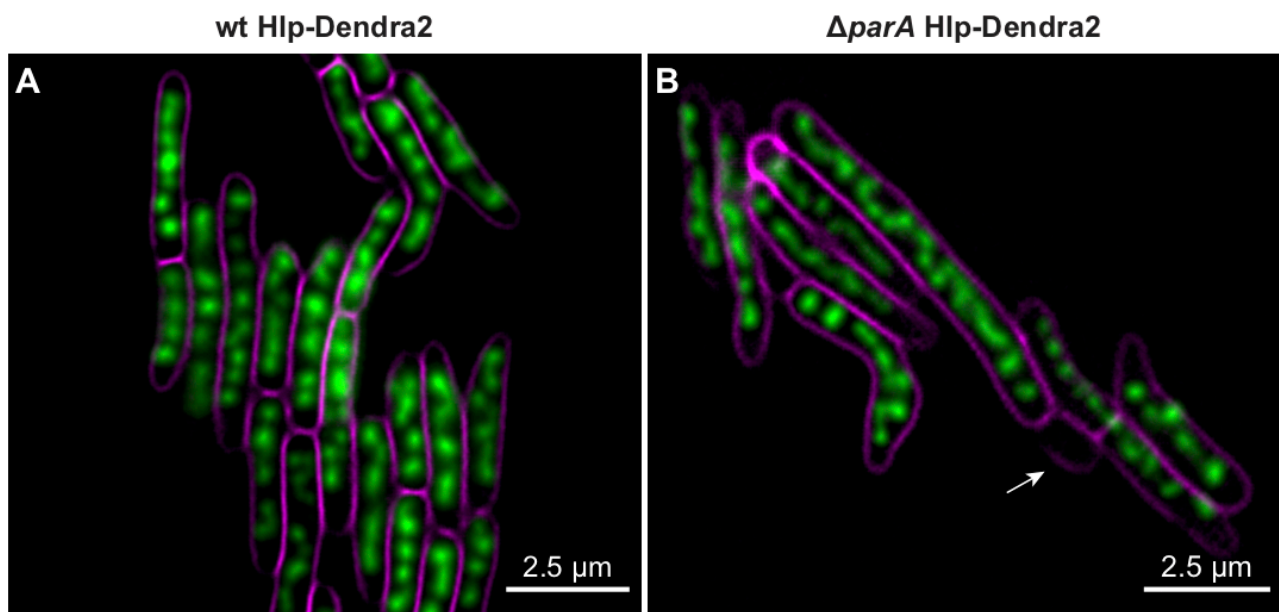
Figure 28. The Hlp-Dendra2 marker is compatible with super-resolution radial fluctuations (SRRF) microscopy

(A) Hlp-Dendra2 cells and **(B)** Δ*parA* Hlp-Dendra2 cells were stained with the membrane dye FM4-64 and imaged by SRRF. Hlp-Dendra2 is shown in green. FM4-64 is shown in magenta. Arrow, anucleate cell.

4.9   Structured illumination (SIM) microscopy reveals disorganization of chromosomal DNA in Δ*parA* Hlp-Dendra2 cells

I wanted to confirm the disorganization of Hlp-Dendra2 in Δ*parA* cells imaged by SRRF using another technique. Therefore, WT, Δ*parB*, and Δ*parA* cells expressing Hlp-Dendra2 were imaged by structured illumination microscopy (SIM) (Rego & Shao 2015) at the EPFL Bioimaging and Optical Platform (BIOP) with the help of Thierry Laroche. The "beads-on-a-string" organization of Hlp-Dendra2 in the WT strain is somewhat disrupted in the Δ*parB* strain, where we sometimes observe double "strings" of smaller and more numerous Hlp "beads" (Figure 29). This disorganized phenotype is even more pronounced in Δ*parA* cells expressing Hlp-Dendra2*.*

We conclude that the subcellular organization of Hlp-Dendra2 is perturbed in Δ*parA* and in Δ*parB* mutant cells, which can be imaged more precisely using super-resolution microscopy techniques such as SIM.
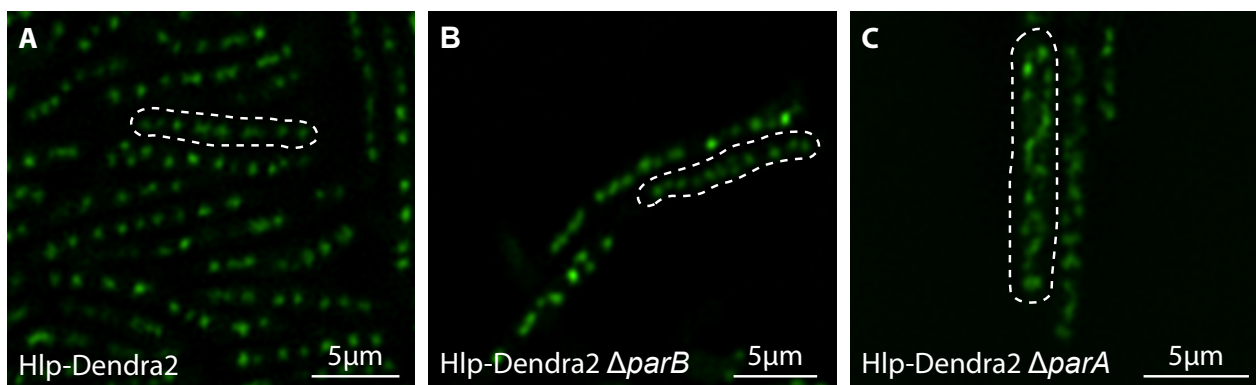
Figure 29. Disorganization of Hlp-Dendra2 in Δ*par* cells observed using structured illumination microscopy (SIM)

Hlp-Dendra2 was imaged by SIM in WT **(A),** Δ*parB*, **(B)**, and Δ*parA* **(C)** strains. The dashed lines indicate examples of individual cell contours.

4.10 ParB-mCherry is localized within the Hlp-Dendra2-tagged nucleoid

In order to compare the localization of Hlp foci to a previously characterized DNA marker for the origin of replication (Santi & McKinney 2015), I constructed a strain expressing Hlp-Dendra2 and the ParB-mCherry protein, which binds to *parS* sequences adjacent to the chromosomal origin of replication (*ori*). This strain was constructed by integrating the plasmid expressing the Hlp-Dendra2 fusion protein from the *hsp*60 promoter at the bacterial *attB* site. By fluorescence time-lapse microscopy (Figure 30) I observed that ParB-mCherry foci are localized close to the cell poles at birth and within the Hlp-Dendra2-stained nucleoid, as expected. ParB is localized at the outer edge of the nucleoid and its position is quite constant. At about three quarters of the cell cycle, the inherited ParB-mCherry is replicated and one ParB-mCherry focus moves towards the future new cell pole, whereas the other ParB focus stays at the outer edge of the nucleoid. A schematic representation of a representative cell was constructed at 15-minute intervals from birth to division (Figure 31).

We conclude that ParB-mCherry is localized within the nucleoid, visualized using the genetically encoded chromosomal marker Hlp-Dendra2. ParB-mCherry localizes to the outer edge of the nucleoid except when ParB-mCherry is replicated. After ParB replication, one focus stays at about the same position, that is, at the outer edge of the nuceoid whereas one focus moves towards the new pole. This finding suggests that the organization in *M. smegmatis* is highly ordered and conserved and might be organized as macro domains similarly to in other organisms. In the well-studied bacteria like *Escherichia coli* and *Bacillus subtilis*, the single circular chromosome is organized into discrete macrodomains with a spatial distribution that favors interactions between specific macrodomains (Boccard et al. 2005, Dame et al. 2011).
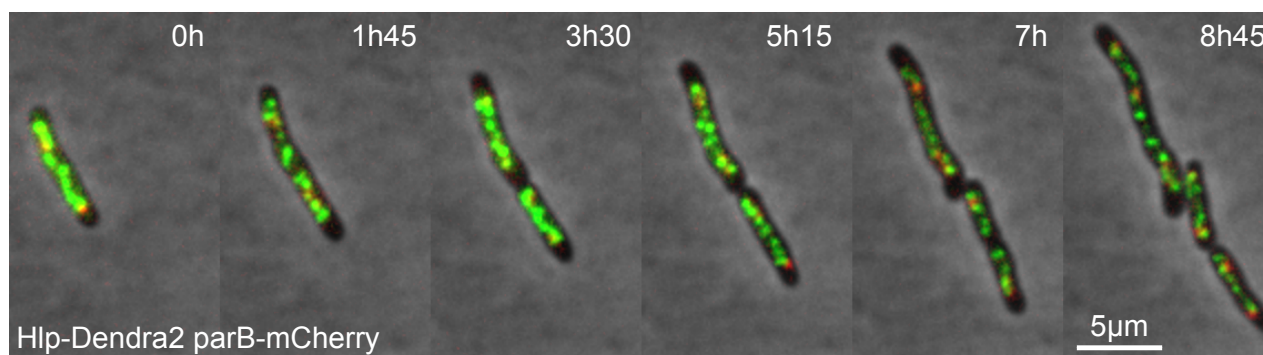
Figure 30. Time-lapse microscopy of cells expressing fluorescent markers of the chromosome (Hlp-Dendra2) and the origin of replication (ParB-mCherry)

A strain of *M. smegmatis* expressing Hlp-Dendra2 (green) and ParB-mCherry (red) was cultured in a micro-fluidic device and imaged by time-lapse microscopy at 15-minute intervals until small colonies were obtained.
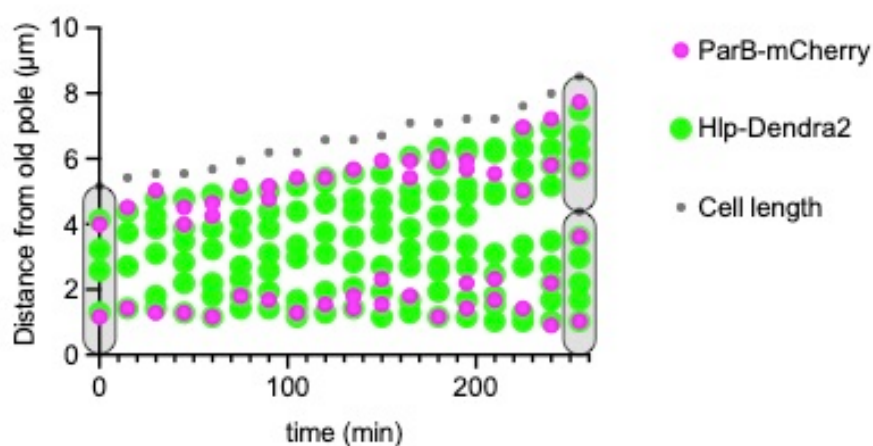
Figure 31. ParB-mCherry localizes to the outer edge of the Hlp-Dendra2-stained chromosome

Schematic representation of Hlp-Dendra2 and ParB-mCherry localization in a representative cell of *M. smegmatis* from birth to division.

4.11 Characterization of the Hlp-Dendra2 marker in Δ*parA* and Δ*parB* mutants of *M. smegmatis*

Δ*parA* and Δ*parB* mutants are known to divide asymmetrically and give birth to small anucleate cells at relatively high frequencies. I wanted to verify if the Hlp-Dendra2 pattern was still visible in both of these mutants and if this marker would be reliable to discriminate between nucleated and anucleate cells. I constructed both the Δ*parA* Hlp-Dendra2 (Figure 32A) and Δ*parB* Hlp-Dendra2 (Figure 32B) reporter strains and imaged them by time-lapse fluorescence microscopy. Based on these images I can make two conclusions. First, the "string" of Hlp-Dendra2 "beads" seems less organized in the Δ*parB* mutant compared to the wild-type Hlp-Dendra2 strain. This difference is even more pronounced in Δ*parA* Hlp-Dendra2 cells, which typically display two "strings" of smaller and more disorganized "beads" compared to the well-aligned single "string" of Hlp-Dendra2 "beads" observed in wild-type cells. Second, the Hlp-Dendra2 "beads" seem to be distributed everywhere along the cell length in both Δ*parA* and Δ*parB* cells, with a small gap at the poles (previously observed Hołówka et al. 2018). However, a short time before division the Hlp-Dendra2 signal seems to concentrate approximately where division will take place (white arrows in Figure 32A and C). The amount of Hlp-Dendra2 protein in the Δ*parA* cell can be represented as a heat map (Figure 32B). At 40 minutes, the concentration of Hlp-Dendra2 fluorescence at the future division site is clearly indicated by the darker stripe. Similar results were obtained with a heat map representation of the Δ*parB* strain (Figure 32D), where two darker stripes of Hlp-Dendra2 fluorescence were observed at 30 minutes and apparently merged into a single darker stripe at 45 and 60 minutes. In both Δ*par* strains this abrupt concentration of Hlp-Dendra2 was observed in every division that resulted in an anucleate daughter cell. This phenomenon always occurs before separation of the two daughter cells (indicated by white stars), and might be explained by a retrograde movement of the DNA from the future anucleate daughter cell into the future nucleated daughter cell.
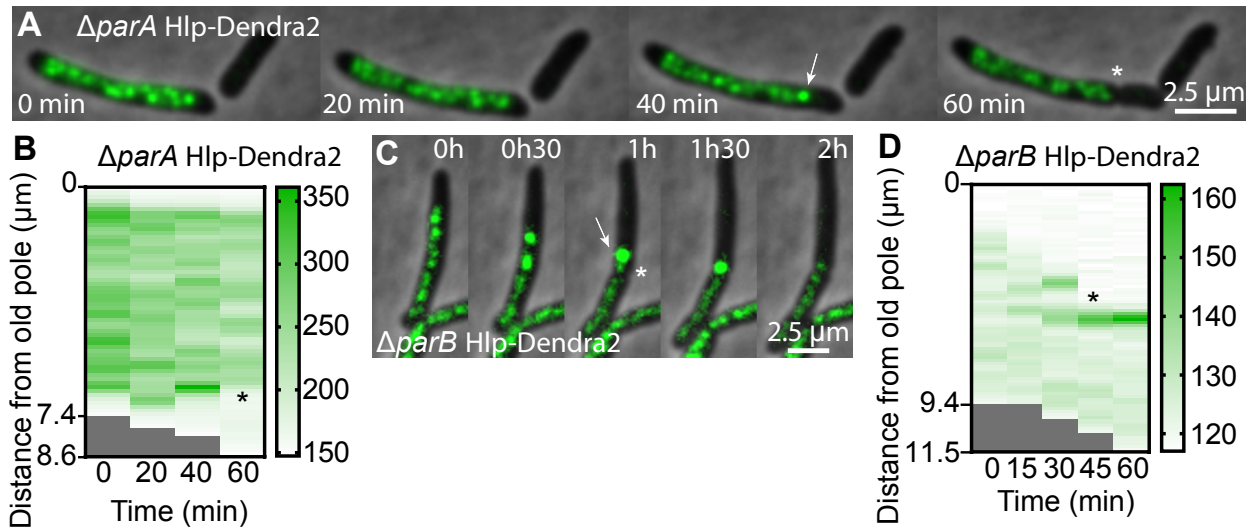
Figure 32. Time-lapse microscopy of the Hlp-Dendra2 displacement in Δ*parA* and Δ*parB* cells

M. smegmatis Δ*parA* Hlp-Dendra2 **(A-B)** and Δ*parB* Hlp-Dendra2 **(C-D)** cells were cultured in a microfluidic device and imaged every 20 or 15 minutes, respectively. **(A)** In Δ*parA* cells, Hlp-Dendra2 is distributed throughout the cell length at 0 and 20 minutes, then DNA is concentrated in foci, indicated by the white arrow at 40 minutes, just before division, indicated by the white star. **(B)** Heat map representation of Hlp-Dendra2 concentration along the cell length from the old pole to the new pole. The black star indicates division and the shaded grey area represents the background. **(C)** In Δ*parB* cells, Hlp-Dendra2 is initially distributed throughout the cell length. Then Hlp-Dendra2 is concentrated in foci, indicated by the white arrow at 1 hour and the cell divides, indicated by the white star. **(D)** Heat map representation of Hlp-Dendra2 concentration along the cell length from the old pole to the new pole. The black star indicates division and the shaded grey area represents the background.

I questioned whether this Hlp-Dendra2 displacement was specific to anucleate cells formation and when in the cell cycle it would occur. The Hlp-Dendra2 distances to the old pole as well as to the new pole were represented in percent of the total cell length for several cells using Δ*parA* Hlp-Dendra2 cells as well as WT Hlp-Dendra2 cells over the cell cycle (Figure 33). For simplicity the middle of the cell, where the future cell separation occurs was not considered.

The Δ*parA* Hlp-Dendra2 cells that give birth to an anucleate new-pole daughter cell (Figure 33A) show a gap without Hlp-Dendra2 at the old cell pole and a fairly constant distribution of Hlp-Dendra2 from 15% to 95% of the cell length on average. However, at about 85% of the cell cycle a change in nucleoid organization was observed as the Hlp-Dendra2 proteins were redistributed from about 10% to 80% of the cell length.

Similarly, the Δ*parA* Hlp-Dendra2 cells that give birth to an anucleate old pole daughter cell (Figure 33B) display a fairly constant distribution of Hlp-Dendra2 along the cell length. The redistribution of Hlp-Dendra2 happens earlier in Δ*parA* anucleate old-pole cells compared to Δ*parA* cells anucleate new-pole cells (Figure 33A), at around 75% of the cell cycle. The spread at the end of the cell cycle is quite broad due to the fact that there is a large variability in the sizes of anucleate cells. The nucleoid distribution shown in green as well as the division site is an average of the different cells.

In Δ*parA* cells as well as wild-type cells (Figure 33C, D) the distribution of Hlp-Dendra2 was very similar at the beginning of the cell cycle, having an empty space at the old pole occupying about 15% of the cell length. In wild-type cells, the gap at the old pole was slightly reduced at division to about 10% of the cell length.

The anucleate new-poles have on average an Hlp-Dendra2 retraction of 20% of the cell length, which happens at 15% before the end of the cell cycle. The anucleate old-poles displacement of Hlp is much larger, on average 50% but happens in a time corresponding to 35% of the cell cycle. The speed of displacement in the anucleate new-pole is faster compared to the anucleate new-pole formation (Table 3).

Anucleate formation	% Retraction	% Cell cyle	Speed (distance/time)
New-pole	20	15	1.3
Old-pole	35	50	0.7

Table 3 Speed of anucleate cell formation

We conclude that Hlp-Dendra2 is a reliable marker to follow DNA redistribution in the anucleate daughters' formation of Δ*parA* cells or DNA stability in the nucleated cell formation in Δ*parA* Hlp-Dendra2 and WT Hlp-Dendra2. Surprisingly, the distribution of Hlp-Dendra2 is quite homogeneous along the length of Δ*parA* cells during most of the cell cycle and DNA seems to move in a rapid movement (average of 0.09 ± 0.05 µm/min on 10 cells) towards the future nucleated cell daughter preceding division. This retraction happens in both anucleate old-pole and anucleate new-pole formation although the speed of dis-placement is faster in anucleate new-poles compared to anucleate old-poles.
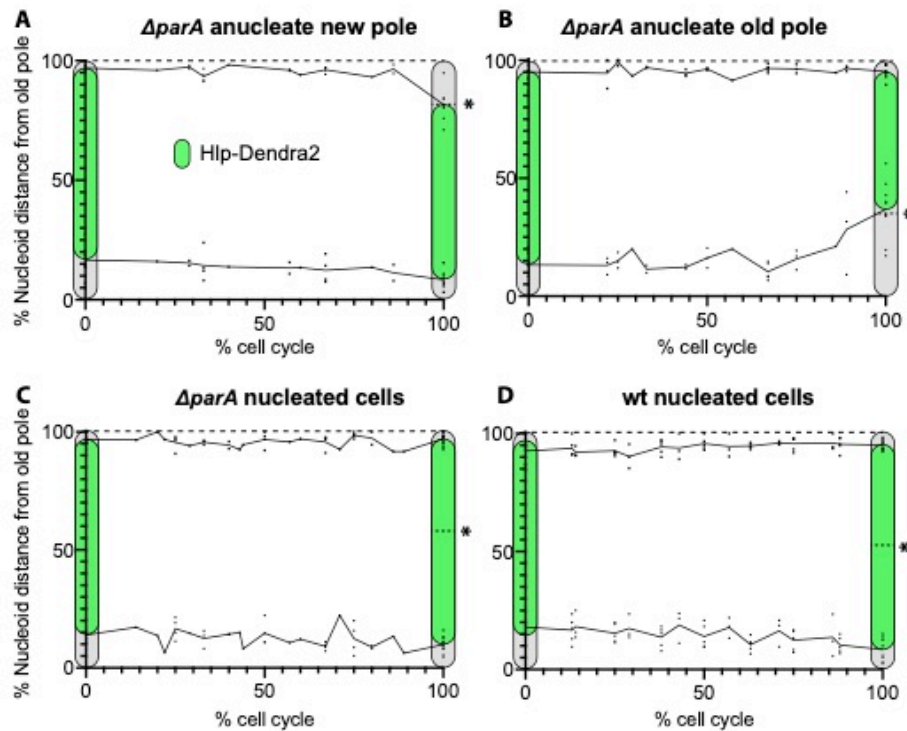
Figure 33. Movement of Hlp-Dendra2 in *ΔparA* and WT cell divisions

M. smegmatis ΔparA Hlp-Dendra2 **(A-C)** and WT Hlp-Dendra2 **(D)** cells were cultured in a microfluidic device and imaged every 15 minutes. Hlp-Dendra2 localization relative to the old cell pole and new cell pole as well as cell length were recorded every 30 minutes from birth to division. ΔparA Hlp-Dendra2 cells were classified in three groups: **(A)** cells that gave birth to an anucleate new-pole daughter (n = 7); **(B)** cells that gave birth to an anucleate old-pole daughter (n = 10); **(C)** cells that gave birth to two nucleated daughters (n = 11). **(D)** All Hlp-Dendra2 cells gave birth to two nucleated daughters (n =8).

4.12 Divisions of Δ*parB* cells that result in formation of an anucleate daughter cell do not generate a detectable SOS response

As the cell division septum sometimes forms over chromosomal DNA (**Chapter 3.7**), and divisions of Δ*par* cells that result in formation of an anucleate daughter cell exhib-

it a retrograde movement of the Hlp-Dendra2 signal towards the nucleated daughter cell, I hypothesized that these division events might result in guillotining of chromosomal DNA by the forming septum. To test this hypothesis, I constructed a fluorescent reporter strain expressing a fusion of the sequence encoding GFP at the C-terminus of the sequence encoding the SOS response protein RecA, whose expression is induced by DNA damage. I then used the the Δ*parB* RecA-GFP strain to investigate whether the DNA damage response is induced during cell divisions that result in formation of one nucleated daughter cell and one anucleate daughter cell. Starting with a wild-type RecA-GFP strain provided by Giulia Manina (a former postdoc in the McKinney lab), I deleted the *parB* gene in this strain by two-step (insertion/excision) homologous recombination with pJGΔ*parB* (or pIS294) a *parB* knockout plasmid provided by Isabella Santi (a former postdoc in the McKinney lab) (Santi et al. 2015). This process uses a suicide vector that contains the kanamycin and hygromycin resistance markers for selection of first-step recombinants (insertion), the *sacB* counterselectable marker that confers sucrose sensitivity to select second-step recombinants (excision), and the 5' and 3' flanking sequences of the *parB* open reading frame (fused in-frame) to promote homologous recombination of the plasmid at the *parB* chromosomal locus (Figure 34). The resulting positive colonies (sensitive to kanamycin and hygromycin but resistant to sucrose) were checked by PCR and DNA sequencing to confirm replacement of the *parB* open reading frame by the Δ*parB* allele in the RecA-GFP strain background. Despite repeated attempts, I was unable to obtain a *parA* gene knockout (Δ*parA*) in the RecA-GFP strain background, as 100% of the second-step recombinants showed reversion to the wild-type *parA* sequence. This could mean that a mutation in both the *parA* gene and recA (modification by fusion with the GFP) is synthetically lethal.
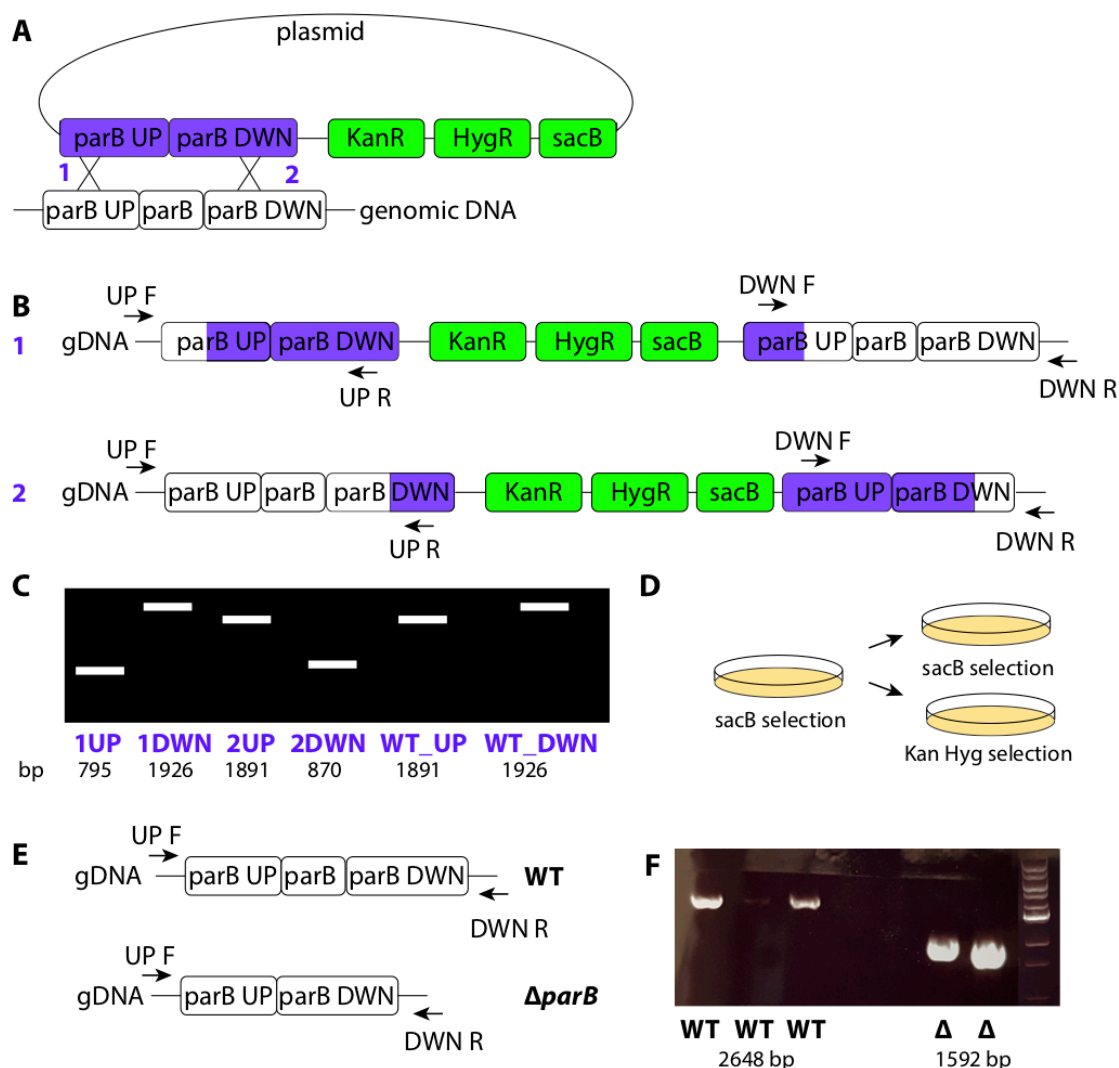
Figure 34. Two-step recombination strategy to delete the chromosomal *parB* gene

(A) Schematic of the first-step recombination between the pJGΔ*parB* knockout plasmid and genomic DNA, which can occur at the upper arm (1) or lower arm (2). **(B)** Resulting sequences for (1) and (2). PCRs are performed on the upper and lower portion to check if a recombination has occured and where. **(C)** Resulting PCRs obtained for a recombination event in the upper arm (1) or lower arm (2) or if no recombination occured (WT). **(D)** Positive clones for the first-step recombination are then cultured and plated on sucrose for *sacB* counter-selection at various dilutions. Colonies are then reselected and grown in parallel to confirm their resistance to sucrose and their sensitivity to kanamycin and hygromycin. **(E)** Schematic of the second-step recombination (and the PCR primers), which can result in reversion back to the WT sequence or in the deletion or insertion of a target gene. **(F)** Agarose gel from the colony PCR to check for positive clones containing the desired Δ*parB* allele after the second-step recombination event.

As the RecA-GFP reporter was previously shown to be upregulated by DNA damaging agents (Giulia Manina, personal communication), I used time-lapse microscopy to assess whether the RecA-GFP reporter is upregulated in a subset of Δ*parB* cells growing under normal conditions (Figure 35A and B). I observed that the RecA-GFP signal is indeed upregulated transiently in a subset of Δ*parB* cells, although in most cells the signal returns to baseline levels by the end of the cell cycle (Figure 35C). This transient upregulation also occurs at similar frequencies in WT RecA-GFP cells. An example of two successive cell divisions is shown in Figure 35D. The first division (indicated by the white star) gives rise to an anucleate daughter cell (indicated by the white arrow). This cell initially has a slight background green signal but the signal diminishes over time. Consistent with its identification as an anucleate cell, its growth stops abruptly after division (in contrast, in time-lapse experiments with wild-type cells every cell grows) and it is an abnormally small cell, although the size of the anucleate Δ*parB* cells is less small compared to the anucleate Δ*parA* cells. The second division occurs after 3 hours (indicated by the white star) and gives rise to two nucleated daughter cells, the lowest cell on the microscope image (indicated by the black arrow) exhibits a transiently increased RecA-GFP signal. The percentage of cells exhibiting a pulse of RecA-GFP expression is about 16%. Surprisingly, all of the cells that were scored as positive for a RecA-GFP pulse arose from divisions that generated two nucleated daughter cells, i.e., none of the cells that exhibited a pulse of RecA-GFP expression corresponded to anucleate daughter cells or to the nucleated siblings of anucleate daughter cells (Figure 35E).

In conclusion, as none of the division, which gave birth to an anucleate daughter cell showed an induction in the RecA-GFP fluorescence signal, it means that SOS response due to guillotining of DNA does not happen in anucleate cell formation favoring the explanation of a DNA rescuing or pulling towards the nucleated daughter cell. Interestingly, RecA-GFP induction happens in Δ*parB* as well as WT cells at a significant proportion (16% of the dividing cells in Δ*parB*), which indicates that some SOS damage response occurs over

the cell cycle in normal growth conditions, maybe indicating some recombination events for instance.
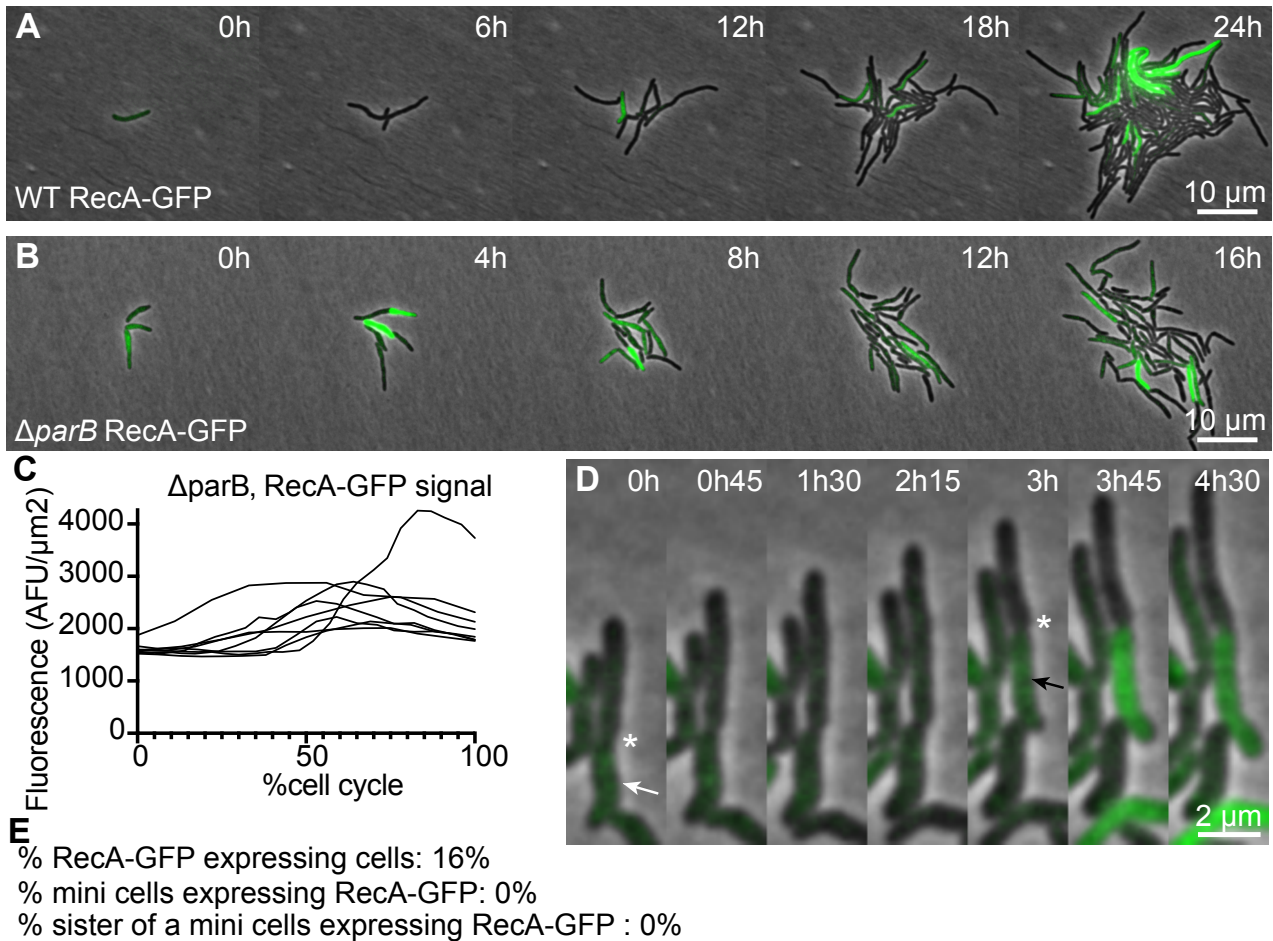
Figure 35. RecA-GFP is not induced in Δ*parB* cell divisions that generate an anucleate daughter cell

M. smegmatis RecA-GFP **(A)** and Δ*parB* RecA-GFP **(B)** strains were cultured in a microfluidic device and imaged every 15 minutes. **(C)** RecA-GFP fluorescence intensity per area in Δ*parB* RecA-GFP cells is represented over the cell cycle (n = 10 cells). **(D)** Representative enlarged magnification images of two successive Δ*parB* RecA-GFP cell division events. The first division (indicated by the white star) gives one nucleated daughter and one anucleate daughter, indicated by the white arrow. The second division at 3 hours gives two nucleated daughter cells, one of which exhibits a pulse of RecA-GFP expression, indicated by the black arrow. **(E)** The percentage of RecA-GFP-expressing cells was calculated, in the Δ*parB* cell population (n = 117 cells), in anucleate minicells or in the nucleated sisters of anucleate minicells (n = 21 dividing sibling cells).

4.13 The number of *M. smegmatis* Hlp-Dendra2 « bead » structure is duplicated over the cell cycle

As mentioned already, time-lapse microscopy of wild-type strains stained with DNA dyes or expressing the Hlp-Dendra2 marker revealed a "beads-on-a-string" subcellular structure. I wanted to investigate if the number of Hlp-Dendra2 "beads" per cell remained constant over time or if the number of "beads" would increase (double) between birth and division.

Analysis of movies from time-lapse microscopy experiments revealed that the number of Hlp-Dendra2 "beads" gradually increases during the course of the cell cycle. On average, cells are born with 5 "beads" and this number is doubled to 10 at division, with a standard deviation of about ± 1 "bead" at birth and division (Figure 36). This regular number could suggest that the spacing between different domains of the chromosome is constant even though Hlp-Dendra2 binds sequence-nonspecifically to DNA (Sharadamma et al. 2011).
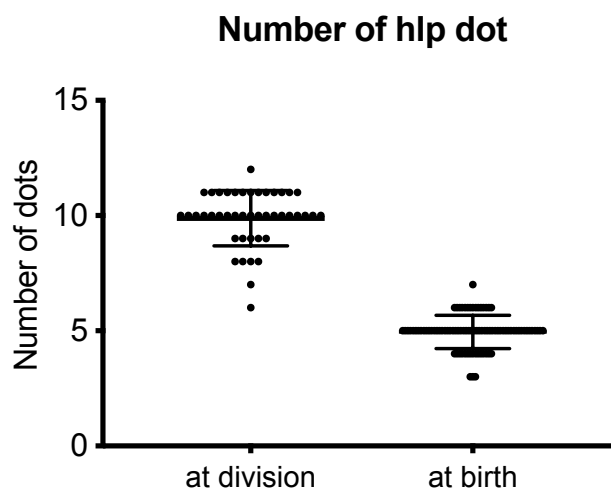
Number of hlp dot

Figure 36. The number of Hlp-Dendra2 "beads" doubles from birth to division

The average number of Hlp-Dendra2 "beads" at division is 9.9 ± 1.2 (n = 44) and at birth 5.0 ± 0.7 (n = 88).

4.14 Photoconversion of Hlp-Dendra2 reveals a biased accumulation of newly synthesized Hlp-Dendra2 near the new cell pole

We saw earlier (**Chapter 4.13**) that the number of Hlp-Dendra2 "beads" at birth or at division was relatively equal between individual cells and doubled over time between birth (n = 5 ± 1) and division (n = 10 ±1). However, we don't know if the new Hlp-Dendra2 "beads" are formed at a specific subcellular site, for example, at the site of DNA replication. In order to understand the dynamics of Hlp-Dendra2 synthesis and chromosome binding, I took advantage of the photoconvertible property of Dendra2 to distinguish the "new" Hlp-Dendra2 proteins synthesized after photoswitching from the "old" Hlp-Dendra2 proteins synthesized before photoswitching. As explained in more detail later (**Chapter 10.3**), after subjecting cells to a pulse of UV light, the "old" Hlp-Dendra2 proteins fluoresce red while the "new" proteins fluoresce green. The photoconvertion rate depends on the time and intensity of UV light exposure. However, UV light is phototoxic. Time-lapse fluorescence microscopy experiments were done where individual cells were allowed to form microcolonies before they were pulsed with different doses of UV light then growth was allowed to resume (Figure 37). These experiments established that time-lapse imaging of photoconverted Hlp-Dendra2 cells required a compromise: a too-strong pulse of UV light caused unacceptable phototoxicity, while a too-weak pulse of UV light did not generate sufficient levels of photoswitched (red) Hlp-Dendra2 for analysis.
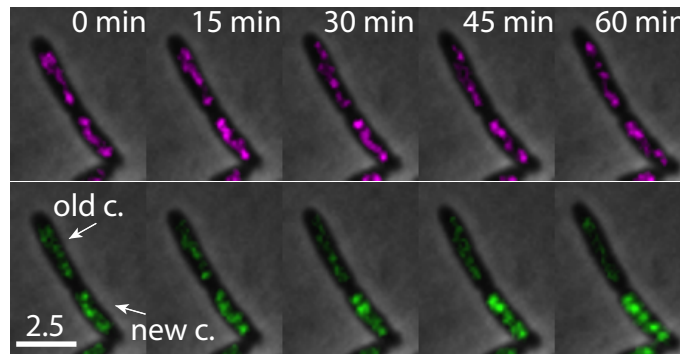
Figure 37. Accumulation of newly synthesized Hlp-Dendra2 proteins is biased towards the new cell pole

M. smegmatis Hlp-Dendra2 cells were cultured in a microfluidic device and imaged by time-lapse microscopy at 15-minute intervals until small colonies were obtained. The cells were were pulsed with UV light right before time 0 and cell division happens at time 0 min. Old-pole cells (old c.) and new-pole cells (new c.) are indicated by white arrows.

To know if the old and new Hlp-Dendra2 proteins had the same subcellular localization, the fluorescence profile along the longitudinal axis of the cell was plotted (Figure 38A). The fluorescence maxima of the new and old proteins do not always match (indicated by the black arrows). Over time the localization of the old and the new proteins changes. What is also interesting to note is the fact that the new Hlp-Dendra2 beads contain new as well as old proteins. The time-lapse experiment in Figure 37 gave the impression that more Hlp-Dendra2 proteins were present in one of the two daughter cells and that this difference increases with time. Therefore, I analyzed 25 pairs of photoswitched new and old sister cells and plotted the difference of fluorescence between 0 minutes and 60 minutes after division (Figure 38B). This analysis confirmed that there are more new Hlp-Dendra2 proteins in the new-pole sibling compared to the old-pole sibling, which is not the case for the old Hlp-Dendra2 proteins. The fluorescence at 0 and 60 minutes after division is plotted for a representative photoconverted cell (Figure 38C).

We conclude that the Hlp-Dendra2 "beads" contain a mix of new and old proteins, suggesting that the process of new "beads" formation is a semi-conservative process and

that there seem to be a biased accumulation of new Hlp-Dendra2 proteins in the new-pole sibling cells.
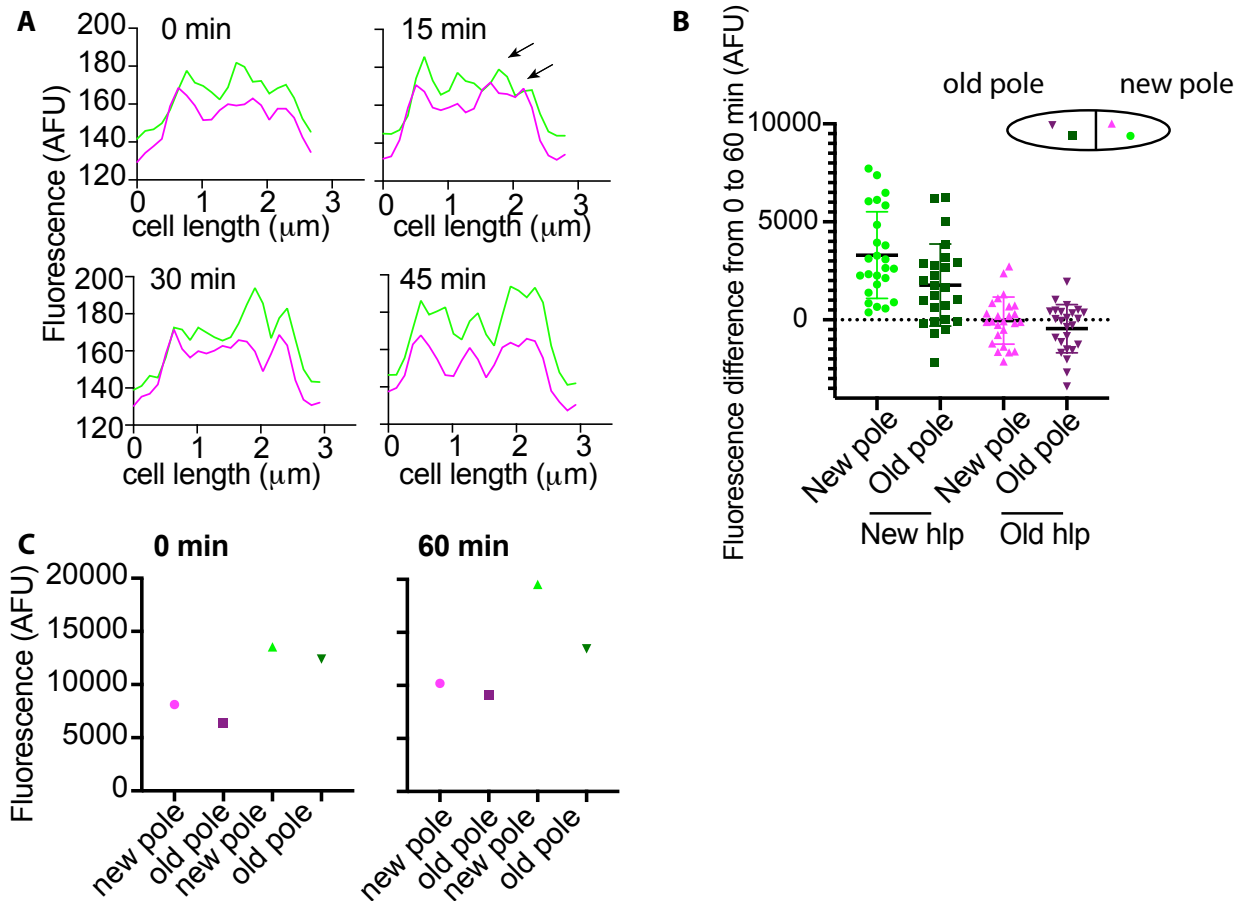
Figure 38. Photoconversion of Hlp-Dendra2 reveals the dynamics of Hlp-Dendra2 synthesis and subcellular localization

(A) Fluorescence intensity over time along the longitudinal axis of the new-pole cell shown in Figure 29 (0 μm corresponds to the old cell pole). The black arrows indicate examples of spatially shifted maxima of old (red) and new (green) Hlp-Dendra2 protein. **(B)** The fluorescence change between 0 and 60 minutes after division of new Hlp-Dendra2 (green) in the new-pole sister cell (light green) and old-pole sister cell (dark green) and old Hlp-Dendra2 (magenta) in the new-pole sister cell (light magenta) and old-pole sister cell (dark magenta) daughters (n = 25 pairs of sister cells). **(C)** Fluorescence of new Hlp-Dendra2 (green) and old Hlp-Dendra2 (magenta) in a representative cell was measured at 0 and 60 minutes after division in the old-pole (dark color) and new-pole (light color) daughter cells.

4.15 The DnaN-mCherry DNA replisome reporter appears earlier in new-pole daughter cells compared to old-pole daughter cells

We know that in *M. smegmatis* a new round of DNA replication usually initiates in the mother cell prior to division, such that newborn daughter cells may inherit an already partially replicated chromosome (Santi et al. 2013; Richardson et al. 2016). If DNA replication initiates earlier for the chromosome located in the new-pole half of the mother cell compared to the chromosome located in the old-pole half of the mother cell, this could provide an explanation for the larger amount of Hlp-Dendra2 observed in new-pole daughter cells (in **Chapter 4.14**). To test this idea, I re-analyzed the archived movies from a time-lapse experiment performed by Isabella Santi (a former postdoc in the McKinney lab) using an *M. smegmatis* reporter strain Wag31-GFP and DnaN-mCherry. Wag31-GFP is a marker of the time and place of cytokinesis, while DnaN-mCherry is a DNA replisome marker that appears at the onset of DNA replication and disappears at the completion of DNA replication (Santi et al. 2013; Santi & McKinney 2015). The DnaN-mCherry marker can appear before (about 80% of cell division events) or after (about 20% of cell division events) the appearance of the Wag31-GFP marker (Figure 39A). I focused on cell division events where the DnaN-mCherry marker appeared before the Wag31-GFP marker and plotted the difference in time between initiation of DNA replication in the new-pole half of the mother cell compared to the old-pole half of the mother cell (Figure 39B). I found that initiation is indeed happening slightly earlier (about 4 minutes on average) in the new-pole half of the mother cell compared to the old-pole half of the mother cell. As DNA replication in *M. smegmatis* proceeds at a rate of approximately 400 base pairs per second (Trojanowski et al. 2015), this difference in the timing of initiation could be sufficient to introduce a bias. Moreover, the movie was recorded at a relatively slow frame rate of 10 minutes and about 29% of the cells showed no difference for the initiation between the old-pole and new-pole halves of the mother cell. If the frame rate were higher, we might be able to detect a greater difference between initation in the new-pole and old-pole cell halves. To have a

more accurate measure, the time-lapse experiment should be redone with a higher imaging frame rate. However, a too-high frame rate might lead to photoxicity.

We conclude that when DNA replication initiates in the mother cell prior to division, initiation usually occurs earlier in the new-pole half of the mother cell compared to the old-pole half of the mother cell. This difference is small but could be one reason why new Hlp-Dendra2 proteins accumulate preferentially in the new-pole daughter cell.
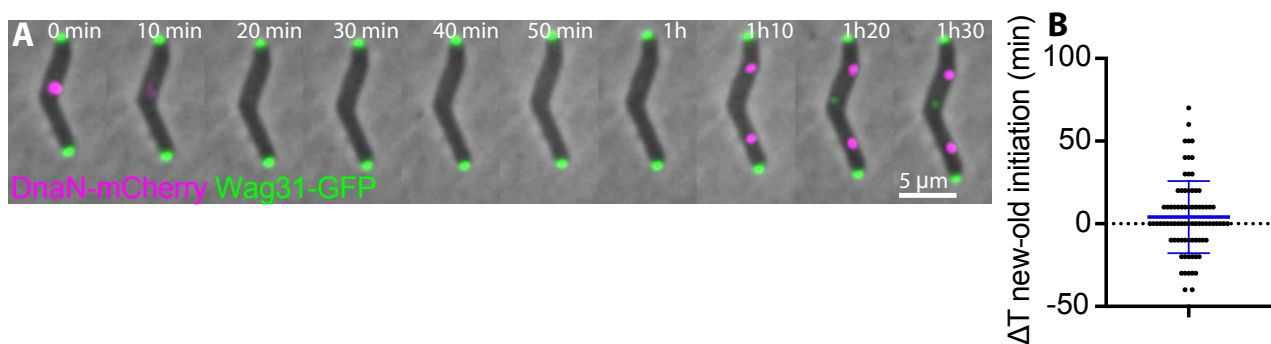
Figure 39. DNA replication initiation occurs earlier in the new-pole half of the mother cell compared to the old-pole half of the mother cell

(A) *M. smegmatis* DnaN-mCherry Wag31-GFP cells were cultured in a microfluidic device and imaged by time-lapse microscopy at 10-minutes intervals. Initiation of chromosome replication is signaled by appearance of a DnaN-mCherry focus. Cytokinesis is signaled by appearance of the Wag31-GFP marker at the division septum. **(B)** The difference between the time when DNA replication initiates in the new-pole half of the mother cell and the time when replication initiates in the old-pole half of the mother cell is plotted for cells that initiate replication before cytokinesis.

4.16 Hlp-Dendra2 imaged by combined fluorescence and atomic force microscopy

A dual instrument that combines an optical (fluorescence) microscope with an atomic force microscope (AFM) was constructed in the Fantner lab (Odermatt et al. 2015). Experiments with this instrument led us to conclude that the surface of *M. smegmatis* is

not flat, but undulating, and the wave troughs, which already exist at birth, correspond to future sites of cell division (Eskandarian et al. 2017; **Chapter 9**). We hypothesized that these wave troughs would correlate with local DNA minima. At that time, I had not yet constructed the *M. smegmatis* Hlp-Dendra2 reporter strain so the DNA dye SYTO17 was used to visualize chromosomes. However, as pointed out in **Chapter 4.4** (Figure 24), SYTO17 has a more diffuse pattern compared to Hlp-Dendra2. Therefore, with the help of Mélanie Hannebelle (a PhD student in the Fantner and McKinney labs), I imaged the *M. smegmatis* Hlp-Dendra2 strain by correlated AFM and fluorescence microscopy (Figure 40). AFM is complementary to fluorescence imaging, as it enables us to image the topology of the bacterial surface with much higher spatial resolution. In parallel, Hlp-Dendra2 was imaged by fluorescence microscopy (Figure 40A). For a precise localization of the cell edges, the dye FM4-64 was used to stain the membrane (Figure 40B). The variation of bacterial cell height can be observed in the AFM height channel (Figure 40C) as well as in the 3D representation of the height (Figure 40E). The cell height and the Hlp-Dendra2 fluorescence profile were plotted along the long axis of a representative cell (Figure 40F), corresponding to cell number 1 in Figure 40C. A correlation score was calculated for each pair of height or Hlp-Dendra2 fluorescencence traces. All scores for the four cells depicted in Figure 40 are below 0.5, which indicates that the Hlp-Dendra2 fluorescence minima and the AFM height minima (wave troughs) are not colocalized (Spearman coefficient for cell 1, 0.139; cell 2, 0.22; cell 3, 0.33; cell 4, 0.10).

We conclude that cell-surface wave troughs do not seem to correlate with intracellular minima of SYTO17-stained DNA localization. Moreover, as shown previously, an average cell contains five Hlp-Dendra2 "beads" (**Chapter 4.13**) but only three cell-surface wave troughs (Eskandarian et al. 2017, **Chapter 9**) at the time of birth, which indicates a different periodicity.
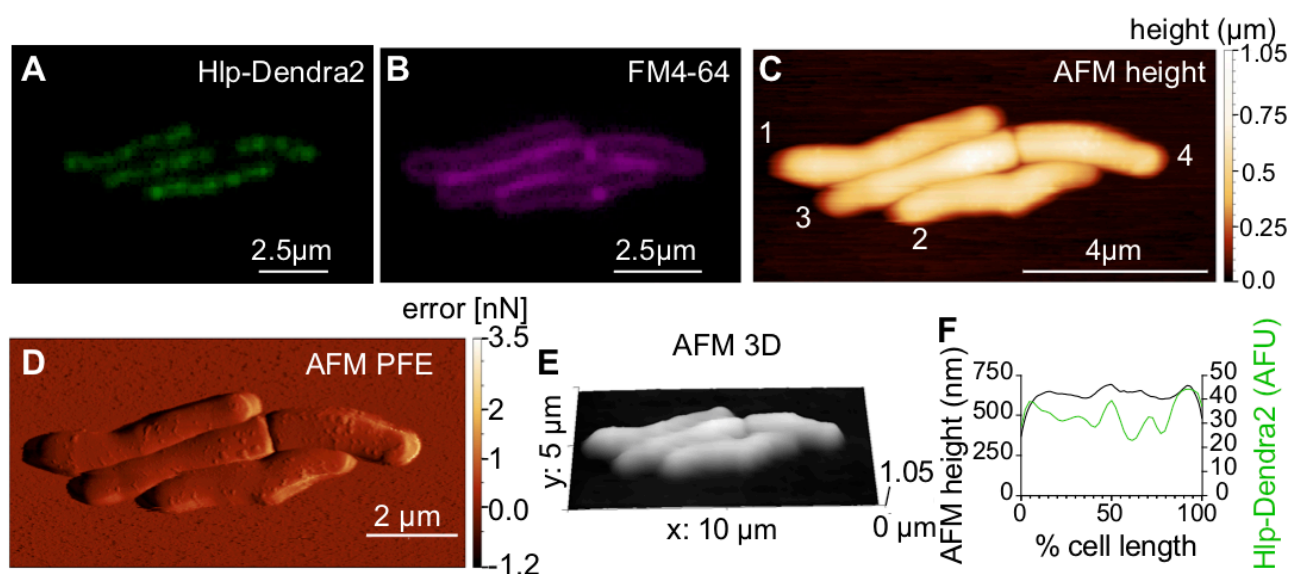
Figure 40. Combined AFM and fluorescence microscopy imaging of *M. smegmatis* Hlp-Dendra2 cells stained with the membrane stain FM4-64

The *M. smegmatis* Hlp-Dendra2 strain was imaged by fluorescence microscopy **(A, B)** and AFM **(C, D, E)**. **(A)** Hlp-Dendra2 fluorescence channel. **(B)** FM4-64 fluorescence channel. **(C)** AFM height channel. **(D)** AFM peak force error channel. **(E)** AFM height channel, 3D representation. **(F)** Correlated Hlp-Dendra2 fluorescence signal and AFM height corresponding to cell number 1 in **(C)**.

4.17 Conclusion

Hlp-Dendra2 is a useful marker to follow the dynamics of chromosome replication and segregation during the cell cycle. It has only been used recently in *M. smegmatis* (Hołówka et al. 2017; Hołówka et al. 2018). However, its stability, lack of toxicity, and a detailed comparison with commonly used DNA dyes have not been reported previously. A precise characterization of the subcellular organization of Hlp-Dendra2 in space and time was also lacking until now. Here, I also show the usefulness of the Hlp-Dendra2 marker to discriminate anucleate cells from nucleated cells. I also show that this marker can be im-

aged at higher spatial resolution using super-resolution microscopy techniques such as SRRF or SIM.

In Δ*par* cells, Hlp-Dendra2 is homogeneously distributed along the cell length for most of the cell cycle (except for "gaps" near the cell poles, especially at the old cell pole where this "gap" is larger), but just before cell division, a rapid movement of the Hlp-Dendra2 signal from the anucleate sister cell towards the nucelated sister cell occurs in Δ*parA* cells. This movement occurs only in asymmetric cell divisions that result in formation of one nucleated daughter cell and one anucleate daughter cell. A similar movement of the Hlp-Dendra2 signal occurs in Δ*parB* cells. We wondered if this DNA movement corresponded to a shift of DNA from the anucleate sister to the nucleated sister, or to degradation of the DNA in the anuclate sister. As none of the Δ*parB* RecA-cell GFP divisions giving rise to an anucleate cell was associated with induction of an SOS DNA damage response, suggesting the absence of damaged chromosomal DNA that we would expect to be associated with DNA degradation, we currently favor the hypothesis that progressive disappearance of chromosomal DNA from the anucleate daughter cell is due to translocation of DNA from the nascent anucleate sister cell to the nascent nucleated sister cell. What could then translocate DNA? FtsK homolog, SpoIIIE is a known DNA translocase which pulls DNA towards the forming forespore through the closing septum during *B. subtilis* sporulation.

Time-lapse microscopy experiments with Hlp-Dendra2 cells revealed a "beads-on-a-string" subcellular structure in which the number of Hlp-Dendra2 "beads" doubles from birth to division. Hlp-Dendra2 is a useful tool as the photoconvertible property of Dendra2 can be used to investigate biological questions. This allowed us to revealed that newly formed Hlp-Dendra2 "beads" contain both old and new Hlp-Dendra2 proteins, suggesting that formation of new "beads" is a semi-conservative process. However, the accumulation of newly synthesized Hlp-Dendra2 seems to be slightly biased towards the chromosome that will be inherited by the new-pole daughter cell, which could be explained in part by

earlier initiation of DNA replication in the new-pole half of the mother cell compared to the old-pole half of the mother cell.

Using a custom-made dual AFM and fluorescence microscopy system, I found that there was no correlation between local minima in the Hlp-Dendra2 signal and local minima (wave troughs) in the AFM height data. However, this preliminary analysis was performed using a small number of cells (n = 4) and further experiments will be necessary to determine whether there might be a correlation between intracellular distribution of chromosomal DNA and cell surface topology at different stages of the cell cyle (see **Chapter 9**).

Chapter 5 The FtsK DNA translocase an active determinant of the cell's ploidy

5.1 Contributions

All of the following work was done by myself. The exceptions are the construction of the FtsK-GFP strain, done by Isabella Santi, a former postdoc in the McKinney lab. The PacBio whole genome sequencing which was done at the UNIL genomic facility. The mass spectrometry analysis which was done at the EPFL mass spectrometry facility.

5.2 Introduction

As seen in the previous chapter, in Δ*par* cell divisions that result in formation of one nucleated daughter cell and one anucleate daughter cell, it appears that chromosomal DNA may be transferred from the anucleate daughter cell to the nucleated daughter cell. It also appears that this transfer can occur after septum formation without apparent guillotining of the transferred chromosome as no SOS response was detected in these divisions. As shown previously, in Δ*parA or* in Δ*parB* cells, Hlp-Dendra2 appeared to be actively translocated towards the nucleated cell (Figure 32). In Δ*par* mutants, chromosome replication is not affected but the distribution of the chromosomes and *ori* positions are affected. The anucleate daughter cell will contain no *ori* whereas the nucleated daughter cell can contain more than 6 *ori* (Ginda et al. 2017). The presence of several *ori* foci does not prove that complete chromosomes are translocated; however, the lack of an SOS response in the divisions resulting in an anucleate sister cell supports the hypothesis of chromosome translocation rather than degradation. Moreover, I observed in time-lapse experiments that cells containing a large number of chromosomes sometimes divide before a new round of replication initiates, resulting after one or more such "reductive divisions" in a normal number of chromosomes per cell. As these cells are viable, it is likely that the full chromosome is present. But what would be responsible for chromosome movement towards the nucleat-

ed cell? In *B. subtilis*, the FtsK homolog SpoIIIE is a known DNA translocase that pulls DNA towards the forming forespore through the closing septum during the process of sporulation. FtsK localizes to the division septum in *M. smegmatis* (Wu et al. 2018); thus, FtsK may play a role in the prevention of DNA guillotining by a closing septum in mycobacteria (Singh et al. 2013). A precise characterization of FtsK in mycobacteria has not been done yet. Nevertheless, it is already known that the FtsZ ring assembles at the nascent division septum before FtsK, and FtsK depends on FtsZ to localize at the septum; in contrast, the divisome proteins FtsQ, FtsB, and FtsL assemble at the septum after FtsK and are not required for FtsK localization at the septum (Wu et al. 2018). It has been suggested that FtsK may play a role in stabilizing the FtsZ ring (Wang & Lutkenhaus 1998).

The aim of this chapter will be to characterize the localization and timing of appearance of FtsK compared to known division reporters such as Wag31. I hypothesize that FtsK would be responsible to pull DNA from the future anucleate daughter cell to the nucleated daughter cell in cells lacking ParA or ParB. If FtsK is responsible for DNA translocation, would this movement be suppressed in cells that lack FtsK?

5.3 Characterization of an *M. smegmatis* FtsK-GFP reporter strain

In model organisms such as *E. coli* the temporal hierarchy of appearance of divisome factors at the nascent division septum is well established (Sánchez-Gorostiaga et al. 2016). In mycobacteria this hierarchy has been only partially described and some dependency relationships, for example, that FtsK ring formation at the septum requires prior assembly of the FtsZ ring (Eskandarian et al. 2017; Wu et al. 2018; Odermatt et al. 2019). To characterize FtsK in a time-dependent manner, I performed a time-lapse microscopy experiment using the *M. smegmatis* FtsK-GFP reporter strain constructed by Isabella Santi, who used a two-step homologous recombination method to replace the chromosomal *ftsK* gene with the engineered *ftsk-gfp* fusion gene (Figure 41). In cycling cells, I found that some cytosolic FtsK-GFP protein assembles before division as two dots at the site of the

future septum, which then form a continuous structure across the cell, and finally assembles at the middle of the cell. This structure looks as a ring, which constricts over time before disappearing around the time of cell division (indicated by the white star in Figure 41). Every cell shows a similar spatiotemporal pattern for FtsK-GFP localization, but there is some cell-to-cell variability for the timing of its assembly and disassembly at the nascent division septum.

FtsK is known to physically interact with FtsZ, and it was recently shown that FtsK did not properly localize at the septum in cells depleted for the FtsZ protein (Wu et al. 2018). These observations suggest that the shape of the FtsK-GFP septal focus may follow the shape of the FtsZ ring and, perhaps, the leading edge of the closing septum until it narrows to a pore that passes through the septum.
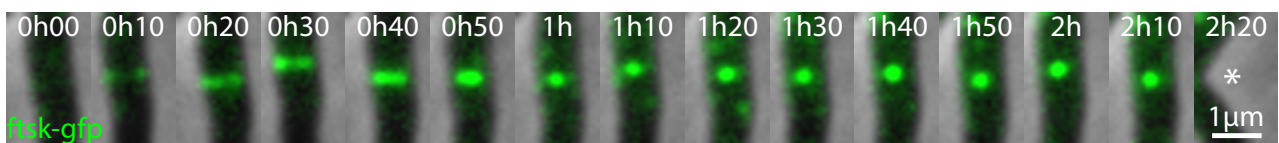
Figure 41. FtsK-GFP localizes at the nascent division septum in a ring-like structure

FtsK-GFP cells were cultured in a microfluidic device and imaged by time-lapse microscopy at 10-minute intervals. The images are zoomed at on the midcell region where the septum forms. Cell separation occurs with an abrupt v-snapping event (indicated by the white star).

5.3.1 FtsK-GFP localizes at the division septum before the Wag31-mCherry cytokinesis marker

FtsK is thought to be a DNA translocase. However, is DNA translocated through the closed septum? Wag31 is a marker for cytokinesis (Santi et al. 2013), which means that the two cytoplasms do not mix anymore, therefore the septum between the two daughter

cells is complete. To investigate if FtsK would translocate DNA through a closed septum thus when cytokinesis has happened, I constructed a reporter strain expressing both FtsK-GFP and Wag31-mCherry. I used a plasmid containing the *hsp*60 promoter driving the expression of the sequence encoding Wag31 fused at its C-terminus with the sequence encoding the mCherry fluorescent protein. This plasmid contained a phage integrase permitting the integration of the construction in the genome of *M. smegmatis* by a site-specific recombination event between a phage attachment site on the plasmid (*attP*) and a bacterial attachment site in the bacterial chromosome (*attB*).

Imaging of the FtsK-GFP Wag31-mCherry strain by time-lapse microscopy (Figure 42A) revealed that two sister cells can have a variable cell cycle duration and, therefore, variable timing of Wag31 appearance at midcell. In both sister cells, FtsK-GFP assembles at the nascent division septum and is present before Wag31-mCherry. However, the interval between appearance of Ftsk-GFP and Wag31-mCherry at the septum is variable. I then analyzed the fluorescence of FtsK-GFP and Wag31-mCherry per unit area at the location of the future division site as a function of the percentage of the cell cycle (Figure 42B, area indicated by the white arrows in A). FtsK-GFP maximum intensity is present on average when Wag31-mCherry accumulates at the septum. Therefore, FtsK appearance precedes Wag31 but the intensity and the duration were variable from cell to cell. However, when we look at individual cells, at 5 hours for the upper cell and at 3h30 for the lower cell, when FtsK is present as a single focus at the middle of the cell, Wag31-mCherry is visible, meaning that cytokinesis has already occurred (Figure 42A).

FtsK-GFP is visible as a single focus in the middle of the cell when cytokinesis has occurred and could then translocate DNA through a closed septum.
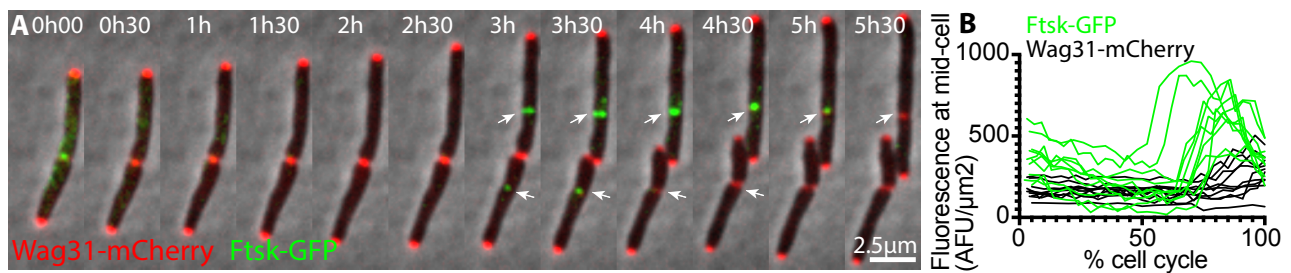
Figure 42. FtsK-GFP localizes to the division septum before Wag31-mCherry

(A) *M. smegmatis* FtsK-GFP Wag31-mCherry cells were cultured in a microfluidic device and imaged by time-lapse microscopy at 10-minute intervals. The white arrow indicates the area analyzed in **(B)** in the two sister cells. **(B)** The fluorescence of FtsK-GFP and Wag31-mCherry per unit area (μm^2) was measured at midcell and normalized from birth to division (n = 10 for each marker). The results are depicted as single-cell line traces.

5.3.2 The septal focus of FtsK-GFP appears on top of the Hlp-mCherry signal while chromosome segregation is still in progress

As we saw in the previous chapter that FtsK is present when cytokinesis has occurred and could translocate DNA through a closed septum, where is then localized DNA relative to FtsK localization?

I successfully constructed an Hlp-Dendra2 strain to image the localization of chromosomal DNA, I attempted to construct a reporter strain expressing both FtsK-mCherry and Hlp-Dendra2 strain in order to assess the timing of apperance and location of FtsK septal focus assembly during the process of chromosome segregation. Unfortunately, I found that mCherry was cleaved from FtsK, which made this approach unfeasible (**Chapter 10.6**). Therefore, I constructed double-reporter strains expressing FtsK-GFP Hlp-DsRed (DsRed monomeric for a more accurate localization) or FtsK-GFP Hlp-mCherry. For these two strains, I constructed the Hlp-DsRed and Hlp-mCherry plasmids using the Gibson assembly method. These plasmids contain the constitutive *hsp*60 promoter driving the expression of Hlp fused at its C-terminus with either the DsRed or mCherry fluorescent protein. These

plasmids contain a phage integrase that mediates the integration of the plasmid into the *M. smegmatis* genome by a site-specific recombination event between a phage attachment site (*attP*) and a bacterial attachment site (*attB*). Unfortunately, the fluorescence of the Hlp-DsRed marker proved to be too faint to be useful for time-lapse imaging. Therefore, I used the FtsK-GFP Hlp-mCherry strain for time-lapse microscopy experiments (Figure 43). The Hlp-mCherry fluorescence is less bright and less well-resolved compared to Hlp-Dendra2, but the localization of FtsK-GFP compared to Hlp-mCherry could still be compared. By drawing the Hlp-mCherry fluorescence profile along the long axis of the cell on the right, I observed that Hlp-mCherry is initially distributed along the length of the cell when FtsK-GFP is not yet assembled at midcell (Figure 43, 0 minutes). As the cell cycle progresses, the FtsK-GFP septal focus appears at midcell on top of the Hlp-mCherry signal (Figure 43, 15 minutes). At 45 minutes As the FtsK-GFP septal focus gradually constricts, the Hlp-mCherry signal separates into two lobes with a gap at mid-cell (Figure 43, 45 minutes). Division occurs after disassembly of the FtsK-GFP septal focus (Figure 43, 60 minutes).

We conclude that in wild-type cells, the FtsK-GFP septal focus appears on top of chromosomal DNA (marked by Hlp-mCherry), which is then segregated into the nascent daughter cells before cell division. The timing of appearance and location of the FtsK-GFP septal focus relative to chromosome segregation is consistent with a role for FtsK in moving chromosomal DNA across the closing septum; however, this association does not prove that chromosome segregation is dependent on FtsK.
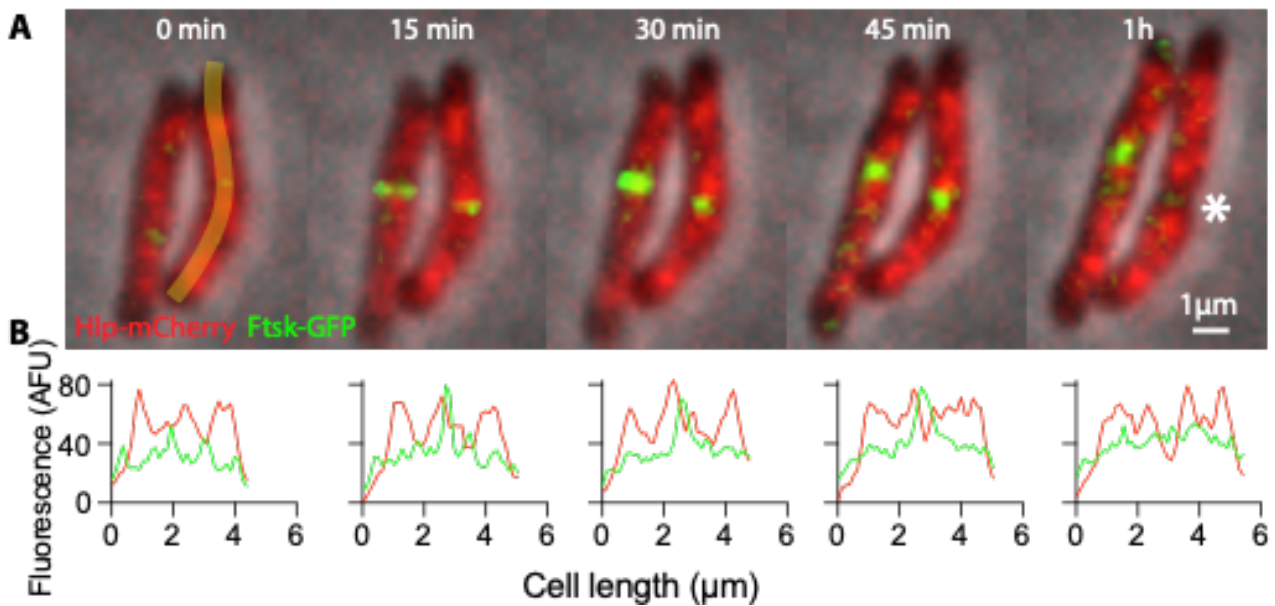
Figure 43. FtsK-GFP appears on top of Hlp-mCherry-stained chromosomal DNA, which is segregated before division.

(A) *M. smegmatis* FtsK-GFP Hlp-mCherry cells were cultured in a microfluidic device and imaged by time-lapse microscopy at 15-minute intervals. In this experiment, the last image frame before the first appearance of Ftsk-GFP at the septum is defined as time = 0 minutes. The white star at 1 hour indicates cell division. **(B)** Fluorescence profiles of FtsK-GFP (green) and Hlp-mCherry (red) along the long axis of the cell indicated in (A). The old cell pole is defined as "0 µm" along the cell length.

5.3.3   FtsK-GFP constricts at the middle of the closing septal membrane stained by FM4-64

I have shown that FtsK is present as a focus when cytokinesis has happened. But where is FtsK localized compared to the invagination of the forming septum?

To analyze the timing of appearance and localization of FtsK-GFP septal focus formation compared to the closing division septum, I performed a time-lapse microscopy experiment of cells expressing FtsK-GFP (Figure 44B) and stained the cells with the membrane stain FM4-64 (Figure 44A). At early stages of the cell cycle, the cell membrane is stained by FM4-64 but neither the septal membrane (Figure 44A, 0 minutes) nor the FtsK-

113

GFP septal focus (Figure 44B, 0 minutes) can be detected. The first appearance of the FtsK-GFP septal focus at midcell (Figure 44B, 15 minutes) slightly precedes the first appearance of the nascent septal membrane stained with FM4-64 (Figure 44A, 30 minutes). Over time, the FM4-64-stained septal membrane gradually closes, as shown by the transveral FM4-64 profile across the cell's short axis (Figure 44C). The timing of septum closure seems to coincide with the constriction of the FtsK-GFP septal focus towards the center of the septum and, by comparison with time-lapses performed with the FtsK-GFP Hlp-mCherry reporter strain (Figure 43), with the time when the two nucleoids are segregated to the daughter cells. However, time-lapse imaging at a higher frequency using a reporter strain expressing fluorescently tagged FtsK and Hlp and stained with FM4-64 would provide a more accurate temporal resolution of these events.
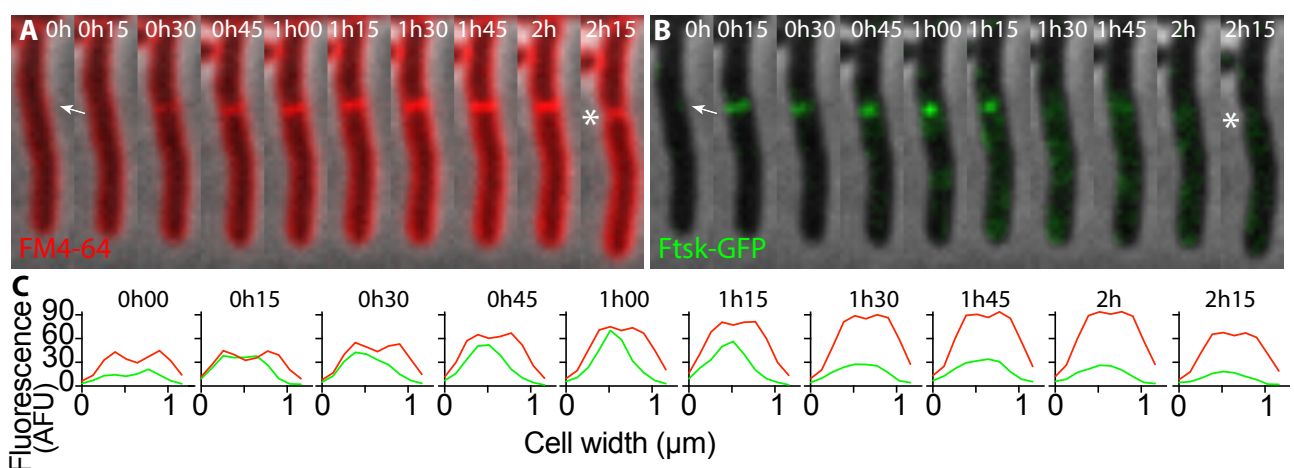
Figure 44. Time-lapse microscopy of *M. smegmatis* FtsK-GFP cells stained with FM4-64

M. smegmatis FtsK-GFP cells were cultured in a microfluidic device and imaged by time-lapse microscopy at 15-minute intervals. The membrane was stained by adding the dye FM4-64 to the microfluidic flow medium. Cell division is indicated by the white star. **(A)** FM4-64 staining. **(B)** FtsK-GFP localization. **(C)** Corresponding transversal profiles of FtsK-GFP (green) and FM4-64 (red) along the cell's short axis at the position indicated by the white arrow in (A) and (B).

This result confirms that FtsK could translocate DNA through a closed septum, shown here with FM4-64 membrane stain.

5.3.3.1 Conclusion – Hierachy of FtsK and other septal factors

In *E. coli*, FtsK was shown to interact with both FtsZ and FtsN, which are respectively the first and last protein to assemble as the divisome complex (Berezuk et al. 2018). FtsN triggers septal peptidoglycan synthesis, which is a relatively late stage in septum formation (Pichoff et al. 2018). FtsK may thus serve a linking role between the early and late divisome components. FtsZ is a protein that forms a discontinuous rotating ring (Holden et al. 2014). According to some models, FtsK may either create a pore through the septal membrane allowing DNA to pass through (Becker Pogliano 2007) or it may serve a checkpoint function to prevent septal membrane closure until completion of chromosome segregation (Dubarry and Barre 2010; Fiche et al. 2013).

We conclude that in *M. smegmatis* the timing of appearance of septal factors follows an organized hierarchy, similar to other organisms (Figure 45). FtsZ localization at the septum precedes FtsK (Wu et al. 2018). The assembly of a ring-like FtsK-GFP structure at the septum precedes the formation, invagination, and closure of the septal membrane. Finally, FtsK constriction at midcell coincides with cytokinesis (Figure 42) as well as the fully formed septum (Figure 44) and the separation of Hlp into two lobes (Figure 43), which supports the hypothesis that FtsK forms a pore that allows translocation of DNA across the closed septum.
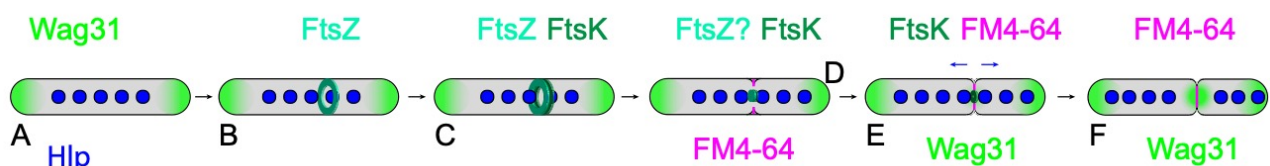
Figure 45 Summary timing of events

(A) Wag31 is present at both poles at the beginning of the cell cycle. **(B)** FtsZ appears at midcell. **(C)** FtsK appears after FtsZ but they are present simultaneously for more than 20% of the cell cycle (Wu et al. 2018). **(D)** The membrane stained with FM4-64 forms after FtsK appearance (Figure 44). **(E)** The invagination of

FM4-64 precedes the appearance of Wag31 by 25±11 min (Santi et al. 2013) and FtsK fades with the appearance of Wag31 (Figure 42). **(F)** FtsK disappears before membrane separation (Figure 44).

5.4   FtsK characterization in Δ*parB* cells

In wild-type cells, the Hlp-Dendra2 signal (and, therefore, chromosomal DNA) seems to be distributed evenly along the cell length and separates into two distinguishable "lobes" (each corresponding, presumably, to a chromosome) just before division. In order to investigate the segregation process in Δ*par* cells, I attempted to construct a Δ*parA* FtsK-GFP mutant. I first constructed a suicide vector using the Gibson assembly method to knock out *parA*. I obtained many first-step ("insertion") recombinants, but never succeeded in obtaining any second-step ("excision") recombinants that replaced the wild-type *parA* gene with the engineered Δ*parA* allele (see Figure 34 for an explanation of the steps involved); instead, I found that 100% of the second-step recombinants had reverted to the wild-type parA configuration. These results suggested that the combination of the FtsK-GFP fusion protein and the Δ*parA* allele might be synthetically lethal. This suggests that *parA* and *parB* also have a separate function from each other as only the Δ*parB* FtsK-GFP could be obtained.

5.4.1   FtsK-GFP fails to localize at the cell division septum in Δ*parB* mutants

Although I was unable to knock out the *parA* gene in cells expressing the FtsK-GFP fusion protein (see previous section), I succeeded in constructing a Δ*parB* FtsK-GFP strain. I used the pJGΔ*parB* plasmid to knock out the *parB* gene in the FtsK-GFP strain by a two-step homologous recombination method (see Figure 34 for an explanation of the steps involved). This strain was confirmed by PCR and sequencing. Unexpectedly, when I imaged

the Δ*parB* FtsK-GFP strain by time-lapse microscopy only a delocalized green fluorescent signal was seen corresponding to FtsK-GFP. In order to compare the fluorescence of wild-type cells expressing FtsK-GFP compared to Δ*parB* cells expressing FtsK-GFP without any bias, I performed a time-lapse experiment in which wild-type FtsK-GFP cells and Δ*parB* FtsK-GFP cells were mixed. The wild-type cells were easily distinguishable from the Δ*parB* cells because they also expressed Wag31-mCherry (Figure 46A and B). In the Δ*parB* FtsK-GFP cells, only small and rapidly moving speckles of FtsK-GFP are observed. These faint FtsK-GFP speckles are localized everywhere in the cells, with no concentration at midcell at any time during the cell cycle and no detectable formation of a ring-like structure.

We conclude that loss of ParB function results in delocalization of the FtsK-GFP protein and failure to form an FtsK-GFP septal focus prior to cell division which might suggest an interaction between these two genes.
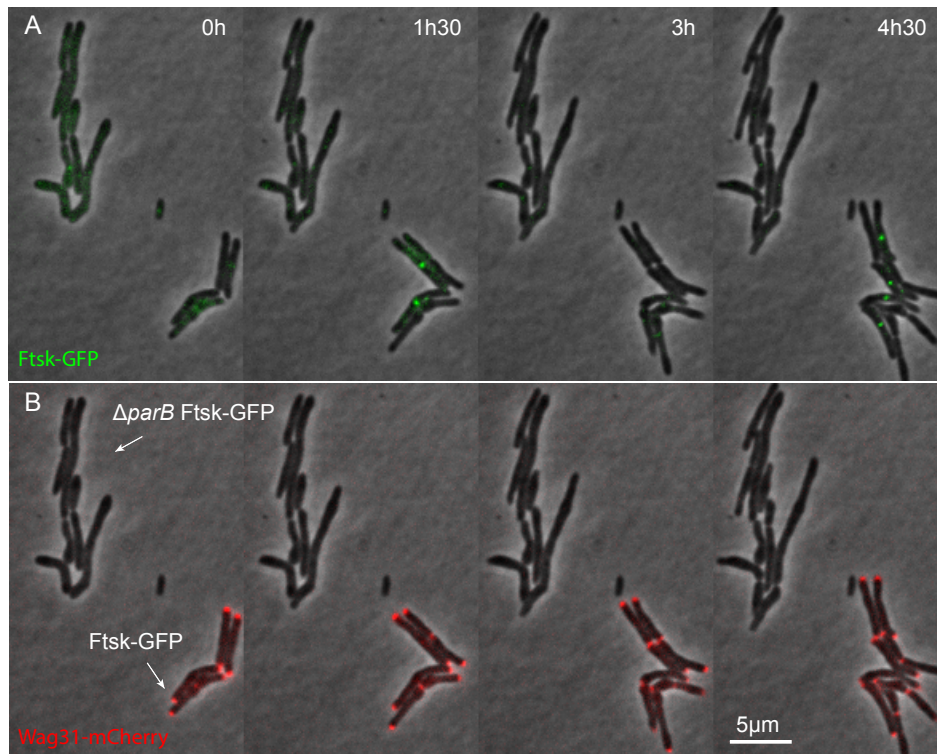
Figure 46. Simultaneous time-lapse microscopy of wild-type FtsK-GFP Wag31-mCherry cells and Δ*parB* FtsK-GFP cells in the same field of view

M. smegmatis FtsK-GFP Wag31-mCherry cells and Δ*parB* FtsK-GFP cells were co-cultured in a microfluidic device and imaged by time-lapse microscopy at 15-minute intervals. Microcolonies of the two strains are indicated by white arrows and are in the same field of view for precise fluorescence comparison. **(A)** FtsK-GFP. **(B)** Wag31-mCherry enables easy distinction between wild-type and Δ*parB* cells.

5.4.2   FtsK-GFP localization is stable in Δ*parB* cells, diminishes and increases in wt cells during the cell cycle

To investigate if the faint fluorescence in Δ*parB* FtsK-GFP cells was transient, I compared the expression of FtsK-GFP over time in wild-type FtsK-GFP cells and Δ*parB* FtsK-GFP cells, FtsK-GFP fluorescence normalized by the cell area was represented as a percentage of the cell cycle (Figure 47). Total FtsK-GFP fluorescence varies according to the cell cycle in wild-type cells, being high at birth and decreasing thereafter until reaching a similar level of flu-

orescence compared to Δ*parB* cells at approximately the middle of the cell cycle, and increasing slightly towards the end of the cell cycle (Figure 47, green). In contrast, FtsK-GFP fluorescence remained relatively constant throughout the cell cycle in Δ*parB* cells (Figure 47, black). FtsK-GFP could be degraded or GFP could be cleaved in the Δ*parB* mutant but it is not clear why the fusion protein would be unstable in Δ*parB* cells yet stable in wild-type cells. As the wild-type strain (*parB*+ FtsK-GFP) was used as the parental strain for deletion of *parB* (Δ*parB* FtsK-GFP), these strains are (presumably) genetically identical except for the *parB* locus. As mentioned later (**Chapter 5.5**), I constructed a FtsK-HA strain in both wild-type, Δ*parB*, and Δ*parA* backgrounds in order to quantify the levels of FtsK-HA protein in each strain by immunblotting with an anti-HA antibody. In principle, these strains could be used for immunostaining of cells with the anti-HA antibody; in practice, however, immunostaining of mycobacterial cells is unusually difficult due to the thickness and complexity of the mycobacterial cell envelope (Cimino et al. 2006).

We conclude that the expression of FtsK-GFP in Δ*parB* FtsK-GFP is stable over time but it diminishes at birth and increases slightly before division in WT FtsK-GFP cells. As a high number of fluorescent molecules should be present at the same localization, the FtsK protein levels in both wt, Δ*parB* and Δ*parA* will be measured later (**Chapter 5.5**).
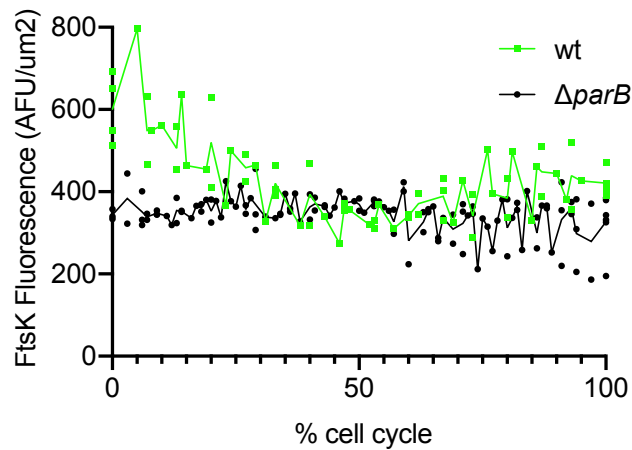
Figure 47. Comparison of total cellular FtsK-GFP fluorescence in wild-type and Δ*parB* cells

Total cellular FtsK-GFP fluorescence in *M. smegmatis* FtsK-GFP Wag31-mCherry cells (wt) and Δ*parB* FtsK-GFP cells (Δ*parB*) over the cell cycle from birth at 0% cell cycle to division at 100% cell cycle (n = 12 cells per strain).

5.4.3 Mislocalization of FtsK-GFP in Δ*parB* cells is not complemented by expression of a functional *parB* gene from a plasmid

To verify that loss of FtsK-GFP septal localization in Δ*parB* cells is due to loss of ParB function *per se*, I attempted to complement the Δ*parB* FtsK-GFP strain by inserting a plasmid expressing *parB* under the control of the strong UV15 promoter (UV15*parB*) at the chromosomal *attB* site (Figure 48A). First, I constructed a plasmid using the Gibson assembly method by inserting the *parB* gene downstream of the UV15 promoter and transformed this plasmid into the Δ*parB* FtsK-GFP strain. Colonies were screened by colony PCR and confirmed by sequencing. I then performed a time-lapse microscopy experiment using the strain Δ*parB* FtsK-GFP:: UV15_*parB.* Unfortunately, this strain still generated minicells (indicated by white arrows in Figure 48A) and septal localization of FtsK-GFP was not restored. I then tried to complement the Δ*parB* FtsK-GFP strain by transforming this strain with a plasmid expressing *parB* under the control of its native promoter (*prom_parB*) inte-

grated at the chromosomal *attB* site (Figure 48B). Colonies were screened by colony PCR and confirmed by sequencing. I then performed a time-lapse microscopy experiment with the strain Δ*parB* FtsK-GFP:: *prom_parB.* The cells seemed to be partially complemented for the minicell phenotype but a few divisions still gave birth to minicells (indicated by the white arrows in Figure 48B). However, septal localization of FtsK-GFP was still not restored. To quantify the complementation of the minicell phenotype, I calculated the percentage of minicell formation (Figure 48C). Surprisingly, the Δ*parB* FtsK-GFP::UV15parB strain pro-duced about 48% of minicells, which is a more than four-fold increase of the percentage of minicells compared to the phenotype of uncomplemented Δ*parB* FtsK-GFP cells. It was previously shown that the overexpression of *M. tuberculosis* (Maloney et al. 2009) or *M. smegmatis* (Uhía et al. 2018) ParA or ParB can increase the percentage of minicells. The complementation of *parB* driven by its own promoter (Δ*parB* FtsK-GFP::prom_*parB* strain) did reduce by about two-fold the percentage of minicells but the wild-type phenotype was not completely restored. As different promoters can drive very different levels of gene ex-pression, it seems likely that the expression level of *parB*, when dis-balanced in either di-rection (up or down), can cause a minicell phenotype. In future, an anti-ParB western blot could be done to measure the levels of ParB protein.

We conclude that adding *parB* at the chromosomal *attB* site, either driven by the strong UV15 promoter or its native promoter, could complement neither the *parB* minicell phenotype nor the FtsK-GFP mislocalization phenotype. Interestingly, the Δ*parB* FtsK-GFP::UV15parB strain generated far more minicells compared to the Δ*parB* strain without a plasmid expressing *parB*.

strain	% mini cells
ΔparB Ftsk-GFP::UV15parB	48.1
ΔparB Ftsk-GFP::prom_parB	5.3
ΔparB Ftsk-GFP	9.9
ΔparB	11.0
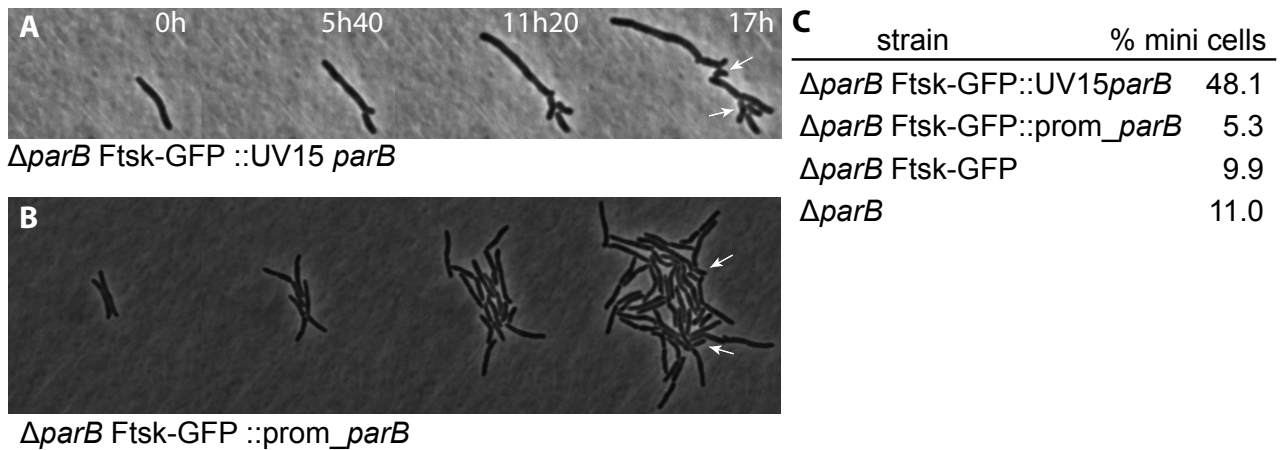
Figure 48. Complementation of ΔparB FtsK-GFP cells by expression of *parB* from a plasmid inserted at the chromosomal *attB* site

M. smegmatis ΔparB FtsK-GFP::UV15*parB* cells **(A)**and ΔparB FtsK-GFP::prom_*parB* cells **(B)** were cultured in a microfluidic device and imaged by time-lapse microscopy at 10-minute intervals. **(C)** The percentage of minicells is listed for the strains ΔparB FtsK-GFP::UV15*parB* (n = 214 cells), ΔparB FtsK-GFP::promoter_*parB* (n = 133 cells), ΔparB FtsK-GFP (n = 354 cells), and ΔparB (n = 200 cells).

5.4.4 FtsK-GFP localization rescued by the ParB complementation in FtsK-GFP ΔparB mutants at the genomic locus

As complementation of ΔparB FtsK-GFP by expression of *parB in trans* from the chromosomal *attB* site was not successful, I attempted to complement the strain using two-step homologous recombination to re-introduce the *parB* gene at its native locus (see Figure 34 for an explanation of the steps involved). I first constructed a suicide plasmid pJG*parB* using the Gibson assembly method and transformed this plasmid into the ΔparB FtsK-GFP strain. Colonies were confirmed by PCR and sequencing. I then performed a time-lapse microscopy experiment using the strain ΔparB FtsK-GFP::*parB*. No more minicells were observed (minicell frequency was less than 1%, comparable to wild-type cells), con-

firming that complementation of this phenotype was successful. However, septal localization of FtsK-GFP was not restored in the ΔparB FtsK-GFP::parB strain (Figure 49A).

We conclude that restoring parB at its native genomic locus complements the minicell phenotype but not the FtsK-GFP mislocalization phenotype of ΔparB FtsK-GFP cells. This might be explained if another mutation occurred elsewhere in the genome and if this second-site mutation were responsible for mislocalization of FtsK-GFP in the ΔparB FtsK-GFP strain. A mutation in the linker could also have happened. Indeed, it was very difficult to construct the ΔparB FtsK-GFP strain and only a single positive clone was obtained which indicated that maybe the strain could only be obtained after aquiring mutations. A western blot anti-GFP could be done to verify that GFP is not cleaved and that FtsK protein levels are the same in wt and ΔparB strains. I tried to do this experiment however the antibody I used was not specific enough, therefore I constructed a strain containing FtsK with an HA tag in wt and Δpar backgrounds to quantify the FtsK levels (**Chapter 5.5**).

strain	% mini cells
ΔparB Ftsk-GFP::parB	0.8
ΔparB Ftsk-GFP	9.9
ΔparB	11.0
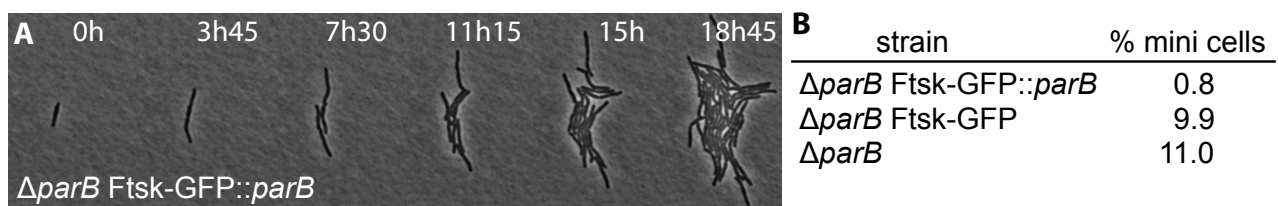
Figure 49. Complementation of ΔparB FtsK-GFP cells by restoring parB at the native chromosomal locus

(A) *M. smegmatis* ΔparB FtsK-GFP::parB cells were cultured in a microfluidic device and imaged by time-lapse microscopy at 15-minute intervals. (B) The percentage of minicells is listed for the strains ΔparB FtsK-GFP::parB (n = 358 cells), ΔparB FtsK-GFP (n = 354 cells), and ΔparB (n = 200 cells).

5.4.5   Whole-genome sequencing of FtsK-GFP Δ*parB* cells

As the minicell phenotype of the Δ*parB* FtsK-GFP strain was complemented by re-introduction of the *parB* gene at the native chromosomal locus (Δ*parB* FtsK-GFP::*parB* strain) without restoring septal localization of FtsK-GFP, wanted to investigate if the phenotype was in fact due to mutations elsewhere in the genome.

I first confirmed that this lack of rescued phenotype was not a single event by analyzing additional clones that were successful for the two-step homologous recombination to re-introduce *parB*. I also tried to re-introduce the suicide plasmid to obtain other colonies successful both for the first and second homologous recombinations. The FtsK-GFP mislocalization phenotype was never complemented and the sequencing results for the chromosomal *parB* and *ftsk* loci did not reveal any unexpected mutations. Therefore, I optimized a protocol to extract *M. smegmatis* genomic DNA of sufficiently good quality to be analyzed by PacBio whole-genome sequencing.

Interestingly, whole-genome sequencing using the PacBio sequencing method done at the UNIL genomic facility of the Δ*parB* FtsK-GFP strain revealed mutations in the *gidB* gene, which is part of the *par* operon (Figure 50A). Indeed *parA*, *parB* and parS sequence are part of the same operon, which also include the *gidB* gene. Each gene in this operon has its own promoter but the pairs *parA-parB* and *gidB-parA* can be cotranscribed (Casart et al. 2008). An extra G in the *giB* gene would therefore change the reading frame and not only affect GidB protein but also, potentially, ParA expression. Interestingly, it was previously shown that a double mutation Δ*parA* Δ*parB* in *M. smegmatis* would reduce the percentage of anucleate cells to 1% (Ginda et al. 2013). If parA was non-fonctional, in the Δ*parB* FtsK-GFP strain, there should be less anucleate cells than 9.9% (**Chapter 5.4.4**). Moreover, if *parA* was non-functional, an minicell phenotype similar to Δ*parA* phenotype would likely be seen in the complemented strain Δ*parB* FtsK-GFP::*parB.* Unless ParA is still partially functional, again highlighting the critical importance of the level of proteins. Two

deletions were also found in the cytochrome C biogenesis protein (Figure 50B). These lat-ter deletions could be confirmed by resequencing, as these deletions are both in the mid-dle of sequences containing repeats of the same nucleotide. Sequencing is less accurate whith a repeat of the same nucleotide. The analysis of the whole genome sequencing was not done in depth as no tool specific for *M. smegmatis* genome exists and other mutations could still exist in the Δ*parB* FtsK-GFP genome analysis.
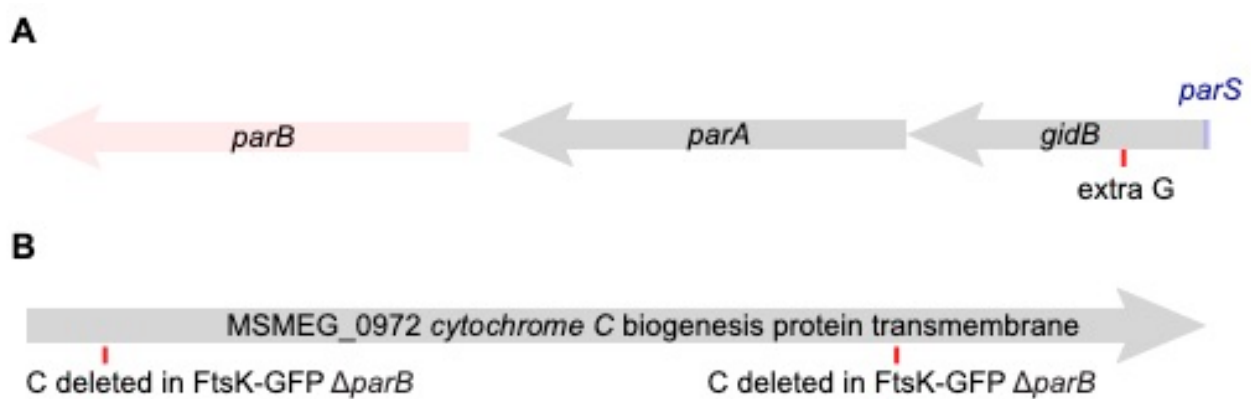
Figure 50. Genome sequence differences between the Δ*parB* FtsK-GFP and FtsK-GFP strains

By analyzing the whole genome sequences of Δ*parB* FtsK-GFP and FtsK-GFP some differences were found in **(A)** the *gidB* gene, which is part of the *par* operon, and **(B)** the MSMEG_0972 gene, which is annotated as encoding a cytochrome C biogenesis transmembrane protein.

5.5 The levels of FtsK protein are comparable in wild-type FtsK-GFP and Δ*par* FtsK-GFP strains

As the fluorescence of FtsK-GFP appeared to be somewhat lower in Δ*parB* cells compared to wild-type cells, I wanted to confirm that the FtsK protein level was lower in the Δ*parB* background.

I first tried to do a Western Blot using anti-GFP antibodies. The antibody did not seem specific enough. Therefore, I constructed a suicide vector, pJGFtsK-HA, containing the *ftsK* gene fused at its C-terminus with a hemagglutinin (HA) tag. I then used a two-step homologous recombination procedure (see Figure 34 for an explanation of the steps involved) to generate three strains: FtsK-HA, Δ*parA* FtsK-HA, and Δ*parB* FtsK-HA. These strains were confirmed by colony PCR and sequencing. I then obtained reproducible western blot results using a conjugated anti-HA antibody with RpoB protein as a loading control (Figure 51). The signal specificity was verified by loading the negative control WT cells, without a HA tag (fourth column). The western blot showed that the amount of FtsK-HA is comparable in both Δ*parA* and Δ*parB* cells compared to wild-type cells. Therefore, there is no difference in total FtsK expression but there is a difference of expression pattern during the cell cycle as well as an FtsK-GFP localization defect in the Δ*parB* FtsK-GFP strain.

We conclude that the amount of FtsK is comparable in wild-type, Δ*parA*, and Δ*parB* strain backgrounds. Therefore, the lack of FtsK localization at the septum is not due to a lower FtsK level in Δ*parB* FtsK-GFP cells. An explanation could be that ParB is required to stabilize FtsK. However, as the FtsK-GFP localization phenotype was not rescued in the complementation of ParB at its native locus unlike the anucleate phenotype, accumulations of mutations in the genome is a more likely explanation for the lack of FtsK-GFP localization at the septum in Δ*parB* cells. It could be interesting to verify the localization of FtsK-HA by immunostaining in wt and Δ*par* strains. If FtsK-HA is properly localized in Δ*par*B FtsK-GFP, there might be mutations preventing its correct localization. Furthermore, if FtsK-HA is properly localized in Δ*par*A FtsK-GFP, GFP might be a too large molecule preventing interaction of FtsK with other proteins.
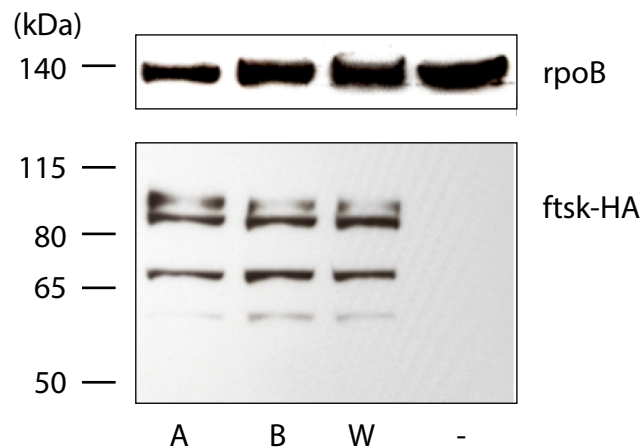
Figure 51. Anti-HA western blot of *M. smegmatis* FtsK-HA, Δ*parA* FtsK-HA, and Δ*parB* FtsK-HA strains

Anti-HA western blot of protein extracts from FtsK-HA (**W**), Δ*parA* FtsK-HA (**A**), and Δ*parB* FtsK-HA (**B**) strains and WT (**-**) as a negative control. RpoB was used as a loading control and detected by a anti-RpoB first antibody and an anti-mouse secondary antibody. Each lane was loaded with 40 μg of total cellular protein.

5.6 Characterization of FtsK essentiality and repression

5.6.1 FtsK is essential in *M. smegmatis*

As observed previously, DNA in anucleate cell formation seemed to be pulled from the anucleate sister cell towards the nucleated sister cell. As I have shown that no SOS response occurs in these divisions, I hypothesize that FtsK would actively pull DNA towards the nucleated cell. To test this hypothesis, I attempted to knock out FtsK which proved to be essential.

In *E. coli*, the N-terminal part of FtsK is essential (Wang and Lutkenhaus 1998) and is predicted to be essential in *M. tuberculosis* using a study by transposon mutagenesis (DeJesus et al. 2017). To the best of our knowledge, the essentiality of *ftsK* has not been

tested in *M. smegmatis*. I first constructed a suicide vector pJGΔ*ftsK* using the Gibson assembly method and attempted to delete the *ftsK* gene using a two-step homologous recombination method (see Figure 34 for an explanation of the steps involved). The first-step recombination ("insertion") was successful but the second-step recombination ("excision") was not. I then constructed an integrative plasmid containing a streptomycin resistance gene and *ftsK* under the control of its native promoter and I inserted this plasmid at the Δ*ftsK* locus by one-step ("insertion") homologous recombination to create a merodiploid strain having one functional copy of *ftsK* and one copy with an in-frame deletion of the ftsK open reading frame (Δ*ftsK*). I then transformed the ftsK/Δ*ftsK* merodiploid strain with an attB-integrating plasmid containing a streptomycin resistance gene and *ftsK* under the control of its native promoter. With a functional second copy of *ftsK* at the *attB* site, I easily obtained the second-step ("excision") recombinant with Δ*ftsK* at the native chromosomal locus (Figure 50). The fact that the Δ*ftsK* mutation could be obtained only when a second and functional copy of *ftsK* was expressed *in trans* from the *attB* locus (Δ*ftsK attB*::*ftsk* strain) suggests that *ftsK* is essential in *M. smegmatis*.

The Δ*ftsK attB*::*ftsk* strain was used to obtain further evidence that *ftsK* is essential in *M. smegmatis* by using a "plasmid swap" method to replace the *ftsK*-expressing plasmid at *attB* with a plasmid expressing a kanamycin resistance gene with (Figure 52A) or without (Figure 52B) a functional copy of *ftsK*. Transformants were plated on medium with kanamycin to select for the incoming plasmid and without streptomycin to permit loss of the outgoing plasmid. Kanamycin-resistant colonies were obtained at high frequency when the incoming plasmid contained a functional copy of *ftsK* (Figure 52A). Most (96/100) of these colonies were streptomycin-sensitive, and the presence of *ftsK* as well as the kanamycin resistance gene was confirmed by PCR analysis. In contrast, very few kanamycin-resistant colonies were obtained when the incoming plasmid lacked a functional *ftsK* gene (Figure 52B), and none of these colonies (0/100) were streptomycin-sensitive. The presence of *ftsK* as well as the kanamycin resistance gene was confirmed by PCR analysis, suggesting that

the incoming plasmid integrated into the chromosome without displacing the resident *ftsK*-expressing plasmid at *attB*.

We conclude that *ftsK* is an essential gene in *M. smegmatis*.
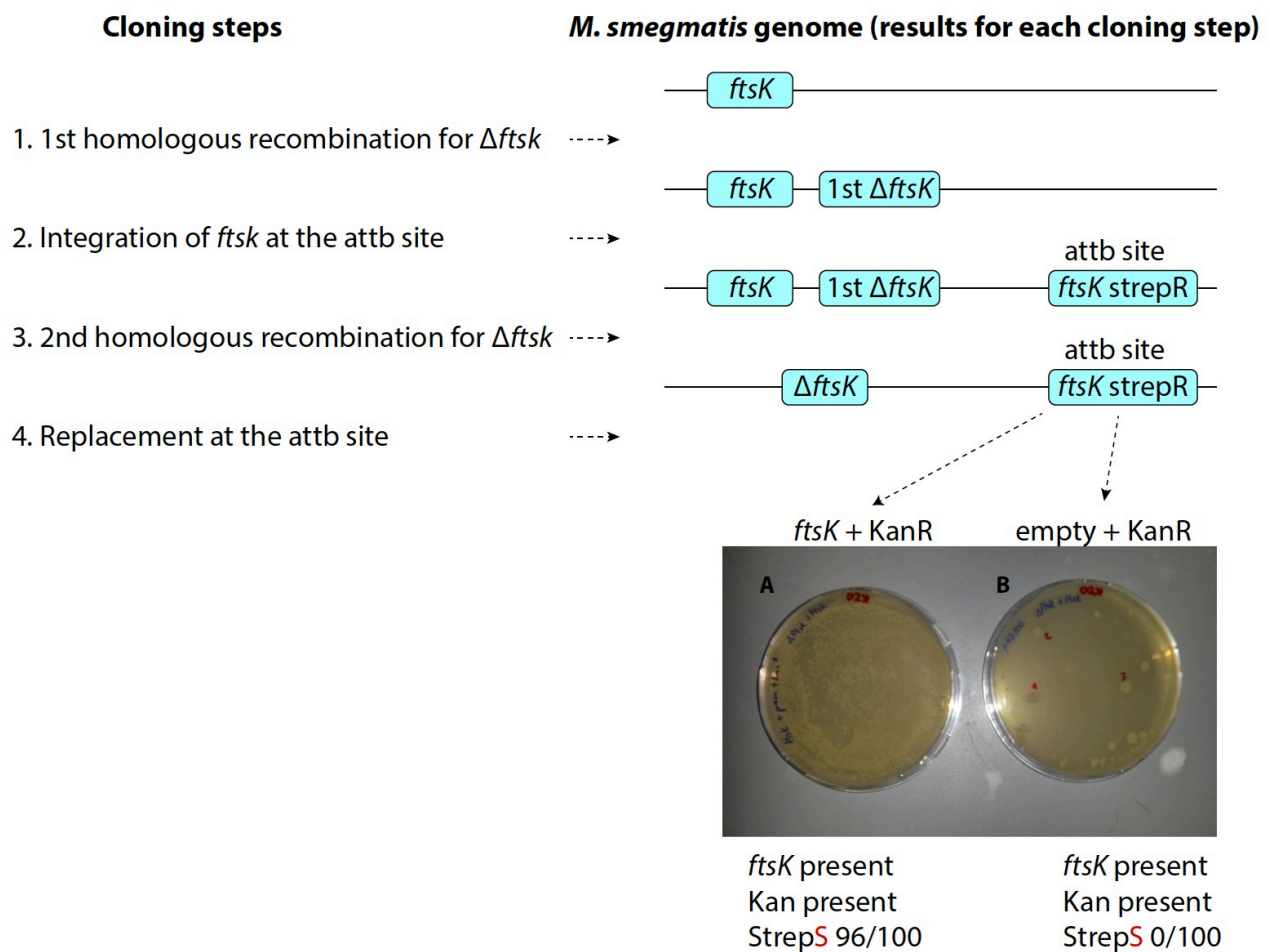
Figure 52. Strategy to evaluate the essentiality of *ftsK* in *M. smegmatis*

Schematic of the "plasmid swap" method to test the essentiality of *ftsK*. After insertion of a plasmid expressing *ftsK* and a streptomycin resistance gene (strepR) at the *attB* site, the second recombination step to delete *ftsK* at the native chromosomal locus was successful. Subsequently, *ftsK* at the *attB* site was successfully replaced by **(A)** a plasmid encoding *ftsK* and a kanamycin resistance gene (kanR), but not by **(B)** the

"empty" vector encoding the kanR marker but not *ftsK*. In both cases, *ftsK* and the kanR cassette were present, as confirmed by PCR analysis.

5.6.2   Dual FtsK repression system

As *ftsK* was proven to be an essential gene in *M. smegmatis*, it was not possible to evaluate the phenotype of an *ftsK* knockout mutant (Δ*ftsK*). As an alternative approach to understand the function of *ftsK*, I constructed an *ftsK* knockdown strain by adapting a previously described dual repression system (Kim et al. 2013) to modulate FtsK protein levels. This system combines simultaneous repression of transcription and controlled proteolysis by anhydrotetracycline (ATC).

In repression systems, a strong promoter drives the expression of a TetR protein. This protein forms a dimer and the addition of ATC induces a conformational change. This change either prevents (Tet ON, Figure 53A) or promotes (Tet OFF, Figure 53B) the binding of TetR to the *tet* operators (*tet*Os) present in the promoter region of the targeted gene (Klotzsche et al. 2009). The binding of TetR dimer prevents the binding of the RNA polymerase to the promoter and inhibits gene transcription (Berens & Hillen 2003).
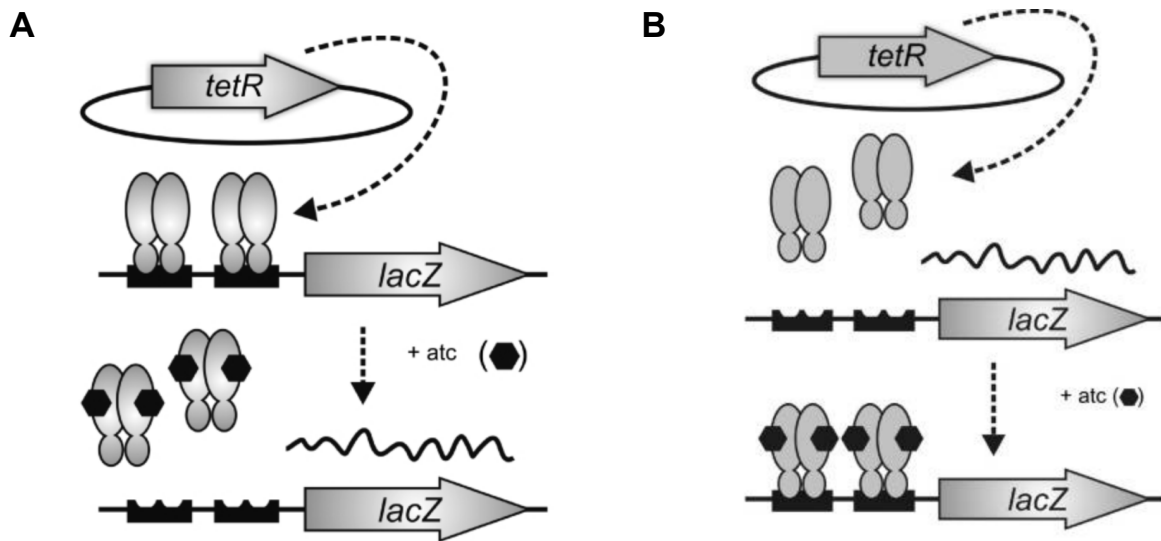
Figure 53 Tet ON and Tet OFF systems

Adapted from (Klotzsche et al. 2009)

The dual repression system (Kim et al. 2013) uses both Tet ON and Tet OFF systems. The Tet ON system drives the expression of SspB, which is an adaptor protein derived from *E. coli* that delivers the tagged protein to a protein degradation machinery (Kim et al. 2011). The protein tag is derived from the *E. coli* SsrA signal, which promotes the degradation of SsrA-tagged proteins by the ClpXP protease in *E. coli* or *M. smegmatis* (Kim et al. 2011). SspB enhances the degradation of the SsrA-tagged protein by the ClpXP protease by tethering the SsrA-tagged protein to ClpXP (Kim et al. 2011). The SsrA signal peptide was mutated (the mutated version is called the "DAS+4 tag") so that the degradation is SspB-dependant, as SspB is not essential for ClpXP degradation of proteins tagged with the wild-type version of SsrA (Kim et al. 2011). The Tet OFF system drives the expression of the DAS+4 tagged protein (Kim et al. 2013).

I modified the Tet OFF system from Kim et al. 2013 so that FtsK is fused in-frame to the DAS+4 tag. This tag is recognized by the SspB protein, which mediates the degradation

of the DAS+4-tagged protein by the endogenous ClpXP protein (Figure 54). For simplicity, from now on, I will only mention SspB but degregation by the endogenous ClpXP protease system is implied. When ATC is added, *ftsK* transcription is repressed and expression of SspB is induced. However, transcriptional repression is usually somewhat leaky. The system therefore involves a second level of regulation at the protein level: in the presence of ATC (+ATC), expression of DAS+4-tagged FtsK is repressed and the small amount of DAS+4-tagged FtsK that is produced is efficiently degraded by the SspB system. I constructed an *attB*-integrating plasmid containing *ftsK* with a DAS+4 tag at its C-terminus driven by an ATC-repressible promoter, and I used this plasmid in a "plasmid swap" strategy to replace an *attB*-integrated plasmid encoding *ftsK* in the Δ*ftsK* attB::*ftsK* strain (described above). I screened for positive clones by colony PCR and sequencing and then integrated a second plasmid expressing *sspB* at the "tweety" *attT* integration site. The final genetic configuration of the ftsK conditional knockdown strain is Δ*ftsK attB*::*ftsk*-DAS+4 *attT*::*sspB* (hereafter referred to as "FtsK knockdown"), in which the chromosomal copy of *ftsK* contains an in-frame deletion of the coding sequence (Δ*ftsK*), a DAS+4-tagged copy of *ftsK* transcribed from by an ATC-repressible promoter is integrated at the chromosomal *attB* site (*attB*::*ftsk*-DAS+4), and *sspB* transcribed by a ATC-induced promoter is integrated at the chromosomal *attT* site (*attT*::*sspB*). In this system, expression of Ftsk-DAS+4 is high when ATC is absent and low when ATC is present.
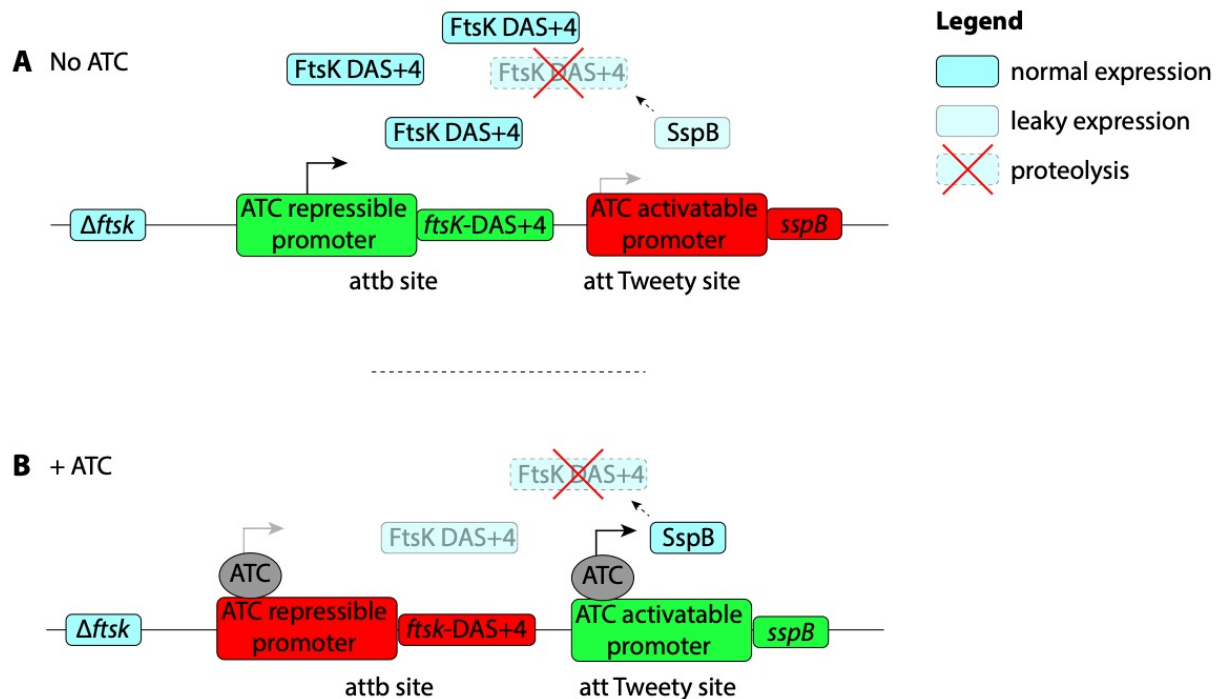
Figure 54. Schematic representation of the dual FtsK repression system

Thue dual repression system is an adaptation of the Kim et al. 2013 system. FtsK here is fused at its C-terminus with a DAS+4 tag is degraded by the SspB protease system. **(A)** When no ATC is present, FtsK is expressed and partially degraded by SspB. **(B)** When ATC is added, the promoter driving *ftsK* expression is repressed; the small amount of FtsK-DAS+4 that is expressed (due to leakiness of the repression system) is degraded by SspB protease system.

5.6.3   FtsK knockdown causes a mild growth defect

I first tried to repress FtsK expression in otherwise wild-type cells using an adapted dual repression system (Kim et al. 2013), and one of my goals was to see what effect this might have on chromosome dynamics using the ParB-mCherry marker, which tags the *parS* loci adjacent to the chromosomal origin of replication (*ori*). As *ftsK* is an essential gene and might be responsible to segregate the chromosomes, I expected to have a strong pheno-type. With this aim, I constructed the strain Δ*ftsK attB*::*ftsK*-DAS+4 *attT*::*sspB parB*-mCherry (hereafter referred as "FtsK knockdown ParB-mCherry") by a two-step recombi-

nation method to replace the native *parB* locus with the *parB*-mCherry fusion gene (see Figure 34 for the steps involved). I used the suicide vector pJG*parB*-mCherry to replace the *parB* gene in the strain Δ*ftsK attB::prom_ftsK.* After confirmation by colony PCR and sequencing, I used a "plasmid swap" strategy to replace the *attB*-integrated plasmid encoding encoding *prom_ftsK* with a plasmid encoding *ftsK*-DAS+4 under the control of an ATC-repressible promoter. A second plasmid expressing sspB from an ATC-driven promoter was then added at the "tweety" *attT* site. As no obious phenotype was detected when switching the medium to the medium containing ATC during a time-lapse experiment, I tried to enhance the effect by pre-incubating the cells in liquid culture with ATC before setting up the culture in the microfluidic device (Figure 55). By observing time-lapse movies of the FtsK knockdown ParB-mCherry strain under repressing (+ATC) conditions, we see that most of the cells have an apparently normal phenotype but some cells show slight swelling at the poles (Figure 55A; abnormal cells are highlighted by the white arrows). Other cells have a more striking phenotype, as they not only swell at the poles, but also elongate and do not divide and seem to contain multiple origins of replication (indicated by multiple ParB-mCherry foci). These abnormal cells eventually lyse (Figure 55B). As some of these cells seemed longer, to clarify if the long cells were actually two cells that failed to separate or a single long cell with multiple origins of replication, I stained the cell membranes with FM4-64 (Figure 55C-E). Most of the cells had an apparently normal morphology but some had bulges with misplaced membranes (Figure 55C and D) or were branching and elongated with multiple internal membranes (indicated by the white arrow in Figure 55E). To verify that the observed phenotype was due to the repression of FtsK, the same strain was imaged without ATC, where the phenotype seemed similar to wild-type cells expressing the fluorescent reporter ParB-mCherry (Figure 55F).

We conclude that repressing FtsK expression resulted in most of the cells retaining an apparently normal morphology. However, some cells showed a severe phenotype: swelling at the cell poles, elongation, branching, multiple internal membranes, as well as multiple origins of replications were observed. This very mild phenotype was unexpected

as *ftsK* is an essential gene, I expected most of the cells to die and those which did not die to have a segregation defect. This could be due to the leakiness of the repression system and a dose dependent effect. A small quantity of FtsK might be sufficient for some essential function such as chromosome resolution. The segregation role of Ftsk might also be required in a low proportion of cells with abnormal position of the chromosomes, backing up other segregation mechanisms. In *S. coelicolor* mutating *ftsK* resulted in an increase of anucleate cells but complete deletion of the gene did not (Dedrick et al. 2009). However, in *B. subtilis*, mutation in SpoIIIE prevents proper partitioning in the formation of the pre-spore but no phenotype is detected during the vegetative growth unless the coordination between the septation and nucleoid partitioning or when the septum is misplaced (Sharpe & Errington 2005). In *E. coli* depleting FtsK results in the formation of filamented cells (Wang & Lutkenhaus 1998).
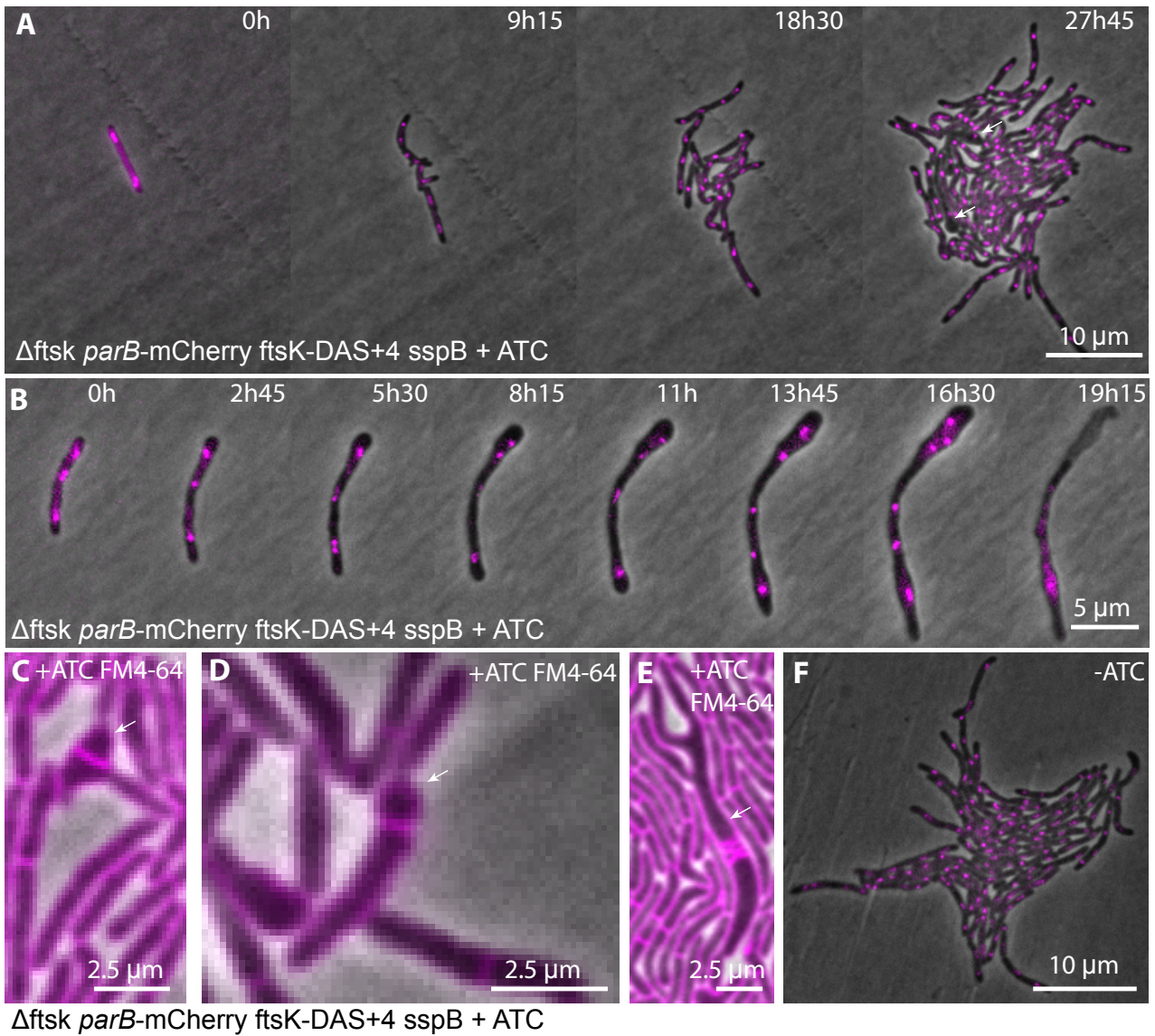
Figure 55. Repression of FtsK in cells expressing the *ori* marker ParB-mCherry

M. smegmatis FtsK knockdown ParB-mCherry cells were cultured in a microfluidic device and imaged by time-lapse microscopy at 15-minute intervals. When indicated, ATC was already added in the overnight batch culture used to inoculate the microfluidic device, as well as during the time-lapse. **(A)** Most *ftsK* knockdown cells seem to have a normal phenotype except for a small number of cells with polar bulges, indicated by white arrows. **(B)** Example of a cell with multiple origins of replication (ParB-mCherry foci). Lysis occurs at 19h15. **(C, D, E)** FM4-64 membrane dye was added. **(C, D)** Swollen cells are indicated by white arrows. **(E)** Branching cells and cells with multiple internal membranes (indicated by white arrows). **(F)** The same strain was imaged without ATC.

5.6.4 FtsK knockdown suppresses the minicell phenotype in Δ*parB* cells

As Δ*par* mutants have a chromosome segregation defect and FtsK is thought to be a DNA translocase, which might potentially translocate DNA from the anucleate daughter cell into the nucleated daughter cell, I wanted to investigate if this DNA movement was suppressed in repressed FtsK cells.

Therefore, I constructed a Δ*parB* Δ*ftsK attB*::*ftsK*-DAS+4 *attT*::*sspB* strain (hereafter referred as "Δ*parB* FtsK knockdown")using the same adapted dual repression system (Kim et al. 2013) that was used for FtsK knockdown in the wild-type strain background (see **Chapter 5.6.3.** above). I used the suicide vector pJGΔ*parB* to delete the *parB* gene using a two-step homologous recombination method (see Figure 34 for the steps involved) in the strain Δ*ftsK attB*::*prom_ftsK*. After confirmation by colony PCR and sequencing, I used a "plasmid swap" strategy to replace the *prom_ftsK* plasmid at *attB* with a plasmid encoding *ftsK*-DAS+4 under the control of an ATC-repressible promoter to generate the strain Δ*ftsK attB*::*ftsK*-DAS+4. A plasmid encoding *sspB* under the control of an ATC-inducible promoter was then added at the chromosomal "tweety" *attT* site. I then imaged the Δ*parB* FtsK knockdown strain by time-lapse microscopy (Figure 56A). Surprisingly, the minicell phenotype caused by deletion of *parB* was suppressed, as the percentage of minicells for this strain under FtsK knockdown conditions (+ATC) was just 0.5% (n = 2031 cells), similar to wild-type cells (Figure 56B). The cells also divided symmetrically, similar to wild-type cells. Furthermore, every cell in my time-lapse experiments grew and divided, suggesting that they had inherited a complete genome (although this was not shown directly, it is unlikely that cells with fragmented genomes would survive).

We conclude that FtsK knockdown in a Δ*parB* genetic background resulted in a phenotype similar to wild-type cells, with very low levels of minicells and with symmetric divisions. Therefore, the combination of FtsK knockdown and Δ*parB* seems to be a case of

"synthetic rescue" because FtsK knockdown eliminate the anucleate cell phenotype of Δ*parB* cells.
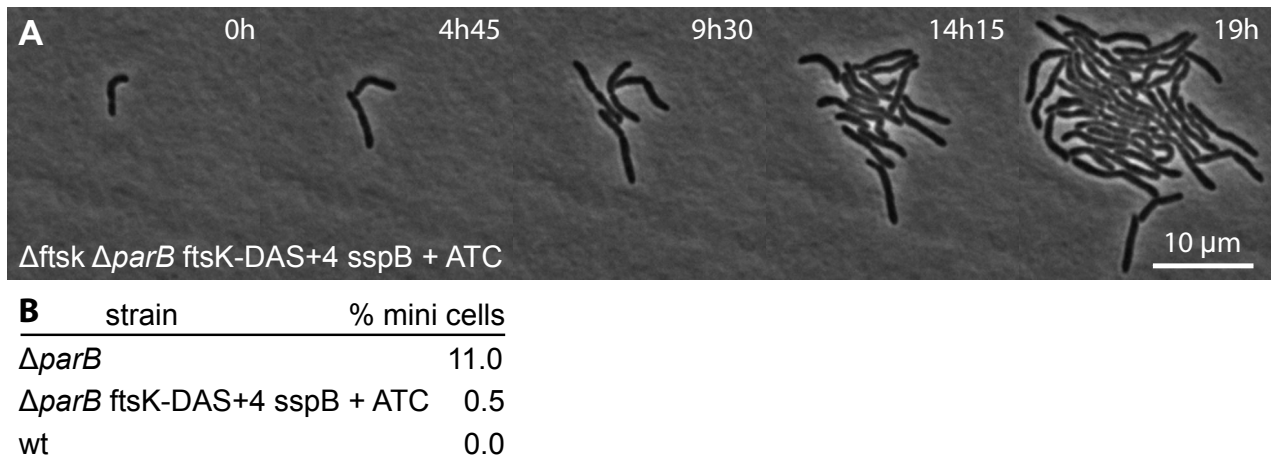
Figure 56. The minicell phenotype is suppressed in the Δ*parB* knock down FtsK strain

(A) *M. smegmatis* Δ*parB* FtsK knockdown was cultured in a microfluidic device and imaged by time-lapse microscopy at 15-minute intervals. ATC (400 ng/ml) was added in the overnight culture as well as during the time-lapse. **(B)** The percentage of minicells was calculated for each strain: Δ*parB* (n=200), Δ*parB* FtsK knockdown +ATC (n = 2031 cells), and wild-type (n = 100 cells).

5.6.5   FtsK knockdown suppresses the anucleate cell phenotype in Δ*parA* cells

As the synthetic rescue phenotype between Δ*parB* FtsK knock down was very surprising and that anucleate minicell phenotype in Δ*parA* cells is more pronounced compared to Δ*parB* cells, I wanted to see if this rescued phenotype also happened in the Δ*parA* background.

Therefore, I constructed a Δ*parA* Δ*ftsK attB*::*ftsK*-DAS+4 *attT*::*sspB* (hereafter referred as "Δ*parA* FtsK knockdown" strain) using an adapted dual repression system (Kim et al. 2013). I used the suicide vector pJGΔ*parA* to delete the *parA* gene by a two-step ho-

mologous recombination method (see Figure 34 for the steps involved) in the strain Δ*ftsK attB*::*prom_ftsK*. After confirmation by colony PCR and sequencing, I used a "plasmid swap" strategy to replace the *attB*-integrated plasmid encoding *prom_ftsK* with the plasmid encoding *ftsK*-DAS+4 controlled by an ATC-repressible promoter to generate the strain Δ*parA* Δ*ftsK attB*:: *ftsK*-DAS+4. I then integrated a plasmid encoding *sspB* under the control of a ATC-induced promoter at the "tweety" *attT* site to generate the strain Δ*parA* Δ*ftsK attB*:: *ftsK*-DAS+4 *attT*::*sspB*. I then imaged the Δ*parA* FtsK knockdown cells by time-lapse microscopy (Figure 57A). Again, the minicell phenotype caused by deletion of *parA* was suppressed and cells divided symmetrically when FtsK expression was knocked down. To confirm the lack of anucleate minicells, I stained the cells with the DNA dye SYTO17 (Figure 57B). As a control I also constructed the strain Δ*parA* Δ*ftsK attB*::*prom_ftsK attT*::*sspB* that has an *attB*-integrated copy of the *ftsK* gene under the control of its own promoter and lacking the DAS+4 destruction tag; the untagged FtsK protein is presumably insensitive to degradation by the SspB protease system. Time-lapse microscopy experiments confirmed that the Δ*parA* minicell phenotype (white arrows) is present when *ftsK* is present (Figure 57C). The percentage of minicells for the Δ*parA* Δ*ftsK attB*::*prom_ftsK attT*::*sspB* strain was 30%, compared to 0% for the Δ*parA* FtsK knockdown strain grown under FtsK knockdown conditions (+ATC) (Figure 57D).
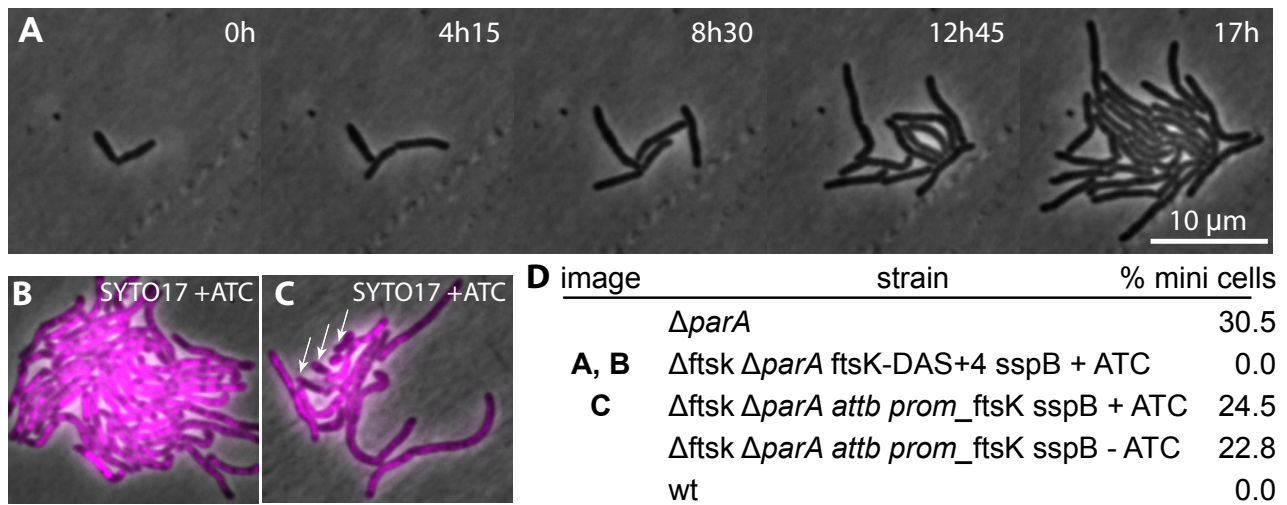
Figure 57. The minicell phenotype is suppressed in the Δ*parB* knock down FtsK strain

(A) *M. smegmatis* Δ*parA* FtsK knockdown cells were cultured in a microfluidic device and imaged by time-lapse microscopy at 15-minute intervals. When indicated, ATC was added in the overnight culture as well as during the time-lapse. **(B, C)** SYTO17 DNA dye was added as an end-point staining for **(B)** Δ*parA* FtsK knock-down +ATC cells, and (**C**) Δ*parA* Δ*ftsK attB*::prom_*ftsK* +ATC cells. **(D)** The percentage of anucleate minicells was calculated for each strain: Δ*parA* (n = 200 cells), Δ*parA* FtsK knockdown +ATC (n = 200), Δ*parA* Δ*ftsK attB*::prom_*ftsK* +ATC (n = 200 cells), Δ*parA* Δ*ftsK attB*::prom_*ftsK* –ATC (n = 92 cells), and wild-type (n = 100 cells).

We conclude that FtsK knockdown in a Δ*parA* genetic background resulted in a phenotype similar to wild-type cells, eliminating the asymmetric divisions and formation of anucleate cells that are characteristic of Δ*parA* cells. As every cell in the time-lapse movies grew, it further supports the hypothesis that every daughter cell inherited a chromosome, as confirmed by SYTO17 staining. Therefore, the combination of FtsK knockdown and Δ*parA* also seems to be a case of "synthetic rescue" because FtsK knockdown eliminate the anucleate cell phenotype of Δ*parA* cells. As the Par and FtsK proteins are currently thought to be important for chromosome segregation in mycobacteria, I might have predicted that combining a knockout of the Par system with a knockdown of FtsK would have resulted in a *stronger* (not a *weaker*) defect in chromosome segregation and a *higher* (not a *lower*) rate of anucleate cell formation. In *S. coelicolor*, the deletion of *ftsK* (Δ*ftsK*) did not result in

any phenotype, however the C-terminal truncation of *ftsK* (which corresponds to the motor domain), resulted in about 15% of anucleate spores. The double mutation of Δ*parB* and Δ*smc* resulted in 24% of anucleate cells. Surprisingly, the triple mutant Δ*parB* Δ*smc* and truncated *ftsK* resulted in only 10% anucleate cells (Dedrick et al. 2009). It would be interesting to know whether a complete deletion of *ftsK* in *S. coelicolor* would completely suppress the anucleate cell phenotype of the Δ*parB* Δ*smc* mutant, as we observed with the Δ*parA* FtsK knockdown and Δ*parB* FtsK knockdown strains in *M. smegmatis*; however, the triple mutant (Δ*parA* Δ*parB* Δ*ftsK*) was not analyzed in *S. coelicolor*. The phenotypic consequences of the same mutations could also be very different in *S. coelicolor* compared to *M. smegmatis*, as the division process is completely different in *S. coelicolor*, which grows as unseptated hyphae up to 50 μm long that contain dozens of copies of the genome. When *S. coelicolor* enters into the sporulation pathway, septa form synchronously over unsegregated copies of the chromosomes, which are thought to be segregated by the Par and FtsK proteins into the forming spores, one chromosome per spore (Dedrick et al. 2009).

In the case of FtsK knockdown in *M. smegmatis*, which appears to completely suppress formation of anucleate cells in the Δ*parA* or Δ*parB* background, what then drives chromosome segregation if neither FtsK nor the ParA/ParB proteins are present?

5.7   Characterization of FtsK-GFP ParB-mCherry cells

5.7.1   The early movement of ParB-mCherry foci in Δ*parA* or wild-type strains determines the future daughters' ploidy

ParB position was suggested to have an impact in *B. subtilis* forespore formation on the direction of the FtsK orienting polar sequences (KOPS), thereby allowing unidirectional permissive pulling of the DNA by FtsK (Becker & Pogliano 2007). Moreover, the ParB

positions in wild-type as well as in Δ*parA* cells have a defined movement during cell cycle progression in *M. smegmatis* (Ginda et al. 2017).

I used ParB-mCherry Wag31-GFP and Δ*parA* ParB-mCherry Wag31-GFP strains, imaged by time-lapse microscopy, to study the movement of the origin of replication (indicated by ParB-mCherry foci) over the cell cycle (Figure 58A). For simplification, the replicated ParB-mCherry foci appearing just before division are not represented in Figure 58C-F, but can be observed in the last panel in the lower cell in Figure 58A. When the two ParB-mCherry foci stay close to the old cell pole the resulting division will give an anucleate new-pole daughter cell; but if one of the ParB-mCherry foci travels towards the new cell pole early in the cell cycle, the resulting division will give two nucleated cells (Figure 58B). The importance of the ParB movement had already been reported in the anucleate cell formation, however there is no mention of anucleate old pole daughter or its relative ParB movement (Ginda et al. 2017). In Δ*parA* cells I distinguish three distinct cases. If both ParB-mCherry foci stay close to the old pole, the division will result in an anucleate new-pole daughter cell (Figure 58C). If both ParB-mCherry foci travel towards the new pole, the division will result in an anucleate old-pole daughter cell (Figure 58D). If only one of the two ParB-mCherry foci travel towards the new pole, the division will result in two nucleated daughter cells (Figure 58E). In wild-type cells, both ParB-mCherry foci seem more closely positioned towards midcell compared to Δ*parA* cells and only one of the two ParB-mCherry foci travels towards the new pole (Figure 58F).

We conclude that the lack of parB-mCherry movement towards the new cell pole at the beginning of the cell cycle correlates with the birth of an anucleate new-pole daughter cell. Conversely, if both parB-mChery foci travel towards the new pole, this will result in generation of an anucleate old-pole daughter cell.
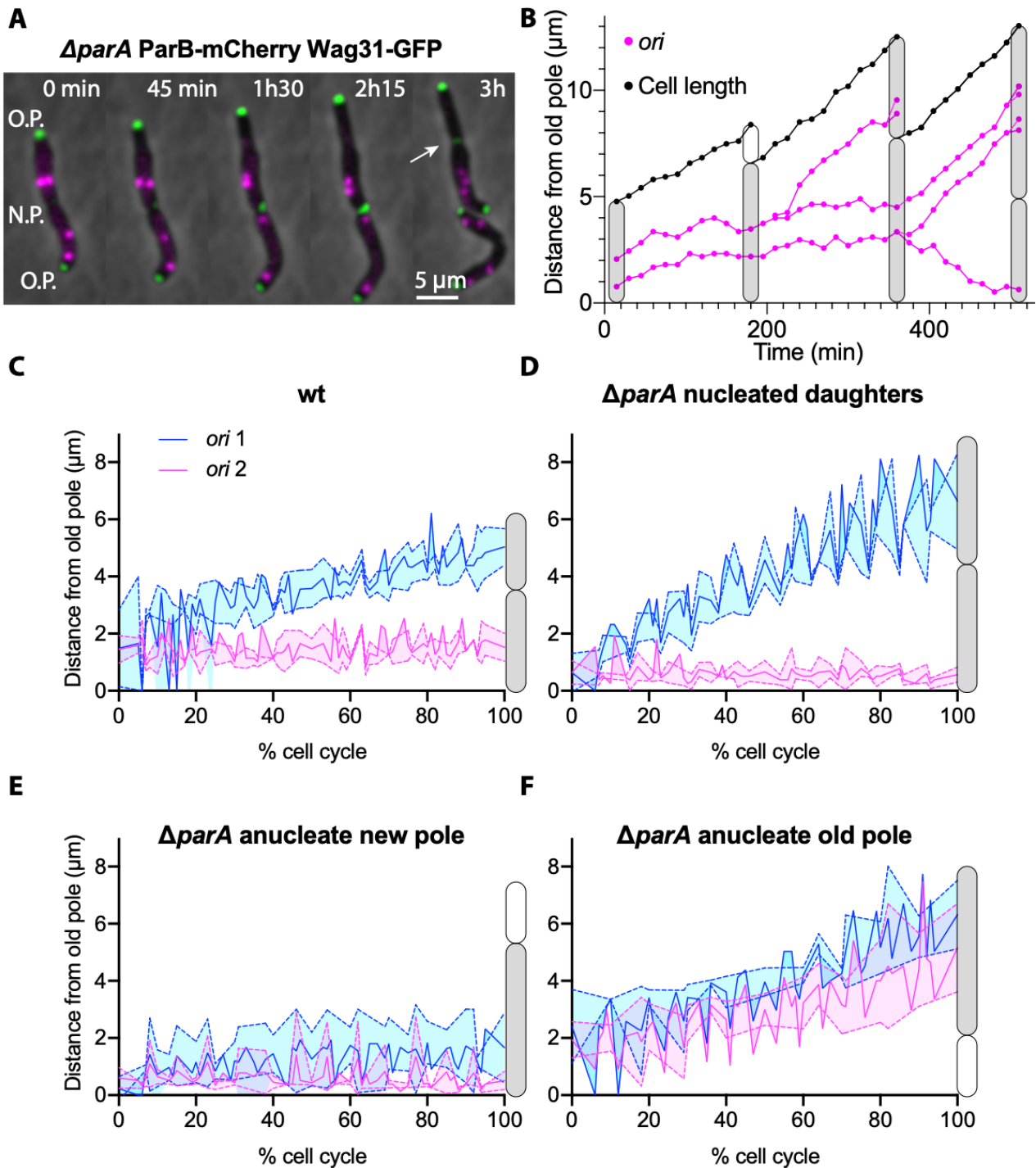
Figure 58. ParB-mCherry movement in wild-type and Δ*parA* cells determines the daughter cells' ploidy

M. smegmatis Δ*parA* **(A,B,D,E,F)** or wild-type **(C)** cells expressing ParB-mCherry and Wag31-GFP were cultured in a microfluidic device and imaged by time-lapse microscopy at 15-minute intervals. **(A)** Δ*parA* ParB-mCherry Wag31-GFP time-lapse representing formation of an anucleate cell (indicated by the white arrow) as well as two nucleated cells. The old poles (O.P.) and new poles (N.P.) are indicated. **(B)** Representation of

the ParB-mCherry positions in Δ*parA* cells during three successive divisions. The first division results in generation of one nucleated old-pole daughter and one anucleate new-pole daughter. **(C)** Average positions of ParB-mCherry foci over the percentage of the cell cycle in wild-type mother cells that divide to give two nucleated daughters (n = 10 cells). **(D)** Average positions of ParB-mCherry foci in Δ*parA* mother cells that divide to give two nucleated daughters (n = 10 cells). **(E)** Average positions of ParB-mCherry foci in Δ*parA* mother cells that divide to give one nucleated old-pole daughter and one anucleate new-pole daughter (n = 9 cells). **(F)** Average positions of ParB-mCherry foci in Δ*parA* mother cells that divide to give one nucleated new-pole daughter and one anucleate old-pole daughter (n = 6 cells). **(C-E)** Lines indicate average ParB-mCherry positions; shading indicates standard deviations.

5.8 The orientation of the chromosomes determines the directionality of FtsK movement

As observed in the previous chapter, the position of the origin determines the future cell's ploidy. I investigated if the orientation of the chromosome was altered in Δ*parB* cells. I was not able to tag the terminus (See **Chapter 10.7**). However, the attB site which is 245° from *ori* was tagged by Isabella Santi a former postdoc in the lab, using the FROS system in both wt and Δ*parB* cells. In wt cells, attB is skewed towards the new pole (Santi & McKinney 2015, Figure 59A). I then analyzed attB-GFP Δ*parB* cells. In Δ*parB* cells which would give birth to two nucleated daughters, the attB site is also skewed towards the new pole. On the contrary, in Δ*parB* cells which gives birth to either an anucleate old pole or new pole, attB is skewed towards the old pole (Figure 59B).
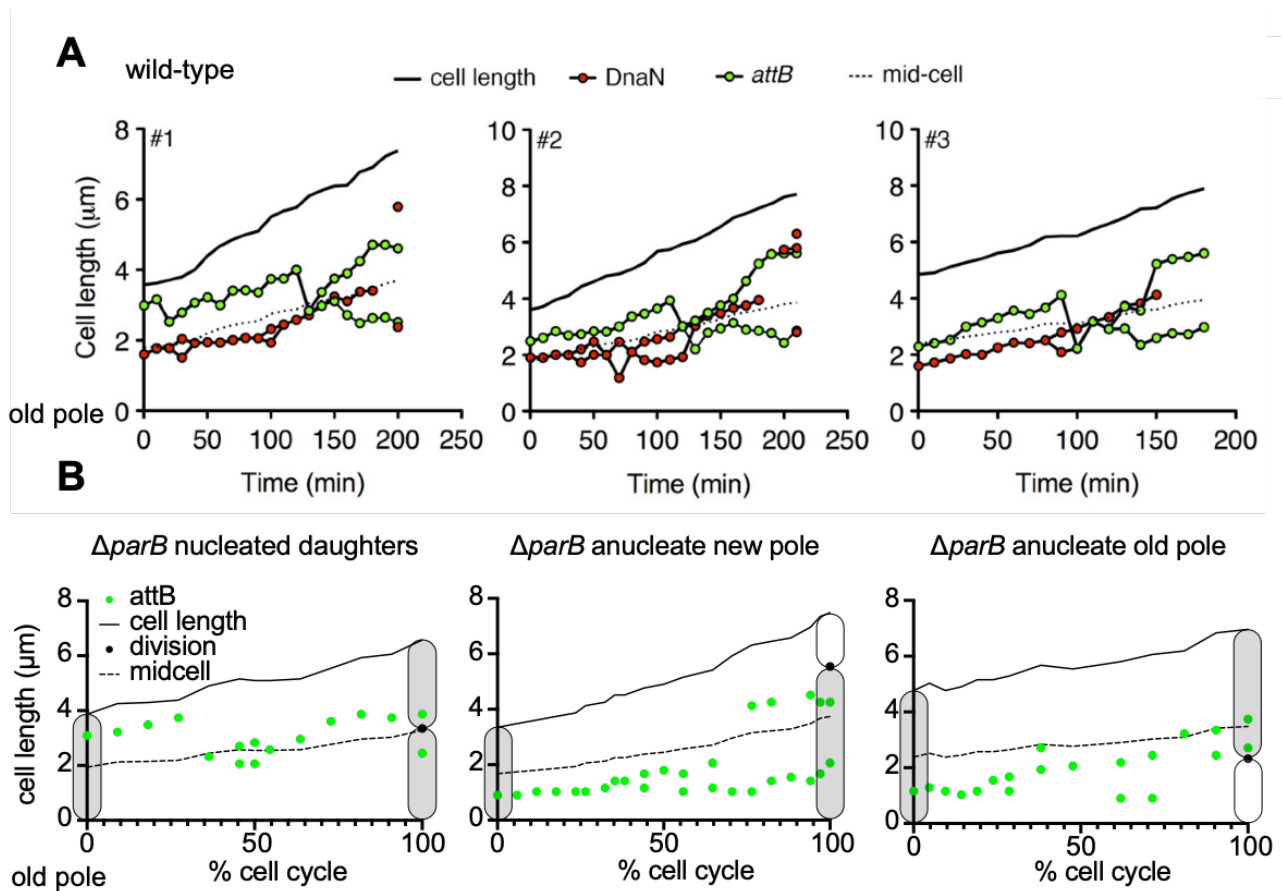
Figure 59 attB localization in wt and Δ*parB* cells

M. smegmatis wild-type **(A)** or Δ*parB* **(B)** cells expressing attB-GFP were cultured in a microfluidic device and imaged by time-lapse microscopy at 10-minute intervals. **(A)** The positions of attB-GFP in three representative wild type cells are represented (Adapted from Santi & McKinney 2015). **(B)** The positions of attB-GFP in three representative Δ*parB* cells are represented. The first cell gives birth to two nucleated cells. The second cell gives birth to an anucleate new pole. The third cell gives birth to an anucleate old pole.

Taking these results combined with the position of *ori* in the Δ*parA* cells, it suggests that the orientation of the chromome in wt cells is such that the origins of replication are localized near the outer poles and the terminus are localized near the newly formed pole (Figure 60A). Whereas in Δ*parA* cells the orientation of the chromomes can either be the same as wt cells (Figure 60Bi), or with both *ori* skewed towards the new pole and the two *ter* skewed towards the old pole. This orientation will then result in an anucleate old pole daughter cell formation (Figure 60Bii). The third possibility is to have both *ori* skewed to-

wards the old pole and the two *ter* skewed towards the old pole. This orientation will result in an anucleate new pole (Figure 60Biii).
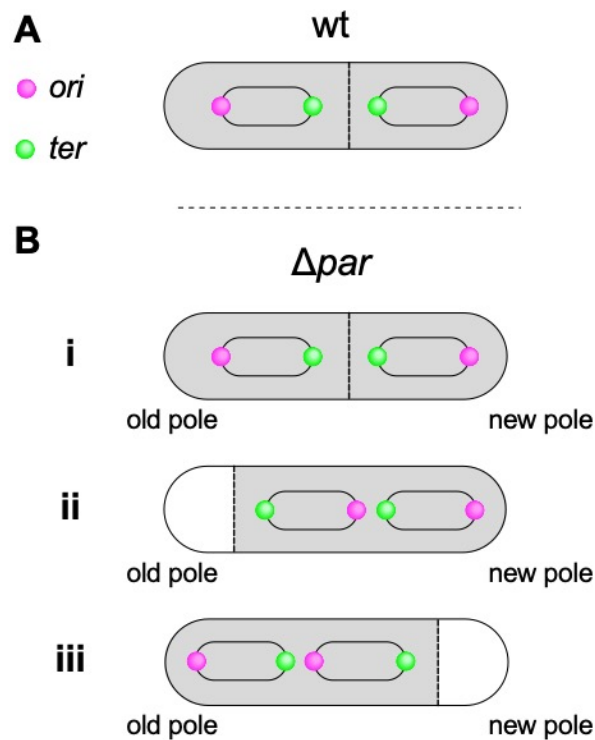
Figure 60 Schematic orientation of the chromosomes in wt and the Δ*par* cells

 (A) Wt cells have the *ori* oriented towards both outer poles and the *ter* oriented towards the newly formed pole. **(B)** Δ*par* cells can either **(i)** give two nucleated daughter cells and have the same chromosome orientation as wt cells. **(ii)** have both *ori* skewed towards the new pole and the two *ter* skewed towards the old pole. This orientation will result in an anucleate old pole (white space). **(iii)** have both *ori* skewed towards the old pole and the two *ter* skewed towards the old pole. This orientation will result in an anucleate new pole (white space).

5.9 Positioning and movement of ParB-mCherry foci in FtsK knock-down cells

As the position of the chromosomal origin of replication (*ori*), visualized microscopically as ParB-mCherry foci, seemed crucial for the daughter cells' ploidy, I investigated if the *ori* position was mislocalized in FtsK knockdown cells using the FtsK knockdown strain expressing ParB-mCherry. As found earlier (see above), when FtsK expression was knocked down the majority of cells still grew and divided normally; therefore, the examples of abnormal cell behavior shown in Figure 55A are comparatively rare. Nonetheless, it was interesting to follow the movement of ParB-mCherry foci in the FtsK knockdown *parB-mcherry* strain, as I observed that the number of ParB-mCherry foci was altered by FtsK knockdown. In cases where a ParB-mCherry focus is duplicated in an FtsK knockdown cell and neither of the chromosomes migrates towards the new cell pole, both of the daughter cells die (Figure 61A). This observation was seen twice. This situation differs from anucleate cell formation in Δ*parA* ParB-mCherry cells (Figure 61E) because only one of the two daughter cells (the anucleate daughter) dies in the absence of ParA. When FtsK expression is knocked down in FtsK knockdown *parB-mcherry* cells, some cells fail to divide but continue to elongate and to replicate their DNA, resulting in cells with multiple ParB-mCherry foci (Figure 55B), and some of these cells die (Figure 61B), even though only one extra ParB-mCherry focus is present. In FtsK knockdown cells, where ParB-mCherry replication and segregation appear to proceed normally, both of the resulting daughter cells survive (Figure 61C,D). However, interdivision time for some cells appears longer (Figure 61D). This particular cell was born large (5 µm) but it will take more than 260 minutes (4h20 minutes) to divide.
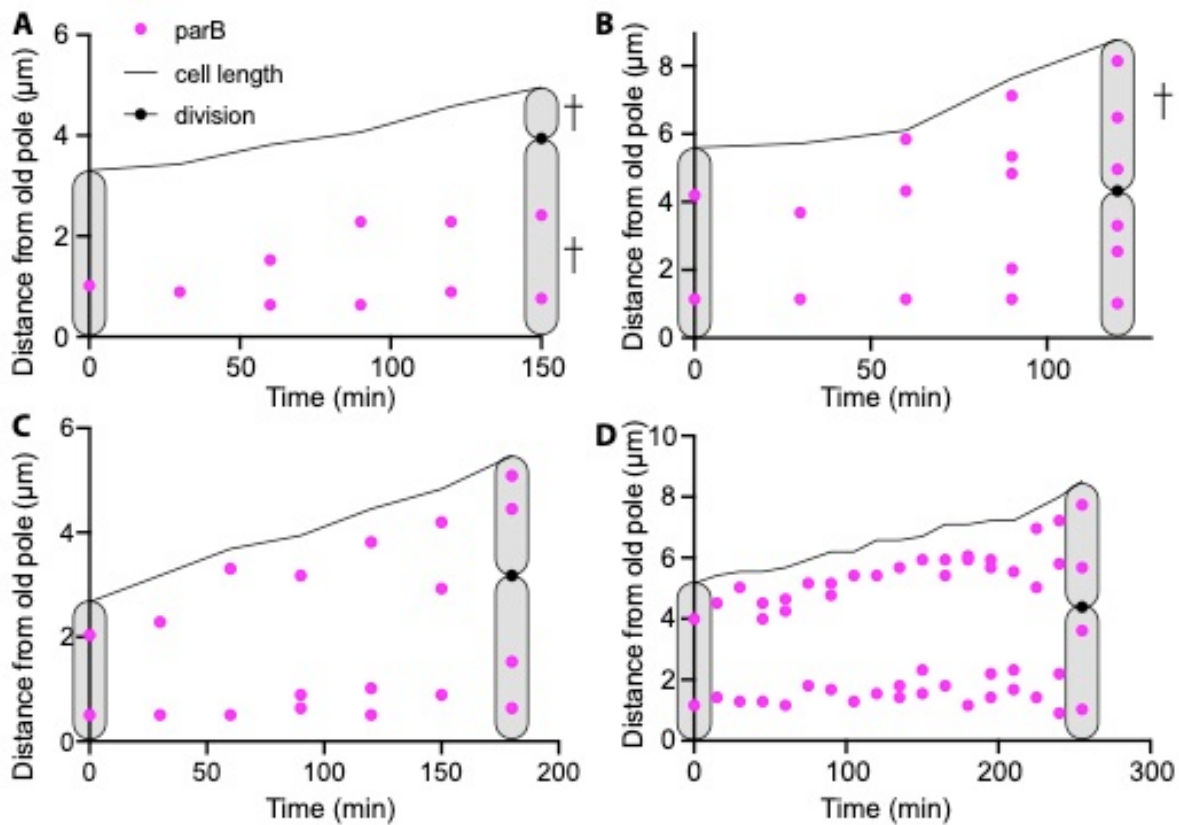
Figure 61. Mislocalized or extra ParB-mCherry foci are associated with cell death in FtsK knockdown cells

(A-C) *M. smegmatis* FtsK knockdown *parB-mcherry* cells were imaged by time-lapse microscopy in a micro-fluidic device at 15-minute intervals. The positions of ParB-mCherry foci relative to the old cell pole are represented. Cell death is indicated by the crosses in A and B.

5.9.1 Analysis of FtsK-GFP and ParB-mCherry (co)localization

When observing FtsK-GFP-expressing cells, I noticed some secondary smaller and less bright foci, which did not localize at the septum position. FtsK is thought to actively segregate sister chromosomes in *E. coli* (Stouf et al. 2013). Therefore, I constructed an FtsK-GFP ParB-mCherry dual reporter strain. I used a suicide vector containing *parB-mcherry* and used a two-step recombination method (Figure 34) to replace *parB* with *parB-*

mcherry at the *parB* chromosomal locus in the FtsK-GFP strain. I then imaged this strain by time-lapse microscopy (Figure 62A) and I analyzed the positions of ParB-mCherry and FtsK-GFP by plotting them as a heat map representation (Figure 62B and C). ParB-mCherry foci are present during the whole cell cycle and are duplicated shortly before or after division. FtsK-GFP localizes as a ring-like structure at the nascent division septum but some secondary weaker foci can also be seen. Interestingly, these secondary foci of FtsK-GFP often seem to localize in the vicinity of replicating ParB-mCherry foci.

We conclude that secondary (non-septal) foci of FtsK-GFP may colocalize with ParB-mCherry foci.
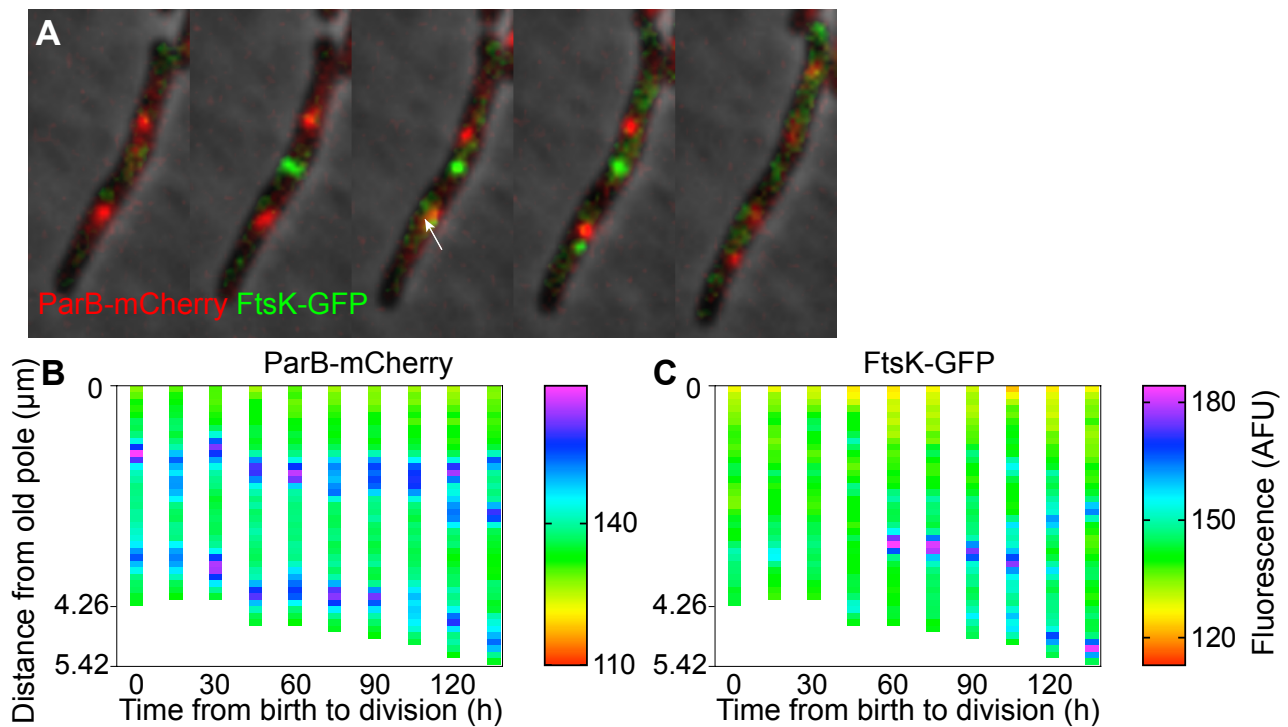
Figure 62. Time-lapse microscopy of a dual reporter strain expressing FtsK-GFP and ParB-mCherry

(A) *M. smegmatis* ParB-mCherry FtsK-GFP dual reporter cells were cultured in a microfluidic device and imaged by time-lapse microscopy at 15-minute intervals. The white arrow indicates FtsK-GFP and ParB-mCherry colocalization. **(B, C)** Heat maps of ParB-mCherry (B) and FtsK-GFP (C) fluorescence intensity relative to the old cell pole from birth to division.

5.9.2 Identification of proteins that physically interact with HA-tagged FtsK by co-immunoprecipitation

Evidence provided above suggests that knockdown of FtsK expression can suppress the anucleate minicell phenotype caused by Δ*parA* or Δ*parB* gene knockouts, and non-septal foci of FtsK-GFP might colocalize with ParB-mCherry foci. These results suggested the possibility of a physical interaction between FtsK and ParB and/or ParA. The aim in the experiment is to verify the possible interaction between FtsK and ParB and/or ParA. Therefore, I prepared whole-cell extracts from cells expressing HA-tagged FtsK and immunoprecipitated FtsK-HA using anti-HA agarose beads. Whole-cell extracts were also prepared from wild-type cells expressing untagged FtsK to serve as a negative control. Immunoprecipitation (IP) was performed in parallel on both cell extracts using anti-HA antibody. This step should enrich proteins that interact with FtsK in the FtsK-HA extract, while identifying proteins that are immunoprecipitated non-specifically in the wild-type extract. The immunoprecipitated proteins were separated by SDS polyacrylamide gel electrophoresis (SDS-PAGE), the gel was silver-stained, and mass spectrometry was used to identify the proteins present in three different selected regions of the gel (Figure 63A). As expected, the anti-HA IP of the FtsK-HA cell extract is indeed enriched in FtsK, whereas the anti-HA IP of the wild-type cell extract is not (Figure 63B). Other proteins, such as a putative membrane protein (Figure 63C), DNA polymerase I (Figure 63D), and DNA topoisomerase I (Figure 63E), are also more abundant in the IP of extracts from FtsK-HA cells compared to the IP of extracts from wild-type cells. Interestingly, it has been reported previously that the complete FtsK-dependent Xer recombination reaction at the *dif* site proceeds efficiently only in the presence of DNA topoisomerase I (Aussel et al. 2002).

We conclude that these preliminary results do not support any strong physical interaction between FtsK and ParA or ParB. However, some proteins seem to interact specif-

ically with FtsK as revealed by their co-immunoprecipitation with HA-tagged FtsK. These interacting proteins include a putative membrane protein, DNA polymerase I, and DNA topoisomerase I. As FtsK is known to have a transmembrane domain, it is likely that it could interact with membrane proteins and it has been shown that FtsK-dependent Xer recombination reaction at the *dif* site proceeds efficiently only in the presence of DNA topoisomerase I. Although HA is a small tag, it might prevent interactions between the C-terminal side of FtsK and other proteins. The identified proteins could be confirmed using appropriate negative controls such another protein with an HA tag.
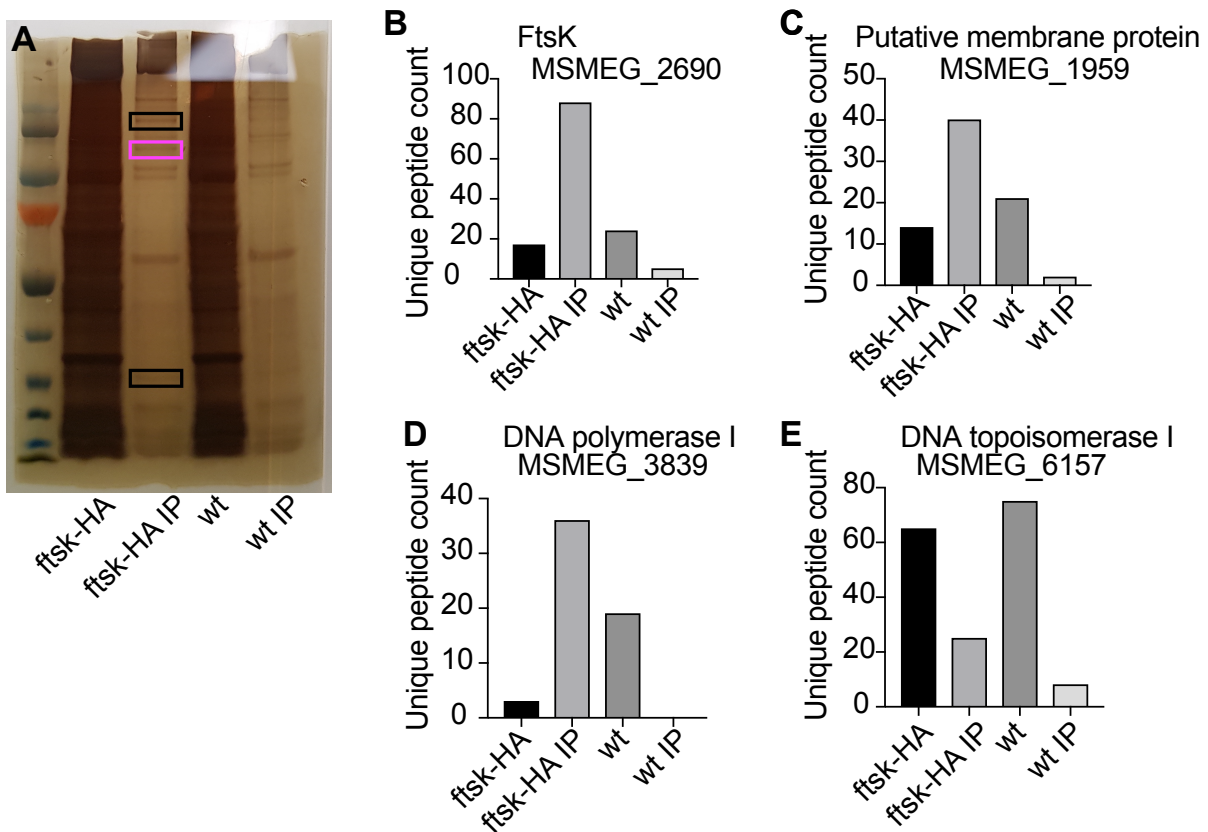
Figure 63. *M. smegmatis* FtsK-HA immunoprecipitates contain a putative membrane protein, DNA polymerase I, and DNA topoisomerase I

(A) Silver staining of a SDS-PAGE gel. Unfractionated whole-cell extracts from FtsK-HA and wild-type cells were loaded in lanes 2 and 4, respectively. An additional IP step was performed using anti-HA agarose beads to IP whole-cell extracts from FtsK-HA and wild-type cells, and the IPs were loaded in columns 3 and

5, respectively. A molecular size marker cocktail was loaded in lane 1. The magenta square indicates the position of FtsK. The three rectangular squares indicate the portions of the gel analyzed by mass spectrometry. **(B-E)** Proteins identified by mass spectrometry as being more abundant in anti-HA IPs of whole cell extracts from FtsK-HA cells compared to wild-type cells.

5.9.3   ParA and ParB proteins are not enriched by FtsK immunoprecipitation

As the aim was to verify the possible interaction between FtsK and ParB and/or ParA and that in the previous chapter, only some selected bands were cut and analyzed by mass spectrometry, I repeated the co-immunoprecipitation experiment with the whole portion of the gel. Indeed, the ParA and/or ParB proteins might not be located in these selected bands. Therefore, the FtsK-HA immunoprecipitated proteins were separated by SDS polyacrylamide gel electrophoresis (SDS-PAGE), stained with Coomassie blue and were analyzed by mass spectrometry without selecting particular regions.

As expected, FtsK is enriched in anti-HA IPs of whole-cell extracts from FtsK-HA cells compared to wild-type cells (Figure 64A). However, ParA (Figure 64B) and ParB (Figure 64C) are equally abundant in anti-HA IPs from FtsK-HA and wild-type cells. Thus, if ParA and/or ParB do interact with FtsK inside living cells, this interaction is apparently too weak to withstand the relatively harsh conditions used for preparing and immunoprecipitating the whole-cell extracts. Other approaches could be taken such as a bacterial two-hybrid experiment, a label transfer protein interaction analysis or a Far–western blot analysis to check the interaction between FtsK and ParA and/or ParB.

We conclude that, despite the evidence for a genetic interaction between *ftsK* and *parA* and *ftsK* and *parB* (i.e., FtsK knockdown suppresses the anucleate minicell phenotype of Δ*parA* and Δ*parB* mutants, as shown in a previous section of this thesis), these results

do not support any physical interaction between FtsK and ParA or ParB that is sufficiently strong to survive the conditions used in co-immunoprecipitation experiments.
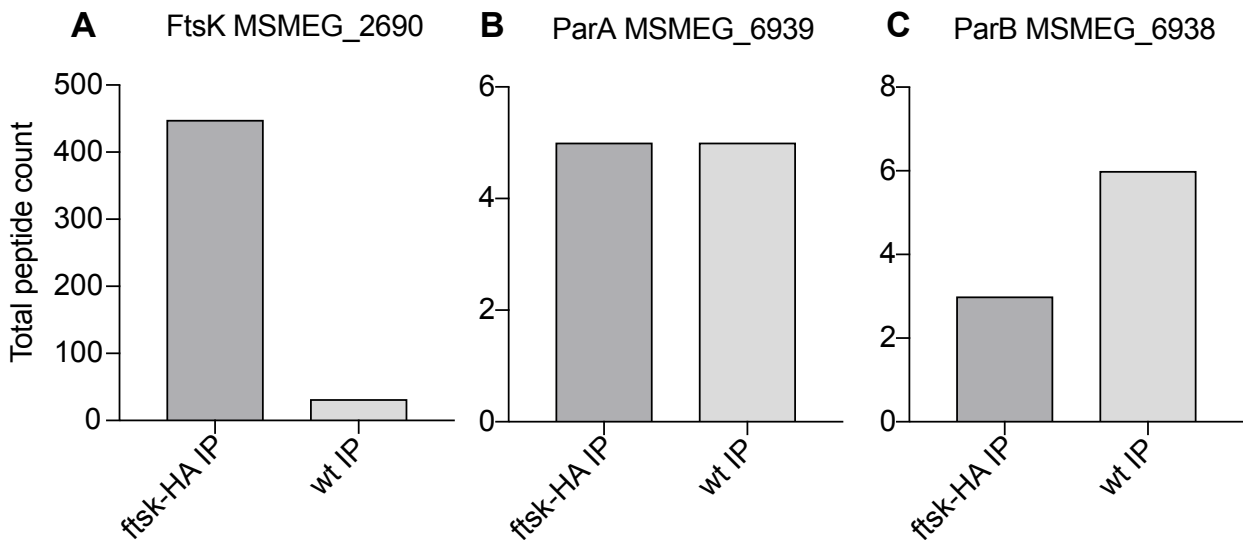
Figure 64. Mass spectrometry analysis of anti-HA immunoprecipitates of whole-cell extracts

Anti-HA immunoprecipitates of whole-cell extracts prepared from FtsK-HA or wild-type cells were run by SDS-PAGE gel, stained by Coomassie blue and analyzed by mass spectrometry. The total peptide count is plotted for **(A)** FtsK, **(B)** ParA, **(C)** ParB.

5.10 Conclusions

Preliminary evidence suggests that FtsK-GFP may adopt a ring-like structure similar to FtsZ. FtsK-GFP localizes at the nascent division septum before the cytokinesis marker Wag31-mCherry and before closure of the septal membrane. The strain Δ*parB* FtsK-GFP has an FtsK localization defect that could not be complemented by restoration of *parB*, as well as a minicell phenotype that could only be complemented by restoring *parB* at its na-

tive chromosomal locus. Levels of FtsK-GFP fluctuated during the cell cycle in wild-type cells but not in Δ*parB* cells. However, the amount of FtsK-HA protein in wild-type, Δ*parA,* and Δ*parB* cells appeared to be equivalent when measured using an anti-HA western blot. Previously published results from genome-level transposon mutagenesis studies predicted that *ftsK* is an essential gene in *M. tuberculosis*. Here, I provide the first direct evidence that *ftsK* is also essential in *M. smegmatis*. As the *ftsK* gene could not be deleted, I adapted a previously published (Kim et al. 2013) dual repression system to study the consequences of knocking down FtsK expression. Most of the FtsK knockdown cells had an apparently normal phenotype. However, a minority of cells were swollen, elongated, and branched, had multiple origins of replication and multiple membranes, and eventually lysed. This mild phenotype was unexpected as the *ftsK* gene is essential. Therefore, knocking down ftsK was expected to be lethal. This mild phenotype could be due to the leakiness of the re-pression system and the quantity of FtsK required to function, which might be low.

Even more suprising, knocking down FtsK expression in Δ*parA or* Δ*parB* cells was a synthetic rescue, completely suppressing their anucleate phenotype.

Normal localization of ParB bound to *parS* sequences (and, closely linked in the chromosome, the origin of replication) is important for maintenance of normal ploidy dur-ing successive division events. In wild-type cells, once ParB is replicated, one of the ParB foci moves towards the new cell pole. This movement of ParB towards the new pole does not occur in Δ*parA* cell divisions that give rise to one anucleate daughter cell and one nu-cleated daughter cell. In such cases, both ParB foci travel towards the same cell pole: to-wards the old cell pole in divisions that give an anucleate new-pole daughter, or towards the new cell pole in divisions that give an anucleate old-pole daughter. In FtsK knockdown cells, this ParB movement also seemed perturbed in the minority of cells that display ab-normal phenotypes. In Δ*parA* and Δ*parB* cells*,* Hlp-Dendra2 (which marks the chromo-someal DNA) is present throughout the cell during most of the cell cycle, but a sudden movement of DNA is observed slightly before division in divisions that give on anucleate

daughter and one nucleated daughter. However, based on the position of the two ParB-mCherry foci near the beginning of the cell cycle, it is possible to predict whether the ensuing division event will give birth to an anucleate daughter cell. The whole genome might be disorganized in Δ*par* cells as suggested by super-resolution imaging as well as some of the widefield fluorescence time-lapse results. Furthermore, the localization of the terminus is also misplaced in Δ*par* cells. In WT cells, the terminus, approximated by the attB-GFP marker is skewed towards the new pole whereas in Δ*par* cells, ter is skewed towards the old pole, reversing the orientation of the chromosomes. Therefore, I predict that *par* is responsible for chromosome orientation defect and not a segregation defect and that FtsK is responsible for chromosome segregation, actively creating anucleate cells when the chrosomsome is misoriented

Chapter 6 Discussion and conclusion

Tuberculosis is still among the major threats worldwide, being among the world's top 10 causes of death and the deadliest among infectious diseases. Therefore, a better understanding of the growth, division, and cell cycle mechanisms of the causative agent, *Mycobacterium tuberculosis*, is crucial in order to find potential new targets for drugs. Indeed, the last first-line anti-tuberculosis drug was discovered in the 1960s and emergence and spread of resistance to antibiotics adds pressure for new drug discoveries.

The cell cycle in mycobacteria is still not well understood, especially compared to well-studied model organisms such as *E. coli* or *B. subtilis*. The dynamics of chromosome replication and segregation and the role of chromosomes in controlling the timing and location of cell division have especially not been fully investigated in mycobacteria. DNA can be visualized using various dyes, but these tend to be toxic and to impair cell growth. Therefore, studies of DNA dynamics using DNA dyes might not provide an accurate picture of time-dependent processes in the cell division cycle. In this thesis, I constructed a genetically encoded Hlp-Dendra2 marker and confirmed its reliability for DNA localization and its suitability for long-term time-lapse microscopy. Hlp-Dendra2, therefore, DNA movements could be investigated during cell division especially in Δ*par* mutants. During most of the cell cycle Hlp-Dendra2 was organized in a "beads-on-a-string" structure that was stably distributed along the cell's long axis and only moved in a rapid movement slightly before division.

In light of our new results (FtsK timing compared to Hlp-Dendra2 dynamics or ParB and relocalization of Wag31-Dendra2), combined with results published by other groups, I propose the following sequence of events for division in mycobacteria (Figure 65). Wag31 interacts with ParA (Pióro et al. 2019). At birth, ParA is localized as a gradient with the highest concentration at the new pole (Pióro et al. 2019; Uhía et al. 2018). ParA relocalizes at the forming septum, the larger cell containing more ParA (Pióro et al. 2019; Uhía et al. 2018). As shown in **Chapter 10.3**, Wag31 relocalizes from the old pole to the new pole

(Hannebelle et al. in review/2019). As both Wag31 and ParA migrate to the forming septum and ParA is an ATPase motor protein, it is likely that Wag31 relocalization could be driven by the ParA gradient relocalization and not the opposite. After replication, one of the ParB foci moves towards the new pole driven by this same ParA gradient. As shown in **Chapter 5.7.1**, the relocalization of one of the ParB foci towards the new pole determines the cell's ploidy. In *C. crescentus* this relocalization has been shown to be a two-step relocalization, in which a slow GapR-mediated segregation of the ParB foci is followed by a ParA-dependent, non-selective rapid movement of ParB towards the new pole (Taylor et al. 2017). FtsK segregates the chromosomal terminus in *E. coli* by interacting with the XerCD recombinase (Fournes et al. 2016). As shown in **Chapter 5.9.1**, some secondary FtsK foci seem to colocalize with ParB, so FtsK could segregate not only the terminus but also *ori.* These secondary FtsK foci could act similarly to GapR and the secondary movement would be ParA-dependent, as in *C. crescentus*. Once *ori* is duplicated (shown by the ParB fluorescent reporter), these secondary foci disappear.

The FtsZ ring localizes at the nascent division septum, where it constricts as division progresses. FtsZ is required for FtsK localization at the septum (Wu et al. 2018) and the localization of FtsK resembles the FtsZ constriction (Figure 41). As shown in **Chapter 5.3.3** (Figure 43), FtsK might localize at the leading edge of the closing membrane, forming a pore in the septum. When FtsK localizes at the septum, Hlp is still distributed regularly with more or less equidistant Hlp foci. Once FtsK constricts at the middle of the cell, Hlp gets separated in two distinct groups (**Chapter 5.3.2**), suggesting the FtsK could form a channel through the closing septum and translocate DNA which is not yet segregated. FtsK might as well have another role as some secondary FtsK foci seem to colocalize with ParB. These two proteins might interact, although no strong interactions where detected by the immunoprecipitation experiment and no interaction between *par* and *ftsk* genes are highlighted in the literature with the exception of *Streptomyces coelicolor*, where a genetic interaction of triple Δ*smc*, Δ*parB*, and Δ*ftsK* deletion results in an increased percentage of minicells formation (Dedrick et al. 2009).
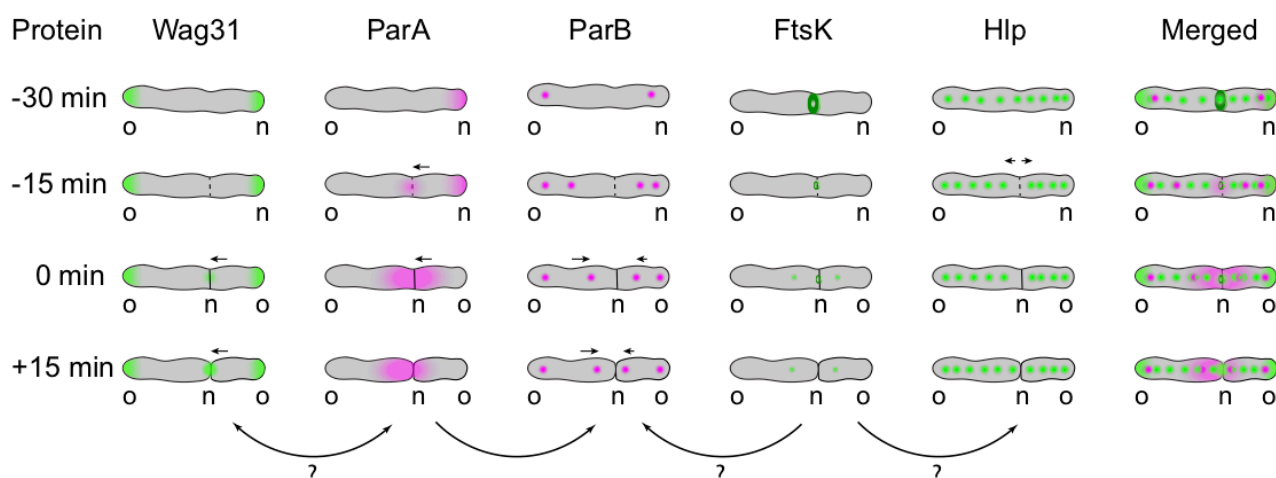
Figure 65 Schematic representation and summary of major key players in mycobacterial division.

0 minutes indicates the time of cell division. The timing of an event in each cell might be slightly different, but the major trends are represented in this Figure. ParA localization is represented according to Pióro et al. 2019 and Uhía et al. 2018. All of the other proteins have been imaged by time-lapse microscopy for this thesis. o = old pole. n = new pole.

The *par* genes are currently thought to be the key players for correct segregation of mycobacterial chromosomes. However, I propose an alternative model where the *par* genes are important for chromosome orientation whereas FtsK is important for chromo-some segregation. As shown in **Chapter 5.6.1 and 5.6.2**, the most striking result in my the-sis, is the rescued anucleate phenotype in either the Δ*parA* or Δ*parB* cells when FtsK is knocked down. This FtsK knocked down was done by adapting a dual repression system (Kim et al. 2013). Based on the position of *ori* and *ter* in wt cells as well as in Δ*par* cells, the orientation of the chromosomes can be predicted. What could then drive the movement of the chromosomes? I hypothesize that FtsK is the motor protein which will actively seg-regate the chromosomes. The translocation directionality of FtsK is dictated by specific DNA sequences (GGGNAGGG), the FtsK orienting polar sequences (KOPS), which are per-missive only in the *ori* to *dif* direction (Ptacin et al. 2008). If these sequences are not in the right orientation, therefore in a non-permissive orientation, translocation by FtsK stops

(Becker & Pogliano 2007, Ptacin et al. 2008). As hypothethized in *B. subtilis*, the localization of *ori* and therefore the orientation of the KOPS sequences, are determinant for the DNA movement directionality (Becker & Pogliano 2007). If *ori* is mislocalized compared to FtsK's position, the remaining part of the chromosome cannot be pulled towards *ori*. In Δ*parA* cells I have shown in **Chapter 5.7.1** (Figure 58), that *ori* localization determines if the cell will divide giving birth to an anucleate new-pole daughter, an anucleate old-pole daughter, or two nucleated daughters. Moreover I showed that not only the position of *ori* was perturbed but the localization of *ter* was also displaced from skewed towards the new pole cell in wt cells or in Δ*parB* cells which will give birth to two nucleated cells, to *ter* being skewed towards the old pole cell in Δ*parB* cells which will give birth to an anucleate daughter cell. These findings suggest that the orientation of the chromosome is sometimes inverted in Δ*par* background strains (Figure 60 and 66). Therefore, I propose a model where the *par* genes are responsible for the correct chromosome orientation and FtsK is responsible for the chromosome segregation (Figure 66). When FtsK is present (Figure 66A), FtsK segregate the chromosome in the *ori* to *ter* direction. As chromosomes are sometimes misoriented in Δ*par* cells, FtsK actively creates an anucleate old pole or new pole daughter cell. However, when FtsK is knocked down (Figure 66B), this active movement does not happen.
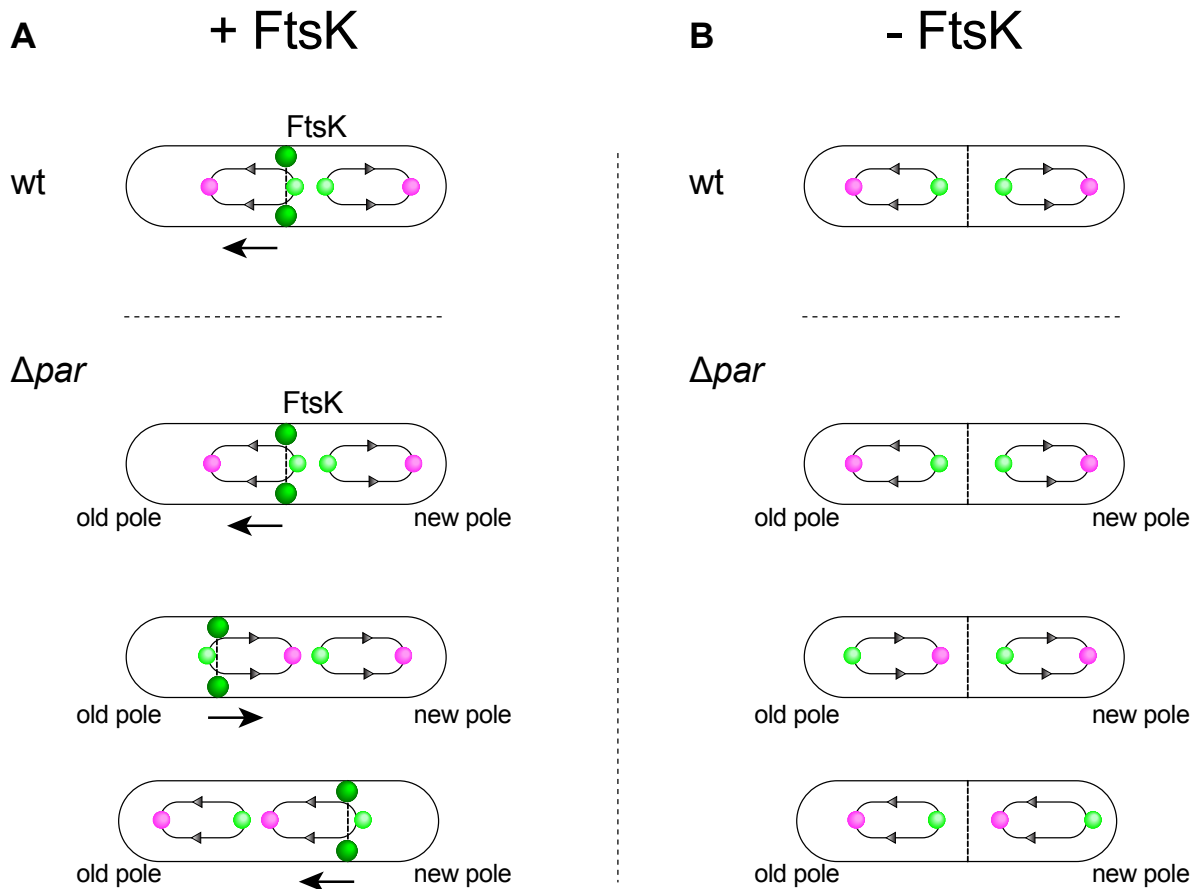
Figure 66 Proposed model: *par* **genes responsible for correct chromosome orientation, FtsK for chromo-some segregation**

 (A) When FtsK is present, FtsK actively segregates the chromosomes in the *ter* to *ori* direction. In Δ*par* cells the orientation of the chromosomes is altered resulting in the active formation of either an anucleate old pole or an anucleate new pole. **(B)** When FtsK is absent, the active movement does not happen and chromosomes could be segregated due to entropy. The orientation of the chromomomes in Δ*par* cells being misoriented.

Another interesting player in the orientation of the chromosome is *smc*. SMC in *M. smegmatis* was suggested to have overlapping roles with ParB (Santi et al. 2015). Deleting *smc* in *M. smegmatis* resulted in a small proportion of anucleate cells (0.3%) as well as cells containing elongated nucleoids and a broader distribution of the septum position. These

observations suggest that SMC may play a role in chromosome compaction, which may in turn affect the positioning of the division septum (Santi et al. 2015). The distribution of the *attB*-GFP chromosomal locus, which is a reporter to approximate the position of the terminus of replication, is similar in Δ*parB* and Δ*smc* cells. In wild-type cells, during replication the distribution of the majority of the chromosome (94%) is symmetrical relative to the septum with the overall organization DnaN - *attB*-GFP - septum - *attB*-GFP – DnaN, but in about 36% of Δ*parB* cells and 31% of Δ*smc* cells the chromosomes are misorientated such that the organization is DnaN - *attB*-GFP - septum - DnaN - *attB*-GFP (Santi et al. 2015). SMC in *B. subtilis* is important for the localization or segregation of *ori*, which is not the case in *M. smegmatis* (Santi et al. 2015). SMC and ParB do not colocalize in *M. smegmatis* but are in close proximity and SMC requires ParB to localize as foci (Santi et al. 2015). So, although the relation between ParB and SMC is not clear, the absence of SMC can lead to misoriented chromosomes. However, the position of *ori*, which dictates the orientation of FtsK movement, does not seem to be affected in Δ*smc* cells. This could explain the low percentage of anucleate cells in Δ*smc* cells even though the chromosome is disorganized (less compacted and, in some cells, misoriented).

In FtsK knockdown cells lacking either ParA or ParB, chromosome segregation seems to proceed efficiently, as formation of anucleate cells was not detected. In the absence of both systems (Par and FtsK), what mechanism could account for chromosome segregation? It has been suggested that entropy-driven disentangling could be the driver for self-segregation of chromosomes in the absence of specific "molecular mechanisms" for chromosome segregation (Jun & Wright 2010).
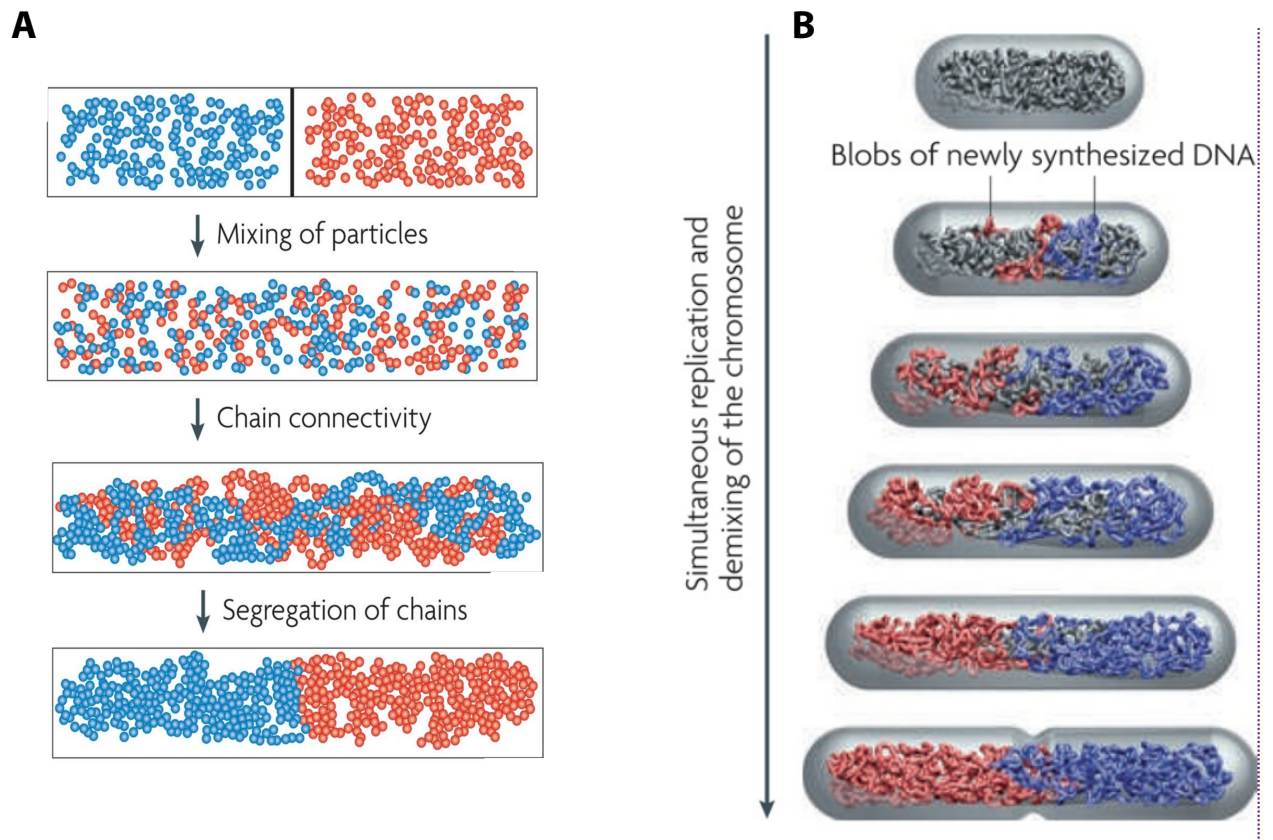
Figure 67 Schematic mixing of unlinked particles versus entropy-driven segregation of chains of linked particles

(A) Schematic representation of particles mixing compared to segregation of chains. **(B)** Segregation of synthesized DNA. (Both panels adapted from Jun & Wright 2010).

When two sets of particles are placed together in a closed volume, they will mix over time (Figure 75). However, in a confined volume, if these particles are connected to one another to form linear polymers (such as chromosomes), they will self-segregate in a manner driven by simple entropy. Segregation occurs because the degrees of liberty increase when the two polymers are disentangled (Jun & Wright 2010). This model may account for our observation that chromosome segregation can apparently proceed efficiently even in the absence of the Par and FtsK systems.

In summary, the findings presented in this thesis provide new insights into the process of chromosome segregation in mycobacteria and suggest a new model in which the Par proteins are responsible for the correct orientation of the chromosomes while the FtsK protein is responsible for the orientation-dependent segregation of chromosomes. Together, these systems contribute to maintenance of the correct ploidy of daughter cells at each division. In the next section, I will explain in my opinion what should be the next immediate key questions to be addressed in order to further test the proposed model.

6.1 **Further perspectives:**

In order to determine the orientation of the chromosome at the single-cell level, it would be important to have both *ori* and *ter* fluorescently labelled in the same strain. Tagging *ter* with the orthogonal ParB/*parS* system from *Lactococcus lactis* (ParB$_{Lla}$/*parS*$_{Lla}$) proved to be unsuccessful because fluorescence of the mKate2-tagged ParB$_{Lla}$ was very bright and diffuse throughout the cytoplasm (see **Chapter 10: Appendix - Tools**). However, it would be worthwhile to repeat this attempt using a weaker promoter to drive expression of the fluorescently tagged ParB$_{Lla}$. Ideally the dual *ori*/*ter* reporter could be combined with a fluorescently tagged Hlp reporter in order to visualize both *ori* and *ter* and the DNA joining them. However, the position of each chromosomal locus might be less clear, as we currently do not know which Hlp "bead" belongs to which chromosome or chromosomal domain. Clearly, further work is needed to determine whether each Hlp "bead" does or does not correspond to a specific chromosomal domain. To test my proposed model, *ter* and *ori* would be fluorescently tagged in a wild-type background as well as Δ*parA* or Δ*parB* background, in both cells expressing normal levels of FtsK and in FtsK knockdown cells. In Δ*parA* FtsK knockdown cells with fluorescently tagged *ori* and *ter* chromosomal loci, I would expect that the majority of cells would have the correct chromosome orientation, but a minority of cells would have a misoriented chromosome, either with both *ori* skewed to-

wards the old pole of both *ori* skewed towards the new pole (Figure 74B). As a first step towards constructing this reporter strain, I have successfully constructed the Δ*parA* Δ*ftsk* prom_*ftsK* ParB-mCherry strain, where *ftsK* is driven by its own promoter at the *attB* site, and I have tried several times without success to replace prom_*ftsK* by the tagged repressible version (*ftsK*-DAS+4) at the *attB* site. As ParB and FtsK might interact, a tagged version of ParB as well as a decreased amount of FtsK might be too much pressure to allow construction of a viable mutant. To further prove that the orientation of the chromosome and, more importantly, that the position of FtsK relative to *ori* and *ter* determines if the cell will divide giving birth to an anucleate daughter cell, I would tag *ter* and *ori* in a Δ*smc* mutant background with or without FtsK knockdown. As *ori* position is not altered in Δ*smc* cells, but *ter* position is, FtsK knockdown in Δ*smc* cells could provide another piece of evidence that FtsK contributes to formation of anucleate cells by actively translocating a chromosome in the wrong direction if and only if the chromosomal *ori* and *ter* regions are mislocalized relative to FtsK.

Moreover, I have shown that *ftsK* is an essential gene. However, as a Δ*parA* FtsK knockdown or a Δ*parB* FtsK knockdown (both having *attB*::*ftsK*-DAS+4) showed a rescued phenotype, would it be possible to replace *attB*::*ftsK*-DAS+4 by a plasmid switch lacking *ftsK*? This would result in a double knockout for *ftsK* and *par.* Should this be the case, I would argue that *ftsK* and *par* genes are not required for chromosome segregation and entropy would be sufficient. However, if the Δ*ftsK* and Δ*par* is not constructible, I would argue that FtsK might have another essential function such as chromosome resolution for instance.

As shown in **Chapter 5.9.2**, the immunoprecipitation results using anti-HA antibody and a strain expressing HA-tagged FtsK indicated that ParA and ParB did not seem to interact strongly with FtsK. However, SDS was added in the protein extraction step, which could denature the proteins and disrupt (weak) protein-protein interactions. I would repeat this experiment, maybe crosslinking the proteins prior to extraction.

I would also construct the repressed FtsK RecA-GFP (Δ*ftsK attB*::*ftsK*-DAS+4 *attT*::*sspB* RecA-GFP) strain. If FtsK expression is knocked down is there a detectable SOS response if chromosomal DNA is not translocated into one of the sister cells and is therefore guillotined by the closing septum?

Another central question that remains is what determines the septum placement? We showed by AFM imaging that the surface of *M. smegmatis* is not flat (shown in **Chapter 4.16** and **Chapter 9**, Eskandarian et al. 2017). It undulates both in wild-type and in Δ*parB* cells, having on average three wave-troughs. As an early event in division site selection, a pre-cleavage furrow appears in the central wave-trough at the future division site at about the same time as the FtsZ ring. But why is the central wave-trough selected? As shown in **Chapter 4.16** the chromosome localization, indicated by Hlp-Dendra2, does not correlate with the AFM height profile. In *B. subtilis*, it has been shown that the deletion of both the Min and Noc proteins, which were thought to determine where FtsZ ring would form, still resulted in formation of FtsZ at midcell (Rodrigues & Harry 2012). Changing the shape of *B. subtilis* cells in complex shapes such as squares, hearts, and stars did not affect the central localization of the FtsZ ring, suggesting that different membrane curvatures did not seem important (Söderström et al. 2018). Therefore, these wave-troughs might not be the reason why FtsZ assembles at this precise locus.

Many questions still remain unanswered but "True science is a known ignorance" (Michel de Montaigne, Les pensées diverses, 1580).

Chapter 7 Material and methods

7.1 Bacterial strains and growth conditions

Mycobacterium smegmatis mc^{2}155 (wild-type) and derivative strains were grown in Middlebrook 7H9 liquid medium (Difco) supplemented with 0.5% albumin, 0.2% glucose, 0.085% NaCl, 0.5% glycerol, and 0.05% Tween-80. Cultures were grown at 37 °C to mid-exponential phase, corresponding to an optical density at 600 nm (OD$_{600}$) of 0.5. Aliquots were stored in 15% glycerol at −80 °C and thawed before use.

7.2 Plasmid construction

Plasmids for reporter strains were constructed using the Gibson assembly NEBuilder HiFi DNA Assembly Master Mix (New England Biolabs) according to the manufacturer's protocol or using the circular polymerase extension cloning (CPEC) method (Quan & Tian 2011). Plasmids were confirmed by restriction digestion and DNA sequencing.

7.3 Competent cell preparation and electrotransformation of *Mycobacterium smegmatis*.

Fresh culture of *Mycobacterium smegmatis* strain mc2155 in 7H9+ADS+Tw (Middlebrook 7H9 base, 0.5% glycerol, 10% Albumin-Dextrose-Saline, 0.05% Tween-80) were grown to mid-log phase (A600 0.5 - 1.0). The cells were centrifuged in a Sorvall RT6000B tabletop centrifuge 3000 g 10 min followed by 3 washes with ice cold 10% glycerol with each time a reduced volume. The cells were resuspended in aliquots of 400 µl with 10% glycerol and ≈ 1 µg transforming DNA in a prechilled Gene-Pulser electroporation cuvette with 0.2 cm electrode gap (BioRad, cat #165-2086) and store on ice. The Gene-Pulser apparatus (BioRad, cat #1652076) set at 2.5 kV, resistance 1000 Ohms, capacitance 25 µFD. After addition of 7H9 the cells were incubate at 37°C for 3 hours to allow cell recovery and expression of antibiotic resistance. The cells were then concentrated by centrifugation and

plated on 7H10 plates containing the appropriate antibiotic. The colonies were confirmed by colony PCR and sequencing. When appropriate the cells were grown overnight in liquid 7H9 cultures for second recombination events and plated at several dilutions. Colonies were then plated in parallel on 10% sucrose containing plates or Kan50 Hyg25 plates. Colonies growing on sucrose and not on antibiotic plates were confirmed by colony PCR and sent for sequencing.

7.4   Fluorescence snapshot microscopy

For snapshot images bacteria were grown to mid-log phase (OD$_{600}$ ~ 0.5) in 7H9 liquid medium and ~ 3 μl of culture were pipetted between glass coverslips. DNA staining was done by incubating the cells in Hoechst 33342 (Thermo Fisher Scientific, 1μg/ml) for 5 min or DAPI (1μg/ml) for 1 hour. Colonies were stained with SYTO 17 Red nucleic acid stain (Thermo Fisher Scientific, 200 nM) after taking the Hlp-Dendra2 images, as SYTO 17 fluorescence creates a crosstalk into the channel used to measure Hlp-Dendra2 fluorescence.

7.5   Fluorescence time-lapse microscopy

For time-lapse microscopy, bacteria were grown to mid-log phase (OD$_{600}$ ~ 0.5) in 7H9 liquid medium, collected by centrifugation (2350 g for 5 min), concentrated 10-fold, and filtered through a 5 μm-pore-size polyvinylidene difluoride syringe filter (Millipore) to remove clumps. Filtered bacteria were spread on a glass coverslip and covered with a semipermeable membrane. Nitrocellulose membranes (5 kDa molecular cut-off, pretreated Spectra/Por®7 dialysis tubing, Spectrum Labs) were prepared as previously described (Dhar & Manina 2015) and were used in all experiments except those involving Hoechst 33342, for which 2% agarose membrane were prepared as described (Toniolo et al. 2018). The membrane was overlaid with a custom-made microfluidic chip and the assembly was clamped in a custom-made holder then mounted on the microscope stage inside a custom-

made environmental chamber maintained at 37˚C. The bacteria were fed with a continu-ous flow of prewarmed (37˚C) 7H9 liquid medium at a flow rate of 25 µl per minute, as de-scribed [13]. Nucleoid staining was done by adding SYTO 17 Red (170 nM final) or Hoechst 33342 (1µg/ml final) to the flow medium after allowing the bacteria to complete about five divisions.

Bacteria were imaged with a DeltaVision Elite inverted microscope (Applied Preci-sion) equipped with a 100X oil immersion objective and a CoolSnap HQ2 camera (Photo-metrics). Phase-contrast images were recorded using an image-based autofocus every 15 minutes with illumination for 0.1 seconds at 50% power. DAPI or Hoechst 3342 fluores-cence (blue) was imaged using a 390/18 nm excitation filter and a 435/48 nm emission fil-ter with illumination for 0.15 seconds at 50% power. GFP fluorescence (green) was imaged using a 475/28-nm excitation filter and 525/48-nm emission filter with illumination for 0.2 seconds at 50% power. SYTO 17 fluorescence (far-red) was imaged using a 632/22 nm CY-5 excitation filter and a 676/34 nm emission filter with illumination for 0.15 seconds at 32% power.

7.6 Western Blot

Bacteria were grown to mid-log phase (OD600 ~ 0.7) in 7H9 medium. 10 ml of cul-ture was centrifuged at 5000g for 10 min. The bacterial pellet was washed with PBS + Tween. Bacteria were resuspended in 500 µL of TBS-Tween20 + Protease inhibitors (cOm-plete mini EDTA free cocktail tablet, Roche), (TBS-T: 25mM Tris pH 7.5, 150mM NaCl, 0.05%Tween20) and 1% SDS. The cells were lysed by bead beating in tubes containing 500 µL of silica beads (0.1 mm zirconia beads) prior to physical disruption using the Precellys24 homogenizer 3 times at 6.5 m/s for 60 sec. Indicated amounts of total proteins from the culture filtrate, total cell lysates and subcellular fractions were resolved in NuPAGE 4-12% bis-Tris gels (Invitrogen). Proteins were transferred to nitrocellulose membranes using the iBlot Gel Transfer System (Invitrogen). Membranes were blocked with 5% milk in TBS (150

mM NaCl, 20 mM Tris-HCl, pH 7.5 and nonfat milk powder) for 1h and then incubated with the required antibody (monoclonal anti-HA antibodies conjugated to Horseradish Peroxidase (HRP) from Cell Signaling and Monoclonal anti-RpoB antibodies from NeoClone) diluted in filtered TBST-1% BSA (TBS, 0.05% Tween-20, BSA) overnight at 4°C. Membranes were washed with TBST 3 times before and after being incubated with the appropriate secondary antibody (polyclonal rabbit anti-mouse) for 30 min at room temperature. The membrane was further washed 2 times with PBS and subsequently developed using a chemiluminescent peroxidase substrate (Sigma-Aldrich). RpoB was used as a loading control for cell lysates

7.7 Immunoprecipitation using anti-HA Agarose Beads

Bacteria were grown to mid-log phase (OD600 ~ 0.7) in 7H9 medium. 36 ml of culture was centrifuged at 5000g for 10 min. The bacterial pellet was washed with PBS + Tween. The pellet was frozen at -80°C. Bacteria were resuspended in 500 μL of TBS-Tween20 + Protease inhibitors (cOmplete mini EDTA free cocktail tablet, Roche), (TBS-T: 25mM Tris pH 7.5, 150mM NaCl, 0.05%Tween20) and 1% SDS. The cells were lysed by bead beating in tubes containing 500 μL of silica beads (0.1 mm zirconia beads) prior to physical disruption using the Precellys24 homogenizer 3 times at 6.5 m/s for 60 sec. The supernatant was transferred to a new tube and the concentration was measured using the Quibit protein assay kit (thermo fisher scientific). The Spin-X centrifuge tubes filter (Costar, 8160) were washed once with 1 mL of PBS by centrifugation at 10 000g for 2 min. 50 μl of Monoclonal Anti-HA Agarose Antibody beads (Sigma-Aldrich, A2095) were incubated with approximately 2 mg of bacterial extract in Spin-X centrifuge tubes for 4 h at 4°C on an orbital shaker. The columns were washed four times in 850 μl PBS. 46.5 μl of PBS and 15.5 μl of NuPage LDS sample buffer (Thermo Fisher Scientific) was incubated at 95°C for 5min. The immunoprecipitated material was eluted from the beads by centrifugation through the columns. Immunoprecipitated proteins were analyzed by Silver staining or Coomassie blue staining followed by mass spectrometry as described (Lou et al. 2017).

7.8 *M. smegmatis* gDNA extraction for PacBio sequencing

DNA extraction was carried out using a custom-designed protocol for mycobacterial DNA. Bacteria were grown to mid-log phase (OD_{600} ~ 0.7) in 7H9 medium. 15ml of bacterial culture was centrifugated at 5000g for 10 min. The bacterial cell pellet was washed with 5mL of phosphate buffer saline (PBS) prior to centrifugation at 5000 g for 10 min. The supernatant was discarded and the pellet was re-suspended in 1 mL of bacterial lysis buffer B1 (50 mM Tris-HCl pH 8.0; 50 mM EDTA pH 8.0; 0.5% Tween 20; 0.5% Triton-X100, Qiagen) containing 45 μL of proteinase K (20 mg/mL) and 20 μL of lysozyme (100 mg/mL). The mixture was then transferred into bead-beating tubes containing 500 μL of silica beads (0.1 mm zirconia beads) prior to physical disruption using the Precellys24 homogenizer at 4 m/s for 5 sec. After incubating at 56°C for 1 h, the mixture was centrifuged and the supernatant was transferred to a new tube. An additional incubation with 20 μL proteinase K (20 mg/mL) was conducted at 56°C for 30 min. The mixture was then incubated at 4°C for 15 min. RNAse A (Sigma) was added and the sample was incubated 30 min at 37°C, followed by the addition of 350 μL of bacterial lysis buffer B2 (3M guanidine hydrochloride, 20% Tween 20, Qiagen), and incubated for 30 min at 50°C. DNA was purified using the Qiagen Genomic-Tip/20G according to the manufacturer's instructions, and eluted in 2 mL elution buffer. The DNA was precipitated using 0.7x volume of isopropanol and centrifuged at 4°C for 15 min. The pellet was washed twice with 700 μL 70% ethanol, air-dried, and suspended overnight in 100 μL 10mM Tris HCl buffer (pH 8.0) at room temperature under continuous shaking. The DNA was then measured by Nanodrop, Qubit 2.0 (Life Technologies) and Fragment Analyzer (Advanced Analytical Technologies).

7.9 PacBio sequencing

DNA was sheared using a Covaris g-TUBE (Covaris S220) to obtain 10 kb fragments and the size distribution was checked using the Fragment Analyzer (Advanced Analytical Technologies). Sheared DNA was used to prepare a SMRTbell library with the PacBio

SMRTbell Template Prep Kit 1 (Pacific Biosciences) according to the manufacturer's recommendations. The resulting library was size-selected using a BluePippin system (Sage Science, Inc.) for molecules larger than 8 kb. The recovered library was sequenced using a SMRT cell with P6/C4 chemistry and MagBeads on a PacBio RSII system (Pacific Biosciences) at 240 min movie length

7.10 Super-resolution radial fluctuations (SRRF) microscopy

Fluorescence SRRF images were acquired with an EMCCD iXon Ultra 897 camera (Andor) mounted on an IX73 inverted optical microscope (Olympus) equipped with an oil immersion objective (UAPON 100x/1.49 Oil, Olympus). Illumination was provided with a mercury lamp (U-HGLGPS, Olympus). Bacteria were grown to mid-log phase (OD$_{600}$ ~ 0.5) in 7H9 liquid medium then incubated with FM4-64 dye (50 µg/µl, Life Technologies) for 15 minutes and ~ 3 µl of the stained bacteria were deposited between glass coverslips. For each SRRF image construction, 400 images were taken using the 1.6X extra magnifier in place, 100% lamp intensity and 150 electron-multiplying gain. For wild-type cells expressing Hlp-Dendra2 each of the 400 images was exposed for 17 milliseconds with a kinetic cycle time of 22 milliseconds. For $\Delta parA$ cells expressing Hlp-Dendra2 each of the 400 images was exposed for 11 milliseconds with a kinetic cycle time of 15 milliseconds. The open-source Fiji plugin NanoJ-SRRF (Gustafson et al. 2016) was used to reconstruct the SRRF images.

Chapter 8 References

Addinall, S. G., E. Bi, and J. Lutkenhaus. "FtsZ Ring Formation in Fts Mutants." *Journal of Bacteriology* 178, no. 13 (July 1996): 3877–84. https://doi.org/10.1128/jb.178.13.3877-3884.1996.

Aguayo, S, N Donos, D Spratt, and L Bozec. "Single-Bacterium Nanomechanics in Biomedicine: Unravelling the Dynamics of Bacterial Cells." *Nanotechnology* 26, no. 6 (February 13, 2015): 062001. https://doi.org/10.1088/0957-4484/26/6/062001.

Aldridge, Bree B., Marta Fernandez-Suarez, Danielle Heller, Vijay Ambravaneswaran, Daniel Irimia, Mehmet Toner, and Sarah M. Fortune. "Asymmetry and Aging of Mycobacterial Cells Lead to Variable Growth and Antibiotic Susceptibility." *Science* 335, no. 6064 (January 6, 2012): 100–104. https://doi.org/10.1126/science.1216166.

Al-Humadi, Hussam W., Rafal J. Al-Saigh, and Ahmed W. Al-Humadi. "Addressing the Challenges of Tuberculosis: A Brief Historical Account." *Frontiers in Pharmacology* 8 (September 26, 2017): 689. https://doi.org/10.3389/fphar.2017.00689.

Alva, Alicia, Fredy Aquino, Robert H. Gilman, Carlos Olivares, David Requena, Andrés H. Gutiérrez, Luz Caviedes, et al. "Morphological Characterization of Mycobacterium Tuberculosis in a MODS Culture for an Automatic Diagnostics through Pattern Recognition." Edited by Vishnu Chaturvedi. *PLoS ONE* 8, no. 12 (December 16, 2013): e82809. https://doi.org/10.1371/journal.pone.0082809.

Ando, Toshio. "High-Speed AFM Imaging." *Current Opinion in Structural Biology* 28 (October 2014): 63–68. https://doi.org/10.1016/j.sbi.2014.07.011.

Anuchin, A. M., A. V. Goncharenko, O. I. Demidenok, and A. S. Kaprel'iants. "[Histone-like proteins of bacteria (review)]." *Prikladnaia Biokhimiia I Mikrobiologiia* 47, no. 6 (December 2011): 635–41.

Aussel, Laurent, François-Xavier Barre, Mira Aroyo, Andrzej Stasiak, Alicja Z Stasiak, and David Sherratt. "FtsK Is a DNA Motor Protein That Activates Chromosome Dimer Resolution by Switching the Catalytic State of the XerC and XerD Recombinases." *Cell* 108, no. 2 (January 2002): 195–205. https://doi.org/10.1016/S0092-8674(02)00624-4.

Bayly, H. W. "Discussion on the Present Position and Treatment of Syphilis." *Proceedings of the Royal Society of Medicine* 3, no. Surg_Sect (June 1910): 238–42. https://doi.org/10.1177/003591571000301626.

Becker, Eric C., and Kit Pogliano. "Cell-Specific SpoIIIE Assembly and DNA Translocation Polarity Are Dictated by Chromosome Orientation." *Molecular Microbiology* 66, no. 5 (December 2007): 1066–79. https://doi.org/10.1111/j.1365-2958.2007.05992.x.

Berens, Christian, and Wolfgang Hillen. "Gene Regulation by Tetracyclines. Constraints of Resistance Regulation in Bacteria Shape TetR for Application in Eukaryotes." *European Journal of Biochemistry* 270, no. 15 (August 2003): 3109–21. https://doi.org/10.1046/j.1432-1033.2003.03694.x.

Berezuk, Alison M., Sabrina Glavota, Elyse J. Roach, Mara C. Goodyear, Jonathan R. Krieger, and Cezar M. Khursigara. "Outer Membrane Lipoprotein RlpA Is a Novel Periplasmic Interaction Partner of the Cell Division Protein FtsK in Escherichia Coli." *Scientific Reports* 8, no. 1 (August 28, 2018): 12933. https://doi.org/10.1038/s41598-018-30979-5.

Bhowmick, Tuhin, Soumitra Ghosh, Karuna Dixit, Varsha Ganesan, Udupi A. Ramagopal, Debayan Dey, Siddhartha P. Sarma, Suryanarayanarao Ramakumar, and Valakunja Nagaraja. "Targeting Mycobacterium Tuberculosis Nucleoid-Associated Protein HU with

Structure-Based Inhibitors." *Nature Communications* 5, no. 1 (December 2014). https://doi.org/10.1038/ncomms5124.

Bigot, Sarah, Viknesh Sivanathan, Christophe Possoz, François-Xavier Barre, and François Cornet. "FtsK, a Literate Chromosome Segregation Machine: FtsK, a Literate Chromosome Segregation Machine." *Molecular Microbiology* 64, no. 6 (June 2007): 1434–41. https://doi.org/10.1111/j.1365-2958.2007.05755.x.

Bisson-Filho, Alexandre W., Yen-Pang Hsu, Georgia R. Squyres, Erkin Kuru, Fabai Wu, Calum Jukes, Yingjie Sun, et al. "Treadmilling by FtsZ Filaments Drives Peptidoglycan Synthesis and Bacterial Cell Division." *Science* 355, no. 6326 (February 17, 2017): 739–43. https://doi.org/10.1126/science.aak9973.

Blair, Jessica M. A., and Laura J. V. Piddock. "How to Measure Export via Bacterial Multidrug Resistance Efflux Pumps." *MBio* 7, no. 4 (September 7, 2016): e00840-16, /mbio/7/4/e00840-16.atom. https://doi.org/10.1128/mBio.00840-16.

Boccard, Frédéric, Emilie Esnault, and Michèle Valens. "Spatial Arrangement and Macrodomain Organization of Bacterial Chromosomes: Macrodomain Organization of Bacterial Chromosome." *Molecular Microbiology* 57, no. 1 (July 2005): 9–16. https://doi.org/10.1111/j.1365-2958.2005.04651.x.

Botella, Helene, Guangli Yang, Ouathek Ouerfelli, Sabine Ehrt, Carl F. Nathan, and Julien Vaubourgeix. "Distinct Spatiotemporal Dynamics of Peptidoglycan Synthesis between *Mycobacterium Smegmatis* and *Mycobacterium Tuberculosis*." Edited by Christina L. Stallings. *MBio* 8, no. 5 (November 8, 2017): e01183-17, /mbio/8/5/e01183-17.atom. https://doi.org/10.1128/mBio.01183-17.

Bouet, J.-Y. "P1 ParA Interacts with the P1 Partition Complex at ParS and an ATP-ADP Switch Controls ParA Activities." *The EMBO Journal* 18, no. 5 (March 1, 1999): 1415–24. https://doi.org/10.1093/emboj/18.5.1415.

Britton, R. A., D. C. Lin, and A. D. Grossman. "Characterization of a Prokaryotic SMC Protein Involved in Chromosome Partitioning." *Genes & Development* 12, no. 9 (May 1, 1998): 1254–59. https://doi.org/10.1101/gad.12.9.1254.

Burton, Briana M., Kathleen A. Marquis, Nora L. Sullivan, Tom A. Rapoport, and David Z. Rudner. "The ATPase SpoIIIE Transports DNA across Fused Septal Membranes during Sporulation in Bacillus Subtilis." *Cell* 131, no. 7 (December 2007): 1301–12. https://doi.org/10.1016/j.cell.2007.11.009.

Cameron, Todd A., John R. Zupan, and Patricia C. Zambryski. "The Essential Features and Modes of Bacterial Polar Growth." *Trends in Microbiology* 23, no. 6 (June 2015): 347–53. https://doi.org/10.1016/j.tim.2015.01.003.

Casart, Yveth, Elida Gamero, Sandra Rivera-Gutierrez, Jorge A González-y-Merchand, and Leiria Salazar. "Par Genes in Mycobacterium Bovis and Mycobacterium Smegmatis Are Arranged in an Operon Transcribed from 'SigGC' Promoters." *BMC Microbiology* 8, no. 1 (2008): 51. https://doi.org/10.1186/1471-2180-8-51.

Chalfie, M., Y. Tu, G. Euskirchen, W. W. Ward, and D. C. Prasher. "Green Fluorescent Protein as a Marker for Gene Expression." *Science (New York, N.Y.)* 263, no. 5148 (February 11, 1994): 802–5.

Cole, S. T., R. Brosch, J. Parkhill, T. Garnier, C. Churcher, D. Harris, S. V. Gordon, et al. "Deciphering the Biology of Mycobacterium Tuberculosis from the Complete Genome Sequence." *Nature* 393, no. 6685 (June 11, 1998): 537–44. https://doi.org/10.1038/31159.

Collier, Justine. "Regulation of Chromosomal Replication in Caulobacter Crescentus." *Plasmid* 67, no. 2 (March 2012): 76–87. https://doi.org/10.1016/j.plasmid.2011.12.007.

Cimino, Mena, Lorenzo Alamo, and Leiria Salazar. "Permeabilization of the Mycobacterial Envelope for Protein Cytolocalization Studies by Immunofluorescence Microscopy." *BMC Microbiology* 6, no. 1 (April 18, 2006): 35. https://doi.org/10.1186/1471-2180-6-35.

Colangeli, Roberto, Danica Helb, Catherine Vilchèze, Manzour Hernando Hazbón, Chee-Gun Lee, Hassan Safi, Brendan Sayers, et al. "Transcriptional Regulation of Multi-Drug Tolerance and Antibiotic-Induced Responses by the Histone-Like Protein Lsr2 in M. Tuberculosis." *PLoS Pathogens* 3, no. 6 (2007): e87. https://doi.org/10.1371/journal.ppat.0030087.

Crozat, Estelle, and Ian Grainge. "FtsK DNA Translocase: The Fast Motor That Knows Where It's Going." *ChemBioChem* 11, no. 16 (November 2, 2010): 2232–43. https://doi.org/10.1002/cbic.201000347.

Dame, Remus T. "The Role of Nucleoid-Associated Proteins in the Organization and Compaction of Bacterial Chromatin: Organization and Compaction of Bacterial Chromatin." *Molecular Microbiology* 56, no. 4 (March 24, 2005): 858–70. https://doi.org/10.1111/j.1365-2958.2005.04598.x.

Dame, Remus T., Olga J. Kalmykowa, and David C. Grainger. "Chromosomal Macrodomains and Associated Proteins: Implications for DNA Organization and Replication in Gram Negative Bacteria." Edited by William F. Burkholder. *PLoS Genetics* 7, no. 6 (June 16, 2011): e1002123. https://doi.org/10.1371/journal.pgen.1002123.

Datta, Chandreyee, Rajiv Kumar Jha, Wareed Ahmed, Sohini Ganguly, Soumitra Ghosh, and Valakunja Nagaraja. "Physical and Functional Interaction between Nucleoid-

associated Proteins HU and Lsr2 of *Mycobacterium Tuberculosis* : Altered DNA Binding and Gene Regulation." *Molecular Microbiology* 111, no. 4 (April 2019): 981–94. https://doi.org/10.1111/mmi.14202.

Dhar, Neeraj, and Giulia Manina. "Single-Cell Analysis of Mycobacteria Using Microfluidics and Time-Lapse Microscopy." *Methods in Molecular Biology (Clifton, N.J.)* 1285 (2015): 241–56. https://doi.org/10.1007/978-1-4939-2450-9_14.

Dedrick, R. M., H. Wildschutte, and J. R. McCormick. "Genetic Interactions of Smc, FtsK, and ParB Genes in Streptomyces Coelicolor and Their Developmental Genome Segregation Phenotypes." *Journal of Bacteriology* 191, no. 1 (January 1, 2009): 320–32. https://doi.org/10.1128/JB.00858-08.

DeJesus, Michael A., Elias R. Gerrick, Weizhen Xu, Sae Woong Park, Jarukit E. Long, Cara C. Boutte, Eric J. Rubin, et al. "Comprehensive Essentiality Analysis of the *Mycobacterium Tuberculosis* Genome via Saturating Transposon Mutagenesis." Edited by Christina L. Stallings. *MBio* 8, no. 1 (March 8, 2017): e02133-16, /mbio/8/1/e02133-16.atom. https://doi.org/10.1128/mBio.02133-16.

Donczew, Magdalena, Paweł Mackiewicz, Agnieszka Wróbel, Klas Flärdh, Jolanta Zakrzewska-Czerwińska, and Dagmara Jakimowicz. "ParA and ParB Coordinate Chromosome Segregation with Cell Elongation and Division during *Streptomyces* Sporulation." *Open Biology* 6, no. 4 (April 2016): 150263. https://doi.org/10.1098/rsob.150263.

Donovan, Catriona, and Marc Bramkamp. "Cell Division in Corynebacterineae." *Frontiers in Microbiology* 5 (April 10, 2014). https://doi.org/10.3389/fmicb.2014.00132.

Dubarry, Nelly, and François-Xavier Barre. "Fully Efficient Chromosome Dimer Resolution in Escherichia Coli Cells Lacking the Integral Membrane Domain of FtsK." *The EMBO Journal* 29, no. 3 (February 3, 2010): 597–605. https://doi.org/10.1038/emboj.2009.381.

Ducret, Adrien, Ellen M. Quardokus, and Yves V. Brun. "MicrobeJ, a Tool for High Throughput Bacterial Cell Detection and Quantitative Analysis." *Nature Microbiology* 1, no. 7 (July 2016): 16077. https://doi.org/10.1038/nmicrobiol.2016.77.

Dufrêne, Yves F. "Atomic Force Microscopy in Microbiology: New Structural and Functional Insights into the Microbial Cell Surface." *MBio* 5, no. 4 (July 22, 2014): e01363-14. https://doi.org/10.1128/mBio.01363-14.

Duigou, Stéphane, and Frédéric Boccard. "Long Range Chromosome Organization in Escherichia Coli: The Position of the Replication Origin Defines the Non-Structured Regions and the Right and Left Macrodomains." Edited by Josep Casadesús. *PLOS Genetics* 13, no. 5 (May 9, 2017): e1006758. https://doi.org/10.1371/journal.pgen.1006758.

Dziadek, J. "Conditional Expression of Mycobacterium Smegmatis FtsZ, an Essential Cell Division Gene." *Microbiology* 149, no. 6 (June 1, 2003): 1593–1603. https://doi.org/10.1099/mic.0.26023-0.

Edwards, David H., and Jeffery Errington. "The *Bacillus Subtilis* DivIVA Protein Targets to the Division Septum and Controls the Site Specificity of Cell Division." *Molecular Microbiology* 24, no. 5 (June 1997): 905–15. https://doi.org/10.1046/j.1365-2958.1997.3811764.x.

Eskandarian, Haig A., Pascal D. Odermatt, Joëlle X. Y. Ven, Mélanie T. M. Hannebelle, Adrian P. Nievergelt, Neeraj Dhar, John D. McKinney, and Georg E. Fantner. "Division Site Selection Linked to Inherited Cell Surface Wave Troughs in Mycobacteria." *Nature Microbiology* 2, no. 9 (September 2017): 17094. https://doi.org/10.1038/nmicrobiol.2017.94.

Fantner, Georg E., Roberto J. Barbero, David S. Gray, and Angela M. Belcher. "Imaging Bacterial Cell Death Induced by Antimicrobial Peptides in Real Time Using High Speed AFM." *Microscopy and Microanalysis: The Official Journal of Microscopy Society of Ameri-*

ca, Microbeam Analysis Society, Microscopical Society of Canada 16, no. Suppl Suppl 2 (July 2010): 466–67.

Fiche, Jean-Bernard, Diego I. Cattoni, Nele Diekmann, Julio Mateos Langerak, Caroline Clerte, Catherine A. Royer, Emmanuel Margeat, Thierry Doan, and Marcelo Nöllmann. "Recruitment, Assembly, and Molecular Architecture of the SpoIIIE DNA Pump Revealed by Superresolution Microscopy." Edited by Matthew K. Waldor. *PLoS Biology* 11, no. 5 (May 7, 2013): e1001557. https://doi.org/10.1371/journal.pbio.1001557.

Fournes, Florian, Estelles Crozat, Carine Pages, Catherine Tardin, Laurence Salomé, François Cornet, and Philippe Rousseau. "FtsK Translocation Permits Discrimination between an Endogenous and an Imported Xer/ *Dif* Recombination Complex." *Proceedings of the National Academy of Sciences* 113, no. 28 (July 12, 2016): 7882–87. https://doi.org/10.1073/pnas.1523178113.

Fu, L. M., and C. S. Fu-Liu. "Is Mycobacterium Tuberculosis a Closer Relative to Gram-Positive or Gram-Negative Bacterial Pathogens?" *Tuberculosis (Edinburgh, Scotland)* 82, no. 2–3 (2002): 85–90.

Gandhi, Neel R., Paul Nunn, Keertan Dheda, H. Simon Schaaf, Matteo Zignol, Dick van Soolingen, Paul Jensen, and Jaime Bayona. "Multidrug-Resistant and Extensively Drug-Resistant Tuberculosis: A Threat to Global Control of Tuberculosis." *Lancet (London, England)* 375, no. 9728 (May 22, 2010): 1830–43. https://doi.org/10.1016/S0140-6736(10)60410-2.

Garner, Ethan C. "MicrobeTracker: Quantitative Image Analysis Designed for the Smallest Organisms: MicrobeTracker: Quantitative Image Analysis." *Molecular Microbiology* 80, no. 3 (May 2011): 577–79. https://doi.org/10.1111/j.1365-2958.2011.07580.x.

Ghosh, Soumitra, Bhavna Padmanabhan, Chinmay Anand, and Valakunja Nagaraja. "Lysine Acetylation of the *Mycobacterium Tuberculosis* HU Protein Modulates Its DNA Binding and Genome Organization: Acetylation of MtHU by Eis." *Molecular Microbiology* 100, no. 4 (May 2016): 577–88. https://doi.org/10.1111/mmi.13339.

Global tuberculosis report, 2018, WHO

Hertog, Alice L. den, Dennis W. Visser, Colin J. Ingham, Frank H. A. G. Fey, Paul R. Klatser, and Richard M. Anthony. "Simplified Automated Image Analysis for Detection and Phenotyping of Mycobacterium Tuberculosis on Porous Supports by Monitoring Growing Microcolonies." Edited by Anil Kumar Tyagi. *PLoS ONE* 5, no. 6 (June 8, 2010): e11008. https://doi.org/10.1371/journal.pone.0011008.

Ginda, Katarzyna, Martyna Bezulska, Małgorzata Ziółkiewicz, Jarosław Dziadek, Jolanta Zakrzewska-Czerwińska, and Dagmara Jakimowicz. "ParA of *Mycobacterium Smegmatis* Co-Ordinates Chromosome Segregation with the Cell Cycle and Interacts with the Polar Growth Determinant DivIVA: The Role of ParA in *Mycobacterium Smegmatis*." *Molecular Microbiology* 87, no. 5 (March 2013): 998–1012. https://doi.org/10.1111/mmi.12146.

Ginda, Katarzyna, Isabella Santi, Djenet Bousbaine, Jolanta Zakrzewska-Czerwińska, Dagmara Jakimowicz, and John McKinney. "The Studies of ParA and ParB Dynamics Reveal Asymmetry of Chromosome Segregation in Mycobacteria: ParAB Dynamics in Mycobacteria." *Molecular Microbiology* 105, no. 3 (August 2017): 453–68. https://doi.org/10.1111/mmi.13712.

Gordon, B. R. G., R. Imperial, L. Wang, W. W. Navarre, and J. Liu. "Lsr2 of Mycobacterium Represents a Novel Class of H-NS-Like Proteins." *Journal of Bacteriology* 190, no. 21 (November 1, 2008): 7052–59. https://doi.org/10.1128/JB.00733-08.

Gradmann, C. "Robert Koch and the Pressures of Scientific Research: Tuberculosis and Tuberculin." *Medical History* 45, no. 1 (January 2001): 1–32.

Grove, Anne. "Functional Evolution of Bacterial Histone-like HU Proteins." *Current Issues in Molecular Biology* 13, no. 1 (2011): 1–12.

Gupta, M., A. Sajid, K. Sharma, S. Ghosh, G. Arora, R. Singh, V. Nagaraja, V. Tandon, and Y. Singh. "HupB, a Nucleoid-Associated Protein of Mycobacterium Tuberculosis, Is Modified by Serine/Threonine Protein Kinases In Vivo." *Journal of Bacteriology* 196, no. 14 (July 15, 2014): 2646–57. https://doi.org/10.1128/JB.01625-14.

Gustafsson, Nils, Siân Culley, George Ashdown, Dylan M. Owen, Pedro Matos Pereira, and Ricardo Henriques. "Fast Live-Cell Conventional Fluorophore Nanoscopy with ImageJ through Super-Resolution Radial Fluctuations." *Nature Communications* 7, no. 1 (November 2016): 12471. https://doi.org/10.1038/ncomms12471.

Gutierrez, M. Cristina, Sylvain Brisse, Roland Brosch, Michel Fabre, Bahia Omaïs, Magali Marmiesse, Philip Supply, and Veronique Vincent. "Ancient Origin and Gene Mosaicism of the Progenitor of Mycobacterium Tuberculosis." *PLoS Pathogens* 1, no. 1 (2005): e5. https://doi.org/10.1371/journal.ppat.0010005.

Hannebelle Mélanie, Ven Joëlle X. Y., Toniolo Chiara, Eskandarian Haig A., Vuaridel Gaëlle, McKinney John D., Fantner Georg E.. "Pole elongation in mycobacteria resembles biphasic "new end take off" (NETO) dynamics in fission yeast", Nature Communications, in review/2019

Harms, Andrea, Anke Treuner-Lange, Dominik Schumacher, and Lotte Søgaard-Andersen. "Tracking of Chromosome and Replisome Dynamics in Myxococcus Xanthus Reveals a Novel Chromosome Arrangement." Edited by William F. Burkholder. *PLoS Genetics* 9, no. 9 (September 19, 2013): e1003802. https://doi.org/10.1371/journal.pgen.1003802.

Hett, E. C., and E. J. Rubin. "Bacterial Growth and Cell Division: A Mycobacterial Perspective." *Microbiology and Molecular Biology Reviews* 72, no. 1 (March 1, 2008): 126–56. https://doi.org/10.1128/MMBR.00028-07.

Holden, S. J., T. Pengo, K. L. Meibom, C. Fernandez Fernandez, J. Collier, and S. Manley. "High Throughput 3D Super-Resolution Microscopy Reveals Caulobacter Crescentus in Vivo Z-Ring Organization." *Proceedings of the National Academy of Sciences* 111, no. 12 (March 25, 2014): 4566–71. https://doi.org/10.1073/pnas.1313368111.

Hołówka, Joanna, Damian Trojanowski, Katarzyna Ginda, Bartosz Wojtaś, Bartłomiej Gielniewski, Dagmara Jakimowicz, and Jolanta Zakrzewska-Czerwińska. "HupB Is a Bacterial Nucleoid-Associated Protein with an Indispensable Eukaryotic-Like Tail." Edited by Manjula Sritharan and Eric J. Rubin. *MBio* 8, no. 6 (November 7, 2017): e01272-17, /mbio/8/6/mBio.01272-17.atom. https://doi.org/10.1128/mBio.01272-17.

Hołówka, Joanna, Damian Trojanowski, Mateusz Janczak, Dagmara Jakimowicz, and Jolanta Zakrzewska-Czerwińska. "The Origin of Chromosomal Replication Is Asymmetrically Positioned on the Mycobacterial Nucleoid, and the Timing of Its Firing Depends on HupB." Edited by Tina M. Henkin. *Journal of Bacteriology* 200, no. 10 (March 12, 2018): e00044-18, /jb/200/10/e00044-18.atom. https://doi.org/10.1128/JB.00044-18.

Hu, Longhua, Anthony G. Vecchiarelli, Kiyoshi Mizuuchi, Keir C. Neuman, and Jian Liu. "Directed and Persistent Movement Arises from Mechanochemistry of the ParA/ParB System." *Proceedings of the National Academy of Sciences*, December 8, 2015, 201505147. https://doi.org/10.1073/pnas.1505147112.

Iniesta, Antonio A. "ParABS System in Chromosome Partitioning in the Bacterium Myxococcus Xanthus." Edited by Adam Driks. *PLoS ONE* 9, no. 1 (January 22, 2014): e86897. https://doi.org/10.1371/journal.pone.0086897.

Ireton, K., N. W. Gunther, and A. D. Grossman. "Spo0J Is Required for Normal Chromosome Segregation as Well as the Initiation of Sporulation in Bacillus Subtilis." *Journal of Bacteriology* 176, no. 17 (September 1994): 5320–29. https://doi.org/10.1128/jb.176.17.5320-5329.1994.

Jakimowicz, D., A. Brzostek, A. Rumijowska-Galewicz, P. Zydek, A. Dolzblasz, A. Smulczyk-Krawczyszyn, T. Zimniak, et al. "Characterization of the Mycobacterial Chromosome Segregation Protein ParB and Identification of Its Target in Mycobacterium Smegmatis." *Microbiology* 153, no. 12 (December 1, 2007): 4050–60. https://doi.org/10.1099/mic.0.2007/011619-0.

Jakobs, S., V. Subramaniam, A. Schönle, T. M. Jovin, and S. W. Hell. "EFGP and DsRed Expressing Cultures of Escherichia Coli Imaged by Confocal, Two-Photon and Fluorescence Lifetime Microscopy." *FEBS Letters* 479, no. 3 (August 18, 2000): 131–35.

Jensen, R. B., and L. Shapiro. "The Caulobacter Crescentus Smc Gene Is Required for Cell Cycle Progression and Chromosome Segregation." *Proceedings of the National Academy of Sciences of the United States of America* 96, no. 19 (September 14, 1999): 10661–66. https://doi.org/10.1073/pnas.96.19.10661.

Jun, Suckjoon, and Andrew Wright. "Entropy as the Driver of Chromosome Segregation." *Nature Reviews Microbiology* 8, no. 8 (August 2010): 600–607. https://doi.org/10.1038/nrmicro2391.

Kapopoulou, Adamandia, Jocelyne M. Lew, and Stewart T. Cole. "The MycoBrowser Portal: A Comprehensive and Manually Annotated Resource for Mycobacterial Genomes." *Tuberculosis (Edinburgh, Scotland)* 91, no. 1 (January 2011): 8–13. https://doi.org/10.1016/j.tube.2010.09.006.

Kieser, Karen J., and Eric J. Rubin. "How Sisters Grow Apart: Mycobacterial Growth and Division." *Nature Reviews Microbiology* 12, no. 8 (August 2014): 550–62. https://doi.org/10.1038/nrmicro3299.

Kim, H. J., M. J. Calcutt, F. J. Schmidt, and K. F. Chater. "Partitioning of the Linear Chromosome during Sporulation of Streptomyces Coelicolor A3(2) Involves an OriC-Linked ParAB Locus." *Journal of Bacteriology* 182, no. 5 (March 2000): 1313–20. https://doi.org/10.1128/jb.182.5.1313-1320.2000.

Kim, Jee-Hyun, Jun-Rong Wei, Joshua B. Wallach, Rebekkah S. Robbins, Eric J. Rubin, and Dirk Schnappinger. "Protein Inactivation in Mycobacteria by Controlled Proteolysis and Its Application to Deplete the Beta Subunit of RNA Polymerase." *Nucleic Acids Research* 39, no. 6 (March 2011): 2210–20. https://doi.org/10.1093/nar/gkq1149.

Kim, J.-H., K. M. O'Brien, R. Sharma, H. I. M. Boshoff, G. Rehren, S. Chakraborty, J. B. Wallach, et al. "A Genetic Strategy to Identify Targets for the Development of Drugs That Prevent Bacterial Persistence." *Proceedings of the National Academy of Sciences* 110, no. 47 (November 19, 2013): 19095–100. https://doi.org/10.1073/pnas.1315860110.

Kois, A., M. Swiatek, D. Jakimowicz, and J. Zakrzewska-Czerwinska. "SMC Protein-Dependent Chromosome Condensation during Aerial Hyphal Development in Streptomyces." *Journal of Bacteriology* 191, no. 1 (January 1, 2009): 310–19. https://doi.org/10.1128/JB.00513-08.

Kolly, Gaëlle S., Francesca Boldrin, Claudia Sala, Neeraj Dhar, Ruben C. Hartkoorn, Marcello Ventura, Agnese Serafini, John D. McKinney, Riccardo Manganelli, and Stewart T. Cole. "Assessing the Essentiality of the Decaprenyl-Phospho- D -Arabinofuranose Pathway in *M Ycobacterium Tuberculosis* Using Conditional Mutants: Druggability of the *M. Tuberculosis* DPA Pathway." *Molecular Microbiology* 92, no. 1 (April 2014): 194–211. https://doi.org/10.1111/mmi.12546.

Klotzsche, Marcus, Sabine Ehrt, and Dirk Schnappinger. "Improved Tetracycline Repressors for Gene Silencing in Mycobacteria." *Nucleic Acids Research* 37, no. 6 (April 1, 2009): 1778–88. https://doi.org/10.1093/nar/gkp015.

Kriel, Nastassja L., James Gallant, Niël van Wyk, Paul van Helden, Samantha L. Sampson, Robin M. Warren, and Monique J. Williams. "Mycobacterial Nucleoid Associated Proteins: An Added Dimension in Gene Regulation." *Tuberculosis* 108 (January 2018): 169–77. https://doi.org/10.1016/j.tube.2017.12.004.

Lawn, Stephen D, and Alimuddin I Zumla. "Tuberculosis." *The Lancet* 378, no. 9785 (July 2011): 57–72. https://doi.org/10.1016/S0140-6736(10)62173-3.

Lee, Ji Yeon. "Diagnosis and Treatment of Extrapulmonary Tuberculosis." *Tuberculosis and Respiratory Diseases* 78, no. 2 (2015): 47. https://doi.org/10.4046/trd.2015.78.2.47.

Lee, Philina S., and Alan D. Grossman. "The Chromosome Partitioning Proteins Soj (ParA) and Spo0J (ParB) Contribute to Accurate Chromosome Partitioning, Separation of Replicated Sister Origins, and Regulation of Replication Initiation in Bacillus Subtilis." *Molecular Microbiology* 60, no. 4 (May 2006): 853–69. https://doi.org/10.1111/j.1365-2958.2006.05140.x.

Lemon, Katherine P, and Alan D Grossman. "Movement of Replicating DNA through a Stationary Replisome." *Molecular Cell* 6, no. 6 (December 2000): 1321–30. https://doi.org/10.1016/S1097-2765(00)00130-1.

Li, Guilian, Jingrui Zhang, Chao Li, Qian Guo, Yi Jiang, Jianhao Wei, Yan Qiu, et al. "Antimycobacterial Activity of Five Efflux Pump Inhibitors against Mycobacterium Tuberculosis Clinical Isolates." *The Journal Of Antibiotics* 69 (October 14, 2015): 173.

Li, S., and R. Waters. "Escherichia Coli Strains Lacking Protein HU Are UV Sensitive Due to a Role for HU in Homologous Recombination." *Journal of Bacteriology* 180, no. 15 (August 1998): 3750–56.

Lim, Hoong Chuin, Ivan Vladimirovich Surovtsev, Bruno Gabriel Beltran, Fang Huang, Jörg Bewersdorf, and Christine Jacobs-Wagner. "Evidence for a DNA-Relay Mechanism in ParABS-Mediated Chromosome Segregation." *ELife* 3 (May 23, 2014): e02758. https://doi.org/10.7554/eLife.02758.

Logsdon, Michelle M., Po-Yi Ho, Kadamba Papavinasasundaram, Kirill Richardson, Murat Cokol, Christopher M. Sassetti, Ariel Amir, and Bree B. Aldridge. "A Parallel Adder Coordinates Mycobacterial Cell-Cycle Progression and Cell-Size Homeostasis in the Context of Asymmetric Growth and Organization." *Current Biology* 27, no. 21 (November 2017): 3367-3374.e7. https://doi.org/10.1016/j.cub.2017.09.046.

Logsdon, Michelle M., and Bree B. Aldridge. "Stable Regulation of Cell Cycle Events in Mycobacteria: Insights From Inherently Heterogeneous Bacterial Populations." *Frontiers in Microbiology* 9 (March 21, 2018). https://doi.org/10.3389/fmicb.2018.00514.

Lou, Ye, Jan Rybniker, Claudia Sala, and Stewart T. Cole. "EspC Forms a Filamentous Structure in the Cell Envelope of *M Ycobacterium Tuberculosis* and Impacts ESX-1 Secretion: Filamentous Structure Formation by EspC." *Molecular Microbiology* 103, no. 1 (January 2017): 26–38. https://doi.org/10.1111/mmi.13575.

McTavish, D., and E. M. Sorkin. "Verapamil. An Updated Review of Its Pharmacodynamic and Pharmacokinetic Properties, and Therapeutic Use in Hypertension." *Drugs* 38, no. 1 (July 1989): 19–76. https://doi.org/10.2165/00003495-198938010-00003.

Maloney, Erin, Murty Madiraju, and Malini Rajagopalan. "Overproduction and Localization of Mycobacterium Tuberculosis ParA and ParB Proteins." *Tuberculosis* 89 (December 2009): S65–69. https://doi.org/10.1016/S1472-9792(09)70015-0.

Marquis, K. A., B. M. Burton, M. Nollmann, J. L. Ptacin, C. Bustamante, S. Ben-Yehuda, and D. Z. Rudner. "SpoIIIE Strips Proteins off the DNA during Chromosome Trans-

location." *Genes & Development* 22, no. 13 (July 1, 2008): 1786–95. https://doi.org/10.1101/gad.1684008.

Martins, Ana, and Leonard Amaral. "Screening for Efflux Pump Systems of Bacteria by the New Acridine Orange Agar Method." *In Vivo (Athens, Greece)* 26, no. 2 (April 2012): 203–6.

Mascarenhas, J. "Cell Cycle-Dependent Localization of Two Novel Prokaryotic Chromosome Segregation and Condensation Proteins in Bacillus Subtilis That Interact with SMC Protein." *The EMBO Journal* 21, no. 12 (June 17, 2002): 3108–18. https://doi.org/10.1093/emboj/cdf314.

Mierzejewska, Jolanta, and Grażyna Jagura-Burdzy. "Prokaryotic ParA-ParB-ParS System Links Bacterial Chromosome Segregation with the Cell Cycle." *Plasmid* 67, no. 1 (January 2012): 1–14. https://doi.org/10.1016/j.plasmid.2011.08.003.

Minnen, Anita, Laetitia Attaiech, Maria Thon, Stephan Gruber, and Jan-Willem Veening. "SMC Is Recruited to OriC by ParB and Promotes Chromosome Segregation in Streptococcus Pneumoniae: Chromosome Segregation in S. Pneumoniae." *Molecular Microbiology* 81, no. 3 (August 2011): 676–88. https://doi.org/10.1111/j.1365-2958.2011.07722.x.

Miyabe, I., Q. M. Zhang, Y. Kano, and S. Yonei. "Histone-like Protein HU Is Required for RecA Gene-Dependent DNA Repair and SOS Induction Pathways in UV-Irradiated Escherichia Coli." *International Journal of Radiation Biology* 76, no. 1 (January 2000): 43–49.

Mohan, Abhilash, Jyothi Padiadpu, Priyanka Baloni, and Nagasuma Chandra. "Complete Genome Sequences of a Mycobacterium Smegmatis Laboratory Strain (MC [2] 155) and Isoniazid-Resistant (4XR1/R2) Mutant Strains." *Genome Announcements* 3, no. 1 (February 26, 2015): e01520-14, /ga/3/1/e01520-14.atom. https://doi.org/10.1128/genomeA.01520-14.

Mohl, Dane A, and James W Gober. "Cell Cycle–Dependent Polar Localization of Chromosome Partitioning Proteins in Caulobacter Crescentus." *Cell* 88, no. 5 (March 1997): 675–84. https://doi.org/10.1016/S0092-8674(00)81910-8.

Mohl, Dane A., Jesse Easter, and James W. Gober. "The Chromosome Partitioning Protein, ParB, Is Required for Cytokinesis in Caulobacter Crescentus: ParB Is Required for Cell Division in Caulobacter." *Molecular Microbiology* 42, no. 3 (July 7, 2008): 741–55. https://doi.org/10.1046/j.1365-2958.2001.02643.x.

Munoz-Elias, E. J., J. Timm, T. Botha, W.-T. Chan, J. E. Gomez, and J. D. McKinney. "Replication Dynamics of Mycobacterium Tuberculosis in Chronically Infected Mice." *Infection and Immunity* 73, no. 1 (January 1, 2005): 546–51. https://doi.org/10.1128/IAI.73.1.546-551.2005.

Mura, Andrea, Daniela Fadda, Amilcar J. Perez, Madeline L. Danforth, Daniela Musu, Ana Isabel Rico, Marcin Krupka, et al. "Roles of the Essential Protein FtsA in Cell Growth and Division in Streptococcus Pneumoniae." Edited by Piet A. J. de Boer. *Journal of Bacteriology* 199, no. 3 (February 1, 2017): e00608-16, /jb/199/3/e00608-16.atom. https://doi.org/10.1128/JB.00608-16.

Nielsen, H. J., B. Youngren, F. G. Hansen, and S. Austin. "Dynamics of Escherichia Coli Chromosome Segregation during Multifork Replication." *Journal of Bacteriology* 189, no. 23 (December 1, 2007): 8660–66. https://doi.org/10.1128/JB.01212-07.

Nolivos, Sophie, and David Sherratt. "The Bacterial Chromosome: Architecture and Action of Bacterial SMC and SMC-like Complexes." *FEMS Microbiology Reviews* 38, no. 3 (May 2014): 380–92. https://doi.org/10.1111/1574-6976.12045.

Nunes-Alves, Cláudio, Matthew G. Booty, Stephen M. Carpenter, Pushpa Jayaraman, Alissa C. Rothchild, and Samuel M. Behar. "In Search of a New Paradigm for Protec-

tive Immunity to TB." *Nature Reviews Microbiology* 12, no. 4 (April 2014): 289–99. https://doi.org/10.1038/nrmicro3230.

Odermatt, Pascal D., Arun Shivanandan, Hendrik Deschout, Radek Jankele, Adrian P. Nievergelt, Lely Feletti, Michael W. Davidson, Aleksandra Radenovic, and Georg E. Fantner. "High-Resolution Correlative Microscopy: Bridging the Gap between Single Molecule Localization Microscopy and Atomic Force Microscopy." *Nano Letters* 15, no. 8 (August 12, 2015): 4896–4904. https://doi.org/10.1021/acs.nanolett.5b00572.

Ogura, Y., N. Ogasawara, E. J. Harry, and S. Moriya. "Increasing the Ratio of Soj to Spo0J Promotes Replication Initiation in Bacillus Subtilis." *Journal of Bacteriology* 185, no. 21 (November 1, 2003): 6316–24. https://doi.org/10.1128/JB.185.21.6316-6324.2003.

Oliferenko, Snezhana. "Understanding Eukaryotic Chromosome Segregation from a Comparative Biology Perspective." *Journal of Cell Science* 131, no. 14 (July 15, 2018): jcs203653. https://doi.org/10.1242/jcs.203653.

Paintdakhi, Ahmad, Bradley Parry, Manuel Campos, Irnov Irnov, Johan Elf, Ivan Surovtsev, and Christine Jacobs-Wagner. "Oufti: An Integrated Software Package for High-Accuracy, High-Throughput Quantitative Microscopy Analysis: Oufti: Image Analysis Software." *Molecular Microbiology* 99, no. 4 (February 2016): 767–77. https://doi.org/10.1111/mmi.13264.

Pandey, S. D., M. Choudhury, S. Yousuf, P. R. Wheeler, S. V. Gordon, A. Ranjan, and M. Sritharan. "Iron-Regulated Protein HupB of Mycobacterium Tuberculosis Positively Regulates Siderophore Biosynthesis and Is Essential for Growth in Macrophages." *Journal of Bacteriology* 196, no. 10 (May 15, 2014): 1853–65. https://doi.org/10.1128/JB.01483-13.

Patino, S., L. Alamo, M. Cimino, Y. Casart, F. Bartoli, M. J. Garcia, and L. Salazar. "Autofluorescence of Mycobacteria as a Tool for Detection of Mycobacterium Tuberculo-

sis." *Journal of Clinical Microbiology* 46, no. 10 (October 1, 2008): 3296–3302. https://doi.org/10.1128/JCM.02183-07.

Pazos, Manuel, Mercedes Casanova, Pilar Palacios, William Margolin, Paolo Natale, and Miguel Vicente. "FtsZ Placement in Nucleoid-Free Bacteria." Edited by Martin G. Marinus. *PLoS ONE* 9, no. 3 (March 17, 2014): e91984. https://doi.org/10.1371/journal.pone.0091984.

Pease, P. J. "Sequence-Directed DNA Translocation by Purified FtsK." *Science* 307, no. 5709 (January 28, 2005): 586–90. https://doi.org/10.1126/science.1104885.

Peña, Carol E.A, Mong Hong Lee, Marisa L Pedulla, and Graham F Hatfull. "Characterization of the Mycobacteriophage L5 Attachment Site, AttP 1 1 Edited by M. Gottesman." *Journal of Molecular Biology* 266, no. 1 (February 1997): 76–92. https://doi.org/10.1006/jmbi.1996.0774.

Pichoff, Sebastien, Shishen Du, and Joe Lutkenhaus. "Disruption of Divisome Assembly Rescued by FtsN–FtsA Interaction in *Escherichia Coli*." *Proceedings of the National Academy of Sciences* 115, no. 29 (July 17, 2018): E6855–62. https://doi.org/10.1073/pnas.1806450115.

Pióro, Monika, Tomasz Małecki, Magda Portas, Izabela Magierowska, Damian Trojanowski, David Sherratt, Jolanta Zakrzewska-Czerwińska, Katarzyna Ginda, and Dagmara Jakimowicz. "Competition between DivIVA and the Nucleoid for ParA Binding Promotes Segrosome Separation and Modulates Mycobacterial Cell Elongation: The Role of ParA-DivIVA Interaction in Mycobacteria." *Molecular Microbiology* 111, no. 1 (January 2019): 204–20. https://doi.org/10.1111/mmi.14149.

Pope, Welkin H., Deborah Jacobs-Sera, Aaron A. Best, Gregory W. Broussard, Pamela L. Connerly, Rebekah M. Dedrick, Timothy A. Kremer, et al. "Cluster J Mycobacterio-

phages: Intron Splicing in Capsid and Tail Genes." Edited by Martin Pavelka. *PLoS ONE* 8, no. 7 (July 9, 2013): e69273. https://doi.org/10.1371/journal.pone.0069273.

Ptacin, Jerod L, Marcelo Nollmann, Eric C Becker, Nicholas R Cozzarelli, Kit Pogliano, and Carlos Bustamante. "Sequence-Directed DNA Export Guides Chromosome Translocation during Sporulation in Bacillus Subtilis." *Nature Structural & Molecular Biology* 15, no. 5 (May 2008): 485–93. https://doi.org/10.1038/nsmb.1412.

Ptacin, Jerod L., Steven F. Lee, Ethan C. Garner, Esteban Toro, Michael Eckart, Luis R. Comolli, W.E. Moerner, and Lucy Shapiro. "A Spindle-like Apparatus Guides Bacterial Chromosome Segregation." *Nature Cell Biology* 12 (July 25, 2010): 791.

Quan, Jiayuan, and Jingdong Tian. "Circular Polymerase Extension Cloning for High-Throughput Cloning of Complex and Combinatorial DNA Libraries." *Nature Protocols* 6, no. 2 (February 2011): 242–51. https://doi.org/10.1038/nprot.2010.181.

Raaphorst, Renske van, Morten Kjos, and Jan-Willem Veening. "Chromosome Segregation Drives Division Site Selection in *Streptococcus Pneumoniae*." *Proceedings of the National Academy of Sciences* 114, no. 29 (July 18, 2017): E5959–68. https://doi.org/10.1073/pnas.1620608114.

Ramirez-Diaz, Diego A., Daniela A. García-Soriano, Ana Raso, Jonas Mücksch, Mario Feingold, Germán Rivas, and Petra Schwille. "Treadmilling Analysis Reveals New Insights into Dynamic FtsZ Ring Architecture." Edited by Jan Löwe. *PLOS Biology* 16, no. 5 (May 18, 2018): e2004845. https://doi.org/10.1371/journal.pbio.2004845.

Rego, E. Hesper, and Lin Shao. "Practical Structured Illumination Microscopy." In *Advanced Fluorescence Microscopy*, edited by Peter J. Verveer, 1251:175–92. New York, NY: Springer New York, 2015. https://doi.org/10.1007/978-1-4939-2080-8_10.

Reyrat, J. M., and D. Kahn. "Mycobacterium Smegmatis: An Absurd Model for Tuberculosis?" *Trends in Microbiology* 9, no. 10 (October 2001): 472–74. https://doi.org/10.1016/s0966-842x(01)02168-0.

Ricard, M., and Y. Hirota. "Process of Cellular Division in Escherichia Coli: Physiological Study on Thermosensitive Mutants Defective in Cell Division." *Journal of Bacteriology* 116, no. 1 (October 1973): 314–22.

Richardson, Tomas T., Omar Harran, and Heath Murray. "The Bacterial DnaA-Trio Replication Origin Element Specifies Single-Stranded DNA Initiator Binding." *Nature* 534, no. 7607 (16 2016): 412–16. https://doi.org/10.1038/nature17962.

Rodrigues, Christopher D. A., and Elizabeth J. Harry. "The Min System and Nucleoid Occlusion Are Not Required for Identifying the Division Site in Bacillus Subtilis but Ensure Its Efficient Utilization." Edited by William F. Burkholder. *PLoS Genetics* 8, no. 3 (March 22, 2012): e1002561. https://doi.org/10.1371/journal.pgen.1002561.

Rowlett, Veronica Wells, and William Margolin. "The Bacterial Min System." *Current Biology* 23, no. 13 (July 2013): R553–56. https://doi.org/10.1016/j.cub.2013.05.024.

Sakatos, Alexandra, Gregory H. Babunovic, Michael R. Chase, Alexander Dills, John Leszyk, Tracy Rosebrock, Bryan Bryson, and Sarah M. Fortune. "Posttranslational Modification of a Histone-like Protein Regulates Phenotypic Resistance to Isoniazid in Mycobacteria." *Science Advances* 4, no. 5 (May 2018): eaao1478. https://doi.org/10.1126/sciadv.aao1478.

Sani, Musa, Edith N. G. Houben, Jeroen Geurtsen, Jason Pierson, Karin de Punder, Maaike van Zon, Brigitte Wever, et al. "Direct Visualization by Cryo-EM of the Mycobacterial Capsular Layer: A Labile Structure Containing ESX-1-Secreted Proteins." Edited by Lalita

Ramakrishnan. *PLoS Pathogens* 6, no. 3 (March 5, 2010): e1000794. https://doi.org/10.1371/journal.ppat.1000794.

Santi, Isabella, Neeraj Dhar, Djenet Bousbaine, Yuichi Wakamoto, and John D. McKinney. "Single-Cell Dynamics of the Chromosome Replication and Cell Division Cycles in Mycobacteria." *Nature Communications* 4, no. 1 (December 2013): 2470. https://doi.org/10.1038/ncomms3470.

Santi, Isabella, and John D. McKinney. "Chromosome Organization and Replisome Dynamics in Mycobacterium Smegmatis." Edited by William Margolin and Steven J. Norris. *MBio* 6, no. 1 (February 17, 2015). https://doi.org/10.1128/mBio.01999-14.

Sao Emani, C., M. J. Williams, P. D. Van Helden, M. J. C. Taylor, C. Carolis, I. J. Wiid, and B. Baker. "Generation and Characterization of Thiol-Deficient Mycobacterium Tuberculosis Mutants." *Scientific Data* 5 (25 2018): 180184. https://doi.org/10.1038/sdata.2018.184.

Shaner, Nathan C, Robert E Campbell, Paul A Steinbach, Ben N G Giepmans, Amy E Palmer, and Roger Y Tsien. "Improved Monomeric Red, Orange and Yellow Fluorescent Proteins Derived from Discosoma Sp. Red Fluorescent Protein." *Nature Biotechnology* 22, no. 12 (December 2004): 1567–72. https://doi.org/10.1038/nbt1037.

Sharadamma, N., Krishnendu Khan, Sandeep Kumar, K. Neelakanteshwar Patil, Seyed E. Hasnain, and K. Muniyappa. "Synergy between the N-Terminal and C-Terminal Domains of Mycobacterium Tuberculosis HupB Is Essential for High-Affinity Binding, DNA Supercoiling and Inhibition of RecA-Promoted Strand Exchange: Mycobacterium Tuberculosis HupB." *FEBS Journal* 278, no. 18 (September 2011): 3447–62. https://doi.org/10.1111/j.1742-4658.2011.08267.x.

Sharpe, M. E., and J. Errington. "Postseptational Chromosome Partitioning in Bacteria." *Proceedings of the National Academy of Sciences* 92, no. 19 (September 12, 1995): 8630–34. https://doi.org/10.1073/pnas.92.19.8630.

Shimomura, O., F. H. Johnson, and Y. Saiga. "Extraction, Purification and Properties of Aequorin, a Bioluminescent Protein from the Luminous Hydromedusan, Aequorea." *Journal of Cellular and Comparative Physiology* 59 (June 1962): 223–39.

Schrager, Lewis K., Rebecca C. Harris, and Johan Vekemans. "Research and Development of New Tuberculosis Vaccines: A Review." *F1000Research* 7 (February 24, 2019): 1732. https://doi.org/10.12688/f1000research.16521.2.

Sharp, M. D., and K. Pogliano. "An in Vivo Membrane Fusion Assay Implicates SpoIIIE in the Final Stages of Engulfment during Bacillus Subtilis Sporulation." *Proceedings of the National Academy of Sciences* 96, no. 25 (December 7, 1999): 14553–58. https://doi.org/10.1073/pnas.96.25.14553.

Shin, Jae Yen, Javier Lopez-Garrido, Sang-Hyuk Lee, Cesar Diaz-Celis, Tinya Fleming, Carlos Bustamante, and Kit Pogliano. "Visualization and Functional Dissection of Coaxial Paired SpoIIIE Channels across the Sporulation Septum." *ELife* 4 (May 7, 2015): e06474. https://doi.org/10.7554/eLife.06474.

Shires, K., and L. Steyn. "The Cold-Shock Stress Response in Mycobacterium Smegmatis Induces the Expression of a Histone-like Protein: Cold-Shock Stress Response in M. Smegmatis." *Molecular Microbiology* 39, no. 4 (December 21, 2001): 994–1009. https://doi.org/10.1046/j.1365-2958.2001.02291.x.

Singh, Bhupender, Ram Gopal Nitharwal, Malavika Ramesh, B. M. Fredrik Pettersson, Leif A. Kirsebom, and Santanu Dasgupta. "Asymmetric Growth and Division in *Mycobacterium* Spp.: Compensatory Mechanisms for Non-Medial Septa: Asymmetric Growth

and Division in Mycobacteria." *Molecular Microbiology* 88, no. 1 (April 2013): 64–76. https://doi.org/10.1111/mmi.12169.

Sivanathan, Viknesh, Jenny E. Emerson, Carine Pages, François Cornet, David J. Sherratt, and Lidia K. Arciszewska. "KOPS-Guided DNA Translocation by FtsK Safeguards *Escherichia Coli* Chromosome Segregation." *Molecular Microbiology* 71, no. 4 (February 2009): 1031–42. https://doi.org/10.1111/j.1365-2958.2008.06586.x.

Slayden, R. A. "Identification of Cell Cycle Regulators in Mycobacterium Tuberculosis by Inhibition of Septum Formation and Global Transcriptional Analysis." *Microbiology* 152, no. 6 (June 1, 2006): 1789–97. https://doi.org/10.1099/mic.0.28762-0.

Söderström, Bill, Alexander Badrutdinov, Helena Chan, and Ulf Skoglund. "Cell Shape-Independent FtsZ Dynamics in Synthetically Remodeled Bacterial Cells." *Nature Communications* 9, no. 1 (October 18, 2018): 4323. https://doi.org/10.1038/s41467-018-06887-7.

Stouf, M., J.-C. Meile, and F. Cornet. "FtsK Actively Segregates Sister Chromosomes in Escherichia Coli." *Proceedings of the National Academy of Sciences* 110, no. 27 (July 2, 2013): 11157–62. https://doi.org/10.1073/pnas.1304080110.

Sukumar, Neelima, Shumin Tan, Bree B. Aldridge, and David G. Russell. "Exploitation of Mycobacterium Tuberculosis Reporter Strains to Probe the Impact of Vaccination at Sites of Infection." Edited by Padmini Salgame. *PLoS Pathogens* 10, no. 9 (September 18, 2014): e1004394. https://doi.org/10.1371/journal.ppat.1004394.

Sullivan, Nora L., Kathleen A. Marquis, and David Z. Rudner. "Recruitment of SMC by ParB-ParS Organizes the Origin Region and Promotes Efficient Chromosome Segregation." *Cell* 137, no. 4 (May 2009): 697–707. https://doi.org/10.1016/j.cell.2009.04.044.

Surovtsev, Ivan V., and Christine Jacobs-Wagner. "Subcellular Organization: A Critical Feature of Bacterial Cell Replication." *Cell* 172, no. 6 (March 2018): 1271–93. https://doi.org/10.1016/j.cell.2018.01.014.

Surovtsev, Ivan V., Hoong Chuin Lim, and Christine Jacobs-Wagner. "The Slow Mobility of the ParA Partitioning Protein Underlies Its Steady-State Patterning in Caulobacter." *Biophysical Journal* 110, no. 12 (June 2016): 2790–99. https://doi.org/10.1016/j.bpj.2016.05.014.

Swindells, Susan. "New Drugs to Treat Tuberculosis." *F1000 Medicine Reports*, June 1, 2012. https://doi.org/10.3410/M4-12.

Taylor, James A., Gaël Panis, Patrick H. Viollier, and Gregory T. Marczynski. "A Novel Nucleoid-Associated Protein Coordinates Chromosome Replication and Chromosome Partition." *Nucleic Acids Research* 45, no. 15 (September 6, 2017): 8916–29. https://doi.org/10.1093/nar/gkx596.

Toniolo, Chiara, Matthieu Delincé, and John D. McKinney. "A Microfluidic Cell-Trapping Device to Study Dynamic Host-Microbe Interactions at the Single-Cell Level." In *Methods in Cell Biology*, 147:199–213. Elsevier, 2018. https://doi.org/10.1016/bs.mcb.2018.06.008.

Trojanowski, Damian, Katarzyna Ginda, Monika Pióro, Joanna Hołówka, Partycja Skut, Dagmara Jakimowicz, and Jolanta Zakrzewska-Czerwińska. "Choreography of the Mycobacterium Replication Machinery during the Cell Cycle." Edited by William Margolin and Steven J. Norris. *MBio* 6, no. 1 (February 17, 2015): e02125-14. https://doi.org/10.1128/mBio.02125-14.

Trojanowski, Damian, Joanna Hołówka, Katarzyna Ginda, Dagmara Jakimowicz, and Jolanta Zakrzewska-Czerwińska. "Multifork Chromosome Replication in Slow-Growing Bacteria." *Scientific Reports* 7 (06 2017): 43836. https://doi.org/10.1038/srep43836.

Uhía, Iria, Miles Priestman, Graham Joyce, Nitya Krishnan, Vahid Shahrezaei, and Brian D. Robertson. "Analysis of ParAB Dynamics in Mycobacteria Shows Active Movement of ParB and Differential Inheritance of ParA." Edited by Joyoti Basu. *PLOS ONE* 13, no. 6 (June 19, 2018): e0199316. https://doi.org/10.1371/journal.pone.0199316.

Viollier, P. H., M. Thanbichler, P. T. McGrath, L. West, M. Meewan, H. H. McAdams, and L. Shapiro. "From The Cover: Rapid and Sequential Movement of Individual Chromosomal Loci to Specific Subcellular Locations during Bacterial DNA Replication." *Proceedings of the National Academy of Sciences* 101, no. 25 (June 22, 2004): 9257–62. https://doi.org/10.1073/pnas.0402606101.

Wada, M., Y. Kano, T. Ogawa, T. Okazaki, and F. Imamoto. "Construction and Characterization of the Deletion Mutant of HupA and HupB Genes in Escherichia Coli." *Journal of Molecular Biology* 204, no. 3 (December 5, 1988): 581–91.

Wakamoto, Yuichi, Neeraj Dhar, Remy Chait, Katrin Schneider, François Signorino-Gelo, Stanislas Leibler, and John D. McKinney. "Dynamic Persistence of Antibiotic-Stressed Mycobacteria." *Science* 339, no. 6115 (January 4, 2013): 91–95. https://doi.org/10.1126/science.1229858.

Wang, L., and J. Lutkenhaus. "FtsK Is an Essential Cell Division Protein That Is Localized to the Septum and Induced as Part of the SOS Response." *Molecular Microbiology* 29, no. 3 (August 1998): 731–40.

Wang, X. "Dancing around the Divisome: Asymmetric Chromosome Segregation in Escherichia Coli." *Genes & Development* 19, no. 19 (October 1, 2005): 2367–77. https://doi.org/10.1101/gad.345305.

Wang, Xindan, Paula Montero Llopis, and David Z. Rudner. "Organization and Segregation of Bacterial Chromosomes." *Nature Reviews Genetics* 14 (February 12, 2013): 191.

Wang, X., P. Montero Llopis, and D. Z. Rudner. "Bacillus Subtilis Chromosome Organization Oscillates between Two Distinct Patterns." *Proceedings of the National Academy of Sciences* 111, no. 35 (September 2, 2014): 12877–82. https://doi.org/10.1073/pnas.1407461111.

Whiteford, D. C., J. J. Klingelhoets, M. H. Bambenek, and J. L. Dahl. "Deletion of the Histone-like Protein (Hlp) from Mycobacterium Smegmatis Results in Increased Sensitivity to UV Exposure, Freezing and Isoniazid." *Microbiology* 157, no. 2 (February 1, 2011): 327–35. https://doi.org/10.1099/mic.0.045518-0.

Woong Park, Sae, Marcus Klotzsche, Daniel J. Wilson, Helena I. Boshoff, Hyungjin Eoh, Ujjini Manjunatha, Antje Blumenthal, et al. "Evaluating the Sensitivity of Mycobacterium Tuberculosis to Biotin Deprivation Using Regulated Gene Expression." Edited by Marcel A. Behr. *PLoS Pathogens* 7, no. 9 (September 29, 2011): e1002264. https://doi.org/10.1371/journal.ppat.1002264.

Wu, Katherine J., Jenna Zhang, Catherine Baranowski, Vivian Leung, E. Hesper Rego, Yasu S. Morita, Eric J. Rubin, and Cara C. Boutte. "Characterization of Conserved and Novel Septal Factors in *Mycobacterium Smegmatis*." Edited by Yves V. Brun. *Journal of Bacteriology* 200, no. 6 (January 8, 2018). https://doi.org/10.1128/JB.00649-17.

Wu, Ling Juan, and Jeff Errington. "A Large Dispersed Chromosomal Region Required for Chromosome Segregation in Sporulating Cells of Bacillus Subtilis." *The EMBO Journal* 21, no. 15 (August 1, 2002): 4001–11. https://doi.org/10.1093/emboj/cdf393.

Wu, Ling Juan, and Jeff Errington. "Nucleoid Occlusion and Bacterial Cell Division." *Nature Reviews Microbiology* 10 (October 24, 2011): 8.

Zhou, Xiaoxue, Frances P. Rodriguez-Rivera, Hoong Chuin Lim, Jason C. Bell, Thomas G. Bernhardt, Carolyn R. Bertozzi, and Julie A. Theriot. "Sequential Assembly of the Septal Cell Envelope Prior to V Snapping in Corynebacterium Glutamicum." *Nature Chemical Biology* 15, no. 3 (2019): 221–31. https://doi.org/10.1038/s41589-018-0206-1.

Curriculum Vitae

Joëlle Xiao Yuan Ven   09.02.1986
Rue du Lac 49   Swiss & Hong Kong ID
1020 Renens   Single
+41 78 666 36 86
joelle.ven@epfl.ch

EMPLOYMENT HISTORY

- **Swiss Federal Institute of Technology (EPFL)**, Lausanne, Laboratory of Microbiology and Microsystems, Doctoral Assistant, Single-cell studies of *Mycobacterium smegmatis* cell cycle using time-lapse fluorescence microscopy, 2014 - present

- **Baxter Biosciences**, Neuchâtel, Microbiology Sterility Expert, Validation of analytical methods (LAL, bioburden), 2014

- **Baxter Biosciences**, Neuchâtel, Quality Analyst, Analysis and validation of analytical methods (LAL, bioburden), 2012 - 2013

- **Baxter Biosciences**, Neuchâtel, Quality Analyst, Analysis for the factor VIII product and environment sterility. Participated in investigation and projects, 2011-2012

- **Nestlé Health Science,** Lutry, R&D, Internship, Recipe Management and Regulatory Affairs Department. Compliance tests on the Nestlé Healthcare products according to the Nestlé Foundation Guidelines and Selling Country Legislations, 2011

- **National University of Singapore**, Singapore, Master thesis, Research laboratory of Developmental Genetics 4, "Development of a positive and negative drug selection system towards gene correction in Medakafish haploid ES cells". Molecular biology, cell culture, transfection, and microscopy, 2009 - 2010.

  Swiss institute for experimental Cancer research (ISREC), Epalinges, Internship, Virology laboratory, "Influence of the MRN complex on Adeno-associated virus repli-

cation". Cell culture, cell infection, immunofluorescence and microscopy. (2 weeks in 2006 and 4 months in 2007)

EDUCATION

- o **Master of Science in Molecular Medicine and Oncology**, Swiss Federal Institute of Technology (EPFL), Lausanne, Life Sciences Faculty, 2008 - 2010

- o **Bachelor in Life Sciences and Technologies**, Swiss Federal Institute of Technology (EPFL), Lausanne, Life Sciences Faculty, 2004 - 2008

- o **Bilingual (English-French) Swiss Federal Maturity**, Denis-de-Rougemont High School with honors, Neuchâtel, maturity work very good, 2001 – 2004

PROFESSIONAL QUALIFICATIONS & COMPUTER SKILLS

- o Time-lapse fluorescence microscopy, microfluidics, atomic force microscopy, western blot, immunoprecipitation, cloning techniques, molecular biology, genomic DNA extraction for PacBio sequencing, image analysis.

- o LAL, Bioburden, Validation, GMP & GLP practices

- o Fiji, Prism, Ilustrator, Snapgene, Microsoft Office, Basic Matlab, Minitab

AWARDS

- o Lycée Denis de Rougemont award for the best English average for a non-native English student, (2001-2004)

- o EPFL Award for the best project in Molecular Medicine and Oncology master (2009-2010)

LANGUAGES

French: Mother Tongue

English: Fluent, C1 Level, Professional experience, lived 5 years in Hong Kong

German: Basic, B1 Level

Chinese: Basic, A2 Level, Lived 5 years in Hong Kong

PUBLICATIONS

H.A. Eskandarian, P.D. Odermatt, J.X.Y. Ven, M.T.M. Hannebelle, A.P. Nievergelt, N. Dhar, J.D. McKinney, G. E. Fantner, Division site selection linked to inherited cell surface wave troughs in mycobacteria, *Nature Microbiology* **volume 2**, Article number: 17094 (2017)

Mélanie T. M. Hannebelle, Joëlle X. Y. Ven, Chiara Toniolo, Haig A. Eskandarian, Gaëlle Vuaridel, John D. McKinney, Georg E. Fantner, Pole elongation in mycobacteria resembles biphasic "new end take off" (NETO) dynamics in fission yeast (in review).

Joëlle X. Y. Ven, Mélanie T. M. Hannebelle, John D. McKinney, Georg E. Fantner, Live-cell imaging of mycobacterial chromosomes with fluorescently tagged histone-like protein (Hlp) (in preparation).

INTERESTS

Triathlon, Diving (PADI certificates acquired in October 2002, December 2010 and June 2018), Ski, Badminton, Photography and Drawing.

Chapter 9 Appendix - Division site selection linked to inherited cell surface wave troughs in mycobacteria

Haig A. Eskandarian[1,2], Pascal D. Odermatt[2], Joëlle X. Y. Ven[1,2], Mélanie T. M. Hannebelle[1,2], Adrian P. Nievergelt[2], Neeraj Dhar[1], John D. McKinney[1]*[†]and Georg E. Fantner[2]*[†]

Affiliations:

[1]School of Life Sciences, Swiss Federal Institute of Technology in Lausanne (EPFL), 1015 Lausanne, Switzerland

[2]School of Engineering, Swiss Federal Institute of Technology in Lausanne (EPFL), 1015 Lausanne, Switzerland

[†]These authors contributed equally to this work.

*Correspondence to: john.mckinney@epfl.ch or georg.fantner@epfl.ch

9.1   My contributions :

- Determining how to prepare the sample for AFM imaging

- Building the homemade heated bubble trap (with Adrian Nievergelt) and fluidic system to image with the multimode AFM.

- Imaging by AFM (with and without INH), (which enabled Figure 1a, suppl. Figure 2 a, b, c, suppl. Figure 3).

- Electroporating FtsZ-GFP plasmid and confirming that the strain was correct by colony PCR and sequencing (which enabled Figure 3 a, c, suppl. figure 12, suppl. figure 13)

- Characterizing wt and Δ*parB* strain for distribution of division site selection, (Figure 4a)

- Imaging by AFM and using the microfluidic device to determine the optimal Ciprofloxacin conditions to induce filamentation. Further experiments were done (which enabled Figure 4e)

- SYTO17 staining in Δ*parB* cells optimization and imaging. Traces of cells with symmetric and asymmetric partitioning before and after cytokinesis (Figure 4d)

- Anucleate cells with division at the old, center or new pole (suppl. Figure 17a)

- Average signal in the anucleate part of the cell and nucleated part of the cell (suppl. Figure 17b)

-

9.2 Supplementary information:

https://www.nature.com/articles/nmicrobiol201794#s1

9.3 Abstract

Cell division is tightly controlled in space and time to maintain cell size and ploidy within narrow bounds. In bacteria, the canonical Minicell (Min) and nucleoid occlusion (Noc) systems together ensure that division is restricted to midcell after completion of chromosome segregation. It is unknown how division site selection is controlled in bacteria that lack homologues of the Min and Noc proteins, including mycobacteria responsible for tuberculosis and other chronic infections. Here, we use correlated optical and atomic force microscopy 3,4 to demonstrate that morphological landmarks (waveform troughs) on the undulating surface of mycobacterial cells correspond to future sites of cell division. New-born cells inherit wave troughs from the (grand)mother cell and ultimately divide at the centre-most wave trough, making these morphological features the earliest known land-mark of future division sites. In cells lacking the chromosome partitioning (Par) system, missegregation of chromosomes is accompanied by asymmetric cell division at off-centre wave troughs, resulting in the formation of anucleate cells. These results demonstrate that inherited morphological landmarks and chromosome positioning together restrict myco-bacterial division to the midcell position.

9.4 Introduction and results

Atomic force microscopy (AFM) has been used previously for static 5,6 or short-term time-lapse imaging of mycobacteria, primarily to study the impact of antibiotics and antimicrobial peptides on nanoscale features of the mycobacterial cell surface. Here, we

use long-term time-lapse AFM to track cell growth and division over multiple generations in Mycobacterium smegmatis, a non-pathogenic relative of Mycobacterium tuberculosis (Fig. 1a, Supplementary Videos 1 and 2 and Supplementary Figs 1 and 2). Unexpectedly, we found that the cell surface undulates along the long axis (Fig. 1b,c) in a roughly repeating waveform pattern with an average wavelength of~1.8 μm (Supplementary Fig. 3). These morphological features are too small in amplitude (~100 nm from wave crest to wave trough) to resolve by conventional optical microscopy and they are morphologically distinct from the previously described 'division scars' (Supplementary Fig. 4, last panel, black arrow). Cell elongation is accompanied by an increase in wave trough number, as cells, on average, are born with three wave troughs and divide with four wave troughs after elongation by 2 μm (Supplementary Table 1). In contrast, the distance between wave troughs does not scale with increasing cell length. Cells filamented with ciprofloxacin exhibit a greater number of wave troughs as a function of increased cell length (Supplementary Fig. 6). Conversely, blocking cell elongation with isoniazid (Supplementary Fig. 2a) prevents the formation of new wave troughs (Supplementary Fig. 7). While the undulating surface morphology is maintained in isoniazid-treated cells, height increases along the cell length (Supplementary Figs 2b and 8), possibly due to sustained metabolic activity. In time-lapse series, we found that centrally located wave troughs correspond to future sites of cell division (Fig. 1c and Supplementary Figs 9–11). The center-most wave trough is localized, on average, at 56% of the cell length relative to the old cell pole, ranging from 49% to 62% (25th to 75th percentiles, respectively). Remarkably, wave troughs that mark future division sites are already present at birth —they form near the cell poles in the mother, grandmother or great-grandmother cell and are passed on to the daughter cells at division (Fig. 2a,b, Supplementary Fig. 11 and Supplementary Table 1). On average, division at a wave trough occurs 1.3 generations after the trough is first established (Fig. 2b and Supplementary Table 1), which corresponds to~4 h for cells growing with an average interdivision time of~3 h (Fig. 2c). Cell elongation gradually shifts the position of wave troughs towards the cell center (Fig. 2a, Supplementary Video 2 and Supplementary Figs 4 and 11).

Inherited wave troughs localize to positions near the midcell~150 min before cell cleavage. In cells inheriting multiple wave troughs, the amount of growth from each cell pole deter-mines which wave trough is located closest to the midcell and becomes the division site. Depletion of RipA, a hydrolase essential for cleavage, results in chains of non-separated daughter cells; cells located internal to the chain (with no free ends) do not elongate and do not form new wave troughs, although they may still form septa within pre-existing wave troughs (Supplementary Video 3 and Supplementary Fig. 5). In a microscope that combines optical (fluorescence) and low-noise AFM-based imaging, time-lapse imaging of single cells revealed a sequence of morphological and molecular events leading up to cell division. Formation of the FtsZ contractile ring at midcell is thought to be the earliest event specifying the cell division site in rod-shaped bacteria 1, 11. In cells expressing FtsZ tagged with green fluorescent protein (GFP), we found that the FtsZ ring forms within a pre-existing wave trough near midcell (Fig. 3a). In cells growing with an average interdivision time of 190 min, formation of the pre-divisional wave trough precedes formation of the FtsZ ring by 120 min on average. Cells filamented with mitomycin C exhibit the formation of multiple FtsZ rings at multiple wave troughs (Supplementary Fig. 12). Formation of the FtsZ-GFP ring near midcell (Fig. 3a and Supplementary Video 4) is followed~30 min later by the appearance of a co-localized 'pre-cleavage furrow' (~50 nm wide and~10 nm deep) in the AFM image, a distinctive topological feature that is too small to detect by optical mi-croscopy (Fig. 3a, black arrows). This feature might correspond to the previously reported 'cell wall.
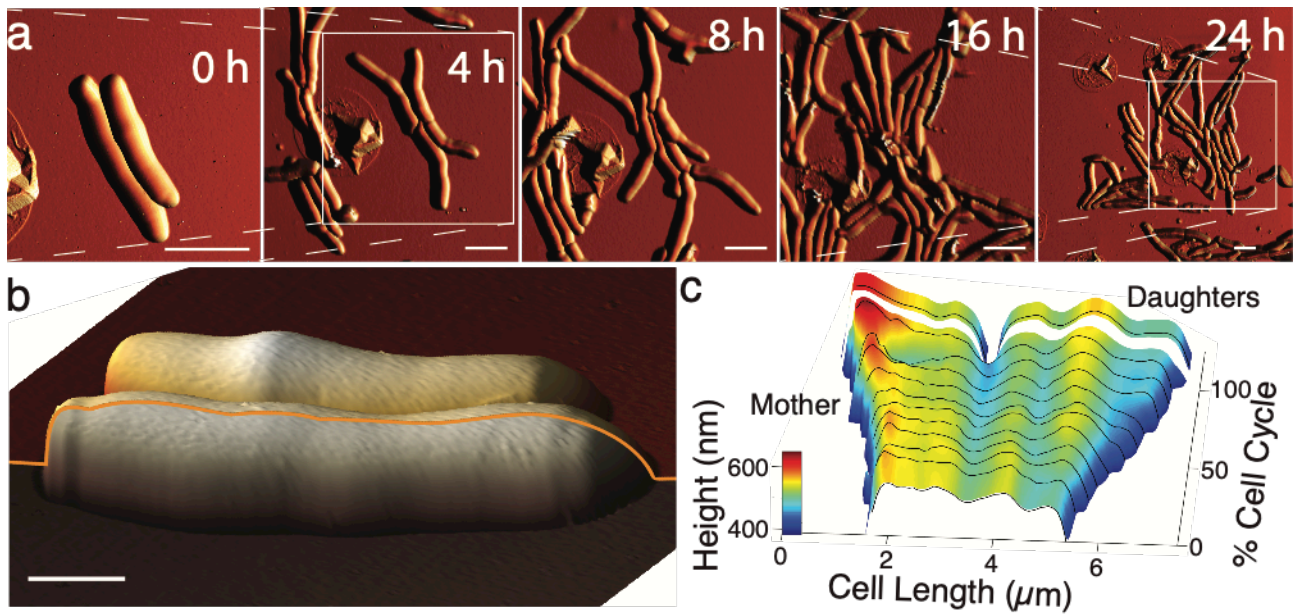
Figure 68 - Figure 1 | Mycobacterial cells divide at cell surface wave troughs.

(A) Time series of three-dimensional AFM height images overlaid with AFM peak force error images for wild-type *M. smegmatis*. Scale bar, 3µm.b, Mycobacterial surface topology. Yellow trace of the cell profile, highlighting the undulating mycobacterial surface morphology. Scale bar, 1µm.c, Kymograph of the cell surface height of a representative cell from birth to division, showing that division occurs within the center-most wave trough. In **(B)** and **(C)**, images are representative of n= 270.
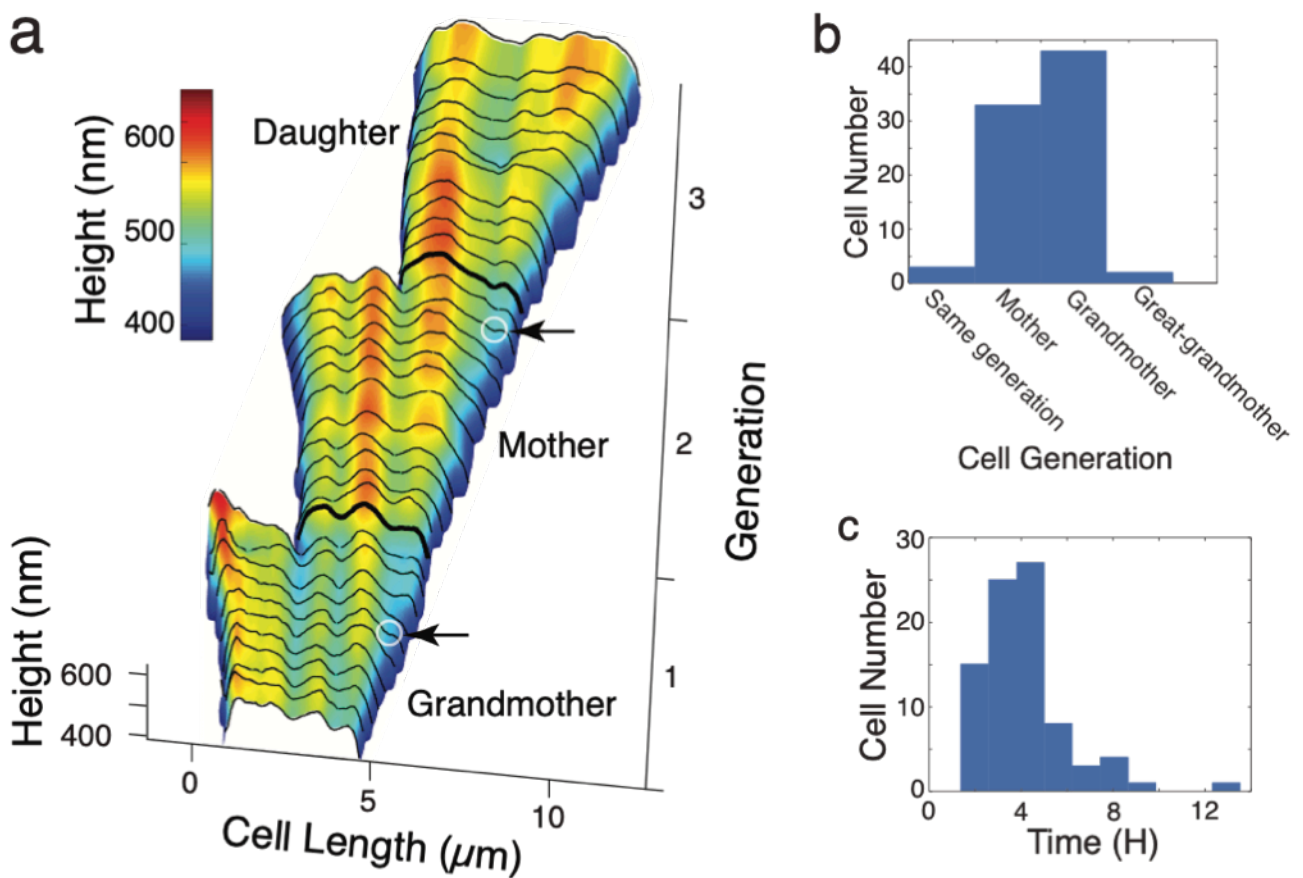
Figure 69- Figure 2 | Wave troughs are inherited from the (grand) mother cell.

(A) Kymograph of cell heights of one cell lineage over three consecutive generations (bottom to top). A wave trough formed in the grandmother cell (arrow) becomes the division site in the mother cell. Similarly, a wave trough formed in the mother cell (arrow) becomes the division site in the daughter cell. The kymograph represents 234 trios of related cells (grandmother–mother–daughter) from 18 unrelated cell lineages. **(B)** Distribution of generations from wave trough formation to cell cleavage. The wave trough where division occurs in the daughter cell (generation 0) is usually formed in the mother cell (generation 1), grandmother cell (generation 2) or great-grandmother cell (generation 3). n= 82 cells. **(C)**, Distribution of time intervals from wave trough formation to cell cleavage. n= 82 cells.

contractile ring' in Mycobacterium sp. JLS, although the latter has been described as a cell surface protrusion rather than an indentation. The pre-cleavage furrow appears at around the same time as the early stages of septum formation, which we visualized by staining the cell membrane with the fluorescent dye FM4-64 (Fig. 3b, Supplementary Fig. 13 and Sup-

plementary Videos 5 and 6). These events precede cytokinesis by~20 min in cells expressing8the cytokinetic marker Wag31-GFP (Fig. 3c and Supplementary Video 7). Cytokinesis is followed by a lag period of~40 min10before physical cleavage of the sibling cells, signaled by an abrupt11 deepening of the pre-cleavage furrow to~100 nm (Fig. 3 and12 Supplementary Video 7). Most mycobacterial cells inherit multiple wave troughs at birth, yet only the center-most wave trough is ultimately selected as the division site. We asked whether off-center wave troughs could16function as alternative sites of cell division in cells lacking the
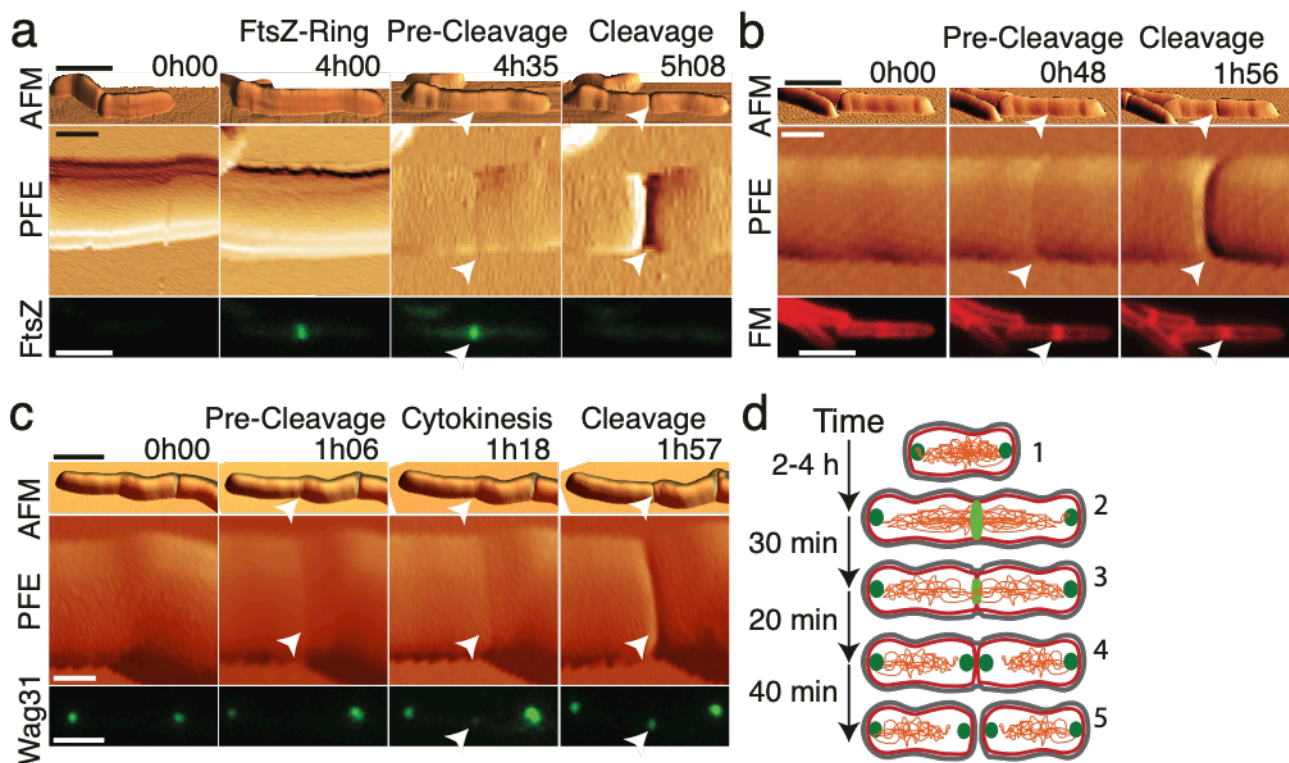
Figure 70 - Figure 3 |Sequence of events from cell birth to cell division.

(A) Cells were imaged by correlated AFM (upper and middle panels) and fluorescence microscopy (bottom panels). Upper panels: three-dimensional representations of AFM topography images. Middle panels: AFM peak force error, which lights the appearance of the pre-cleavage furrow and cleavage (white arrowheads). Numbers indicate time elapsed since birth. Scale bars (upper and bottom), 3μm;(middle), 500 nm. Images are representative of n> 10.a, Cells expressing FtsZ-GFP. The FtsZ ring co-localizes with the pre-cleavage

furrow (images are representative of n= 17). **(B)** Cells with FM4-64-stained plasma membrane. Septum invagination co-localizes with the pre-cleavage furrow (images are representative of n= 15). **(C)** Cells expressing the cytokinesis marker Wag31-GFP. Cytokinesis is completed before cell cleavage (images are representative ofn= 50). **(D)** Schematic of the sequence of events culminating in cell division. At birth, Wag31-GFP (dark green) localizes exclusively at the cell poles (1). FtsZ-GFP (light green) forms a circumferential ring within the central wave trough (2–3). A pre-cleavage furrow then appears (indentation in the outer grey layer of the cell surface) and co-localizes with the FtsZ ring (3). Septum formation then proceeds and culminates in cytokinesis, which is marked by the appearance of a Wag31-GFP ring that co-localizes with the pre-cleavage furrow (4). Cell cleavage results in physical separation of the newborn sibling cells (5).

ParB chromosome-partitioning protein. Consistent with recent studies12–14, we found that ΔparB cells frequently undergo asymmetric cell divisions (Fig. 4a) within off-center wave troughs (Fig. 4b,c and Supplementary Fig. 14). Divisions occurring at off-center wave troughs are skewed towards the old or new cell6pole (15% or 25%, respectively), with the remainder of divisions (60%) occurring at the center-most wave trough. Divisions in ΔparB cells often occur in newly formed wave troughs (Supplementary Fig. 15). Time-lapse fluorescence microscopy revealed that midcell divisions in ΔparB cells are associated with normal chromosome partitioning (Fig. 4d). We never observed divisions occurring at a local DNA maximum (Supplementary Figs 16 and 17). These results suggest that chromosomes might play a negative regulatory role in determining which wave trough is selected as the division site. Cells treated with the DNA gyrase inhibitor ciprofloxacin form elongated filaments with multiple wave troughs (Fig. 4e,first time point). Appearance of a pre-cleavage furrow in afilamented19cell corresponds spatially to a local DNA minimum (Fig. 4e, arrows; Supplementary Fig. 6b and 6c). Previous studies using AFM6,7,15, electron cryotomography16,17,22or scanning electron microscopy8identified a variety of bacterial surface features associated with initiation or completion of cell division. To the best of our knowledge, inherited morphological features associated with division site selection have not been identified until now. Although the well-characterized Min and Noc systems serve as negative regulators of FtsZ ring formation in evolutionarily divergent bacteria, emerging evidence suggests that these systems might not be responsible for initial specification of

the division site per se1. Rather, these mechanisms may function at later steps to help ensure that the FtsZ ring forms only at an appropriate place (distant from the cell poles and membrane-tethered DNA) and at the correct time relative to nucleoid segregation. What, then, are the mechanisms responsible for specifying the future division site? In Streptococcus pneumoniae, the MapZ protein localizes as a circumferential band at midcell and sets the orientation of the FtsZ ring. However, most bacteria, including mycobacteria, do not encode a MapZ homologue. We show here that mycobacterial cell division occurs within wave troughs on the undulating cell surface. Various bacterial proteins are known to localize to negative or positive membrane curvatures. Mycobacterial proteins that target curved membranes within wave troughs might serve as beacons for FtsZ ring assembly, while proteins with preferential affinity for wave crests might serve to repress division. Alternatively, peptidoglycan architecture might direct the formation of surface undulations and mark wave troughs as future division sites. In spirochetes, peptidoglycan crosslinking has been reported to impact cell shape and to direct the division machinery to an inherited zone of active peptidoglycan synthesis. Although mycobacterial wave troughs are preferred sites for cell division, chromosomes also seem to play a negative regulatory role in division site selection. Unlike wild-type cells, which always divide within a center-most wave trough, strains with defects in chromo- some partitioning divide asymmetrically at an off-center wave trough when unpartitioned chromosomes are retained in the distal cell half. These observations suggest that mycobacteria might possess a mechanism analogous but not homologous to the Noc system to prevent cell division over unsegregated chromosomes. Like Noc, this mechanism might serve as a 'failsafe' when chromosome replication or partitioning is severely impaired, as in ParB-deficient cells. In wild-type mycobacteria, nascent septa have been observed to form over chromosomes that are still in the process of segregating, and assembly of FtsZ rings over chromosomes has been observed in E. coli with diffuse nucleoids. These
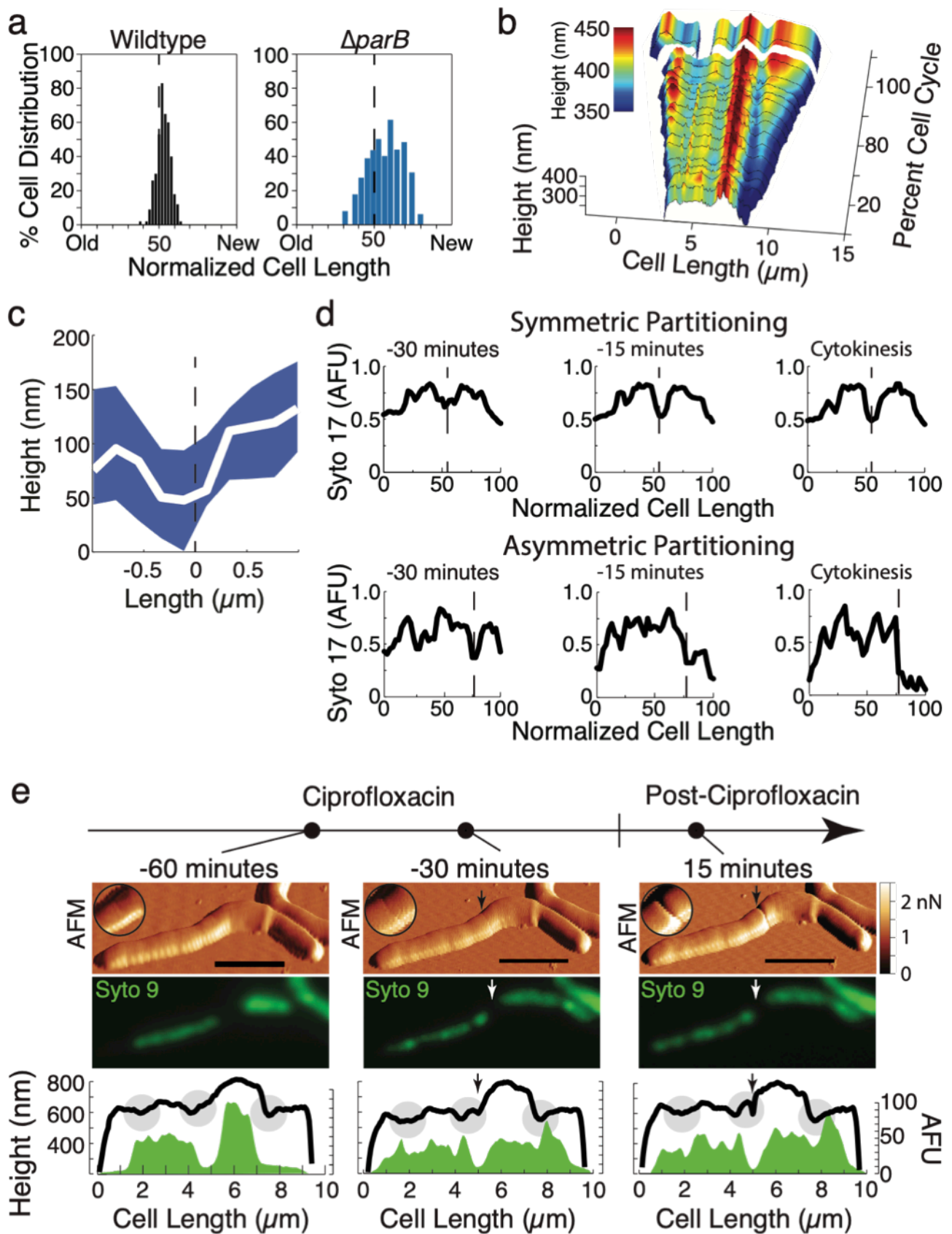
Figure 71 - Figure 4 |Asymmetric divisions occur at off-centre wave troughs.

(A) Distribution of division site selection in wild-type cells (black histogram) (n= 520) and ΔparB cells (blue histogram) (n= 278). **(B)** Kymograph of cell height of a representative ΔparB cell from birth to division, showing asymmetric division within an off-center wave trough (n= 27). **(C)** Averaged surface height around future sites of off-center divisions (n= 27). White line: average height within a range ± 1µm in each direction of the cleavage site. Blue background: variation (25th and 75th percentiles) in surface height. **(D)** Representative graphs depicting the distribution of DNA along the cell length of ΔparB cells at 30, 15 and 0 min before cytokinesis. Top: examples of symmetric nucleoid partitioning (n= 18). Bottom: examples of asymmetric nucleoid partitioning leading to the formation of an anucleate new-pole daughter cell (n= 48). Dashed lines correspond to future division sites, which often correspond to local minima of chromosomal DNA. **(E)** AFM (upper) and fluorescence (middle) images of a representative wild-type cell before (−60 and−30 min) and after (+15 min) release from a ciprofloxacin block. Longitudinal height profiles (black lines) stacked on top of DNA profiles (green plots) of the same cell show that the future division site (arrows) occurs at a local DNA minimum within a wave trough (grey shaded circle). AFM images are three-dimensional representations of the height with the peak force error (PFE) signal overlaid as a skin. The PFE signal scale baris expressed in nN. Scales bar (AFM images), 3µm. Image sequence is representative of n=7.

observations suggest that the degree of nucleoid concentration or compaction might affect the activity of the nucleoid occlusion system. We propose a bipartite model of division site selection, in which cell-surface wave troughs are 'licensed' sites for cell division and segregated chromosomes suppress division at off-center wave troughs. Although the molecular factors involved in division site selection in mycobacteria are unknown, the observation that cell divisions occur within wave troughs will refocus the search for such factors to a point much earlier in time than FtsZ ring formation, which is currently the earliest known event in division site selection in rod-shaped bacteria.

9.4.1 Methods

Bacteria. Mycobacterium smegmatis mc²155 (wild-type) and derivative strains were grown in Middlebrook 7H9 liquid medium (Difco) supplemented with 0.5% albumin, 0.2% glucose, 0.085% NaCl, 0.5% glycerol and 0.05% Tween-80. Cultures were grown at 37 °C to mid-

exponential phase (optical density at 600 nm (OD600) of~0.5). Aliquots were stored in 15% glycerol at−80 °C and thawed at room temperature before use. The ΔparB strain with an unmarked in-frame deletion of the parB gene has been described previously[13]. The attB-integrating plasmid expressing a Wag31-GFP fusion protein has also been described previously [2]. The Mycobacterium smegmatis RipA conditional knockdown strain was cultured and manipulated as described previously[10]. Wild-type cells were filamented with 500 ng ml^{-1} Ciprofloxacin (Sigma) or 50 ng ml^{-1}mitomycin C (Sigma).

FtsZ-GFP reporter. The open reading frame (ORF) encoding M. smegmatis FtsZ was PCR-amplified using primers MsmftsZ-F (gctagcatgacccccccgcataactacctcg) and MsftsZ-R (ggactagttcctcctgatcctcctccacctgaaccaccaccacctgaaccaccaccac-ctgaaccaccggt9gtgccgcatgaagggcg) with genomic DNA as the template. The underlined sequence in primer MsmftsZ-R represents the linker sequence encoding four repeats of Gly-Gly-Ser-Gly-Gly. The amplicon was ligated into vector pCR2.1 (Invitrogen) and verified by DNA sequencing, then excised as an NheI-SpeI fragment and ligated into the unique NheI site in the attB-integrating vector pND250, which encodes a hygromycin resistance marker. The resulting plasmid (pND275, provided by N. Dhar) expresses ftsZ-gfp (in-frame fusion) from a strong anhydrotetracycline (ATc)-inducible promoter. pND275 was electroporated into M. smegmatisand transformants were selected by plating on solid medium containing 50 μg ml^{-1} hygromycin (Sigma).

Microscopy. For time-lapse fluorescence microscopy, bacteria were grown to mid-exponential phase (OD600≈0.5) in 7H9 liquid medium, collected by centrifugation (2,400g, 5 min), concentrated 30-fold in fresh 7H9 medium (37 °C) and passed through a polyvinylidene difluoride syringe filter (Millipore, 5 μm pore size) to remove clumps. The declumped bacteria were spread on a glass coverslip, covered with a semipermeable membrane and cultured in a custom-made microfluidic device with a continuous flow of 7H9 medium at 37 °C (flow rate, 25 μl min^{-1}), as described previously[26]. Nucleoid staining was accomplished by adding SYTO 17 Red (170 nM final) in the flow medium. Bacteria were imaged at

15 min intervals with a DeltaVision personal DV microscope (Applied Precision) equipped with a ×100 oil-immersion objective and in an environmental chamber maintained at 37 °C (ref. 2). Images were recorded on phase-contrast and fluorescence channels (475/28 nm excitation and 525/48 nm emission filters for FITC; 575/25 nm excitation and 632/22 nm emission filters for CY-5) with a CoolSnap HQ2 camera.

AFM. Coverslips were prepared by mixing polydimethylsiloxane (PDMS) (Sylgard184, Dow Corning) at a ratio of 15:1 (elastomer: curing agent). Air bubbles in the mixture were re-moved under negative pressure for 15 min. The PDMS mixture was dropped onto a 22 mm glass coverslip (VWR) and spin-coated at 8,000 r.p.m. (SUSS MicroTec LabSpin6) for 30 s. PDMS-coated coverslips were baked at 80 °C for 10 min before use. A 3 ml aliquot of mid-exponential phase cell culture was filtered through a 5 μm pore size PVDF filter (Millipore) to remove cell clumps and concentrated into 200 ml final volume by pelleting cells (2,400g, 8 min). A 50 μl aliquot was deposited on the hydrophobic surface of a PDMS-coated co-verslip and incubated for 20 min to increase the surface interactions between bacteria and coverslip. A constant flow (140 μl min−1) of 7H9 medium was supplied by a syringe pump. Where indicated, isoniazid (Sigma) was added to the flow medium at 5 μg ml^{-1} (1 × MIC) or 50 μg ml^{-1} (10 × MIC). The flow medium was preheated in a custom-made chimney that served as a bubble trap and heating element for maintaining fluid at 37 °C in the sample space. Bacteria were imaged by a Peak Force QNM with a Nanoscope 5 controller (Veeco Metrology) at a scan rate of 0.5 Hz and a maximum Z-range of 5 μm. A ScanAsystfluid can-tilever (Bruker) was used. Continuous scanning provided snapshots at 10 min intervals. Height, peak force error, adhesion, dissipation, deformation, DMTQ7modulus and log DMT modulus were recorded for all scanned images. The peak force error yields affine repre-sentation of the height on the order of 10 nm in the Z axis; this is computed as the differ-ence between the peak force setpoint and the actual value. Images were processed using a custom-made MATLAB program or Gwyddion (Department of Nanometrology, Czech Me-trology Institute). ImageJ was used for extracting bacterial cell profiles in a tabular form.

MATLAB scripts were developed for automating the analysis of experimental data sets and generating graphical representations of data.

Correlated fluorescence and AFM. Correlated fluorescence and AFM images were acquired as described in ref. 4. Briefly, fluorescence images were acquired with an electron-multiplying charge-coupled device (EMCCD) iXon Ultra 897 camera (Andor) mounted on an IX71 inverted optical microscope (Olympus) equipped with an UAPON100XOTIRF ×100 oil immersion objective (Olympus) with the ×2 magnifier in place. Illumination was provided by an MLC (monolithic laser combiner, Agilent) using the 488 or 561 nm laser output coupled to an optical fibre with appropriate filter sets: F36-526 for GFP and F72-866 for FM4-64 (AHF Analysetechnik). For membrane staining, 0.2 µg ml^{-1}FM4-64 or 15 µg ml^{-1}FM1- 43 (Life Technologies) was used. The AFM was mounted on top of the inverted microscope, and images were acquired with a Dimension Icon scan head (Bruker) using ScanAsystfluid cantilevers (Bruker) with a nominal spring constant of 0.7 N m−1in peak force tapping mode at a setpoint <2 nN and typical scan rates of 0.5 Hz. The samples were maintained at 37 °C in 7H9 liquid medium heated by a custom-made coverslip heating holder controlled by a TC2-80-150 temperature controller (Bioscience Tools).

Cell measurements Cell growth measurements. Cell length was measured as the sum of short linear segments tracking along the midline of individual cells. Cell lengths at birth (Lb) and division (Ld) were defined as distances between cell ends. Interdivision time (It) was defined as the time between birth and division. Elongation velocity averaged over the81lifetime of the cell was defined as (Ld–Lb)/It. Elongation rate averaged over the lifetime of the cell was defined as (Ld/Lb)/It. Elongation rate averaged over a specific time interval was defined as (Ln/Li)/(tn–ti), where Li is the initial cell length at time ti and Ln is the cell length at a later time tn. Cell volume was calculated as the sum of the cylindrical volume of each incremental pixel along the midline of the cell using the height as the diameter. Volumes at birth (Vb) and division (Vd) were defined for each cell. The velocity of volume change averaged over the lifetime of the cell was defined as (Vd–Vb)/It. The rate of

volume change averaged over the lifetime of the cell was89defined as (Vd/Vb)/lt. The rate of volume change averaged over a specific time interval was defined as (Vn/Vi)/(tn–ti), whereViis the initial cell length at timeti, andVnis the cell length at a later timetn. Cell profiles were traced along the ridgeline, defined as the highest point in the lateral axis following the length of the cell.

Identifying wave troughs. The longitudinal midline along the length of the cell was extracted manually from the AFM height images for each individual cell at each time point. To reduce the possibility of misidentifying small fluctuations between adjacent height values as waveform undulations, we applied a moving average filter with an averaging window of 100–200 nm. This smoothing treatment of the height profiles did not affect the interpretation of our data, because the distances between undulations are an order of magnitude greater than the smoothing window. The cell profile was flattened by conducting a second-order polynomial fit of the height profile (Supplementary Figs 9b and 18). The points falling below the curvefit and exhibiting opposing slopes on either side are local minima. The second-order polyfit localizes the wave trough position to less than 100 nm of the center of a wave trough. The points localized above the curvefit and exhibiting opposing slopes on either side are local maxima. Wave troughs were annotated in at least two successive time points within a certain spatial range corresponding to the relative increase in cell length over the observed time period (see MATLAB code infile: Cell_Physiology_Analysis, lines 175–179, within the Supplementary Section 'Flatten the cell height'). Identifying the central wave trough. The wave trough closest to the cell center throughout the life of the cell is defined as the central wave trough.

Calculating the average cell surface shape at the site of cell division. Average dimensions of the central wave trough were calculated over the interdivision time (birth to cell cleavage) by averaging the flattened surface height within a range of 1 µm to the left and right of the division position (see MATLAB code infile: TroughProfile_Morphology). Data were collected at 197 distinct time points throughout the interdivision times of all untreated wild-type

cells. For ease of graphical representation, data from time points were binned into 15 groups. Binned data were graphed in a three-dimensional surface plot. Plotting DNA distributions and identifying anucleate daughter cells. SYTO 17-stained cells were imaged by fluorescence time-lapse microscopy and dual AFM-optical microscopy. Cell profiles were obtained by tracing longitudinal lines along the midlines of the cells. In ΔparB cells, highly asymmetric divisions may lead to the formation of anucleate daughter cells, which were identified as cells with very low or absent DNA signals that cease to grow and divide after birth

9.4.2 References:

1   Monahan, L. G., Liew, A. T., Bottomley, A. L. & Harry, E. J. Division site positioning in bacteria: one size does not fit all. *Front Microbiol* **5**, 19 (2014).

2   Santi, I., Dhar, N., Bousbaine, D., Wakamoto, Y. & McKinney, J. D. Single-cell dynamics of the chromosome replication and cell division cycles in mycobacteria. *Nat Commun* **4**, 2470 (2013).

3   Fantner, G. E., Barbero, R. J., Gray, D. S. & Belcher, A. M. Kinetics of antimicrobial peptide activity measured on individual bacterial cells using high-speed atomic force microscopy. *Nat Nanotechnol* **5**, 280-285 (2010).

4   Odermatt, P. D. *et al.* High-resolution correlative microscopy: bridging the gap between single molecule localization microscopy and atomic force microscopy. *Nano Lett* **15**, 4896-4904 (2015).

5   Dufrene, Y. F. Towards nanomicrobiology using atomic force microscopy. *Nat Rev Microbiol* **6**, 674-680 (2008).

6   Meniche, X. *et al.* Subpolar addition of new cell wall is directed by DivIVA in mycobacteria. *Proc Natl Acad Sci U S A* **111**, E3243-3251 (2014).

7   Mannik, J. & Bailey, M. W. Spatial coordination between chromosomes and cell division proteins in *Escherichia coli*. *Front Microbiol* **6**, 306 (2015).

8   Wu, Y., Sims, R. C. & Zhou, A. AFM resolves effects of ethambutol on nanomechanics and nanostructures of single dividing mycobacteria in real-time. *Phys Chem Cgem Phys* **16**, 19156-19164 (2014).

9   Trojanowski, D. *et al.* Choreography of the *Mycobacterium* replication machinery during the cell cycle. *mBio* **6**, e02125-02114 (2015).

10   Santi, I. & McKinney, J. D. Chromosome organization and replisome dynamics in *Mycobacterium smegmatis*. *mBio* **6**, e01999-14 (2015).

11   Dufrene, Y. F. Atomic force microscopy in microbiology: new structural and functional insights into the microbial cell surface. *mBio* **5**, e01363-14 (2014).

12   Touhami, A., Jericho, M. H. & Beveridge, T. J. Atomic force microscopy of cell growth and division in *Staphylococcus aureus*. *J Bacteriol* **186**, 3286-3295 (2004).

13   Li, Z., Trimble, M. J., Brun, Y. V. & Jensen, G. J. The structure of FtsZ filaments in vivo suggests a force-generating role in cell division. *EMBO J* **26**, 4694-4708 (2007).

14   Moll, A., Schlimpert, S., Briegel, A., Jensen, G. J. & Thanbichler, M. DipM, a new factor required for peptidoglycan remodelling during cell division in *Caulobacter crescentus*. *Mol Microbiol* **77**, 90-107 (2010).

15   Takade, A., Takeya, K., Taniguchi, H. & Mizuguchi, Y. Electron microscopic observations of cell division in *Mycobacterium vaccae* V1. *J Gen Microbiol* **129**, 2315-2320 (1983).

16   Fleurie, A. *et al.*   MapZ marks the division sites and positions FtsZ rings in *Streptococcus pneumoniae*. *Nature* **516**, 259-262 (2014).

17   Lutkenhaus, J., Pichoff, S. & Du, S. Bacterial cytokinesis: from Z ring to divisome. *Cytoskeleton* **69**, 778-790 (2012).

18   Huang, K. C. & Ramamurthi, K. S. Macromolecules that prefer their membranes curvy. *Mol Microbiol* **76**, 822-832 (2010).

19   Laloux, G. & Jacobs-Wagner, C. How do bacteria localize proteins to the cell pole? *J Cell Sci* **127**, 11-19 (2014).

20   Ramamurthi, K. S., Lecuyer, S., Stone, H. A. & Losick, R. Geometric cue for protein localization in a bacterium. *Science* **323**, 1354-1357 (2009).

21   Huang, K.C., Mukhopadhyay, R., Wen, B., Gitai, Z., Wingreen, N.S. Cell shape and cell-wall organization in Gram-negative bacteria. *PNAS* **105**, 19282-19287 (2008).

22   Jutras, B. L., Scott, M., Parry, B., Biboy, J., Gray, J., Vollmer, W., Jacobs-Wagner, C. Lyme disease and relapsing *Borrelia* elongate through zones of peptidoglycan synthesis that mark division sites of daughter cells. *PNAS* **113**, 9162-9170 (2016).

23   Bernhardt, T. G. & de Boer, P. A. SlmA, a nucleoid-associated, FtsZ binding protein required for blocking septal ring assembly over chromosomes in *E. coli*. *Mol Cell* **18**, 555-564 (2005).

24   Singh, B. *et al.*   Asymmetric growth and division in *Mycobacterium* spp.: compensatory mechanisms for non-medial septa. *Mol Microbiol* **88**, 64-76 (2013).

25   Sun, Q. & Margolin, W. Effects of perturbing nucleoid structure on nucleoid occlusion-mediated toporegulation of FtsZ ring assembly. *J Bacteriol* **186**, 3951-3959 (2004).

26   Wakamoto, Y. *et al.* Dynamic persistence of antibiotic-stressed mycobacteria. *Science* **339**, 91-95 (2013).

27   Zhang, W. Y., Ferguson, G. S., Tatic-Lucic, S. Elastomer-supported cold welding for room temperature wafer-level bonding. *Proc IEEE Micr Elect* 741-744 (2004).

28   Erickson, B. W., Coquoz, S., Adams, J. D., Burns, D. J., Fantner, G. E. Large-scale analysis of high-speed atomic force microscopy data sets using adaptive image processing. *Beilstein J Nano* **3**, 747-758 (2012)

29   Hett, E. C., Chao, M. C., Deng. L. L., Rubin, E. J. A mycobacterial enzyme essential for cell division synergizes with Resuscitation-Promoting Factor. *PLoS Pathog* **4**, e1000001 (2008)

30   Ginda, K., Bezulska, M., Siolkiewicz, M., Dziadek, J., Zakrzewska-Czerwinska, J., Jakimowicz, D. ParA of *Mycobacterium smegmatis* co-ordinates chromosome segregation with the cell cycle and interacts with the polar growth determinant DivIVA. *Mol Micro* 87(5), 998-1012 (2013)

Chapter 10   Appendix - Tools

10.1 Introduction

In this chapter, several experiments are presented. They are separated from the other chapters as they have been done either for other projects or failed to produce satisfactory results and would be improved if I had more time.

10.2 AFM fluidic system

To image live bacteria under optimal conditions using the AFM Multimode 5 (Figure 72), a fluidic system had to be built and conditions for imaging had to be established. The optimal flow rate of the medium had to be determined in order to maintain a sufficient temperature and fresh nutrient supply in the imaging chamber while keeping the flow rate low enough so as to avoid washing the cells away or introducing imaging noise by physically perturbing the submerged cantilever. In the setup that we settled on, a two-syringe pump pushes the flow medium through an inflow connected to small-bore tubing; the inflow tubing is connected to the imaging chamber and the outflow tubing allows removal of the waste medium from the opposite side of the imaging chamber.
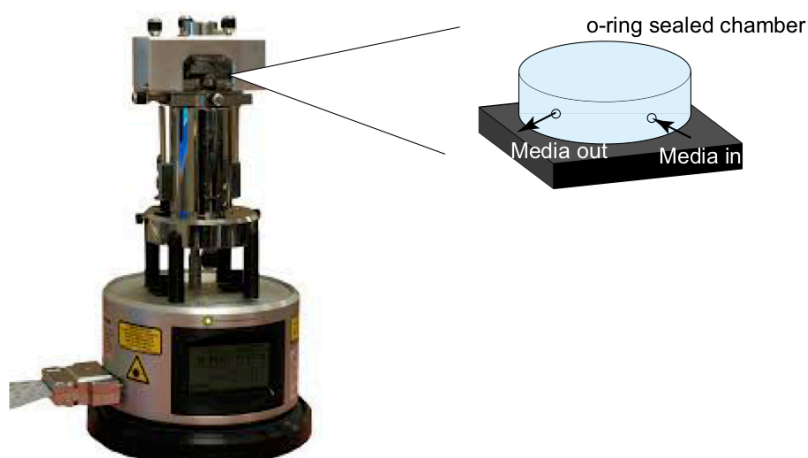
Figure 72 Schematic representation of the Multimode Fluidic Path

The Multimode AFM has an o-ring sealed imaging chamber with a media inlet and outlet. Image adapted from the Multimode Instruction Manual Bruker.

In most experiments we used standard Middlebrook 7H9 medium. When we tried preheating the medium to 37°C we found that bubbles would form and enter the imaging chamber; these bubbles disrupted imaging by deflecting the cantilever-focused laser. To overcome this problem, we tried several different designs for bubble traps and finally settled on a metal-housing bubble trap construction (Figure 73). The idea of the trap is to prevent bubbles from entering the inflow tubing and to keep some medium stored in the trap in order to maintain a constant flow of medium even when bubbles are present. When bubbles enter the trap, they accumulate at the upper part of the trap while medium continues to flow through the outlet, which is lower than the inlet. A coil with high resistance is rolled around the cylindrical part of the trap. The electrical current through the coil is controlled by a temperature controller element, which can be set at the desired temperature. The reduced distance between the heater and the imaging chamber allowed us to reduce the heater from 65°C to 45°C in order to obtain the target temperature of 37°C in

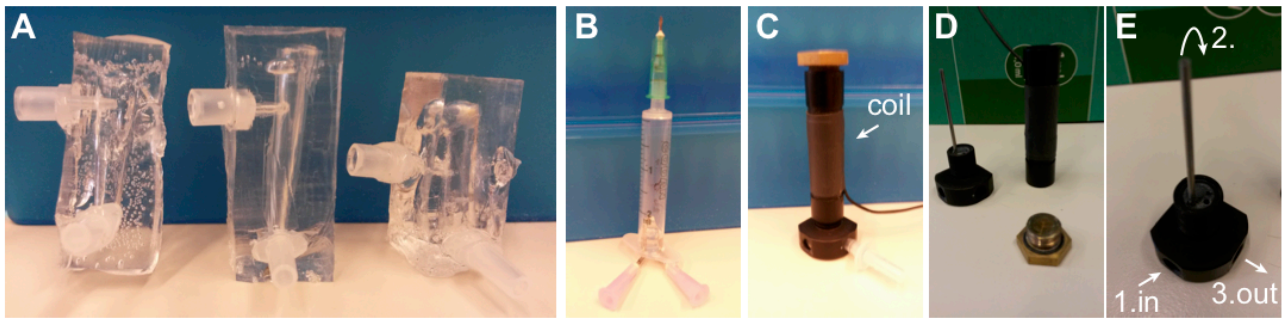the imaging chamber at a constant flow velocity of 120 µl/min.

Figure 73 Homemade heating bubble trap evolution and schematic

Bubble traps were constructed first (**A**) in PDMS, (**B**) in plastic and PDMS with a cap, (**C**) machined in metal with a heating coil. (**D**) Separate elements are shown disassembled. (**E**) Representation of the 7H9 media path.

10.3 Photoswitched Wag31-Dendra2 relocalizes at the new septum

Previously in our laboratory the Wag31 marker was shown to localize at the cell poles. When a new pole is produced, Wag31 appears at the septum location and is a marker for cytokinesis as the two cytoplasms are then separated (Santi et al. 2013).

We observed that the amount of Wag31 protein decreases at the old pole when it increases at the new pole. In order to understand if this accumulation of Wag31 at the new pole was solely due to the new production of Wag31 or if the septal Wag31 was a re-localization of the polar Wag31, I constructed a Wag31-Dendra2 *M. smegmatis* strain (Figure 74). I constructed a plasmid containing the Wag31 protein fused with the Dendra2 photoswitchable fluorescent protein by Gibson assembly method. Before photoswitching, the Dendra2 protein emits in Green. After a pulse of blue light (350nm), which needed to be optimized for *M. smegmatis* growing in a time-lapse experiment, a partial conversion of the protein is made. The majority of the proteins have then a shifted fluorescent spectrum.

This tool allows the distinction between « old proteins » in red and « new proteins » in green. The red protein concentration will decrease over time due to dilution and slightly due to photobleaching. The green protein concentration on the other hand will increase as new proteins are constantly produced (Figure 74A). A time-lapse experiment was set up in a microfluidic device using the strain *M. smegmatis* Wag31-Dendra2. The cells were imaged for a few hours until small colonies were obtained. After photoswitching they were further imaged in FITC and TRITC channels. The old Wag31-Dendra2 proteins in red were localized at the newly formed poles indicating a relocalization of the protein from the old poles (white arrow Figure 74B, Hannebelle & al. in review/2019).

We conclude that the photoswitching Dendra2 protein enables us to follow old and new proteins production, therefore allowing us to discover the relocalization of Wag31 from the old poles to the new poles.
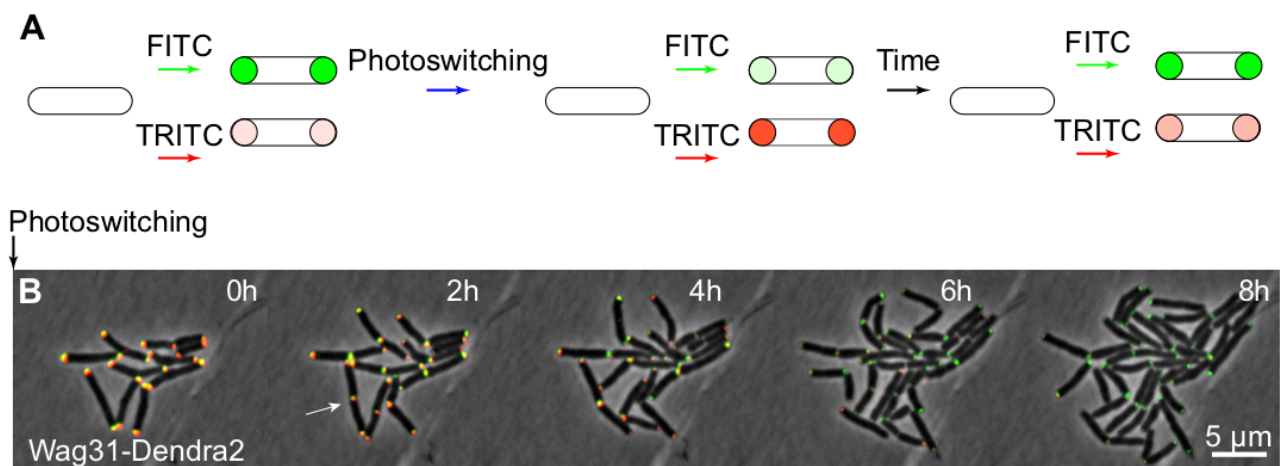
Figure 74. Wag31-Dendra2 and photoswitching

(A) Schematic representation of Dendra2 photoswitching. When a cell is imaged with FITC and TRITC, it emits in green and red respectively. By shining blue light, fluorophores are partially converted from green to red. New fluorophores are produced in Green. **(B)** *M. smegmatis* Wag31-Dendra2 was cultured in a microfluidic device and imaged by time-lapse microscopy at 10-minute intervals and imaged in fluorescence by FITC and TRITC. Some proteins are relocalized (shown by the white arrow).

10.4 **Wag31-Dendra2 localizes along the chained ΔripA mutant**

The peptidoglycan hydrolase, Rpf-interacting protein A, RipA (MSMEG_3153) forms chains of cells when the gene is knocked out (Hett & Rubin 2008, Odermatt et al. accepted/2019). In these studies, a *ripA* gene is under the control of the tetracycline repressor gene integrated at the *attB* site. The membrane stain FM4-64 revealed that the elongated phenotype was actually a chain of cells. As FM4-64 can only be used for short time-lapse due to its toxicity, I constructed the strain Δ*ripA* Wag31-Dendra2. I first constructed an integrative plasmid by fusing Wag31 to the Dendra2 fluorescent protein by Gibson assembly method. Clones were confirmed by PCR and sequencing. This strain was constructed for further experiments (Figure 75).

We conclude that the chained phenotype in Δ*ripA* Wag31-Dendra2 RipA depleted strain is composed of several cells separated by septums and is not cells with a filamented phenotype.
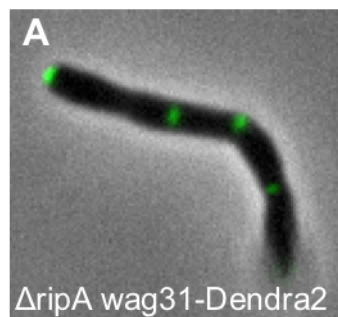
Figure 75. Snapshot fluorescence image of *M. smegmatis* Δ*ripA* Wag31-Dendra2

Multiple Wag31-Dendra2 foci are localized in a single cell.

10.5 Importance of the Shine-Dalgarno sequence for FtsZ-Dreiklang imaging by super-resolution optical fluctuation imaging

To image FtsZ rings using super-resolution optical fluctuation imaging (SOFI), the strain FtsZ-Dreiklang was constructed to have a suitable fluorophore for SOFI imaging. I first constructed an integrative plasmid containing FtsZ under the control of the UV15 promoter, fused to the Dreiklang fluorescent protein. Colonies were confirmed by PCR and sequencing.

The FtsZ-Dreiklang strain showed multiple rings and strong cytoplasmic expression. According to a previous study (Woong Park et al. 2011, Figure 76A), a single nucleotide change in the Shine-Dalgarno sequence can decrease the amount of expression. We constructed two strains containing the Shine-Dalgarno sequence n°3 and n°4. The strain with the sequence n°4 showed a phenotype similar to the FtsZ-GFP strain (Figure 76B). Mélanie Hannebelle and Azat Sharipov further used it for super-resolution imaging of the FtsZ-Dreiklang ring (Figure 76C).

This experiment shows the importance of the Shine-Dalgarno sequence in the amount of expressed proteins and the usability of the FtsZ-Dreiklang for SOFI imaging.
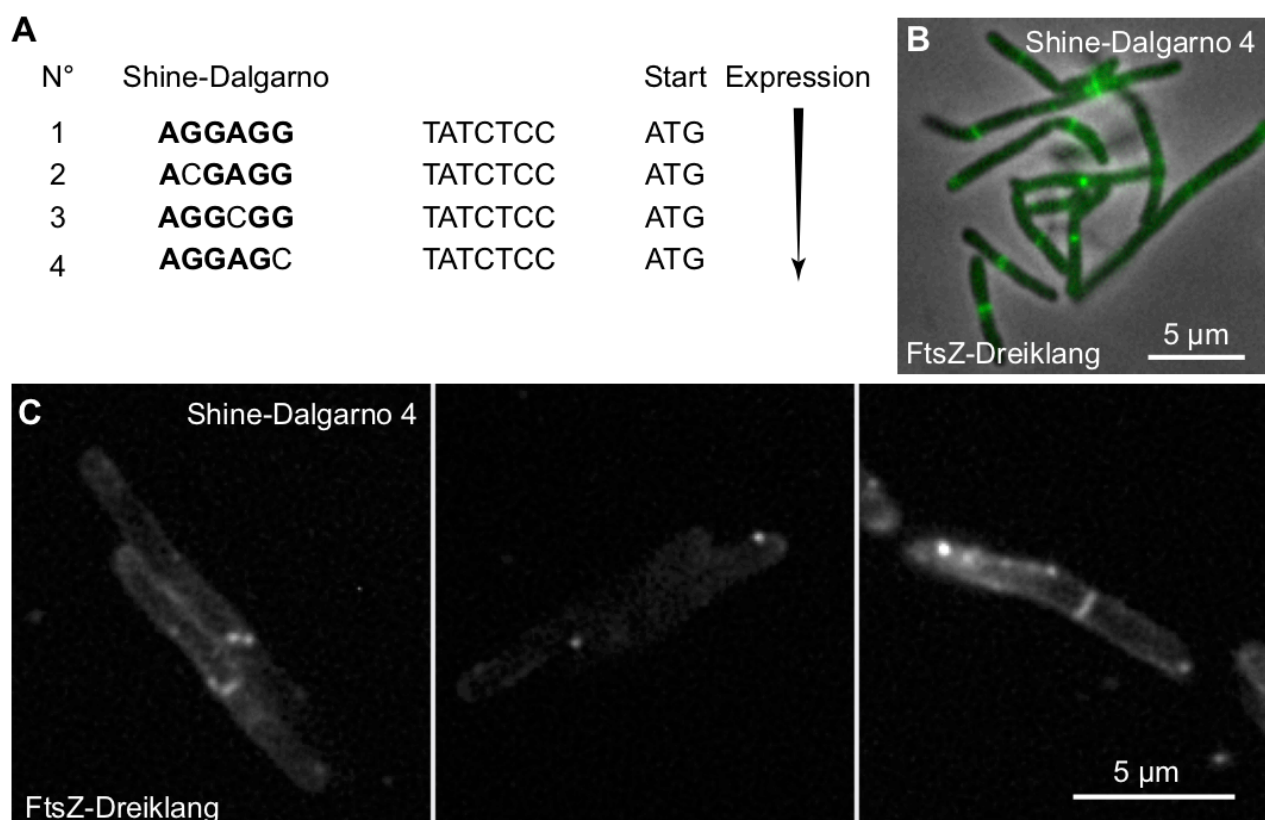
Figure 76. FtsZ-Dreiklang and mutated Shine-Dalgarno sequences

(A) Adapted from (Woong Park et al. 2011), Changing one base in the Shine Dalgarno sequence gives a decreasing amount of protein produced from sequence n°1 to sequence n°4. **(B)** Wide-field fluorescent microscopy snapshot taken from *M. smegmatis* FtsZ-Dreiklang, Shine-Dalgarno sequence n°4. **(C)** SOFI image taken by Mélanie Hannebelle and Azat Sharipov of *M. smegmatis* FtsZ-Dreiklang, Shine-Dalgarno sequence n°4.

10.6 Cloning FtsK-mcherry

As one of my goals was to characterize the timing of FtsK appearance compared to other cell division proteins, I constructed a red version of the *M. smegmatis* FtsK-GFP strain. This FtsK-mCherry was constructed by double recombination using a suicide plasmid based on pJG1100 (Figure 33 for recombination steps). The successful first recombination

was confirmed by PCR and sequencing. Unfortunately, the second recombination was correct according to the PCRs and sequencing results but the mCherry proteins seemed to be cleaved from the FtsK protein (Figure 77).

We conclude that mCherry fluorescent protein is more easily cleaved compared to other fluorescent proteins and the cleavage of the fluorescent protein should be checked in case of a homogenous distribution in the cell.
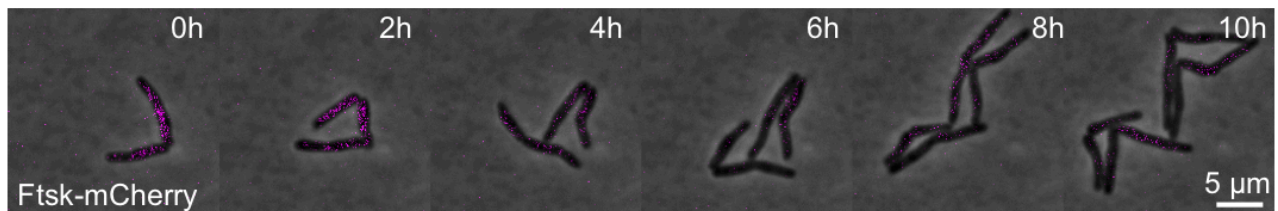
Figure 77. Time-lapse imaging of *M. smegmatis* FtsK-mCherry

FtsK-mCherry was cultured in a microfluidic device and imaged by time-lapse microscopy at 15-minute intervals until small colonies were obtained. mCherry seemed to be a protein more easily cleaved than GFP from its fusion protein.

10.7 Tagging the mycobacterial terminus using a *parB* and *parS* from *Lactococcus lactis* and the prophage attΩ

In *M. smegmatis* replication starts at the origin of replication (*ori*) and finishes at the terminus of replication (*ter*). During division the origin is duplicated and is segregated in the two daughter cells. *ter* is known to be localized at the future septum location and is then present in each daughter cell. To investigate if the terminus is sometimes located at the other side of the forming septum, especially in ΔparA or ΔparB cells, I constructed a parB-mKate2 *parS* strain. I first constructed a plasmid containing the ParB protein from

Lactococcus lactis (*L. lactis*), fused to the mKate2 protein. I integrated this construction at the prophage site attb behind the hsp60 strong promoter. ParB from *L. lactis* was shown to bind specifically to the *parS* sequence from *L. lactis* (van Raaphorst et al. 2017). I constructed a plasmid where the *parS* sequence from L. *lactis* was added in a plasmid containing the prophage system attΩ (Pope et al. 2013), (Figure 78A). Therefore, parS from L. *lactis* was integrated at the *M. smegmatis* terminus of replication. However, a first strain was constructed where the ParB-mKate2 and the parS sequence were integrated at the attB site and attΩ sites respectively. This strain did not show a dotted phenotype indicating the location of the terminus. The second strain was constructed as a control, where ParB-mKate2 was integrated at the attB site but no *parS* sequence was added.

We conclude that tagging the terminus using the ParB/*parS* system and the attΩ site was unsuccessful maybe due to the choice of promoters.
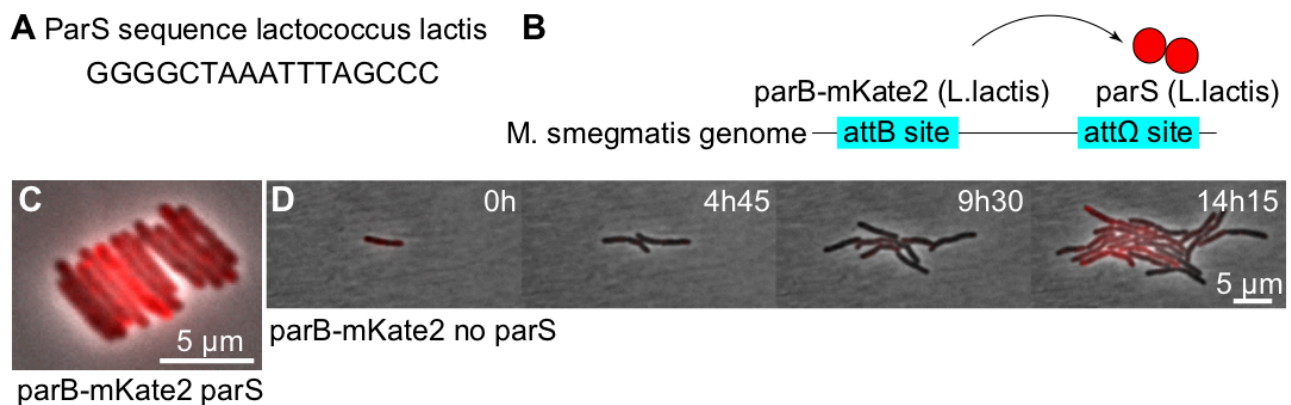
Figure 78. Tagging mycobacterial terminus

(A) Palindromic *parS* sequence of *Lactococcus lactis* **(B)** The mycobacterial prophages systems are used to integrate ParB-mKate2 at the attB site and *parS* at the attΩ site. **(C)** *M. smegmatis* snapshot of parB-mKate2 *parS* **(D)** Time-lapse microscopy imaging of parB-mKate2 without *parS* sequence.

10.8 Conclusion

In this chapter I presented some work done for other projects such as the setting up of the AFM fluidic system as well as building a metal heated bubble trap. I also constructed some mutants such as Wag31-Dreiklang which was used for another story (Hannebelle & al. in review/2019). The constructed strains presented in this chapter highlight the importance of a promoter or its Shine-Dalgarno sequence, therefore the importance of the expression level of a given protein for a correct localization.

Chapter 11

11.1 List of constructed strains and corresponding plasmid used

New strain constructed	plasmid used	background strain
ΔparA hlp-dendra2	Hlp-Dendra2	ΔparA
ΔparB ftsk gfp	pJG ΔparB =pIS294	ftsk-gfp
ΔparB ftsk gfp::parB +its promoter	parB +its promoter	ΔparB ftsk gfp
ΔparB ftsk gfp::parB +UV15 promoter	UV15 promoter	ΔparB ftsk gfp
ΔparB ftsk gfp::parB	pJGparB	ΔparB ftsk gfp
ftsk gfp	pJG ftsk-GFP = pIS245	wt mc^{2}155
ftsk gfp wag mcherry	Wag31-mCherry = pIS233	ftsk gfp
ftsk gfp parB mcherry	parBmcherry =pIS251	ftsk gfp
ftsk-gfp hlp-mcherry	hlp-mcherry	ftsk gfp
recA gfp ΔparB	pJG ΔparB = pIS294	recA gfp
ftsk mcherry	pJG-ftsk mcherry	wt mc^{2}155
wt ftsk-HA	pJG ftsk-HA	wt mc^{2}155
ftsk-HA ΔparA	pJG ΔparA	wt ftsk-HA
ftsk-HA ΔparB	pJG ΔparB =pIS294	wt ftsk-HA
Δftsk ftsk +promoter	ftsk +promoter	Δftsk 1st HR
Δftsk ftsk DAS+4 sspB	ftsk DAS+4; sspB	Δftsk prom_ftsk
Δftsk ΔparA ftsk DAS+4 sspB	ftsk DAS+4; sspB	Δftsk ΔparA prom_ftsk

Δftsk ΔparA ftsk + promoter	pJG ΔparA	Δftsk prom_ftsk
Δftsk ΔparA ftsk + promoter sspB	sspB	Δftsk ΔparA prom_ftsk
Δftsk ΔparB ftsk + promoter	pJG ΔparB = pIS294	Δftsk + ftsk + promoter
Δftsk ΔparB ftsk DAS+4 sspB	ftsk DAS+4; sspB	Δftsk ΔparB prom_ftsk
Δftsk parBmcherry ftsk + promoter	pJGparBmcherry =pIS251	Δftsk ftsk prom_ftsk
Δftk parBmcherry ftsk DAS+4 sspB DAS+4	sspB	Δftsk parBmCherry ftsk DAS+4
Δftsk parBmcherry ftsk DAS+4 rom_ftsk	ftsk DAS+4	Δftsk parBmcherryp-
Δftsk ΔparA parB-mcherry ftsk+promoter mcherry prom_ftsk		pJG ΔparA Δftsk parB-
Wag-Dendra2	Wag-Dendra2	wt mc^{2}155
ΔparB ftsZ-GFP	ftsZ-GFP=pND275	ΔparB
ftsZ-mEos2	ftsZ-mEos2	wt mc^{2}155
ftsZ-Dreiklang	ftsZ-Dreiklang	wt mc^{2}155
ftsZ-Dreiklang shine dalgarno 4	ftsZ-Dreiklang sh. d. 4	wt mc^{2}155
parB-mCherry Hlp-Dendra2	Hlp-Dendra2	parB-mCherry
wt Hlp-Dendra2	Hlp-Dendra2	wt mc^{2}155
wt Hlp-mCherry	Hlp-mCherry	wt mc^{2}155
ΔripA Wag31-Dendra2	Wag31-Dendra2	ΔripA
lsr2-Dendra2	lsr2-Dendra2	wt mc^{2}155

11.2 List of plasmid, description and source information

Plasmid Name	Description	Source
pJG1100	Km^R, Hyg^R, *sacB*. Allelic-exchange suicide vector containing *aph*, *hyg*, and *sacB* markers.	J. Gomez
pIS251	Km^R, Hyg^R, *sacB*. pJG1100::*parB_mCherry* translational fusion for allelic exchange.	I. Santi
pIS294	Km^R, Hyg^R, *sacB*. pJG1100 *ΔparB* to delete *parB* gene by allelic exchange.	I. Santi
pIS245	Km^R, Hyg^R, *sacB*. pJG1100::*ftsK_GFP* translational fusion for allelic exchange.	I. Santi
pJGΔparA	Km^R, Hyg^R, *sacB*. pJG1100 *ΔparA* to delete *parA* gene by allelic exchange.	J. Ven
pJG parB	Km^R, Hyg^R, *sacB*. pJG1100::*parB* translational fusion for allelic exchange.	J. Ven
pJG ftsK-HA	Km^R, Hyg^R, *sacB*. pJG1100::*ftsK-HA* translational fusion for allelic exchange.	J. Ven
pGMS2	Km^R, Hyg^R, *sacB*. pJG1100::*recA-GFP$_{des}$* transcriptonal fusion for allelic exchange.	G. Manina
pIS233	Km^R. pMV361 containing Wag31-mCherry expressed from hsp60 promoter. integrates into the mycobacteriophage att-L5 site.	I. Santi
pIS220	Km^R. pMV361 containing *wag31-gfp* under the control of the *hsp60* promoter. integrates into the mycobacteriophage att-L5 site.	I. Santi

Hlp-Dendra2	Km^R. pIS220 containing *hlp-dendra2* under the control of the *hsp60* promoter. integrates into the mycobacteriophage att-L5 site.	J. Ven
prom_parB	Km^R. pIS220 containing *parB* under the control of its native promoter. integrates into the mycobacteriophage att-L5 site.	J. Ven
UV15_parB	Km^R. pIS220 containing *parB* under the controlof the *UV15* promoter. integrates into the mycobacteriophage att-L5 site.	J. Ven
hlp-mcherry	Km^R. Hlp-Dendra2 plasmid containing *hlp-mcherry* under the control of the *hsp60* promoter. integrates into the mycobacteriophage att-L5 site.	J. Ven
ftsk + promoter		J. Ven
ftsk DAS+4	Km^R. pGMCK-T38S38-750-luxAB-DAS+4 based vector where luxAB is replaced in frame by ftsk. integrates into the mycobacteriophage att-L5 site.	J. Ven
pGMCtN-TSC10M1-sspB	Nourseothricin^R. pDE43-MCtN based vector. TSC10M1-sspB. integrates into the mycobacteriophage att-Tweety site.	D. Schnappinger Addgene # 49521
ftsZ-mEos2	Hyg^R. pND275 based vector. Containing *ftsZ-mEos2* under the control of the *UV15* promoter. integrates into the mycobacteriophage att-L5 site.	J. Ven
ftsZ-Dreiklang	Hyg^R. pND275 based vector. Containing *ftsZ-Dreiklang* under the control of the *UV15*	J. Ven

	promoter. integrates into the mycobacteriophage att-L5 site.	
ftsZ-Dreiklang shine dalgarno 4	Hyg^R. pND275 based vector. Containing *ftsZ-Dreiklang* under the control of the *UV15* promoter. Mutated Shine-Dalgarno sequence. integrates into the mycobacteriophage att-L5 site.	J. Ven
Hlp-mCherry	Km^R. pIS233 based vector. Containing *hlp-mCherry* under the control of the *hsp60* promoter. integrates into the mycobacteriophage att-L5 site.	J. Ven
Wag31-Dendra2	Km^R. pIS220 based vector. Containing *wag31-dendra2* under the control of the *hsp60* promoter. integrates into the mycobacteriophage att-L5 site.	J. Ven
Lsr2-Dendra2	Km^R . Hlp -Dendra2 based vector. Containing lsr2-Dendra2 under the control of the *hsp60* promoter. integrates into the mycobacteriophage att-L5 site.	J. Ven
pGMCK-T38S38-750-luxAB-DAS+4	Km^R. expresses luxAB-DAS+4 under the control of a promoter containing PtetO-4C5G; constitutively expresses reverse TetR (tetR38); integrates into the mycobacteriophage att-L5 site.	D. Schnappinger Addgene # 49518
pKR03	Hyg^R. Omega integration region.	Welkin Pope
pGEX6P-1-Dendra2	Ampicillin^R. Dendra2 under the control of the *tac* promoter.	P. Pantazis Addgene # 82436

Km^R : Kanamycin resistant

Hyg^R : Hygromycin resistant

11.3 List of plasmid and oligo used

Plasmid	Cloning method used	Primers or oligos used (5'- 3')
pJG ΔparA	Gibson assembly	parA UP F: gccgatccccgtcccccgcg-tATCCGTTCCTGCGACCCC parA UP R: atcatgctgcaGCTCATCTCCTGCCCGTTC parA DWN F: aggagatgagcTGCAGCATGATCAG-TAGGCGTACAGC ParA DWN R: aaggtgaatcccataatctgcGGAGCGAC-CGATGCGCGC pJG 3199 R: ACGCGGGGGACGGGGATC pJG 3199 F: GCAGATTATGGGATTCACC
pJG ΔparA	Colony PCR	Dtct D_ParA UP F: GGGAGTGCGGAGGATGTTT Dtct D_ParA UP R: CGTCTCCTGCTCATCACTGC Dtct D_parA DWN F: CAAACCGGGACGGAACAAGT Dtct D_parA DWN R: AAAGTACACCCGCCGCG
pJG ΔparB	Colony PCR	Detect DparB UP F: AGTCCCCCAACACCTTCACC Detect DparB UP Rn: ATCAGTAGGCGTACAGCGGG Dtct DparB DWN Fn: ACCGGCGAACTGTCACAGTG Detect DParB DWN R: CGTCGGCAAGACGACGA
pJG ParB-mCherry	Colony PCR	Detect DparB UP F: AGTCCCCCAACACCTTCACC Detect DParB UP R: GAGTTCGGGTCGGTGGA D_parbmCh DWN F: AGTGACAAAACGAGCGCGT

		D_parBmch DWN R: ATCGAACCGAACCCGCG
pJG Ftsk-GFP	Colony PCR	Dtct FtsK_gfp_UP_F: CGCCGACCTCATGATGACC
		Dtct FtsKn UP R: CCTCGGCAACACGCGAATG
		Dct FtsK_gfp DWN F: AACGGTGCCGAACCCGAG
		Dtct FtsKn DWN R: ATCGGATCGGCCAGTGCA
pJG ftsk-HA	CPEC cloning	pJG FtsK HA R: GAACTCCTCGCCGTCCTC
		pJG FtsK HA F: GCCGAGAGTCCTACAGGGTC
		HA with stop F: CAT ACG ATG TTC CAG ATT ACG CTT GAG CCG AGA GTC CTA CAG GGT C
		HA with stop R: GAC CCT GTA GGA CTC TCG GCT CAA GCG TAA TCT GGA ACA TCG TAT G
pJG ftsk-HA	Colony PCR	colony PCR HA F: GGTGAAACCCGAGGATCTGG
		colony PCR HA R: CGCCGAGTTCCTCGACC
pJG parBc	Gibson assembly	pJG3199 digested by EcorV and PacI.
		parBc_DWN2 F: CCT CGA CGA CCT CGA CTC TAG ACT TAA TCG CCG ACA GCA GGC CGG
		parBc_DWN2 R: CCA GAA CGA GTA AAA GTC GGT GTC AGC GGA CGA CC
		parB2_F: CTG ACA CCG ACT TTT ACT CGT TCT GGG CGC TC
		parB2_R: GCA GGA GAC GAG CAT GAA TCA GCC GGC ACG C
		parBc_UP2_F: CCG GCT GAT TCA TGC TCG TCT CCT GCT CAT CAC TGC

		parBc_UP2_R: TAA AAA CGC AAA AGA AAA TGC CGA TCG ACC CCC AGG GCA ACG C
pJG parBc	Colony PCR	Detect DparB UP F: AGTCCCCCAACACCTTCACC Detect DparB UP Rn: ATCAGTAGGCGTACAGCGGG Dtct DparB DWN Fn: ACCGGCGAACTGTCACAGTG Detect DParB DWN R: CGTCGGCAAGACGACGA
Wag31- Dendra2	Gibson assembly	dendra2_wo_STARTF : AGT TCA ACC GCG GCA ACA ACA ACA CCC CGG GAA TTA ACC dendra2_wo_STARTR : GGC CAT TGC GAA GTC ATT ATT TAC CAC ACC TGG CTG GG pIS220 wag F : ATA ATG ACT TCG CAA TGG CCA AG pIS220 wag R : GTT GTT GCC GCG GTT GAA C
Hlp-Dendra2	Gibson assembly	wag_dendra2F : AAC ACC CCG GGA ATT AAC CTG wag_dendra2R : CAT ATG TAT ATC TCC TTC TTA GAT TCC TCC GG hlp_no_STOP_F : TCT AAG AAG GAG ATA TAC ATA TGA TGA ACA AAG CGG AGC TCA TCG AC hlp_no_STOP_R : AGG TTA ATT CCC GGG GTG TTC TTG CGG CCC TTC TTG GC
Hlp-mCherry	Gibson assembly	wag_mcherry R: GATTCCTCCGGATCGGGG wag mcherry F: GGCTCAGGTGCTAGCGTG hlp mch F: atccccgatccggaggaatcATGAACAAAGCG-GAGCTCATCGAC hlp mch R: ctcacgctagcacctgagccCCTGCGGCCCTTCTT-

		GGC
ParB +its promoter	Gibson assembly	parB promoter_F: tcccgttgaatatggctcatGGACGAT-TACCCCCTTTG parB promoter_R: ctcgtctcctGGCAATCTCTCCTTGTATTC SD_+_parB F: agagattgccAGGAGACGAGCATGAATCAG SD_+_parB R: aacgcaaaaa-gccccccctccTTACTCGTTCTGGGCGCTC
ParB +UV15 promoter	Gibson assembly	UV15 F: tcccgttgaatatggctcatAGAAA-TATTGGATCGTCGG UV15 R: ctcgtctcctTTAAGCATGCGGATCGTG SD_+_parB F: gcatgcttaaAGGAGACGAGCATGAATCAG SD_+_parB R: aacgcaaaaa-gccccccctccTTACTCGTTCTGGGCGCTC
Ftsk + pro-moter	Gibson assembly	wag den_ftsk_F: AATAATGACTTCGCAATGGCCA wag den_ftsk_R: CATATGTATATCTCCTTCTTAGAT-TCCTCCG ftsk_gfp F: tctaagaaggagatatacatatgTTGCTCATACAAC-GATCAC ftsk gfp R: gccattgcgaagtcattattCTATTT-GTATAGTTCATCCATGCC
Ftsk DAS+4	Gibson assembly	pGM_ftsk_gfp_DASR: GTT GTA AAA CGA CGG CCA GTG AAT TAT CAA C pGM_ftsk_gfp_DASF: ACT CGG AAC TTG TTT ATT GCA GCT TAT AAT GGT TAC hsp_hlp_dendra2 R: AAG CTG CAA TAA ACA AGT TCC

		GAG TTT ACC ACA CCT GGC TGG G hsp_hlp_dendra2 F: AAT TCA CTG GCC GTC GTT TTA CAA CTA GAG GTG ACC ACA ACG ACG
Lsr2-Dendra2	Gibson assembly	lsr2 no STOP F: tctaagaaggagatatacatatgATGGCAAA-GAAAGTGACCGTC lsr2 NO STOP R: aggttaattcccgggggtgttAGTT-GCCGCGTGGAATGC hlp dendra F: AACACCCCGGGAATTAAC hlp_dendra R: CATATGTATATCTCCTTCTTAGAT-TCCTCCGGATC
pJG ΔFtsK	Gibson assembly	FtsKn UP F: ctcgactctagacttaatCCGGCCACCGAACTGATC FtsKn UP R: ctctcggcGGAGCCGTGCGTACATGC FtsKn DWN F: acggctccGCCGAGAGTCCTACAGGG FtsKn DWN R: cgcaaaagaaaatgccgatGTCGAAC-CGGTCGGTGATG
pJG ΔFtsK	Colony PCR	Dtct FtsKn DWN F: GCTTGGCCTTCATGGTGGC Dtct FtsKn DWN R: ATCGGATCGGCCAGTGCA Dtct FtsKn UP F: GACTATGCCGTGCTTGGCG Dtct FtsKn UP R: CCTCGGCAACACGCGAATG